

Understanding emplacement of  
rapidly-emplaced volume-limited lava  
flows from Mount Etna's 2011-2012  
eruption: a multidisciplinary study

Anson Hancock  
MSc (University of Portsmouth)

Submitted in fulfilment of the requirements for the  
degree of Doctor of Philosophy at the University of  
Lancaster, July 2018

## Declaration

I, Anson Hancock, hereby declare that the contents of this thesis are from my own work, except where otherwise stated, and that no part of the work has been submitted for a higher degree elsewhere.

Anson Hancock

July 2018

# Abstract

While the study of emplacement in most literature focuses on long-duration cooling-limited lava flows, the short duration and rapid emplacement of many volume-limited flows impedes their analysis. This thesis aims to improve understanding of the emplacement of short-duration volume-limited lava flows by: (1) employing long-range ground-based visible time-lapse data and thermo-rheological modelling to understand and analyze the importance of different factors which influence lava flow emplacement, and (2) developing a workflow for improving the application of long-range ground-based thermal cameras for studying lava flows.

Results from (1) agreed with previous studies, showing strong correlations between final flow length and the following: total volume, duration, flow field width, number of bifurcations in the proximal zone of the flow, number of confluences, average and maximum advance rate in the proximal zone, and duration of fire fountaining. However, unlike previous studies, no correlation was found between final flow length and mean output rate. Visual analysis identified two flow groups based on morphology within the proximal zone of the flow, and results indicated that differences in advance rates and at-vent initial effusion rates dictated the morphology observed for the two groups. Analysing flow confinement indicated a strong relationship between final length and the distance of confinement of the primary flow. Utilising multiple regression analysis, maximum flow width, duration of flow, and maximum advance rate in the proximal zone produced the best model for flow length in terms of explanatory and predictive power.

By substituting flow widths estimated from the time-lapse data for channel widths, FLOWGO-modelled effusion rates and total volumes were obtained for the primary flows of the 12 May and 19 July 2011 episodes at Mt. Etna which were within the range of values estimated by previous studies. Additionally, using FLOWGO to model flow thickness changes due to

bifurcations of the primary flow produced average flow thickness estimates for the semi-channelized 12 May flow that agreed with estimates from previous studies. However, no thickness estimates were possible using this method for the unconfined 19 July flow. This suggests that substituting flow width for channel width in FLOWGO for unconfined flows is inappropriate and should only be applied to flows with a more channel-like morphology.

A workflow was developed to achieve objective (2) and applied to the 29 August 2011 episode at Mt. Etna to correct ground-based thermal data for atmospheric and viewing effects due to long viewing paths along two different viewing geometries (horizontal- and slant-path). Estimates of flow area, volume, and mean output rate using both viewing geometries were within the range of values reported in the literature. Estimates of surface temperature using the slant-path geometry were within the range of values given by previous studies which measured active lava channels at 0-70 metres distance; however, the complexity of the atmospheric model associated with this viewing geometry made it difficult to automate. Some errors resulted from the large pixel area ( $25 \text{ m}^2$ ) of the long-range thermal data resulting in a greater area of temperature integration. The radiant heat flux profiles produced by the workflow followed the same trends as the SEVIRI-derived profile, although the intensity of the SEVIRI-derived profile was up to five times greater than the workflow profiles.

# Auxiliary Content

Included with this thesis is one DVD, which contains the time-lapse sequences (\*.jpg) used in chapters 3 and 4. The DVD is arranged in the following folders:

- Time-lapse visible images
- Thermal camera images

# Acknowledgements

I would like to thank Dr. Mike James and Dr. Alan Blackburn for all their support, encouragement, and advice throughout the course of my PhD. I would also like to thank Dr. Gaetana Ganci for her hospitality while working with her at INGV Catania. The expertise and guidance provided by Dr. Ganci during my time in Catania helped lay the foundation for the work presented in Chapter 5. Many thanks to Dr. Andrew Harris for his help and insight into the complexities of MODTRAN, FLIR cameras and FLOWGO. A very big thank you to my friends and family for all their support over the course of my PhD. I would also like to thank my wife, Vanessa, for all her endless words of encouragement, her advice and thoughts, and having the patience to lend a hand in editing. Finally, I would like to thank my uncle, Fred Dayton, as without his help and support I would not have made it as far as I have.

# Table of Contents

Abstract.....	II
Auxiliary Content.....	IV
Acknowledgements.....	V
List of Figures .....	IX
List of Tables .....	XIII
Nomenclature .....	XIV
Glossary.....	XVIII
Chapter 1 Introduction .....	1
Chapter 2 Research Background.....	5
2.2 Basaltic Lava Flows.....	5
2.2.1 Surface Morphology of 'A'ā and Pahoehoe Lava .....	5
2.2.2 Cooling- and Volume-Limited Flows .....	8
2.2.3 Simple and Compound Lava Flows .....	9
2.3 Factors Influencing Lava Flow Length .....	10
2.3.1 Rheology.....	10
2.3.2 Effusion Rate .....	10
2.3.3 Erupted Volume .....	12
2.3.4 Cooling Rate .....	13
2.3.5 Slope and Topography .....	14
2.3.6 Channel Complexity .....	16
2.4 Short-Duration Volume-Limited Lava Flows .....	18
2.5 Thermal Remote Sensing .....	20
2.5.1 Principles of Thermal Remote Sensing.....	21
2.5.2 Correction of Thermal Data .....	23
2.5.3 Additional Corrections for Ground-Based Thermal Data.....	26
2.5.4 Calculating Atmospheric Correction Values.....	27
2.5.5 Application of Remote Sensed Thermal Data .....	29
2.6 Time-Lapse Visible Imaging.....	35
2.7 Lava Flow Modelling .....	39
2.8 FLOWGO.....	41
2.9 Mt. Etna.....	43
2.9.1 Background .....	43
2.9.2 Monitoring Mt. Etna .....	45
2.10 Summary .....	46

Chapter 3 Using long-range ground-based visible time-lapse imagery to analyse flow emplacement: a study of short-duration volume-limited lava flows at Mt. Etna from 2011 to 2012 .....	47
3.1 Introduction .....	47
3.2 Volcanic Activity .....	48
3.3 Methodology .....	55
3.3.1 Time-Lapse Data Collection .....	55
3.3.2 Lava Flow Emplacement Analysis .....	57
3.3.3 Statistical Analysis .....	61
3.4 Results .....	65
3.4.1 Flow Emplacement and Morphology Observations and Correlations .....	65
3.4.2 - Flow Front Advance Rates .....	92
3.4.3 Regression Analysis for Flow Length .....	98
3.5 Discussion .....	102
3.5.1 Flow Emplacement and Morphology .....	102
3.5.2 Flow length model .....	108
3.6 Conclusion .....	110
Chapter 4 Using time-lapse imagery and FLOWGO to constrain properties of short-duration volume-limited lava flows .....	111
4.1 Introduction .....	111
4.3 FLOWGO Model and Physical Principles .....	115
4.3.1 Velocity and Effusion Rate Calculations .....	115
4.3.2 Mass Conservation .....	116
4.3.3 Rheology Calculations .....	116
4.3.4 Thermal Conditions in FLOWGO .....	117
4.3.5 Source Terms .....	119
4.3.6 Stopping Conditions .....	119
4.4 Methodology .....	122
4.4.1 Time-lapse Camera Data .....	122
4.4.2 Estimating Flow Front Advance Rates and Flow Widths .....	123
4.4.3 FLOWGO Analysis .....	127
4.5 Results .....	131
4.6 Discussion .....	135
4.6.1 Flow Thickness .....	135
4.6.2 Effusion Rate and Total Volume .....	137
4.6.3 Limitations and Errors .....	138
4.8 Conclusion .....	140

Chapter 5 Improving long-range ground-based thermal remote sensing of lava flows.....	141
5.1 Introduction .....	141
5.2 Workflow for Processing Long-Range Ground-Based Thermal Data .....	145
5.3 Sensitivity to Atmospheric Conditions.....	148
5.4 Case Study: 29 Aug 2011 Event, Mt. Etna.....	148
5.6 Results.....	152
5.6.1 Sensitivity to Atmospheric Conditions.....	152
5.6.2 Case Study.....	152
5.7 Discussion.....	159
5.7.1 Sensitivity .....	159
5.7.2 Case Study.....	159
5.7.3 Viewing Geometries.....	161
5.7.4 Limitations and Application .....	162
5.8 Conclusions .....	163
Chapter 6 Discussion and Conclusions.....	165
6.1 Emplacement of Short-Duration Volume-Limited Lava Flows at Mt. Etna: 2011 and 2012 .....	165
6.2 Comparison to Long-Duration Cooling-Limited Flows at Mt. Etna .....	173
6.3 Long-Range Ground-Based Visible Time-Lapse Data – Monitoring Applications .....	174
6.3 Long-Range Ground-Based Thermal Data.....	178
6.4 Future Work .....	182
6.5 Conclusions .....	183
Works Cited.....	188
Appendix 1 – MODTRAN output file of transmittance and upwelling radiance calculated from LTN file at 100 m steps for a range of 0-100 km using a horizontal-path geometry .....	209
Appendix 2 – Excerpt from MODTRAN LTN file for a horizontal-path viewing geometry.....	216
Appendix 3 – Matlab code for extracting transmittance and upwelling radiance from MODTRAN outputs .....	217
Appendix 4 – Excerpt from MODTRAN LTN file for a slant-path viewing geometry .....	219
Appendix 5 – Matlab code for generating viewing distance map from DEM.....	220
Appendix 7 – Comparison of meteorological data for 29/05/2011 Event, Mt. Etna, Sicily...	228
Appendix 8 – Model atmospheres for slant-path geometry .....	232
Appendix 9 – Calculated surface temperatures for an apparent temperature of 500 K using model atmospheres created with the NCEP/NCAR Reanalysis 1 meteorological data for 29/08/2011 12:00. ....	236
Appendix 11 – vbs code used by Ganci et al. (2013) for temperature correction which caused the source of the bug in the correction. ....	239

# List of Figures

Figure 2.1 – (a) The typical flow structure of an ‘a’ā flow for an open channel (below) which forms a simple flow front (above). The arrow shows the direction of flow of the molten material (black zones). Large ‘a’ā flows can have flow fronts up to 10 m wide (A-B). (b) Pahoehoe lava flow fronts are typically comprised of multiple small individual lobate structures referred to as “tongues” and “toes” which are fed by lava tube systems. Pahoehoe flow fronts can be up to several meters in width (C-D) (Kilburn, 2000). (c) Active pahoehoe flow (left) flowing over an older ‘a’ā flow, in front of an active ‘a’ā flow (right) (Volcano.oregonstate.edu, 2018). ..... 7

Figure 2.2 – Plot of length versus average effusion rate for 40 lava flows from 19 different volcanoes. Basaltic lavas, ●: A, Askja 1961 (Iceland); C, Cerro Negra 1968; E, Etna (1, 1669; 2, 1911; 3, 1923; 4, 1928; 5, 1971); G, Gituro 1948 (Congo); K, Kīlauea (1, 1955; 2, 1965); L, Laki, 1783 (Iceland); Lp, La Palma 1585; M, Mauna Loa (1, 1851; 2, 1852; 3, 1868; 4, 1887; 5, 1907; 6, 1916; 7, 1919; 8, 1926; 9, 1935; 10, 1942; 11, 1949; 12, 1950); O, Oosima 1951; T, Tenerife 1705; S, Sakurajima 1946. Basaltic andesite lavas, ▲: Ag, Mt Agung 1963 (Bali); H, Hekla (1, 1845/6; 2, 1947); N, Ngauruhoe (1, 1949; 2, 1954); Pc, Pacaya 1961 (Guatemala); Pr, Paricutin (first 8 months 1945); Sn, Santiaguita (Guatemala). Andesite/dacite lavas, Δ: Hb, Hibok-Hibok 1948; Tr, Trident 1953 (Walker, 1973). ..... 11

Figure 2.3 – Plot of flow length against effusion rate (a) and flow volume (b) by Malin (1980) for historic basaltic lava flows at Kīlauea volcano (circles) and Mauna Loa (triangles). Open symbols indicate flows which entered the ocean (Harris & Rowland, 2009). ..... 12

Figure 2.4 – Plot of Malin’s (1980) data from Pinkerton and Wilson (1994) showing the relationship between flow duration, length, and effusion rate (a), and Malin’s (1980) data for high duration (greater than 45 hours) channel-fed flows and the limits of Walker (1973) given as solid lines, with tube-fed and flows with a duration of less than 30 hours removed (Harris & Rowland, 2009). ..... 14

Figure 2.5 – Surface temperature of molten basalt (image shown is 45 seconds after interaction with the obstacle). Blue arrows show the calculated velocity field and show the decrease in velocity prior to and after branching caused by interaction with the obstacle (Dietterich et al., 2015). ..... 17

Figure 2.6 – The spectral density of electromagnetic radiation emitted from blackbody surfaces (an idealized body that absorbs all electromagnetic radiation independent of frequency and incidence angle) for temperatures between -50 °C and 1200 °C (Harris, 2013). ..... 22

Figure 2.7 – The total number of published studies using satellite-based thermal sensors for volcanological applications from 1985-2005 by (a) journal type, (b) feature type studied and (c) main parameters extracted (Harris, 2013). ..... 31

Figure 2.8 – Publications by year from 2000-2010 for studies which used ground-based thermal cameras for volcanological applications by (a) frequency distribution and (b) cumulative total (Harris, 2013). ..... 32

Figure 2.9 – The methodology used by James et al. (2016) for assigning 3D point coordinates to an observed feature in a time-lapse image sequence. (a) Observation points assigned to an object in the registered time-lapse image, C. (b) Using the perspective centre of the camera, p, observation points can be assigned real-world x, y and z coordinates by projecting the point onto the surface of a DEM (modified from James et al., 2016). ..... 36

Figure 2.10 – The photogrammetric processing workflow used by James and Robson (2014) (James & Robinson, 2014). ..... 37

Figure 2.11 – Primary steps and loop processes used in the FLOWGO model (Harris & Rowland, 2015). ..... 42

Figure 2.12 – (a) Tectonic domains and dynamics of Southern Italy. Red outlined area corresponds with the red rectangle marked in Fig. 2.1b. (b) Digital Elevation Model of Mt. Etna. (c) 2011-2014 lava flow field; NSEC (read circle) = New Southeast Crater, SEC = Southeast Crater, BN = Bocca Nuova, C = Voragine Chasm, NEC = Northeast Crater (Viccaro et al., 2015). ..... 44

Figure 3.1 – Map of the flow fields emplaced during 2011 to 2012 at Mt. Etna. NEC = Northeast Crater, VOR = Voragine, BN = Bocca Nuova, SEC = Southeast Crater, NSEC = New Southeast Crater. Red boxes identify the episodes examined in this chapter. Figure edited from Behncke et al., 2014. ..... 49

Figure 3.2 – Location and field of view of the four installation sites. Cameras are coded by colour with coloured cones showing the approximate field of view. ....	56
Figure 3.3 – Selected reference image from the Zoccolaro camera (image taken 13/05/2011 04:33) (a) showing the viewing scene to be geo-referenced to the projected DEM, in red (b). ....	58
Figure 3.4 – (a) Initial fit of the DEM to the Zoccolaro reference image done by Pointcatcher. (b) Final fit of DEM to reference image after manual adjustments. For best results the DEM should be matched to stationary image features. ....	59
Figure 3.5 – Re-projection methodology used in Pointcatcher for assigning 3D coordinates to a feature point in a time-lapse image sequence (James et al., 2012; 2016). Using two of the cameras employed in this study, observation points are assigned to features in the geo-referenced time-lapse images (red circles in inset images). Using the perspective centre of the camera (purple squares), observation points are given real-world x, y and z coordinates by re-projecting the point from the geo-referenced image onto the surface of the DEM (black circles). ....	60
Figure 3.6 – (a) The division of the flow field into three zones based on the slope of the Valle del Bove, where the boundary between Zone 1 and 2 marks the start of the headwall of the Valle del Bove and the boundary between Zone 2 and 3 marks the transition from the headwall to the floor of the Valle del Bove and (b) the slopes within each zone. NSEC = New Southeast Crater. ....	71
Figure 3.7 – Comparison of the two morphologies observed in Zone 1 and the corresponding advance rates. The 12/05/2011 (a) and 24/04/2012 (c) flows are examples of those belonging to Group 1, while the 05/08/2011 (b) and 19/07/2011 flows (d) represent those flows which belong to Group 2. Red boxes delineate the corresponding period of advance rates to the example images. Images are from the Serracozza camera. Background colours: blue = Zone 1, red = Zone 2, green = Zone 3 (Figure 3.7 continues onto the next page). ....	74
Figure 3.8 – Emplacement of the 12 flow fields (a-m) through time. Flow field outlines were created using images from the Zoccolaro camera as they provided the most complete view of the final flow field. The 24 April 2012 flow field (Episode 25) includes a second emplacement map using the Serracozza camera (l) as the Zoccolaro camera (m) inadequately covered the entire flow field due to a viewing misalignment caused by a rock fall. Solid, dashed, and dotted lines show the direction of flow. * identifies those flows which belong to Group 1. (Figure 3.8 continues onto the next 11 pages). ....	76
Figure 3.9 – Examples of the changes in morphology as flows transitioned from Zone 2 to Zone 3 and continued into Zone 3 (the floor of the Valle del Bove) (as seen from Zoccolaro). The changes in morphology all occurred over similar slopes (20°-22°). Blue dashed lines mark the transition from Zone 2 to Zone 3, and red arrows identify the advance of lava flows due to coalescing flow fronts at the Zone 2 and 3 boundaries. ....	91
Figure 3.10 – (a) Visualisation of the error in flow front feature point placement due to oblique view of the cameras, uncertainties in camera orientation, and error in the DEM. The point locations converge as the flow approaches the top of the headwall (transition from Zone 1 to Zone 2) of the Valle del Bove, where viewing direction becomes more orthogonal. (b) Despite the differences in point locations, calculated advance rates from the two cameras are in good agreement and a combined advance rate profile can be determined using a moving average regression (window span of 5). ....	93
Figure 3.11 – Primary flow front advance rates for the 12 episodes. The timing of the first point represents when an estimate for advance rate was possible after the start of effusive activity. Background colour: blue = Zone 1, red = Zone 2, green = Zone 3. Titles highlighted in red mark those flows belonging to Group 1 (flows which initially advanced as slow moving discrete flows within Zone 1 with average advance rate of 0.05 or less). Figure 3.11 continued on the following three pages. ....	94
Figure 3.12 – Relationship between measured length and modelled length for the lava flows produced during the 12 episodes using model 4. Markers are labelled with the corresponding episode number. ....	101
Figure 3.13 – Surface elevation transects (a) for Zone 1 (b), Zone 2 (c), and Zone 3 (d). Figure continues onto the following page. ....	104
Figure 3.14 – Relationship between final length and length of confinement for the 12 episodes. ....	106
Figure 4.1 – Workflow of the FLOWGO model. Operations are listed on the left-hand side of the figure with equations (listed in sequence) given on the right-hand side (modified from Harris et al., 2015). 121	121

Figure 4.2 – Time-lapse camera installation at Mt. Etna. (a) Shaded relief map of the Valle del Bove created from the Laboratorio di Aerogeofisica-Sezione Roma2 2012 DEM (De Beni et al., 2015), showing the camera location, the New South East Crater (NSEC) which sourced the observed flows, and the area of flow emplacement (outlined in red). (b) An example image from the Zoccolaro time-lapse sequence. (c) A typical camera installation. .... 122

Figure 4.3 – Selection of time-lapse images from Zoccolaro showing the evolution of the flow fields for the 12 May (top sequence) and 19 July 2011 (bottom sequence) episodes. The right-most images were those used for flow width estimates. The red line denotes the primary flow unit with blue dashed lines marking secondary flows produced by bifurcations of the primary flow. Purple dashed line identifies the crest of the Valle del Bove headwall. .... 125

Figure 4.4 – Lava flow outlines for the (a) 12 May and (b) 19 July 2011 episodes examined in this study (solid lines: primary flow unit = red, secondary flows = blue, black, and purple). The flow emplacement area has been divided into three zones defined by the breaks in slope which mark the transition onto the Valle del Bove headwall and the transition onto the valley floor. (b) Dashed line identifies the segment of the 19 July 2011 flow where flow widths could not be estimated using the time-lapse data and were instead estimated by extending a line from the earliest width estimate possible to the first estimate located at the transition from Zone 1 to Zone 2. \*lava flow field thicknesses by zone estimated by Behncke et al. (2014) for the 25 paroxysmal events which occurred in the 2011-2012 period. .... 126

Figure 4.5 – Time-lapse estimated flow widths and the corresponding smoothed widths for the 12 May 2011 primary flow. .... 127

Figure 4.6 – Modelled widths for the 12 May (top) and 19 July (bottom) primary flows. Dashed red box outlines the proximal section of the flows (i.e. the segment of the flows within Zone 1). .... 134

Figure 4.7 – FLOWGO-estimated channel depths for the “cold” lava model (top) and “hot” lava model (bottom) for the 12 May (solid lines: primary flow unit = red, secondary flows =, blue, black, and purple) and 19 July 2011 (dashed line: primary flow unit = red) flows. \*Field-based thickness estimates for each Zone given by Behncke et al. (2014). .... 136

Figure 5.1 – Typical viewing scenarios for ground-based thermal cameras: (a) horizontal view-path and (b) slant view-path, where  $\alpha$  is the viewing angle and  $\Delta\text{Height}$  is the difference in height between the target and the camera..... 143

Figure 5.2 – Outline of the processing workflow used in this study to correct long-range ground-based thermal time-lapse data on a pixel-by-pixel basis. .... 147

Figure 5.3 – Selection of thermal images from the time-lapse sequence of the 29 August 2011 episode. .... 150

Figure 5.4 – A hill-shaded DEM (2005 DEM from the V3-LAVA project database) of Mt. Etna, showing the location of the INGV-Catania fixed ground-based thermal camera (EMCT) at Mount Cagliato to the east of the Valle del Bove. .... 152

Figure 5.5 – Calculated surface temperatures for apparent temperatures of 400 K, 500 K, and 600 K plotted against viewing distance for (a) atmospheric temperature (5 °C steps from 15-25 °C at 50 % relative humidity), (b) relative humidity (steps of 10 from 40-60 % relative humidity at 20 °C), (c) atmospheric pressure (steps of 50 mb from 1000-800 mb at 20 °C and 50 % relative humidity), and (d) with and without aerosols (‘Rural, Visibility = 23 km’ aerosol model at 20 °C 50% relative humidity). Dot-dash line = lowest range for atmospheric conditions, dash line = middle range for atmospheric conditions, solid line = highest range for atmospheric conditions..... 154

Figure 5.6 – Difference in surface temperatures calculated for an apparent temperature of 500 K for a 3, 5, 8, and 15-layer model atmosphere created using the NCEP/NCAR Reanalysis 1 data and INGV-Catania fix ground-based thermal camera viewing geometry. The 5 and 8-layer models accounted for the minimum and maximum calculated surface temperature of all the models tested. For more information on the models tested and the calculated surface temperatures for each see Appendix 3 & 4..... 155

Figure 5.7 – Differences in atmospherically corrected surface temperature between the horizontal and slant-path viewing geometry for the 29/08/2011 lava flow at 04:35. Dashed black line shows the approximate location of start of the Valle del Bove headwall. .... 157

*Figure 5.8 – 29 Aug 2011 04:35 corrected and georeferenced temperature map and associated histogram for a target temperature range of 400-1350 K using a horizontal (a & c) and slant-path (b & d) viewing geometry. The thermal image and associated histogram represents the maximum radiant heat flux produced during the duration of the eruption. Dashed white line show approximate location of the start of the Valle del Bove headwall..... 158*

*Figure 5.9 – Comparison of radiant heat flux profiles for the 29 Aug 2011 event calculated using the EMCT data with a horizontal and slant-path viewing geometry and SEVERI data. .... 160*

*Figure 6.1 – Examples of the same viewing scene taken using a visible and an IR-modified dSLR camera at night (top) and obscured by clouds (bottom)..... 177*

*Figure 6.2 – Effect of the bug discovered when using the Ganci et al. (2013) automated processing visual basic (vbs) script with ThermaCam Researcher..... 181*

# List of Tables

<i>Table 2.1 – List of well-studied short-duration volume-limited lava flows.</i>	19
<i>Table 2.2 – Viewing geometry parameters used by MODTRAN</i>	28
<i>Table 2.3 – Viewing path options available in MODTRAN</i>	28
<i>Table 2.4 – Slant-path cases for known parameters.</i>	28
<i>Table 2.5 – Publications from 2000-2016 in which hand-held thermal cameras were used to observe and analyse active lava flows. Citations marked with a * indicate studies which used permanently installed thermal cameras.</i>	33
<i>Table 2.6 – Example geological studies in which ground-based time-lapse data were acquired using dSLR cameras.</i>	38
<i>Table 2.7 – Input and output parameters for the listed lava flow models. Table adapted from Proietti et al. (2009).</i>	40
<i>Table 3.1 – Volcanological parameters of the 25 lava flows from Behncke et al. (2014). Red box identifies episodes captured by time-lapse data. Red text identifies the episodes examined in this chapter.</i>	50
<i>Table 3.2 – Temporal eruption data from Behncke et al. (2014) covering the 25 episodes between 2/1/2011 and 24/4/2012, delineating duration of both lava fountaining phases and the full episodes. Red text identifies those episodes examined in this chapter.</i>	52
<i>Table 3.3 – Visibility and coverage of the 12 selected episodes. Episodes where the entirety of the flow was visible are labelled as “Good,” while episodes where the body of the flow was obscured from view but advancing flow fronts were visible are labelled as “Partial.”</i>	67
<i>Table 3.4 – Lava flow emplacement factors for the 12 episodes. Text in red indicate those flows which belong to Group 1.</i>	68
<i>Table 3.5 – Pearson correlation (r) for all factors.</i>	89
<i>Table 3.6 – Regression models for flow length produced from best subset selection.</i>	98
<i>Table 3.7 – VIF and p-values for each regression coefficient in each model.</i>	100
<i>Table 3.8 – Evaluation statistics for the selected models.</i>	101
<i>Table 3.9 – List of final flow lengths and length of flow confinement to the primary flow for the 12 Episodes.</i>	103
<i>Table 3.10 – Advance rates for Zone 1 and interval between start of lava emission and onset of fire fountaining divided by the two different morphologies observed in Zone 1.</i>	108
<i>Table 4.1 – Eruption parameters for the 12 May and 19 July 2011 paroxysmal events at Mt. Etna, given by Behncke et al. (2014).</i>	114
<i>Table 4.2 – End-member lava flow models used to best-fit FLOWGO estimated flow widths to measured flow widths. The sources of these values can be seen in Table 4.3.</i>	128
<i>Table 4.3 – Full list of parameters used in FLOWGO to determine the best fit model for the 12 May and 19 July 2011 episodes.</i>	129
<i>Table 4.4 – FLOWGO-modelled flow properties for the “cold” and “hot” models, and time-lapse estimated advance rates for the 12 May and 19 July 2011 primary flow units. Mean values are in brackets.</i>	133
<i>Table 5.1 – Calculated values for flow area, volume and maximum radiant heat flux for the 29 Aug 2011 fire fountaining episode</i>	156
<i>Table 6.1 – Emplacement data on 12 Etnean flows and four Hawaiian short-duration volume-limited flows.</i>	172

# Nomenclature

$\emptyset$  = crystal content of lava (%)

$A$  = area ( $m^2$ )

$ANGLE$  = Zenith angle at  $H1$  (radians)

$AR$  = advance rate ( $m s^{-1}$ )

$B$  = number of bifurcations

$BETA$  = Earth-centre angle (radians)

$C$  = number of confluences

$K$  = the thermal conductivity ( $W m^{-1} K^{-1}$ )

$L$  = flow length (m)

$M$  = spectral intensity ( $W sr^{-1} m^{-1}$ )

$MOR$  = mean output rate ( $m^3 s^{-1}$ )

$R$  = inverse of maximum solids concentration

$RANGE$  = distance of the path-length between  $H1$  and  $H2$

$HMIN$  = minimum altitude of the path-length (km)

$T$  = temperature (K)

$U$  = wind speed ( $m s^{-1}$ )

$V$  = volume ( $m^3$ )

$H1$  = sensor or observer altitude (km)

$H2$  = final altitude (km)

$a$  = empirically-derived coefficient that relates  $f$  to  $v$

$c$  = the speed of light ( $m s^{-1}$ )

$d$  = thickness (m)

$f$  = the fraction of crust coverage defined by the portion of the flow surface occupied by  $T_c$

$g$  = acceleration due to gravity ( $m s^{-2}$ )

$k$  = the Boltzmann constant ( $J K^{-1}$ )

$h$  = Planck's constant ( $J s$ )

$n$  = channel shape

$r$  = radius of lava channel (m)

$t$  = time (s)

$x$  = down-flow increment (m)  
 $z$  = path-length (m)  
 $\Delta\phi/\Delta T$  = rate of crystallization (%)  
 $\Delta\phi/\Delta x$  = mass fraction of crystallization per distance  
 $\Delta T$  = cooling range (K)  
 $\Delta T/\Delta x$  = heat lost per distance  
 $\alpha$  = underlying slope (radians)  
 $\epsilon$  = emissivity  
 $\eta$  = lava viscosity (Pa s)  
 $\lambda$  = wavelength (m)  
 $v$  = lava flow velocity (m s<sup>-1</sup>)  
 $\rho$  = density of lava (kg m<sup>-3</sup>)  
 $\sigma$  = Stefan-Boltzmann constant (W m<sup>-2</sup> K<sup>-4</sup>)  
 $\tau$  = transmissivity  
 $\phi_b$  = vesicularity (%)  
 $\phi_{max}$  = maximum crystal content a lava can reach before flow is impossible (%)  
 $A_o$  = constant related to the composition of the lava (K<sup>-1</sup>)  
 $A_{surface}$  = area of emitting surface (m<sup>2</sup>)  
 $B_o$  = lava compositional dependent constant (Pa)  
 $B_{Z1}$  = number of bifurcations in Zone 1  
 $C_o$  = lava compositional dependent constant (K<sup>-1</sup>)  
 $E_{in}$  = volume of lava entering a channel (m<sup>3</sup> s<sup>-1</sup>)  
 $E_r$  = effusion rate (m<sup>3</sup> s<sup>-1</sup>)  
 $E_{vent}$  = volume of lava leaving the source vent (m<sup>3</sup> s<sup>-1</sup>)  
 $L_{at-sensor}$  = radiance received at sensor (W sr<sup>-1</sup> m<sup>-1</sup>)  
 $L_{corrected}$  = atmospherically corrected radiance (W sr<sup>-1</sup> m<sup>-1</sup>)  
 $L_{integrated UpRad}$  = integrated upwelling radiance along a path-length (W sr<sup>-1</sup> m<sup>-1</sup>)  
 $L_{reflected}$  = radiance reflected by a surface (W sr<sup>-1</sup> m<sup>-1</sup>)  
 $L_{scatter}$  = upward scattered solar radiance (W sr<sup>-1</sup> m<sup>-1</sup>)  
 $L_{surface}$  = radiance emitted by a surface (W sr<sup>-1</sup> m<sup>-1</sup>)  
 $L_{upwelling}$  = radiance emitted by the atmosphere (W sr<sup>-1</sup> m<sup>-1</sup>)  
 $L_{hc}$  = latent heat of crystallization (J kg)

$MOR_{mean}$  = mean MOR given by Behncke et al. (2014) ( $m^3 s^{-1}$ )  
 $MOR_{time-lapse}$  = MOR derived using time-lapse data ( $m^3 s^{-1}$ )  
 $M_{rfd}$  = radiant flux density ( $W m^{-2}$ )  
 $Q_{conv}$  = heat loss due to convection (J)  
 $Q_{cond}$  = heat loss due to conduction (J)  
 $Q_{rad}$  = heat loss due to radiation, also referred to as radiant energy (J)  
 $Rad_{at-sensor}$  = radiance received at sensor ( $W m^{-2} m^{-1}$ )  
 $Rad_{reflected}$  = radiance reflected by the surface ( $W m^{-2} m^{-1}$ )  
 $Rad_{scatter}$  = upward solar radiance ( $W m^{-2} m^{-1}$ )  
 $Rad_{surface}$  = radiance emitted by the surface ( $W m^{-2} m^{-1}$ )  
 $Rad_{upwelling}$  = radiance emitted by the atmosphere ( $W m^{-2} m^{-1}$ )  
 $RH$  = relative humidity (%)  
 $T_a$  = atmospheric temperature (K)  
 $T_{air}$  = temperature of the air (K)  
 $T_b$  = temperature buffer (K)  
 $T_{base}$  = temperature of the lava flow at its base (K)  
 $T_{bright}$  = temperature derived from  $L_{at-sensor}$  (K)  
 $T_c$  = crustal temperature of lava (K)  
 $T_{core}$  = core temperature of the lava flow (K)  
 $T_{conv}$  = surface temperature for convection (K)  
 $T_e$  = effective radiation temperature of the lava surface (K)  
 $T_{eruption}$  = eruption temperature (K)  
 $T_h$  = remaining surface of flow occupied by higher temperature molten material, defined by 1-f  
 $T_o$  = liquidus temperature of lava (K)  
 $T_{right}$  = brightness temperature (K)  
 $V_{mean}$  = mean total volume given by Behncke et al. (2014) ( $m^3 s^{-1}$ )  
 $W_{max}$  = maximum flow width (m)  
 $W_{max,Z1}$  = maximum flow width in Zone 1 (m)  
 $\Phi_{rad,flux}$  = radiant flux ( $W$  or  $J s^{-1}$ )  
 $a_{1-4}$  = constant derived from  $T_a$  and  $RH$  for  $\tau_{avg,trans}$  look-up table  
 $adv_{avg,Z1}$  = average advance rate in Zone 1 ( $m s^{-1}$ )

$adv_{avg,Z2}$  = average advance rate in Zone 2 ( $m s^{-1}$ )  
 $adv_{avg,Z3}$  = average advance rate in Zone 3 ( $m s^{-1}$ )  
 $adv_{avg}$  = average advance rate ( $m s^{-1}$ )  
 $adv_{max,Z1}$  = maximum advance rate in Zone 1 ( $m s^{-1}$ )  
 $adv_{max,Z2}$  = maximum advance rate in Zone 2 ( $m s^{-1}$ )  
 $adv_{max,Z3}$  = maximum advance rate in Zone 3 ( $m s^{-1}$ )  
 $adv_{max}$  = maximum advance rate ( $m s^{-1}$ )  
 $b_{1-4}$  = constant derived from  $T_a$  and RH for  $L_{integrated UpRad}$  look-up table  
 $cp_{air}$  = air specific heat capacity ( $J kg K$ )  
 $d_{head}$  = depth at channel head (m)  
 $h_{base}$  = distance between  $T_{core}$  and  $T_{base}$  (m)  
 $h_c$  = convective heat transfer coefficient  
 $w_{head}$  = mean width at the head of the channel (m)  
 $\alpha_{Z1}$  = average underlying slope in Zone 1 (radians)  
 $\alpha_{Z2}$  = average underlying slope in Zone 2 (radians)  
 $\alpha_{Z3}$  = average underlying slope in Zone 3 (radians)  
 $\alpha_{avg,all}$  = average underlying slope (radians)  
 $\eta_f$  = dynamic viscosity ( $Pa s$ )  
 $\eta_o$  = viscosity of lava at liquidus temperature ( $Pa s$ )  
 $t_{cp}$  = duration of cooling dominant phase (s)  
 $t_{eff\ to\ ff}$  = time from start of lava emission to onset of fire fountaining (s)  
 $t_{ff}$  = duration of fire fountaining (s)  
 $t_{flow}$  = duration of flow (s)  
 $t_{flow\ time-lapse}$  = duration of flow from time-lapse data (s)  
 $v_{mean}$  = mean lava flow velocity ( $m s^{-1}$ )  
 $v_{mean,head}$  = mean velocity of the lava at the head of the channel ( $m s^{-1}$ )  
 $\rho_{air}$  = air density ( $kg m^{-3}$ )  
 $\rho_b$  = bulk density ( $kg m^{-3}$ )  
 $\rho_{DRE}$  = dens rock density ( $kg m^{-3}$ )  
 $\tau_{avg\ trans}$  = average atmospheric transmittance  
 $\tau_o$  = yield strength (Pa)  
 $\tau_b$  = basal shear stress (Pa)

# Glossary

The terms listed below are used throughout this thesis to describe lava flows and remote sensing techniques. This glossary lists the definitions for each term as they pertain to the work presented in this thesis.

**cooling-limited flow:** a lava flow in which the effects of heat loss play the dominate role in determining its final length, i.e. a flow that continues to advance until the flow front cools to such an extent that it is no longer able to move. Flows of this type have a generally steady instantaneous effusion rate lasting for more than 24 hours (e.g. Walker, 1971; Guest et al., 1987; Wilson et al., 1993).

**effusion rate:** The rate of supply of erupted lava, given in  $\text{m}^3 \text{s}^{-1}$ , that is feeding flow at any specific point in time (e.g. Lipman & Banks, 1987; Harris et al., 2007a).

**long-range:** for a ground-based sensor, a viewing distance of more than one kilometre.

**long-duration:** more than 24 hours (e.g. Walker, 1971; Kilburn & Lopes, 1988; Harris & Rowland, 2009).

**mean output rate (MOR):** the final total erupted volume of lava divided by the total duration of activity (e.g. Walker 1973; Barberi et al., 1993; Harris et al., 2007a).

**short-duration:** less than 24 hours (e.g. Walker, 1971; Alparone et al., 2003; Behncke et al., 2006; Harris & Rowland, 2009).

**short-range:** for a ground-based sensor, a viewing distance of one kilometre or less.

**volume-limited flow**: a lava flow in which the final length is dictated primarily by the supply of material. Volume-limited flows will continue to advance until the supply of material from the source vent ceases. Central flow channels may be drained, supplying molten material to the flow front, resulting in continued advance but at a reduced rate (e.g. Walker, 1971; Guest et al., 1987; Wilson et al., 1993).

# Chapter 1 Introduction

Lava flows represent a minimal danger to human life but can greatly affect critical infrastructure such as roads, housing, and public utilities (e.g. Barberi et al., 1993; 2003; Behncke et al., 2005; Bisson et al., 2009). It is therefore essential to understand the processes which control and influence their emplacement and development. Lava flows are formed when molten rock is extruded at the surface of the Earth and can produce flow fields reaching distances of up to 100 km from the eruptive vent and being several kilometres wide (Macdonald, 1953; Walker, 1971; Lipman & Banks, 1987; Kilburn, 2000). The hazard posed by lava flows necessitates active and robust monitoring at many active volcanoes, not only for a warning system, but also to understand flow emplacement processes better. To help mitigate hazards, volcanologists require measurements or estimates of flow properties including the effusion rate, length and advance rate, and the area of inundation.

Volcano observatories employ a variety of techniques to collect such measurements. Typically, ground-based measurements have been used during field surveys and can include direct sampling and observation of lavas (e.g. Peterson & Tilling, 1980; Cashman et al., 1994; Hon et al., 1994; Pinkerton & Sparks, 1978; Kauahikaua et al., 2003), observations made by ground-based LiDAR and visible photography (e.g., Zlotnicki et al., 1990; Robson & James, 2007; James et al., 2009; Slatcher et al., 2015), and temperature measurements using direct (e.g., Hon et al., 1993; Pinkerton, et al., 2002) and short-range indirect methods (e.g. Keszthelyi et al., 2003; Harris et al., 2003; 2005a; 2005b; Calvari et al., 2004; Bailey et al., 2005; Ball & Pinkerton, 2006; James et al., 2006; Spampinato et al., 2011). However, field surveys of large areas require a significant amount of manpower and are logistics-heavy. Additionally, in many situations, inaccessible topography or hazardous conditions caused by eruptive activity may prevent field-based work. Furthermore, for short duration volume-limited flows, emplacement can cease long before a survey team can gain access, resulting in limited analytical study. These

difficulties have been particularly prevalent during the recent fire fountaining activity at Mt. Etna (e.g. Ganci et al., 2012a; Behncke et al., 2014; De Beni et al., 2015). The lack of analysis of short-duration volume-limited lava flows has left volcanologists with no clear quantitative assessment of how different emplacement factors affect the morphology of these flows.

One method to capture and record this style of activity is by using long-range ground-based thermal monitoring systems. Volcano observatories use long-range ground-based thermal cameras to detect and record the emplacement of lava flows (e.g. Calvari et al., 2004; Ganci et al., 2013; Patrick et al., 2014) as well as other volcanic phenomena (e.g. Calvari et al., 2004; Patrick et al., 2007; 2016; Spampinato et al., 2011). Cameras can acquire data at a high temporal rate (either as continuous acquisition or in intervals of a few minutes) and can be placed at ranges up to 10 km from the target area, making them resilient to damage or loss in the event of an eruption. Measured surface temperature from ground-based cameras can be used to check the accuracy of surface temperature measurements acquired from satellite-based sensors. This is important because satellite-based thermal measurements are widely used in estimating eruption factors such as effusion rates and volume, which are used in lava flow hazard modelling (e.g. Harris et al., 1998; Ganci et al., 2011; 2012b; 2013). However, quantitative analysis of lava flow data acquired at these long distances is seldom carried out due to the atmospheric and viewing conditions which limit the accuracies of apparent surface temperatures measured by the camera (e.g. Ball & Pinkerton, 2006; Harris, 2013). Currently, researchers use long-range thermal camera data to visually identify, track, and map the development of lava flows (e.g. McGimsey et al., 1999; James et al., 2010; Lyons et al., 2010; Wessels et al., 2013). A review of the application of ground-based thermal cameras to study active lava flows carried out in Chapter 2 of this thesis identifies a lack of processed quantitative long-range thermal data. One study has attempted to use long-range ground-based data to extract quantitative information, particularly radiant heat flux, during the

emplacement of a lava flow (Ganci et al., 2013). This provided a sound methodology but was hindered by a bug in the commercial software used.

Permanent installations of ground-based thermal cameras can be expensive (Patrick et al., 2014) and require regular maintenance to keep them calibrated. As a result, this monitoring option is often out of reach for many volcano observatories. Another limitation of permanently-installed thermal cameras is that they cannot be easily redirected or repositioned when new areas of activity develop. One response to these limitations is to use commercial-grade dSLR cameras and telemetered webcams (Orr et al., 2015) to acquire non-thermal (visible) time-lapse image sequences to augment traditional field surveys and permanent thermal camera installations. The affordability, portability and resolution offered by modern dSLR cameras makes them ideal for long-term (months to years), campaign-style deployment for long-range monitoring and study of lava flows. Long-range visible time-lapse imagery has been used to track lava flow advances and lava flow field morphology (Orr et al., 2015), but has thus far not been used to perform quantitative analysis on lava flow emplacement.

It is the aim of this thesis to improve our understanding of the emplacement of short-duration volume-limited lava flows through using long-range ground-based optical sensors. Previous studies have analysed emplacement factors to evaluate their influence on final flow lengths (e.g. Walker, 1973; Wadge, 1978; 1979; Malin, 1980; Pinkerton & Wilson, 1994; Calvari & Pinkerton, 1998), focussing on long-duration, cooling-limited lava flows. Thus, current emplacement models may not be applicable to short-duration volume-limited flows.

To achieve the aim of this study, the work presented here addresses the following objectives:

(1) Develop a method for remote analytical study of short-duration volume-limited flows using long-range ground-based visible time-lapse data and thermo-rheological modelling.

(2) Improve the application of long-range ground-based thermal cameras for studying lava flows.

For this research, Mt. Etna was selected as the study area due to the high recurrence of short-duration volume-limited lava flows from 2011-2014 and the availability of both long-range ground-based time-lapse visible data acquired from a long-term deployed dSLR camera array and long-range ground-based time-lapse thermal data acquired by the INGV-Catania fixed thermal camera. Chapter 2 of this thesis introduces and discusses background information pertinent to this research. The first part of objective 1 is addressed in Chapter 3 which presents the use of long-range ground-based time-lapse data acquired using dSLR cameras to analyse the emplacement of short-duration volume-limited lava flows at Mt. Etna. Chapter 4 addresses the second part of objective 1 by examining the use of the FLOWGO thermo-rheological model to estimate lava flow emplacement properties, such as effusion rate, total volume, and thickness, by inputting extracted flow geometries from the long-range ground-based time-lapse images as well as petrological properties typical of Etnean lavas. Chapter 5 addresses objective 2 through the development of a semi-automated workflow to accurately correct long-range ground-based thermal data of actively-emplaced lava flows for the various transmittance and upwelling radiance values present in the viewing scene. Results from Chapters 3-5 are then summarized and discussed, with future research and concluding remarks given, in Chapter 6.

## Chapter 2 Research Background

The following sections will provide background for the principles and methods used in this thesis to complete the objectives listed in Chapter 1. First, a review of basaltic lava flow morphology and the factors that influence it are given. Following this, is an introduction to previously studied short-duration volume-limited lava flows. Next is a review of currently employed thermal remote sensing techniques using space and ground-based sensors followed by a discussion of the application of time-lapse imagery to volcanological studies. Then an introduction of currently used lava flow models is presented followed by a description of the FLOWGO thermo-rheological lava flow model and its application to volcanological research. Finally, a broad overview of the volcanic history and monitoring of Mt. Etna (the study area for this research) is given.

### 2.2 Basaltic Lava Flows

#### 2.2.1 Surface Morphology of 'A'ā and Pahoehoe Lava

Early attempts to categorise and define different types of lava based on their surface morphology utilised comparisons to other geological/natural phenomena, such as glaciers and mounds of scoria (Ellis, 1825; von Buch, 1836; Gemmellaro, 1858; Scrope, 1858). In 1883, Clarence Dutton introduced the use of the Hawai'ian words 'a'ā and pahoehoe to the geologic community to describe the two types of lava flows he observed in Hawai'i. Following Dutton (1883), Dana (1891) and Hitchcock (1909) added to and refined the geological definitions for 'a'ā and pahoehoe. The Hawai'ian terminology was later adopted by Mercalli (1907) to describe similar lava flows observed at Mt. Etna. The terms 'A'ā and pahoehoe are now used world-wide to describe the two most common forms of basaltic lava flows, like those seen in Hawai'i and at Mt. Etna.

'A'ā flows are characterised by rough, highly fractured surfaces made up of 'clinker' formed by the autobrecciation of the surface and basal crusts of the flow as it advances (Figure 2.1) (Dutton, 1883; Macdonald, 1953). 'A'ā flows can range in thickness from half a meter up to tens of meters and typically transition during cooling from hot fluid sheets to more solid masses which fragment along the advancing front of the flow (Jones, 1937; 1943; Peterson & Tilling, 1980; Kilburn, 1981; 2000; Cashman et al., 1999; Hon et al., 2003). 'A'ā flows are often a result of eruptions with high effusion rates (greater than  $5\text{-}10\text{ m}^3\text{ s}^{-1}$ ) (Rowland & Walker, 1990). In contrast, the surface of pahoehoe flows are characterised by a smooth, mostly continuous glassy surface with occasional folded features referred to as "ropes" (Jones, 1937; 1943; Macdonald, 1953; Swanson, 1973; Rowland & Harris, 2015). Pahoehoe flows are made up of multiple (often numbering from hundreds to thousands) small individual lobate structures with dimensions (lengths and widths) typically less than 0.5 m (Peterson & Tilling, 1980; Hon et al., 1994; Rowland & Harris, 2015). Often, lava flows will create and flow down channels, formed as the margins of a flow cool and solidify, forming levees which confine and channel the flow (e.g. Hulme, 1974; Sparks et al., 1976).

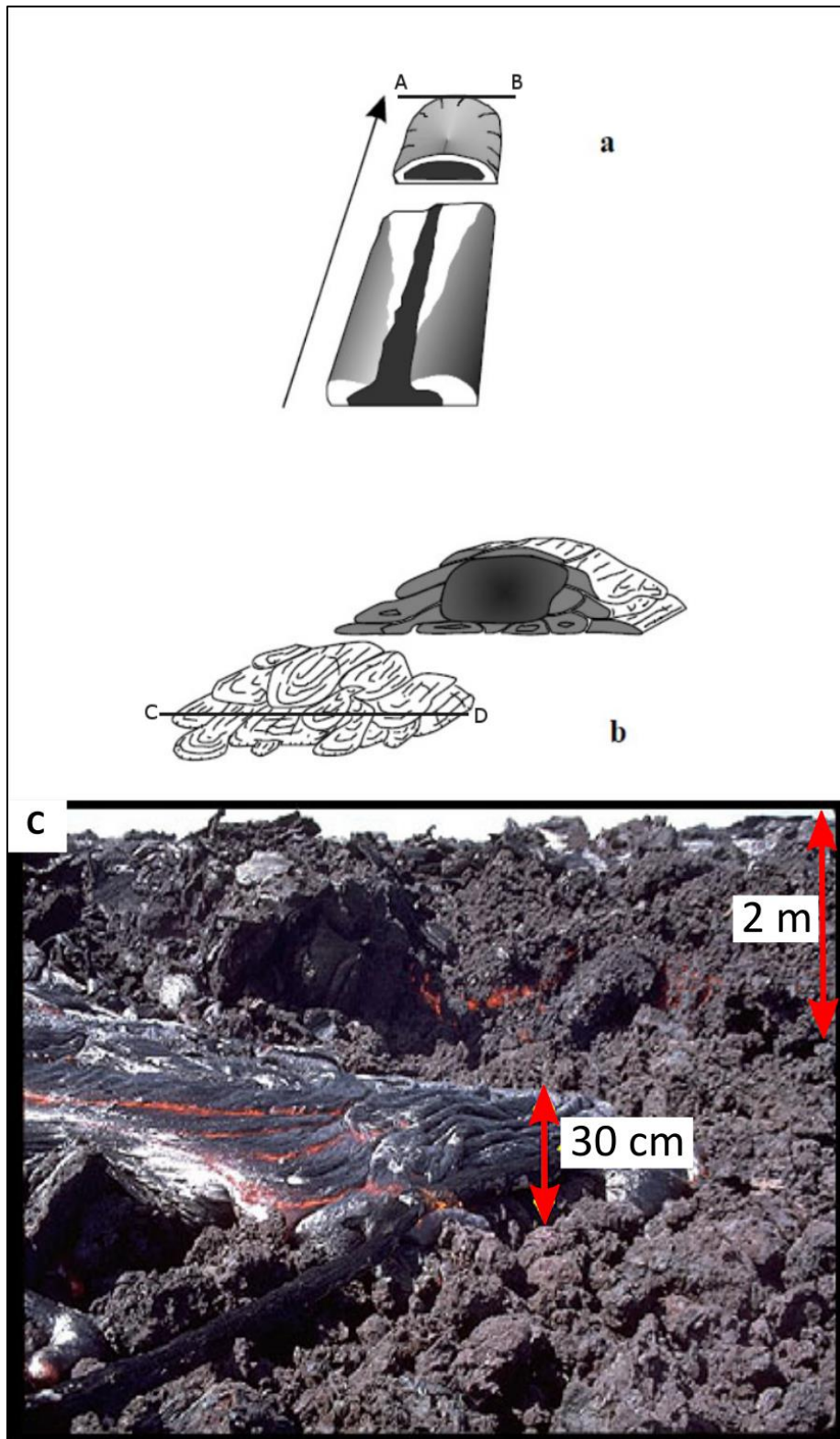


Figure 2.1 – (a) The typical flow structure of an 'a'ā flow for an open channel (below) which forms a simple flow front (above). The arrow shows the direction of flow of the molten material (black zones). Large 'a'ā flows can have flow fronts up to 10 m wide (A-B). (b) Pahoehoe lava flow fronts are typically comprised of multiple small individual lobate structures referred to as "tongues" and "toes" which are fed by lava tube systems. Pahoehoe flow fronts can be up to several meters in width (C-D) (Kilburn, 2000). (c) Active pahoehoe flow (left) flowing over an older 'a'ā flow, in front of an active 'a'ā flow (right) (Volcano.oregonstate.edu, 2018).

### 2.2.2 Cooling- and Volume-Limited Flows

Lava flows can also be classified into two types based on the primary mechanism which causes them to stop advancing (Walker, 1971). The first are flows where the maximum length is controlled by the cooling of the flow due to heat loss, referred to as cooling-limited flows. The second are lava flows where the maximum length is determined by cessation of the supply of material, known as volume-limited flows.

Cooling-limited flows are flows in which the effects of cooling play the dominant role in determining the final length of the lava flow. Flows of this type are long-duration and generally have a steady effusion rate (Guest et al., 1987). Cooling-limited flows will continue to advance until the flow front cools to such an extent that it is no longer able to move. If effusion is still active, new flows will be produced by break-outs at the margins of the stalled flow, caused by over-pressurisation of the molten core material (Wilson et al., 1993; Kilburn, 1996).

Volume-limited flows are lava flows where the final length is dictated by the cessation of supply of material (Walker, 1971). Volume-limited flows will continue to advance until the supply of material from the source vent ceases (Guest et al., 1987). When this occurs, the remaining molten material still in the flow channel will continue to flow to the flow front resulting in continued advance but at a reduced rate (Wilson et al., 1993). At this point, the effect of cooling on the remaining supply of material plays a much greater role in any additional extension of the flow front due to the lack of thermal recharge from newly-supplied lava from the vent (Swanson, 1973; Harris & Rowland, 2009; Rhéty et al., 2017). Due to the termination of effusion, volume-limited flows do not produce break-out flows such as those associated with cooling-limited flows and are always shorter in length, assuming all other parameters are identical (Guest et al., 1987; Harris & Rowland, 2009).

### 2.2.3 Simple and Compound Lava Flows

Lava flows can be further classified by the complexity and number of individual lava flow units present. Nichols (1936) defined a flow unit as a lava flow that has cooled and solidified its surface prior to another flow being emplaced on top of it. Using this definition, Walker (1972) divides flows into two categories: simple flow fields and compound flow fields. These categories are linked to the flows discussed in Section 2.2.2, with simple flow fields being associated with volume-limited flows and compound flow fields being associated with cooling-limited flows (Walker, 1971; Guest et al., 1987).

Simple flow fields consist of a single lava flow or are composed of a few individual flow units and are longer than they are wide (Walker, 1971; Kilburn & Lopes, 1988). Simple flow fields are typically produced by short-duration eruptions with initially high, rapidly decreasing effusion rates (Walker, 1971; Wadge 1981; Harris & Rowland, 2009), and are often associated with 'a'ā lavas (e.g. Walker, 1971; Kilburn & Lopes, 1988; Wilson et al., 1993). Examples of simple lava flow fields are the 1981 Etna flow (Guest et al., 1987), lava flows produced by fire fountaining activity at Mt. Etna from 2011-2014 (Behncke et al., 2014; De Beni, et al., 2015), and most Hawai'ian channel-fed lava flows (Rowland & Walker 1990).

Compound flow fields are composed of multiple simple lava flows erupted during the same event and emplaced next to and on top of one another (Walker, 1971). Compound flow fields are associated with long-duration events with steady, low effusion rates, and are comprised of both 'a'ā and pahoehoe lava (Kilburn & Lopes, 1988). As a result, they tend to form well-defined channel networks and flow fields as wide as they are long. Compound lava flow fields are typical products of sustained volcanic activity at Kīlauea Volcano in Hawai'i and Mt. Etna in Sicily. Compound lava flows were produced at Kīlauea Volcano in the current and past activity associated with the Pu'u 'O'o eruption (e.g. Hon et al., 1993; 1994; Garcia et al., 2000)

and at Mt. Etna during the 1983 (Frazzetta & Romano, 1984; Guest et al., 1987), 1991-93 (Calvari et al., 1994) and 2001 (Applegarth et al., 2010) lava flows.

## 2.3 Factors Influencing Lava Flow Length

The potential maximum length attainable by a lava flow is influenced by factors including the lava rheology, the rate and duration of effusion, erupted volume, topography, and the complexity of the lava channel network.

### 2.3.1 Rheology

Erupted lava is a complex mixture of gas bubbles, crystals, and liquid melt. As a result, a lava flow's rheology is determined by the temperature, chemical composition, crystal content, and gas bubble content (e.g. Emerson, 1926; Jagger, 1930; Macdonald, 1953; Kouchi et al., 1986; Crisp et al., 1994; Griffiths, 2000). However, the bulk rheology of a lava can be described by its viscosity and yield-strength (e.g. Nichols, 1939; Shaw et al., 1968; 1969; Macdonald; 1972; Hulme, 1974). As a lava flow cools, its crystallinity increases (e.g. Pinkerton & Sparks, 1978; Crisp et al., 1994; Cashman et al., 1999; Griffiths, 2000; Lyman et al., 2005). Increasing the crystallinity of a lava flow increases its viscosity and yield strength (e.g. Hulme, 1974; Marsh, 1981; Metzner, 1985; Ryerson et al., 1988; Pinkerton & Stevenson, 1992; Hoover et al., 2001). Eventually the increase in crystal content associated with flow cooling will raise the yield strength to a point where the flow is no longer able to advance. It is this process which is referred to when the term "cooling-limited" is used.

### 2.3.2 Effusion Rate

Walker (1973) challenged the early assumption that rheology (particularly viscosity) was the primary factor in determining final lava flow length. By analysing the average and initial viscosity, average thickness, and length of 896 lava flows (479 basalt and 417 trachyte, andesite/dacite, and rhyolite) Walker (1973) found that viscosity only played a minimal role in determining final flow length. Instead, based on observations of the emplacement of lava

flows on Etna in 1966 (Walker, 1967), Walker (1973) surmised that effusion rate was the controlling factor in final flow length. To test this hypothesis, Walker (1973) examined 40 lava flows at 19 different volcanoes and compared the final flow length against the mean output rates and found a positive correlation between high Mean Output Rate (MOR) and the distance a flow could travel (Figure 2.2). The conclusion that flow length was determined by effusion rate was later supported by Wadge (1978; 1979). Walker (1972) also postulated that additional factors may be at work in influencing flow length (e.g. angle of slope of underlying surface, heat loss per unit volume of thin flows versus thicker flows) but that they are of secondary importance compared to the influence of effusion rate. It should also be noted that the data used by Walker (1973), while derived from multiple volcanoes, consisted primarily of data for lava flows on Mt. Etna, as did the studies undertaken by Wadge (1978; 1979). Additionally, Walker (1973) only used data from eruptions that lasted between 30 hours and nine months.

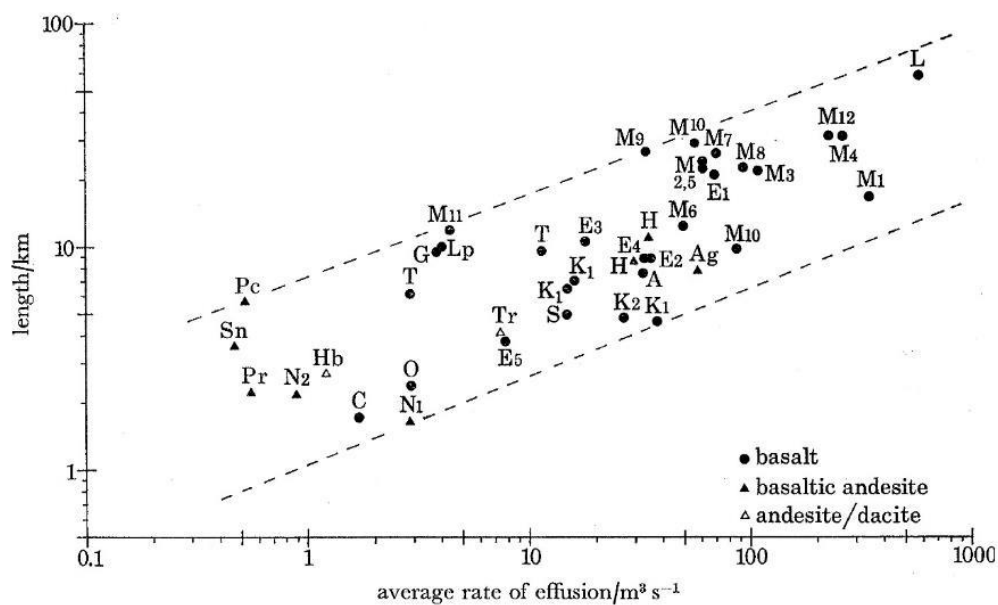


Figure 2.2 – Plot of length versus average effusion rate for 40 lava flows from 19 different volcanoes. Basaltic lavas, ●: A, Askja 1961 (Iceland); C, Cerro Negra 1968; E, Etna (1, 1669; 2, 1911; 3, 1923; 4, 1928; 5, 1971); G, Gituro 1948 (Congo); K, Kīlauea (1, 1955; 2, 1965); L, Laki, 1783 (Iceland); Lp, La Palma 1585; M, Mauna Loa (1, 1851; 2, 1852; 3, 1868; 4, 1887; 5, 1907; 6, 1916; 7, 1919; 8, 1926; 9, 1935; 10, 1942; 11, 1949; 12, 1950); O, Oosima 1951; T, Tenerife 1705; S, Sakurajima 1946. Basaltic andesite lavas, ▲: Ag, Mt Agung 1963 (Bali); H, Hekla (1, 1845/6; 2, 1947); N, Ngauruhoe (1, 1949; 2, 1954); Pc, Pacaya 1961 (Guatemala); Pr, Paricutin (first 8 months 1945); Sn, Santiaguita (Guatemala). Andesite/dacite lavas, △: Hb, Hibok-Hibok 1948; Tr, Trident 1953 (Walker, 1973).

### 2.3.3 Erupted Volume

Building on the theory presented by Walker (1973), Malin (1980) conducted a similar analysis of 87 long-duration cooling-limited Hawai'ian lava flows (44 flows on Kīlauea and 43 flows on Mauna Loa). Plotting the data from Mt. Etna against that of Mauna Loa, Malin (1980) found that the scatter for the Mauna Loa data was much greater than that of the Etna data. Furthermore, Malin (1980) found that the data from Hawai'i indicated a stronger correlation between the erupted volume of lava and flow length than effusion rate (Figure 2.3). Malin (1980) identified the presence of lava tubes and partially covered channels as a possible source of error between his results and those of Walker (1973). In his conclusion, Malin (1980) also acknowledged the potential influence of other factors which may have caused the discrepancy in results, such as cross-sectional area of a flow and rheology.

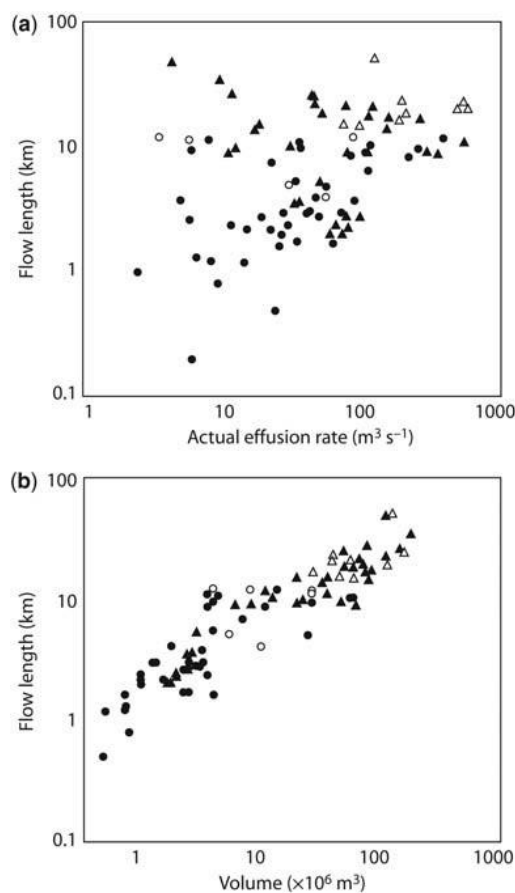


Figure 2.3 – Plot of flow length against effusion rate (a) and flow volume (b) by Malin (1980) for historic basaltic lava flows at Kīlauea volcano (circles) and Mauna Loa (triangles). Open symbols indicate flows which entered the ocean (Harris & Rowland, 2009).

#### 2.3.4 Cooling Rate

Studies by Swanson (1973), Greenley (1976), and Greenley et al. (1976) suggested that lava tubes can greatly affect the final length of a lava flow and that formation of tube systems is more common for Hawai'ian flows than for lava flows on Mt. Etna. Both Walker (1973) and Malin (1980) acknowledged that reducing the cooling rate of a lava due to flow insulation has some influence on final flow length. Lava-tube-supplied flows and partially-insulated channels reduce heat loss through insulation of a roof or tube which allows lava to travel greater distances before reaching sufficiently low temperatures to cause solidification to stagnate progression (Guest et al., 1980; Keszthelyi & Self, 1998). As a result, tube-fed flows and flows with partially insulated channels have a greater cooling-limited final length.

However, Walker (1973) believed that this insulation effect was secondary when compared to the effect of effusion rate. To better understand the significance of cooling rates on final flow lengths, Pinkerton and Wilson (1994) compared the results of Walker (1973) and Malin (1980) but removed tube-fed and short-duration flows from the comparison. The results from Malin (1980) then became consistent with those of Walker (1973) and emphasised the effect of reduced cooling rates due to lava tubes on flow lengths (Figure 2.4). The importance that lava tubes and heat loss play in the formation of flows and flow fields is now widely recognized (Calvari & Pinkerton, 1998; Harris & Rowland, 2009). Additionally, a study by Wooster et al. (1997) examined the role of different cooling mechanisms for the 1991-1993 flow at Mt. Etna and determined that the main source of heat loss came from radiative and conductive processes. Additionally, Wooster et al. (1997) found that the power lost was roughly equivalent between the two. The magnitude of radiative power lost was greatest when open channels were present, exposing a greater portion of the lava core and surface to the atmosphere (Rothery et al., 1992; Calvari et al., 1994; Wooster et al., 1997).

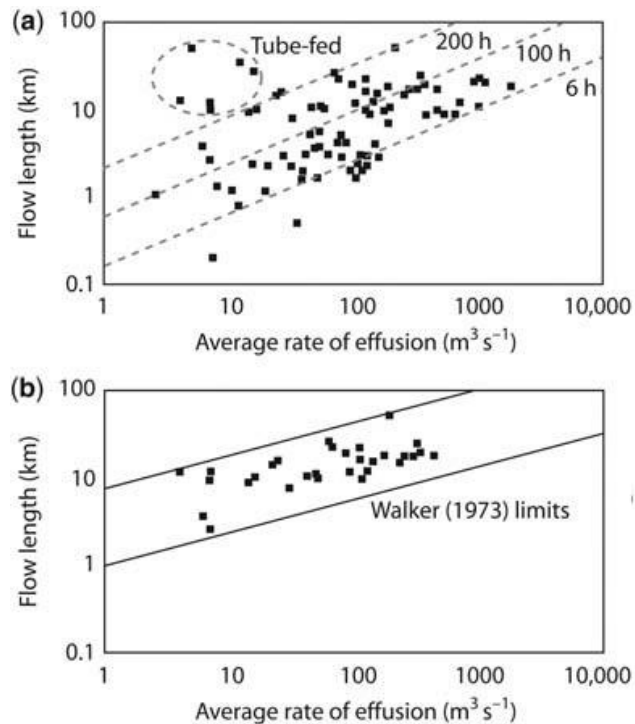


Figure 2.4 –(a) Plot of Malin’s (1980) data from Pinkerton and Wilson (1994) showing the relationship between flow duration, length, and effusion rate, and (b) Malin’s (1980) data for high duration (greater than 45 hours) channel-fed flows and the limits of Walker (1973) given as solid lines, with tube-fed and flows with a duration of less than 30 hours removed (Harris & Rowland, 2009).

Power to conduction was greatest when the lava flow was unconfined and allowed to spread (Calvari et al., 1994; Keszthel, 1995; Wooster et al., 1997). This allowed the flow to have much greater contact of basal and lateral zones with surrounding country rock, resulting in a greater area for conduction to occur.

### 2.3.5 Slope and Topography

The angle of the underlying slope on which a lava flow is emplaced can affect flow length through the increase of flow velocity and the formation of lava tubes and channels (e.g. Hulme, 1974; Pinkerton & Wilson, 1994; Calvari & Pinkerton, 1998; Palacci & Papale, 1999; Tallarico & Dragoni, 1999; Lodato et al., 2007; Favalli et al., 2009). Keszthelyi and Self (1998) studied the physical conditions needed for the creation of long basaltic flows (over 100 km) and discussed the role of slope in the formation of these types of flows. They determined that an average slope angle of about  $5\text{-}6^\circ$  is needed to reproduce flow lengths which fit observations

of historical terrestrial long basaltic flows and flows located at Olympus Mons on Mars. In contrast, Gregg and Fink (2000) modelled flow morphology in a laboratory using polyethylene glycol (PEG) to analyse the effect that slope, effusion rate, and cooling have on flow morphology, and to examine the relationship between the three. In the study, it was found that increasing slope angles up to 30° had a similar effect to increasing the effusion rate on flow length (Gregg & Fink, 2000). However, for slopes of 40° and greater it was found that the opposite was true, and that flow length decreased. Given that PEG flows are thought to represent useful analogues of real lava flow mechanics and rheologies, these results show the potential for flows with low effusion rates emplaced on steeper slopes to attain longer distances or for flows with a high effusion rate emplaced on considerably steep slopes to have a much shorter final length.

In addition to slope angle, the surface topography of the flow emplacement area can also affect flow length. Pinkerton and Wilson (1994) examined this influence and suggested that underlying topographic features, such as linear depressions, can “capture” a flow and channel it. This has the effect of keeping the flow from spreading laterally and widening, thus keeping the supply of lava confined to a single channel and therefore increasing the depth of the flow. As discussed in Section 2.3.4, flow confinement will reduce the basal and lateral contact area of the flow with the cooler surrounding country rock, thus reducing conductive heat loss. Pinkerton and Wilson (1994) also observed that captured flows were generally longer than flows that could widen. The relationship between flow confinement and length was also identified by Heliker et al. (2001) during Episodes 40 and 43 of the 1983-1986 Pu’u ‘O’o eruption at Kīlauea volcano, Hawai’i. Both Episodes 40 and 43 were short-duration lava flows, lasting 14 hours and 12 hours respectively. Additionally, average effusion rates for the two Episodes were similar (230 and 280 m<sup>3</sup> s<sup>-1</sup>) and the average underlying slope for both flows was ~3°. However, the Episode 40 lava flow was confined within a topographic low. As a result, the Episode 40 lava flow attained a length of 8.4 km in 14 hours, while the unconfined Episode

43 lava flow reached a length of 5.3 km in 12 hours. Additionally, field measurements of the 1983-1986 episodes of the Pu'u 'O'o eruption at Kīlauea volcano made by Wolf (1988) and Heliker et al. (2001), and laboratory experiments using both syrup and molten basalt carried out by Dietterich et al. (2015) identified that flow advance accelerated due to topographic confinement.

### 2.3.6 Channel Complexity

Factors such as slope, effusion rate, erupted volume, topographic confinement, and whether a lava flow is volume-limited or cooling-limited affects channel stability and the overall complexity of the channel network. The complexity of a lava flow channel network can be defined by the number of bifurcations and confluences which occur within the network (Dietterich & Cashman, 2014). Complex channel networks are present in cooling-limited, compound lava flow fields and are typical of long-duration events. Dietterich and Cashman (2014) examined the influence of channel network on flow emplacement behaviour and flow morphology. By analysing the number of bifurcations and confluences present within a channel network Dietterich and Cashman (2014) classified channel systems as either distributary (dominated by bifurcations) or tributary (dominated by confluences) and found that channel network complexity is greatly influenced by underlying slope. Dietterich and Cashman (2014) found that flow segments which had a greater number of bifurcations would result in thinner and wider flows and were associated with increases in slope. This observation supports previous observations made by Guest et al. (1987) that compound lava fields are typically as wide as they are long. Additionally, Dietterich and Cashman (2014) found that when bifurcations occurred, flow advance rates decreased by ~50 % and flows were significantly shorter in length than non-bifurcated flows. Wolfe (1988) and Heliker et al. (2001) observed a similar reduction in advance rate and flow length when bifurcation occurred for active flows in Hawaii.

Experimental work by Dietterich et al. (2015), examining the effect of diverting lava flows, also showed a similar reduction in flow advance rates and length due to bifurcation (Figure 2.5). The experimental work of Dietterich et al. (2015) showed that when advancing flows bifurcate due to an interaction with an obstacle, they thicken at the point of branching. When a flow encounters an obstacle, it is forced to flow along the margins of the obstacle. As the flow interacts with the margins of the obstacle it begins to cool due to conductive heat transfer from the hotter flow to the cooler contact surface of the obstacle (e.g. Crisp & Baloga, 1994; Wooster et al., 1997; Keszthelyi & Self, 1998). As the flow cools along the obstacle it produces a locally thicker flow which results in the formation of a bow wave (Dietterich et al., 2015) (Figure 2.5). The flow will continue to thicken until it has reached a point where the flow rate leaving the obstacle is equal to the incoming flow rate (Dietterich et al., 2015).

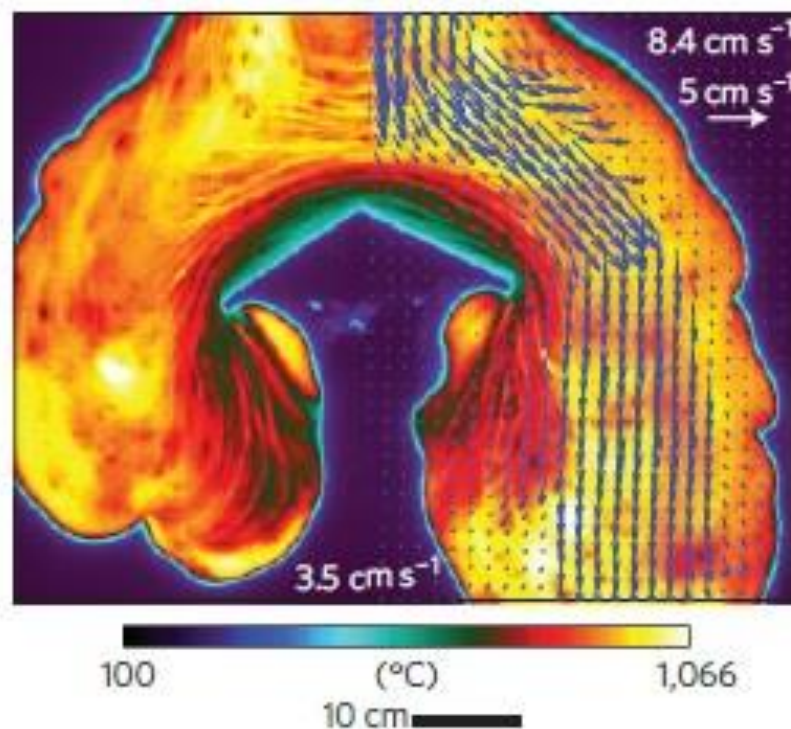


Figure 2.5 – Surface temperature of molten basalt (image shown is 45 seconds after interaction with the obstacle). Blue arrows show the calculated velocity field and show the decrease in velocity prior to and after branching caused by interaction with the obstacle (Dietterich et al., 2015).

## 2.4 Short-Duration Volume-Limited Lava Flows

The studies discussed in Section 2.3 were significant in improving lava flow hazard assessment by increasing understanding and prediction of the maximum length achievable by a flow. However, these studies used data gathered from long-duration, cooling-limited lava flows. Additionally, detailed studies of volume-limited flows have mainly focused on those with longer durations (> 24 to < 72 hours) such as the 1971 Chaillupen valley lava flow at Villarrica volcano, Chile (Castruccio & Contreras, 2016), the 1999 lava flows at Mount Cameroon volcano (Suh et al., 2011), and 1981 flow at Mt Etna (Guest et al., 1987).

Four examples of well-studied short-duration volume-limited lava flows exist. These are Episodes 40 and 43 of the 1983-1986 Pu'u 'O'o eruption at Kīlauea volcano, Hawai'i (Wolfe, 1988; Heliker et al., 2001; 2003; Dietterich & Cashman, 2014) and the 19 July (Moore & Kachadorian, 1980; Soule et al., 2004) and 21 December (Lockwood et al., 1999; Soule et al., 2004) 1974 flows at Kīlauea (Table 2.1). Short-duration volume-limited flows differ from longer-duration cooling-limited flows in duration and effusion rate. Short-duration flows, such as those listed in Table 2.1 and those which occur at Mt. Etna (e.g. Alparone et al., 2003; Behncke et al., 2006; 2014; Ganci et al., 2012a; De Deni et al., 2015), have durations less than 24 hours and estimated effusion rates of  $\sim 60$  to  $980 \text{ m}^3 \text{ s}^{-1}$  (e.g. Soule et al., 2004; Behncke et al., 2006; 2014; De Beni et al., 2015). These values are considerably different than those of long-duration flows, such as the 1983, 1991-93, July-August 2001, 2004, and 2006 eruptions at Mt Etna, which had durations ranging from 24 hours to 473 days and estimated effusion rates of  $0.2$ - $60 \text{ m}^3 \text{ s}^{-1}$  (e.g. Guest et al., 1987; Calvari et al., 1994; Calvari & Pinkerton, 1998; Mazzarini et al., 2005; Favalli et al., 2010; Lombardo, 2016).

Table 2.1 – List of well-studied short-duration volume-limited lava flows.

Lava Flow	Duration (s)	Effusion Rate ( $\text{m}^3 \text{s}^{-1}$ )	Volume ( $10^6 \text{ m}^3$ )	Average Slope (Degrees)	Length (m)	Average Advance Rate ( $\text{m s}^{-1}$ )	Eruption Temperature ( $^{\circ}\text{C}$ )	Study
Episode 40, 1983-1986 Pu'u 'O'o eruption, Kīlauea	50400 (14 h)	230	11.6	~3	8400	0.17	–	Wolfe (1988), Heliker et al., (2001; 2003), Dietterich & Cashman (2014)
Episode 43, 1983-1986 Pu'u 'O'o eruption, Kīlauea	43200 (12 h)	280	12.1	~3	5300	0.12	–	Wolfe (1988), Heliker et al., (2001; 2003), Dietterich & Cashman (2014)
19 Jul 1974, Kīlauea	10800-18000 (3-5 h)	150-275	3.5	< 5	2000	0.1-1.6	1150	Moore & Kachadoria (1980), Soule et al. (2004)
21 Dec 1974, Kīlauea	21600 (6 h)	270	5.9	< 5	12400	1.4-2.2	1168	Lockwood et al. (1999), Soule et al. (2004)

“–” indicates information not reported

## 2.5 Thermal Remote Sensing

One of the most widely used methods for estimating lava flow properties, such as effusion rate and volume, and for capturing and analysing volcanic activity is thermal remote sensing. As such, thermal remote sensing has proved a valuable resource in the study and monitoring of volcanoes and their hazards (e.g. Calvari et al., 1994; Harris & Maciejewski, 2000; Calvari et al., 2004; Harris et al., 2007a; Bonaccorso et al., 2011; Spampinato et al., 2011; Ramsey & Harris, 2012; Patrick et al., 2014; Blackett, 2017). Satellite and ground-based sensors have been employed in many studies at various volcanoes and have been used to collect data on lava flows, lava domes, explosive activity, pyroclastic deposits, and fire fountains (Spampinato et al., 2011; Ramsey & Harris, 2013). Thermal methodologies either use satellite-based sensors, such as the Spinning Enhanced Visible and Infrared Imager (SEVIRI), Geostationary Operational Environmental Satellite (GOES), Advanced Very High Resolution Radiometer (AVHRR), Landsat Thematic Mapper (TM), Along-Track Scanning Radiometer (ATSR), Moderate-Resolution Imaging Spectroradiometer (MODIS), and Hyperion, or ground-based sensors such as those manufactured by FLIR (either as permanent monitoring installations or in short-duration field surveys).

Each method has advantages and disadvantages. Satellite-based sensors commonly used for thermal remote sensing of active volcanic process offer a large spatial coverage, at the expense of lower pixel resolution (> one km). Ground-based sensors are easy to operate and can be hand-held or mounted on tripods (e.g. Calvari et al., 2004; Spampinato et al., 2011; Harris, 2013; Patrick et al., 2014). This portability allows thermal cameras to be relocated and moved as situations demand or deployed to cover specific areas for extended periods of time, giving them relatively high temporal resolution (acquisition intervals can be continuous to every few minutes). This flexibility in deployment gives ground-based sensors the benefit of moderate to high spatial resolution as well as a high temporal resolution. Additionally,

advances in thermal camera technology and reductions in price have greatly increased their use in volcanological research and monitoring.

### 2.5.1 Principles of Thermal Remote Sensing

Both satellite and ground-based thermal sensors use the established principles of thermography to collect data on active volcanic process. In remote sensing, thermography is the measurement of radiant temperatures of surfaces on the Earth using the infrared radiation (IR) emitted by an object (Spampinato et al., 2011). These measurements are carried out using the thermal portions of the IR spectral band, called thermal infrared radiation (TIR). TIR falls between the wavelengths of 3 to 14  $\mu\text{m}$  on the electromagnetic spectrum, with most broadband TIR remote sensors operating within a wavelength range of 7.5-13  $\mu\text{m}$ . In addition to TIR, some sensors also operate in the short-wave infrared or SWIR (1.4-3.0  $\mu\text{m}$ ) and the mid-infrared or MIR (3.0-8.0  $\mu\text{m}$ ) ranges.

Thermography relies on the radiation emitted from surfaces with a higher temperature than absolute zero. Increasing the temperature of a material produces greater spectral intensity,  $M$ , (Figure 2.6) as described by the Plank equation,

$$M(\lambda, T) = 2\pi hc^2 \lambda^{-5} [e^{\frac{hc}{\lambda k T}} - 1]^{-1} \quad 2.1$$

where  $T$  is the surface temperature,  $\lambda$  is the wavelength,  $h$  is Planck's constant ( $6.6256 \times 10^{-34}$  J s),  $c$  is the speed of light ( $2.9979 \times 10^8$  m s<sup>-1</sup>) and  $k$  is the Boltzmann constant ( $1.38 \times 10^{-25}$  J K<sup>-1</sup>). The measurement and analysis of the radiated energy gives the radiant temperature of the material, referred to as the apparent temperature (Shaw & Burke, 2003; Spampinato et al., 2011).

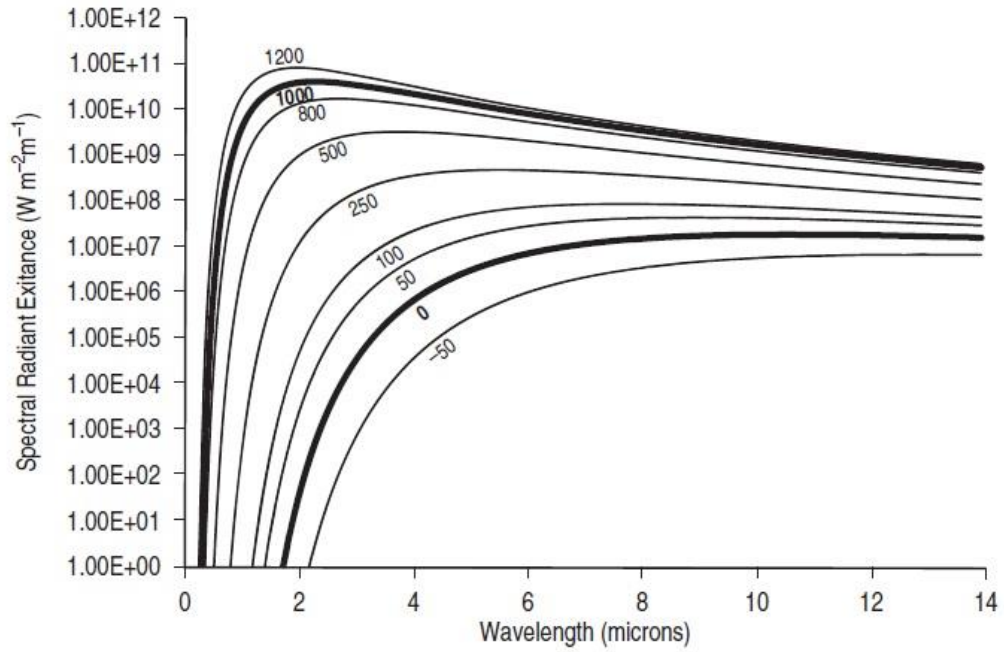


Figure 2.6 – The spectral density of electromagnetic radiation emitted from blackbody surfaces (an idealized body that absorbs all electromagnetic radiation independent of frequency and incidence angle) for temperatures between -50 °C and 1200 °C (Harris, 2013).

By integrating the Planck equation over all wavelengths for a blackbody, the radiant flux density ( $M_{rfd}$ ) of a material can be determined:

$$M_{rfd} = \int_0^{\infty} M(\lambda, T) d\lambda = \int 2\pi hc^2 \lambda^{-5} [e^{\frac{hc}{\lambda kT}} - 1]^{-1} d\lambda \quad 2.2$$

giving,

$$M_{rfd} = \frac{2\pi^5 k^4}{15c^2 h^3} T^4 \quad 2.3.$$

Combining all the constant terms gives the Stefan-Boltzmann constant,  $\sigma = 5.67 \times 10^{-8} \text{ W m}^{-2} \text{ K}^{-4}$ , and allows Equation 2.3 to be rewritten as Stefan's law:

$$M_{rfd} = \sigma T^4 \quad (\text{W m}^{-2}) \quad 2.4.$$

This equation gives the radiant power (heat flux per unit area) of a blackbody surface and describes how increases in temperature result in greater spectral radiant exitance.

If Equation 2.4 is multiplied by the area of the emitting surface ( $A_{surface}$ ), the radiant flux ( $\Phi_{rad\_flux}$ ) can be calculated:

$$M_{rfd} A_{surface} = \Phi_{rad\_flux} \quad (J s^{-1} \text{ or } W) \quad 2.5$$

Finally, if radiant flux is multiplied by time ( $t$ ) the radiant energy,  $Q_{rad}$ , released from the surface is determined:

$$\Phi_{rad\_flux} t = Q_{rad} \quad (J) \quad 2.6.$$

When apparent temperature is calculated using measurements collected by remote sensing platforms, the resultant value is not representative of the actual surface temperature of the material. The calculation of apparent temperatures relies on the assumption that the temperature surface is homogeneous. As a result, corrections for these and other additional factors must first be applied to the data before analysis can be undertaken (Ball & Pinkerton, 2006; Spampinato et al., 2011). Radiation traveling through the atmosphere changes intensity and direction due to atmospheric and environmental absorption and scattering (Kruse, 1994; Goetz et al., 1997; Rees, 2001; Aspinall et al., 2002; Shaw & Burke, 2003; Bohren & Clothiaux, 2006). Additionally, the emissivity ( $\varepsilon$ ) of the surface must be considered. Emissivity is a measurement of a material's ability to emit infrared radiation. Different materials have different emissivity values depending on their composition and surface texture. For basaltic lavas, calculated emissivity values range from 0.74-1.00 (Moxham, 1971; Ball & Pinkerton, 2006; Harris, 2013).

### 2.5.2 Correction of Thermal Data

To calculate accurate apparent surface temperatures, measured at-sensor radiance values must first be corrected for a variety of factors such as the emissivity of the material, atmospheric transmissivity (fraction of radiant energy that passes through a material), radiance emitted by the atmosphere (e.g. upwelling radiance), and radiance reflected by the surface of the Earth (e.g. reflected radiance).

Before radiance emitted by a surface reaches the sensor, some portion of it will be attenuated due to absorption and scattering by the atmosphere. This loss of energy is described by atmospheric transmissivity ( $\tau$ ). The magnitude of this loss is dependent on atmospheric conditions (atmospheric temperature and relative humidity) along the viewing-path, the presence and amount of greenhouse gases and aerosols in the atmosphere along the viewing-path, and by the length of the viewing-path. Increasing the atmospheric temperature or relative humidity, or the amount of greenhouses along a viewing path decrease the amount of emitted energy received by the sensor from a radiating target. This decrease is due to scattering and absorption of energy by the water content and presence of other gases in the atmosphere. The amount of water vapour in the air is influenced in two ways. The first is simply by the increase in relative humidity of the atmosphere. Relative humidity is the ratio of how much water vapour is in the air compared to how much the air can hold at that temperature. Higher relative humidity means that there is more water vapor in the air along the view-path which reduces the transmissivity of the air. The second involves the increase in water content in the atmosphere through increased atmospheric temperature. As atmospheric temperature increases, the amount of water the air can hold increases, which in turn lowers the relative humidity. So, to maintain the relative humidity of the air prior to the increase in temperature, a greater amount of water is required.

Additional radiance reflected by the atmosphere and reflected off the surface of the target and into the viewing path will also contribute to the total radiance received at the sensor. Like atmospheric transmissivity, the contribution of this additional radiance is dependent on atmospheric conditions, aerosols and the viewing path-length (Harris, 2013). The radiance received at the sensor can be broken down into three sources:

$$L_{at-sensor}(\lambda) = L_{surface}(\lambda) + L_{upwelling}(\lambda) + L_{reflected}(\lambda) + L_{scatter}(\lambda) \quad 2.7$$

where  $L_{surface}(\lambda)$  is the radiance emitted by the surface (described by the radiance leaving the surface multiplied by the emissivity of the surface),  $L_{upwelling}(\lambda)$  is the radiance emitted by the atmosphere,  $L_{reflected}(\lambda)$  is the radiance reflected by the surface, and  $L_{scatter}(\lambda)$  is the upward scattered solar radiance. Converting the at-sensor radiance to temperature gives the brightness temperature ( $T_{bright}$ ), which is the sum of radiance from all sources received at-sensor,

$$L(\lambda, T_{bright}) = L_{surface}(\lambda) + L_{upwelling}(\lambda) + L_{reflected}(\lambda) + L_{scatter}(\lambda) \quad 2.8.$$

By removing the unwanted radiance contributions from the at-sensor radiance and correcting the remaining radiance for atmospheric transmittance and emissivity, the actual radiance emitted by the surface can be calculated, so that

$$L_{surface}(\lambda) = \frac{L_{at-sensor}(\lambda) - L_{upwelling}(\lambda) - L_{reflected}(\lambda) - L_{scatter}(\lambda)}{\varepsilon(\lambda) \tau(\lambda)} \quad 2.9.$$

Depending on the sensor (satellite or ground-based) and the region of the IR spectrum in which it operates, Equation 2.9 can be adjusted to include additional terms or remove terms which have a negligible effect. For instance, if the sensor is operating in the SWIR, reflected atmospheric radiance in the form of upwelling radiance accounts for a negligible contribution to the total radiance received at the sensor, meaning that Equation 2.9 can be simplified to

$$L_{surface}(\lambda) = \frac{L_{at-sensor} - L_{reflected}(\lambda)}{\varepsilon(\lambda) \tau(\lambda)} \quad 2.10.$$

However, Harris (2013) showed that upward scattered solar radiance accounts for up to 15 % of the at-sensor radiance for measurements made in the SWIR. As a result,  $L_{scatter}(\lambda)$  must be included in Equation 2.10 when calculating surface temperatures in the SWIR:

$$L_{surface}(\lambda) = \frac{L_{at-sensor} - L_{reflected}(\lambda) - L_{scatter}(\lambda)}{\varepsilon(\lambda) \tau(\lambda)} \quad 2.11.$$

For sensors operating in the TIR we can simplify Equation 2.9 by removing  $L_{reflected}(\lambda)$  as its contribution to the at-sensor radiance is negligible (Harris, 2013):

$$L_{surface}(\lambda) = \frac{L_{at-sensor} - L_{upwelling}(\lambda)}{\varepsilon(\lambda) \tau(\lambda)} \quad 2.12.$$

Sensors operating in the MIR require the correction to surface radiance shown in Equation 2.9 but also need to be corrected for  $L_{scatter}(\lambda)$ , due to a significant contribution to at-sensor radiance from upward scattered solar radiance (like that seen within the SWIR) (Harris, 2013):

$$L_{surface}(\lambda) = \frac{L_{at-sensor} - L_{upwelling}(\lambda) - L_{reflected}(\lambda) - L_{scatter}(\lambda)}{\varepsilon(\lambda) \tau(\lambda)} \quad 2.13.$$

### 2.5.3 Additional Corrections for Ground-Based Thermal Data

Both atmospheric transmittance and atmospheric emitted radiance are influenced by the magnitude of the path-length. Ball and Pinkerton (2006) examined the effect of path-length on measured apparent temperatures due to changes in pixel resolution as viewing distance changes and found that for an increase in path-length from 1.5 to 250 m apparent temperatures decreased by ~326 K. Ball and Pinkerton also state that, when applying atmospheric corrections, difference in path-length for each pixel of an image must be considered to apply the appropriate atmospheric correction. This can be accomplished by correcting an image on a per pixel basis by modifying Equation 2.9, such that

$$L_{surface}(\lambda) = \frac{L(\lambda, x, y, z)^* - L_{upwelling}(\lambda, z) - L_{reflected}(\lambda, z)}{\varepsilon(\lambda) \tau(\lambda, z)} \quad 2.14$$

$L(\lambda, x, y, z)^*$  is the radiance of the pixel located at the image coordinate  $x, y$  and path-length  $z$ ,  $\tau(\lambda, z)$  is the atmospheric transmissivity for the pixel at path-length  $z$ ,  $L_{upwelling}(\lambda, z)$  is the upwelling radiance for a pixel at path-length  $z$ , and  $L_{reflected}(\lambda, z)$  is the reflected radiance for a pixel at path-length  $z$ .

In addition to composition and surface texture, the angle at which a measurement of a target surface is taken can affect the emissivity of a material. Ball and Pinkerton (2006) identified a significant decrease in apparent temperature due to a decrease in the emissivity of a smooth

basalt surface as the measurement angle of the hand-held thermal sensor used was increased above 30° from perpendicular to the surface. Observations made using the same experimental setup, but with a rough basalt surface, also showed a decrease in apparent temperature as the viewing angle became less perpendicular to the surface. However, Ball and Pinkerton (2006) attribute this decrease to the obscuring of depressions in the surface of the basalt from the sensor due to surface roughness as the viewing angle becomes closer to the horizontal, rather than to a decrease in emissivity.

#### 2.5.4 Calculating Atmospheric Correction Values

To determine the transmissivity of an atmosphere and the magnitude of the different contributing radiance sources along a view path, atmospheric transmission models are used. Two of the most commonly used methods for both satellite and ground-based thermal remote sensing are the Moderate Atmospheric Transmission code (MODTRAN) and the Low-Resolution Transmittance code (LOWTRAN) (Kneizys et al., 1988; Berk, 1989; Abreu & Anderson, 1996; Anderson et al., 1996).

LOWTRAN and MODTRAN are used to calculate atmospheric propagation of electromagnetic radiation for wavelengths of 0.2  $\mu\text{m}$  or greater (Kneizys et al., 1988) but differ in several ways. The first difference is in spectral resolution and frequency step size; LOWTRAN has a resolution of 20  $\text{cm}^{-1}$  and a step size of 5  $\text{cm}^{-1}$ , MODTRAN has a resolution of 2  $\text{cm}^{-1}$  and a step size of 1  $\text{cm}^{-1}$  (Berk, 1989; Abreu & Anderson, 1996). The two models also differ in their approach to calculating molecular transmittance. The LOWTRAN model was designed for low altitude paths at a temperature of 296 K. As a result, spectral radiances calculated using LOWTRAN above an altitude of 30 km were much lower than actual measured values (Abreu & Anderson, 1996; Anderson et al., 1996). Finally, in MODTRAN, users have the option to select either a horizontal or a slant-path viewing geometry while this choice is not available in LOWTRAN. The MODTRAN slant-path function integrates transmittance and upwelling radiance calculated

along a path-length to calculate the total transmittance and radiance contributors along a slant-path geometry. To calculate transmittance and upwelling radiance values, the MODTRAN user can select a pre-defined model atmosphere and aerosol model or create their own using measured values for atmospheric temperature, relative humidity, pressure and aerosol content. Then they input the geometry of the viewing scene using a set of viewing parameters (Table 2.2), specifying one of three viewing paths (Table 2.3). For slant-path viewing geometries, only three of the viewing path parameters need to be known, as the final unknown parameter is then calculated by MODTRAN to complete the computation (Table 2.4). The option of either a horizontal- or slant-path viewing geometry offered by MODTRAN allows calculation of upwelling radiance and atmospheric transmittance for a range of volcanological-relevant ground-based or satellite imaging scenarios.

*Table 2.2 – Viewing geometry parameters used by MODTRAN*

Viewing Path Parameter	Description
H1	Sensor or observer altitude
H2	Final altitude
ANGLE	Zenith angle at H1
BETA	Earth-centre angle
RANGE	Distance of the path-length between H1 and H2
HMIN	Minimum altitude of the path-length

*Table 2.3 – Viewing path options available in MODTRAN*

View Path Option	Path Description
1	Horizontal homogeneous path with constant atmospheric temperature, relative humidity, pressure and aerosol content.
2	Vertical or slant path between H1 and H2.
3	Vertical or slant path to space from H1.

*Table 2.4 – Slant-path cases for known parameters.*

Slant-Path Parameter Case	Known Specified Parameters
Case 1	H1, H2, ANGLE
Case 2	H1, ANGLE, RANGE
Case 3	H1, H2, RANGE
Case 4	H1, H2, BETA

### 2.5.5 Application of Remote Sensed Thermal Data

Once thermal data have been atmospherically corrected they can be used to estimate temperatures and identify a variety of volcanic features and phenomena. Harris (2013) and Ramsey and Harris (2012) provide an extensive review of works published using thermal remote sensing for both satellite-based (e.g. Figure 2.7) and ground-based sensors. The widespread value of these techniques is illustrated by the rapidly increasing number of publications in which they have been used. This is particularly true for ground-based thermal cameras (Figure 2.8). The first use of a ground-based “infrared camera” for volcanological purposes was by Shimozuru and Kagiya (1978). However, the “camera” used was a broadband (8-12.5  $\mu\text{m}$ ) bolometer-based radiometer attached to a scanning device, not a true hand-held infrared camera. Following this, Yuhara et al. (1981) and Ballestracci and Nougier (1984) both reported the use of a thermal scanning system for volcanological survey that worked similarly to a television camera, storing information on magnetic tape (Yuhara et al., 1981). The first reported use of a true camcorder style thermal camera was by McGimsey et al. (1999), who used a FLIR Systems SAFIRE model camera mounted on the underside of an aircraft to image eruptive activity at Pavlov and Shishaldin volcanoes in the Aleutian Islands, Alaska. The year 2002 saw the first publications in which a true hand-held thermal camera was used to collect data of volcanic phenomena (Dehn et al., 2002; Honda & Nagai, 2002; Kaneko et al., 2002; Nye et al., 2002; Ohba et al., 2002; Oppenheimer & Yirgu, 2002; Wright et al., 2002). While these studies marked the entry of hand-held thermal cameras into volcanology, the first application of hand-held thermal cameras to study lava flows did not appear in volcanological literature until 2003 (Table 2.5).

Table 2.5 lists papers where hand-held thermal cameras were used to study active lava flows and lava tubes. Of the 34 listed studies, only three collected data for analysis with path-lengths greater than 5 km. Of those three studies, two (Lyons et al., (2010) and Wessels et al., (2013)) used the thermal data to track and map lava flows and other eruptive activity. In the other of

these three studies, Ganci et al. (2013) used thermal data collected during the 12 August 2011 fire fountaining event at Mt. Etna by the INGV-Catania fixed thermal camera to calculate lava flow area, volume and radiant heat flux. These values, in combination with results calculated from SEVIRI data, were used to identify and separate the thermal signatures of the fire fountain from the lava flow produced by the fountain. Results given in the study show good agreement in calculated radiant heat flux between the ground-based and SEVIRI data sets. While the methodology used by Ganci et al. (2013) was essentially sound, subsequent investigation, done as part of this thesis, identified an error in the automated processing code of FLIR's processing software, ThermaCam Researcher, to adjust atmospheric temperature and relative humidity values for each thermal image using recorded values taken throughout the acquisition period. This error caused the atmospheric temperature and relative humidity to be fixed at 25 °C and 50 % for every image in the sequence, which resulted in a significant overestimate of actual surface temperatures (Appendix 11).

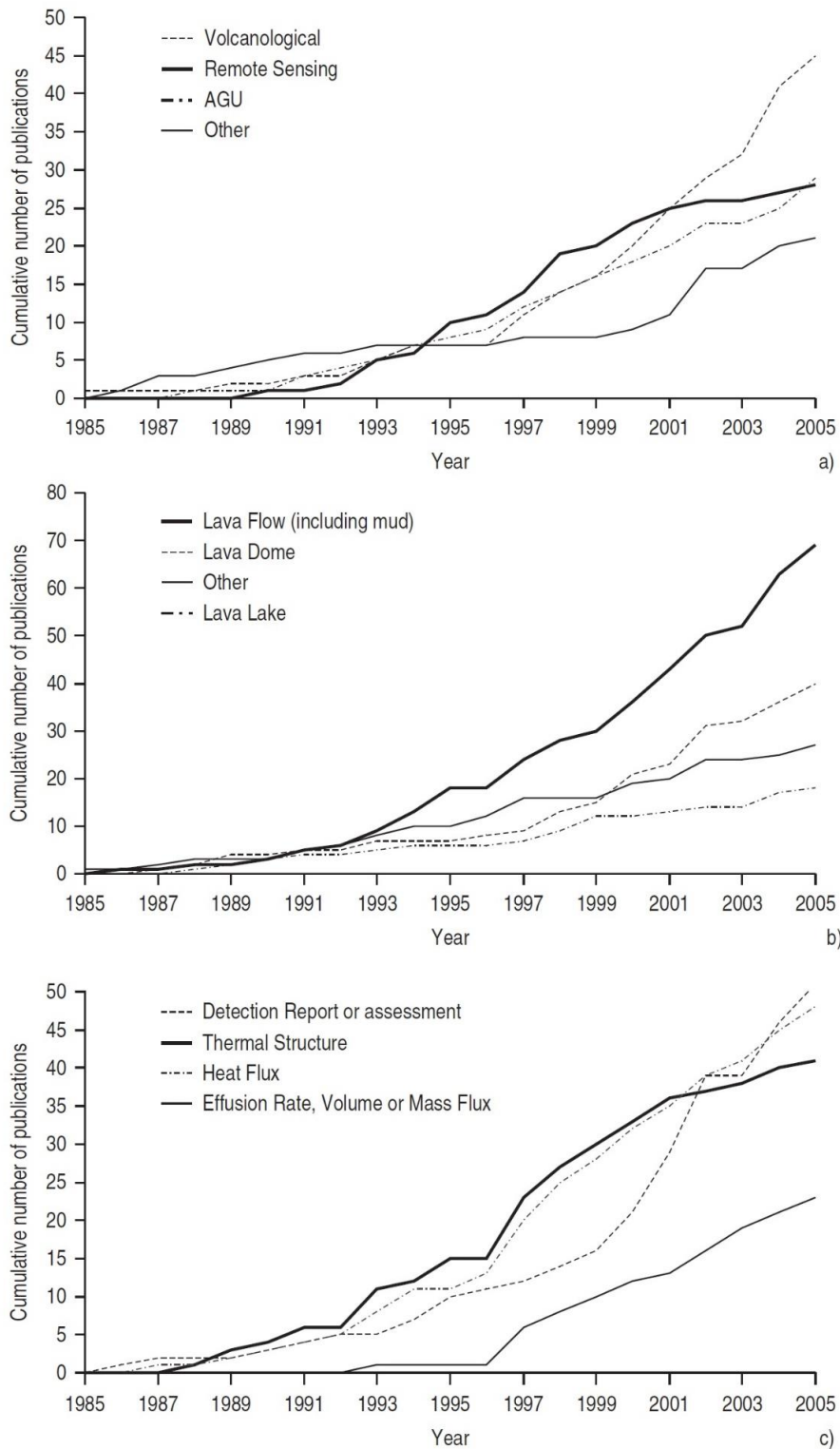


Figure 2.7 – The total number of published studies using satellite-based thermal sensors for volcanological applications from 1985-2005 by (a) journal type, (b) feature type studied and (c) main parameters extracted (Harris, 2013).

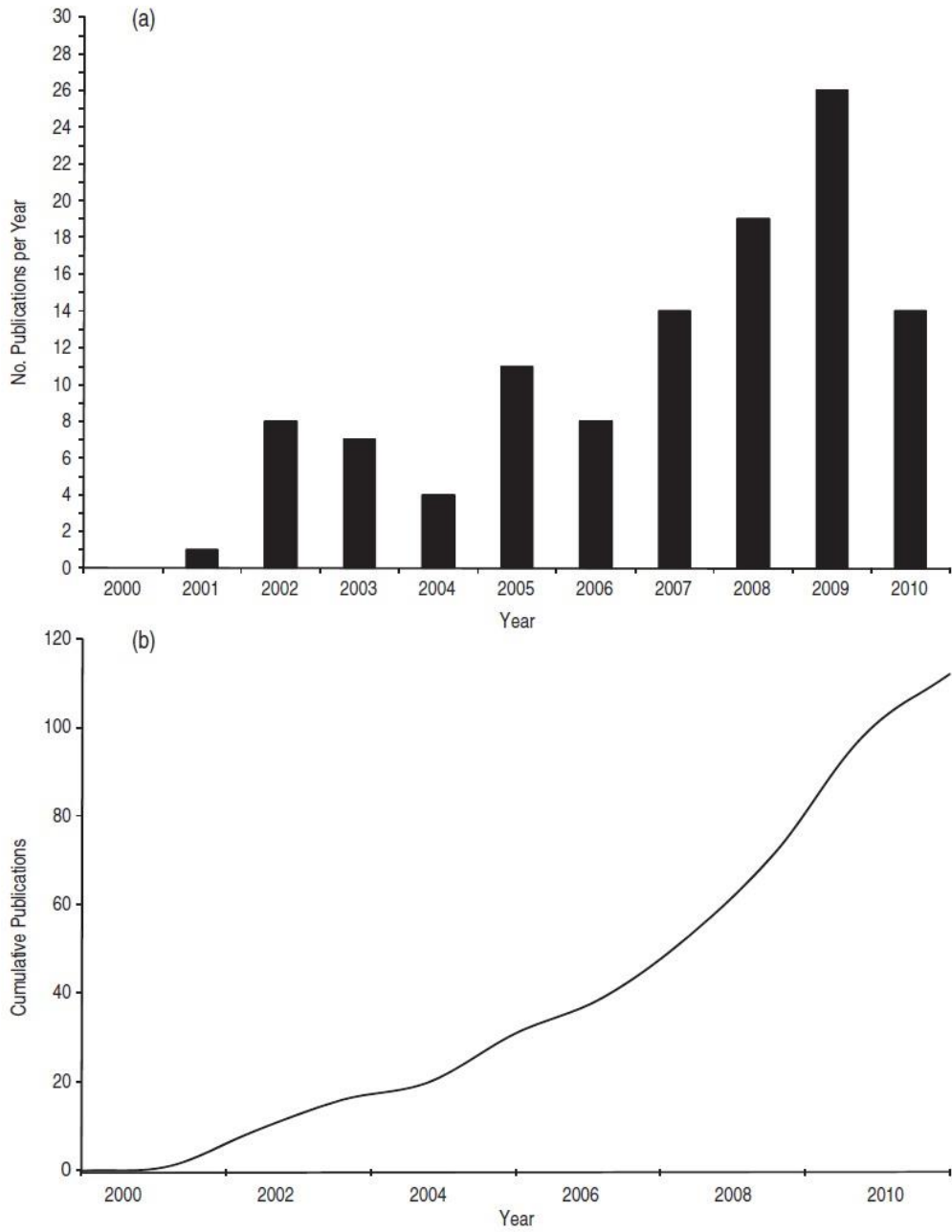


Figure 2.8 – Publications by year from 2000-2010 for studies which used ground-based thermal cameras for volcanological applications by (a) frequency distribution and (b) cumulative total (Harris, 2013).

Table 2.5 – Publications from 2000-2016 in which hand-held thermal cameras were used to observe and analyse active lava flows. Citations marked with a \* indicate studies which used permanently installed thermal cameras.

Volcano	Range (km)	Ground-Based	Airborne	Study
Kīlauea	–		√	Kauahikaua et al. (2003)
Kīlauea	0.005	√		Keszthelyi et al. (2003)
Kīlauea	0.003	√		Wright and Flynn (2003)
Etna	–	√		Lautze et al. (2004)
Etna	–		√	Andronico et al. (2005)
Etna	–	√	√	Burton et al. (2005)
Stromboli	1.0-2.0	√	√	Calvari et al. (2005)
Piton de la Fournaise	0.14-0.71	√		Coppola et al. (2005)
Stromboli	0.75-1.0	√	√	Harris et al. (2005a)
Etna	0.0-0.07		√	Harris et al. (2005b)
Etna	1.0		√	Ball and Pinkerton (2006)
Etna	0.1	√		Bailey et al. (2006)
Etna	0.1-0.4	√		James et al. (2006)
Augustine	–		√	Power et al. (2006)
Piton de la Fournaise	0.14	√		Coppola et al. (2007)
Kīlauea	0.2-0.75		√	Harris et al. (2007b)
Stromboli	1.0-2.0	√	√	Lodato et al. (2007)
Etna	0.7	√		James et al. (2007)
Kīlauea	0.008	√		Witter and Harris (2007)
Etna	–	√	√	Del Negro et al. (2008)
Kīlauea	0.005-0.01	√		Ball et al. (2008)
Stromboli	1.0-2.0		√	Spampinato et al. (2008)
Stromboli	0.5-1.0	√		Barberi et al. (2009) *
Etna	3.5	√		James et al. (2009)
Stromboli	0.45	√		Ripepe et al. (2009) *
Etna	–	√	√	Applegarth et al. (2010)
Piton de la Fournaise	0.17-0.71	√		Coppola et al. (2010)
Etna	2.0-5.0	√		James et al. (2010)
Fuego	~8.0	√		Lyons et al. (2010)

“–” indicates information not reported

Table 2.5 continued

Volcano	Range (km)	Ground-Based	Airborne	Study
Piton de al Fournaise	0.4-0.93	√		Staudacher (2010)
Stromboli	0.8	√		Bonaccorso et al. (2012)
Etna	8.5	√		Ganci et al. (2013) *
Redoubt	1.0-7.3 (avg of 1.6 km)		√	Wessels et al. (2013)
Kīlauea, Mauna Loa	0.5-2.0	√		Patrick et al. (2014)
Kīlauea	0.005-2.0	√		Carling et al. (2015)

"-" indicates information not reported

## 2.6 Time-Lapse Visible Imaging

Another method for capturing volcanic activity is using ground-based time-lapse imagery. The recent increase in resolution and quality of consumer dSLR cameras, combined with the reducing price of digital cameras, has allowed increasing use of ground-based visible time-lapse data collection. The small size and weight of consumer dSLR cameras allows for rapid deployment and easy relocation when needed, while their low cost means that replacing them in the event of damage or loss is much easier. Additionally, deployment of multiple units in an array to cover a large area and get multiple views of features is possible with a lower overall cost. Time-lapse visible photography has been used in a variety of applications (Table 2.6) and can be deployed in campaign-style surveys or as semi-permanent to permanent installations. Time-lapse visible photography has generally been used in three ways:

1. to visually capture and record processes;
2. to quantify processes by integrating images with a digital elevation model (DEM) to assign real-world x, y and z coordinate values to points in the sequence (Figure 2.9) and then track those points through sequences to calculate the displacement/movement of the point;
3. to derive DEMs directly through stereo image sequences (Figure 2.10).

Qualitative and quantitative time-lapse studies have previously been carried out on active lava flows (Table 2.6). Much of this work used short-term camera deployments at close ranges to active lava flows. However, few studies have been done to assess the viability of using long-range long-term time-lapse camera deployments to both visually analyse lava flow emplacement and to extract quantitative information.

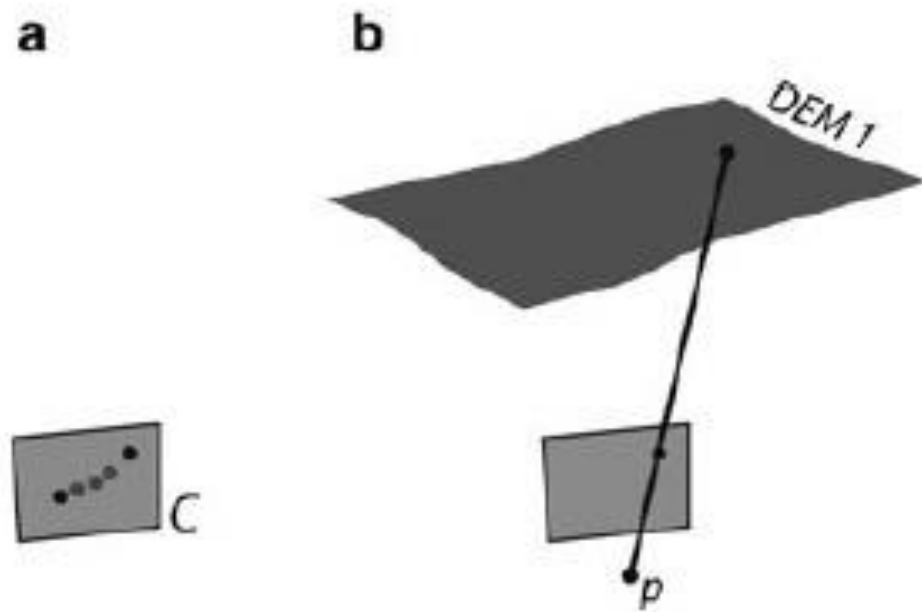


Figure 2.9 – The methodology used by James et al. (2016) for assigning 3D point coordinates to an observed feature in a time-lapse image sequence. (a) Observation points assigned to an object in the registered time-lapse image, C. (b) Using the perspective centre of the camera,  $p$ , observation points can be assigned real-world  $x$ ,  $y$  and  $z$  coordinates by projecting the point onto the surface of a DEM (modified from James et al., 2016).

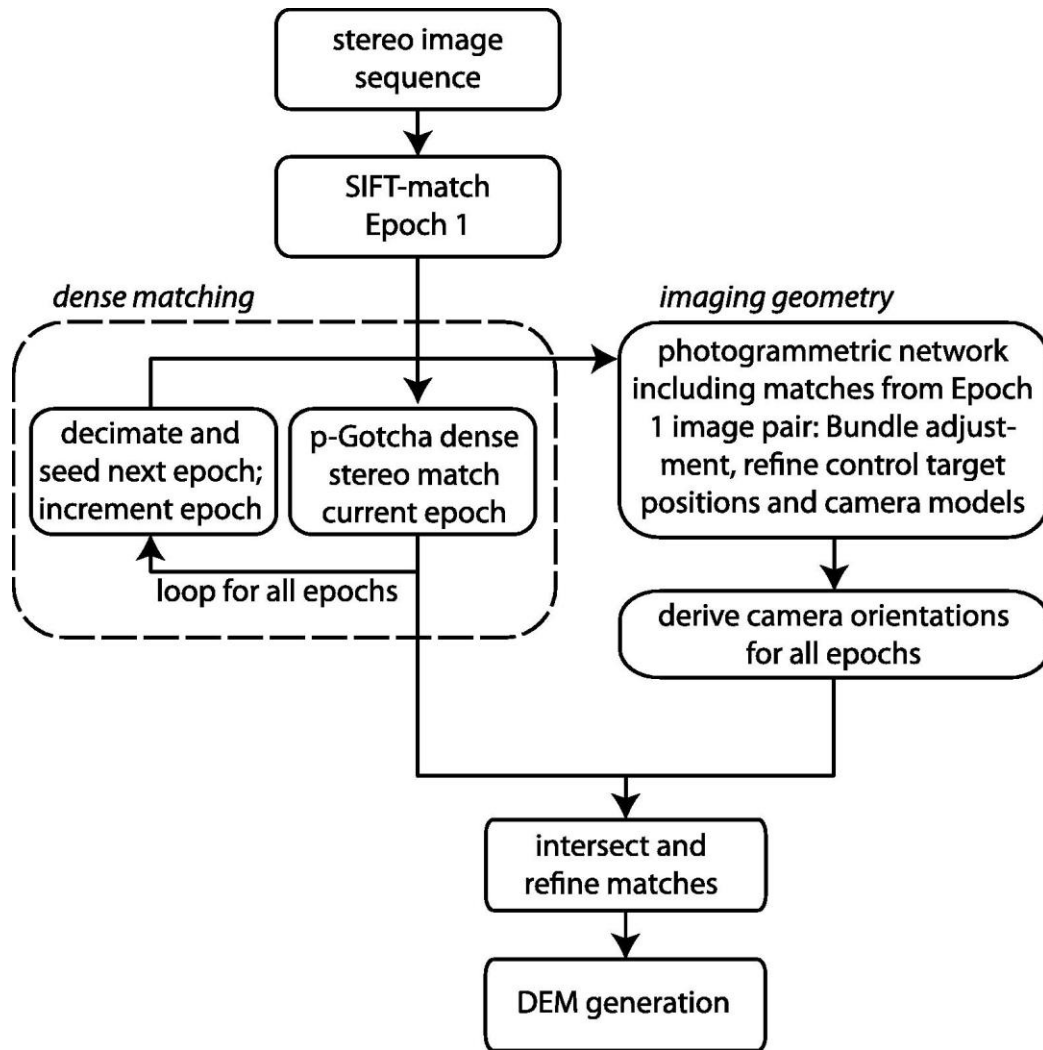


Figure 2.10 – The photogrammetric processing workflow used by James and Robson (2014).

Table 2.6 – Example geological studies in which ground-based time-lapse data were acquired using dSLR cameras.

Application						Analysis				Deployment		Study
LF	LL	EX	LD	DF/HT	LS	G	SM	PT	VO	Short	Long	
				√					√		√	Honda and Nagai (2002)
√							√			√		James et al. (2006)
√							√			√		James et al. (2007)
			√						√		√	Poland et al. (2008)
√									√	√		James et al. (2009)
			√				√	√				Major et al. (2009)
		√							√		√	Bonaccorso et al. (2012)
			√				√			√		James and Varley (2012)
√							√	√				James et al. (2012)
									√		√	Kendrick et al. (2012)
	√								√	√		Orr and Rea (2012)
					√			√				Travelletti et al. (2012)
		√							√		√	Calvari et al. (2014)
√							√			√		James and Robson (2014)
			√						√		√	Dzurisin et al. (2015)
				√			√			√		Lewis et al. (2015)
√									√		√	Orr et al. (2015)
√								√		√		Slatcher et al. (2015)
					√		√			√		Stumpf et al. (2015)
					√			√			√	Gabrieli et al. (2016)
						√		√			√	James et al. (2016)
	√						√			√		Smets et al. (2017)

\*Application: LF=lava flows, LL=Lava Lakes, EX=Explosive activity, LD=Lava Domes, DF/HT=Deformation/Hydrothermal Studies, LS=Landslides, G=Glaciers; Analysis: SM=3D Surface Models (DEMs, point clouds), PT=Point/Object Tracking (displacement studies), VO=Visual Observations; Deployment: Short=survey or campaign (days to one month), Long=semi-permanent to permanent deployment (greater than one month).

## 2.7 Lava Flow Modelling

Numerical models are increasingly used to augment current monitoring and analysis methods of lava flows. Numerical models allow scientists to estimate unknown morphological and rheological properties of lava flows by constraining models or validating model results with field-based and remote-sensing data (e.g. Young & Wadge, 1990; Crisci et al., 1999; Harris & Rowland, 2001; Hidaka et al. 2005; Vicari et al., 2007). Lava flow models can consider 1, 2 or 3-dimensions. The most commonly used 1-D model, FLOWGO (Harris and Rowland, 2001; 2015), will be discussed in-depth in Chapter 4.

The most common 2-D models are Cellular Automata (CA). These models operate by evolving cells through a given time step using a defined set of rules based on the states of surrounding cells. These rules are then applied iteratively for the specified time step. The three most commonly used 2-D CA models are SCIARA (e.g. Crisci et al., 1999; Avolio et al., 2006; Oliverio et al., 2011; Spataro et al., 2012; D'Ambrosio et al., 2014), FLOWFRONT (Young & Wadge, 1990; Wadge et al., 1994), and MAGFLOW (e.g. Vicari et al., 2007; Del Negro et al., 2008; Herault et al., 2009; Bilotta et al., 2012; Cappello et al., 2016; Kereszturi et al., 2016). The most prominent 3-D model is LavaSIM (e.g. Hidaka et al., 2005; Proietti et al., 2009; Fujita & Nagai, 2016). Table 2.7 gives the input and output parameters for the models discussed here. While models can provide a range of outputs, implementing the more complex models (i.e. the 2 and 3-D models) to run in real-time can be prevented due to the number and complexity of the input parameters required by these models to operate. Additionally, lava flow models such as SCIARA and MAGFLOW are used in a hazard assessment capacity. Outputs from these models focus on estimating the physical characteristics of the lava flow (e.g. flow length, area, and thickness of flow) for use in assessing the potential hazard posed (Ganci et al., 2011; 2012b). In situations when rheological properties are desired, the 1-D thermo-rheological FLOWGO model can be used. Not only can the FLOWGO model provide rheological estimates for lava

flows, its flexibility with starting flow geometry allows the model to estimate either down-flow channel width or depth. Additionally, the recent implementation of FLOWGO in Excel (Harris et al., 2015) allows the framework of the model to be constructed in a few hours.

*Table 2.7 – Input and output parameters for the listed lava flow models. Table adapted from Proietti et al. (2009).*

Model	Input Parameters	Output Parameters
FLOWGO	At-vent channel width, depth, slope, starting temperature, rheological and textural conditions, and effusion rate	Channel length, down-flow channel width or channel depth (depending on which parameter has not been measured in the field) thermal and rheological properties
FLOWFRONT	DEM, min flow thickness, critical thickness, slope angle, lava volume at each iteration	Lava thickness
SCIARA	DEM, vent location, effusion rate, lava solid temperature, intermediate temperature cooling parameters	Lava thickness and 2-D temperature
MAGFLOW	DEM, vent location, effusion rate, physical properties of lava	Lava thickness, 2-D temperature
LavaSIM	DEM, effusion rate, vent location, chemical and physical properties of lava	Lava thickness, 3-D velocity, temperature and state (liquid or solid)

## 2.8 FLOWGO

FLOWGO is a single-dimension thermo-rheological model developed by Harris and Rowland (2001). FLOWGO uses a cooling model based on the principles of radiative, convective and conductive heat loss to model changes in velocity and rheology of a basaltic lava flow as it moves down a pre-established open channel (Harris et al., 2015). The cooling model is used to calculate temperature and crystallinity for a specified step-value down the channel. FLOWGO then calculates viscosity, yield strength and velocity at each step using the values for temperature and crystallinity obtained from the preceding step's calculations (Figure 2.11).

Previous studies have used FLOWGO to examine best fit conditions between measured and model output changes in lava channel dimensions (Harris et al., 2007c) crystallinity (Riker et al., 2009) and temperature (Robert et al., 2014) and the model has been applied to lava flows at Mauna Loa and Kīlauea (Harris & Rowland, 2001; Rowland et al., 2005; Harris & Rowland, 2015), Mt. Etna (Harris et al., 2005b; 2007c; Robert et al., 2014), Mt. Cameroon (Wantim et al., 2013) and Piton de la Fournaise (Harris et al., 2015). Since its first implementation by Harris and Rowland (2001) FLOWGO has experienced two iterations. The first of these involved the combination of the model with the DOWNFLOW algorithm (Wright et al., 2008). FLOWGO uses DOWNFLOW to calculate the line of steepest descent using a DEM to determine a slope profile for the flow. The second is FLOWGO's implementation in Microsoft Excel.

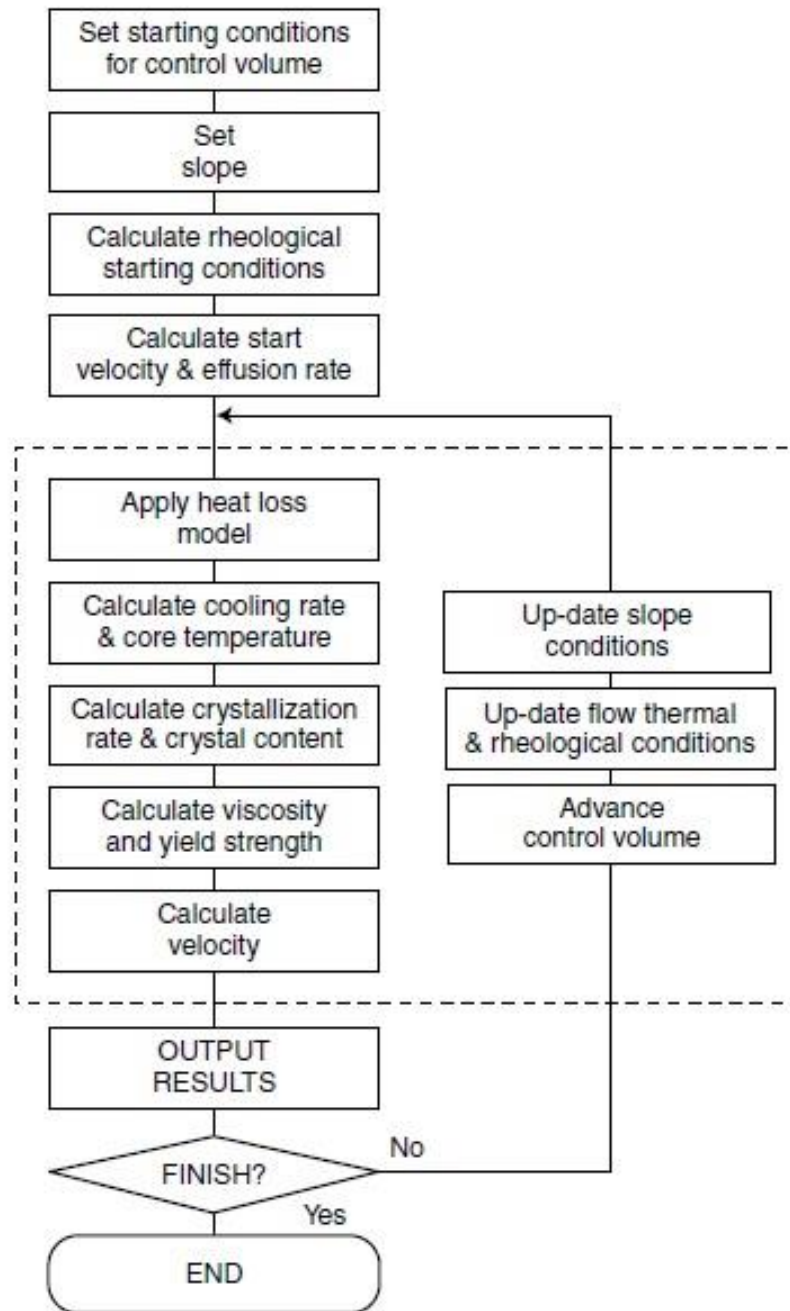


Figure 2.11 – Primary steps and loop processes used in the FLOWGO model (Harris & Rowland, 2015).

## 2.9 Mt. Etna

### 2.9.1 Background

Mt. Etna was selected as the study area for the work presented in this thesis due to the number and recurrence of short-duration volume-limited flows at the volcano. Mt. Etna is a basaltic volcano located on the island of Sicily in the Mediterranean at the front of the Apennine-Maghrebian thrust belt (e.g. Cristofolini et al., 1985; Bousquet & Lanzafame, 2004). Around 122,000-130,000 years ago, eruptive activity at Mt. Etna became dominated by Strombolian- to Plinian-style eruptions from edifices located within the present-day Valle del Bove (Branca et al., 2011). 15,000 years ago, activity at the volcano became more effusive, with occasional intense explosive activity, and has since become dominated by effusive-style eruptions paired with Strombolian-style explosive activity (Branca et al., 2011). Effusive eruptions at Mt. Etna can occur at summit vents or at lateral vents on the flanks of the volcano (e.g. Acocella & Neri, 2003; Burton et al., 2005; Spampinato et al., 2008). The summit of Mt. Etna is dominated by five summit craters: Southeast Crater (SEC), New Southeast Crater (NSEC), Bocca Nuova (BN), Voragine Chasm (C), and Northeast Crater (NEC) (Figure 2.12).

During 2011-2014, activity at Mt. Etna was focussed at the summit, dominated by discrete episodes of intense Strombolian activity, transitioning to sustained fire fountaining. Lava flows produced by the fire fountaining were rapidly emplaced (flows with duration of less than 24 hours, which attain nearly all their final length during this time) towards the southeast, into the Valle del Bove (Ganci et al., 2012a; Behncke et al., 2014; De Beni, et al., 2015; Viccaro et al., 2015) (Figure 2.12). 44 of these fire fountain events, known as paroxysmal events (e.g. Alparone et al., 2003; Behncke et al., 2006), occurred between 2011-2014 (Behncke et al., 2014; De Beni et al., 2015; Viccaro et al., 2015) and produced flows 0.4-4.3 km long (Behncke et al., 2014; De Beni, et al., 2015). The first 25 paroxysms (2011-2012) resulted in the birth and growth of the NSEC (Behncke et al., 2014) with all subsequent paroxysms (2013-2014) being

confined to the NSEC (Viccaro et al., 2015; De Beni et al., 2015). A period of inactivity lasting approximately 10 months followed the end of activity in 2012. Paroxysmal events generally ranged in duration from tens of minutes to several hours, with interval periods between events in 2011-2012 and 2013-2014 ranging from days to weeks (Behncke et al., 2014; De Beni et al., 2015; Viccaro et al., 2015).

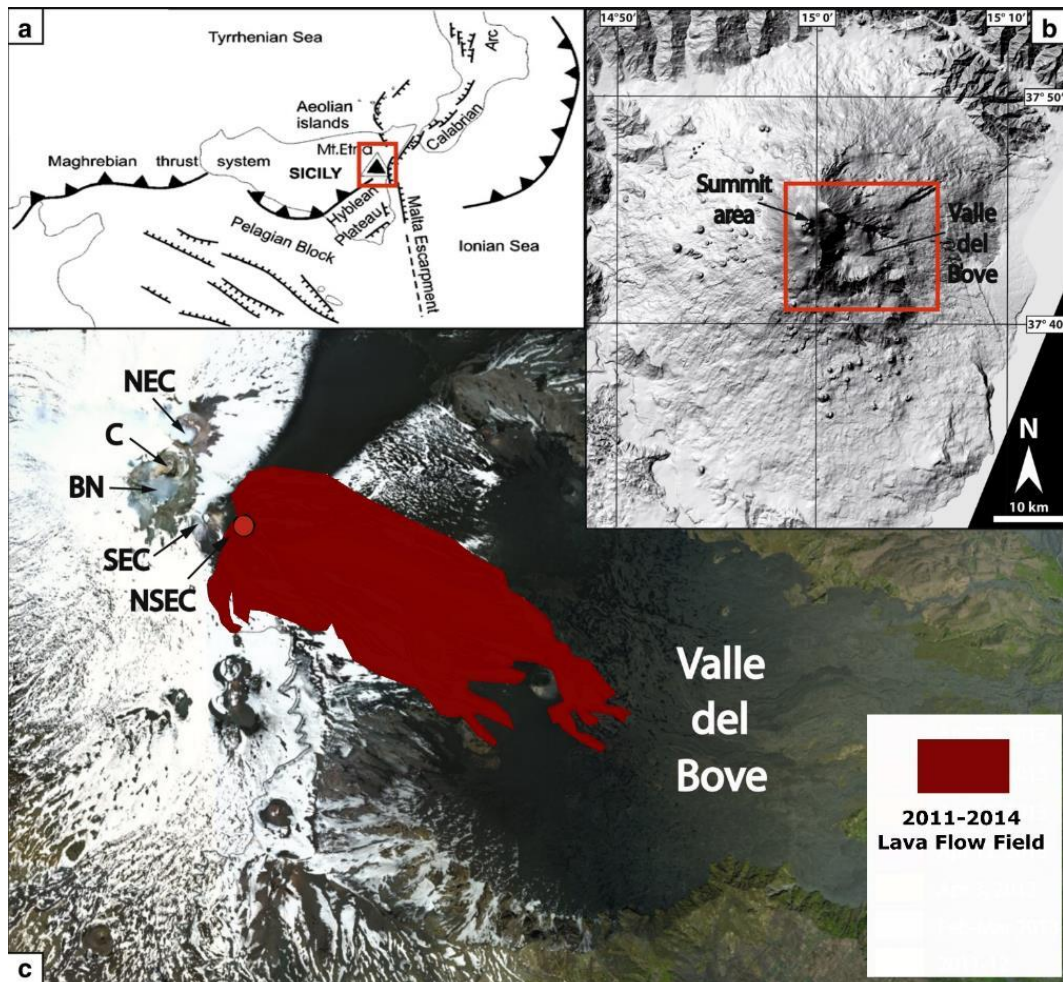


Figure 2.12 – (a) Tectonic domains and dynamics of Southern Italy. Red outlined area corresponds with the red rectangle marked in Fig. 2.12b. (b) Digital Elevation Model of Mt. Etna. (c) 2011-2014 lava flow field; NSEC (red circle) = New Southeast Crater, SEC = Southeast Crater, BN = Bocca Nuova, C = Voragine Chasm, NEC = Northeast Crater (Viccaro et al., 2015).

### 2.9.2 Monitoring Mt. Etna

The first dedicated observation and study of Mt. Etna was in 1876, when the decision to construct the V. Bellini observatory was made. However, within ten years the observatory was closed, and it was not until 1926 that the idea of a volcano observatory was given new life in the form of the Etnean Observatory (Behncke, 2018). In 1933, the Volcanological Institute was established at the University of Catania, Sicily. This institute was the first modern organization dedicated to the scientific study and monitoring of volcanic activity at Mt. Etna. In 1968 the Volcanological Institute was replaced with the International Volcanological Institute of the Italian Research Council. In 1999 the International Volcanological Institute was merged with the Sistema Poseidon to create the National Institute of Geophysics and Volcanology, Catania section (Behncke, 2018).

Like other volcano observatories of its kind, INGV-Catania uses visual observations, records of past eruptions, and instrumental surveillance to monitor and study activity at Mt. Etna. Monitoring programs at Mt. Etna typically consist of the tracking and recording of volcanic activity using seismic and infrasound data (e.g. Cosentino et al., 1982; Ferrucci et al., 1990; Cannata et al., 2009; Di Grazia et al., 2009; D'Agostino et al., 2013), petrographic analysis (e.g. Cristofolini & Romano, 1982; Tanguy et al., 1997; Taddeucci et al., 2002; Corsaro & Miraglia, 2005; Branca et al., 2011; Viccaro et al., 2015), measurement of gases (e.g. Malinconico Jr., 1979; Edner et al., 1994; Badalamenti et al., 1994; Francis et al., 1998; Burton et al., 2003; Corradini et al., 2003; Pugnaghi et al., 2006), ground deformation (e.g. Wadge, 1976; Murray & Guest, 1982; Massonnet et al., 1995; Nunari & Puglisi, 1995; Murray, 1997; Neri et al., 2009; Del Negro et al., 2013; Nahar & Mahmud, 2015), and thermal remote sensing (e.g. Bianchi et al., 1990; Bonneville & Gouze, 1992; Harris et al., 1997a; 1997b; Calvari et al., 2004; Lautze et al., 2004; Burton et al., 2005; Harris et al., 2005b; Bailey et al., 2006; James et al., 2007; Ganci et al., 2012a; 2013). INGV-Catania also uses a system which combines satellite-based thermal remote sensing and lava flow modelling for near-real-time monitoring and hazard forecasting

at Mt. Etna. This system, called HOTSAT, uses data from the Spinning Enhanced Visible and Infrared Imager (SEVIRI), Moderate-Resolution Imaging Spectroradiometer (MODIS), and Advanced Very High-Resolution Radiometer (AVHRR) satellite-based sensors to identify active lava flows and calculate their radiant heat flux (Ganci et al., 2011). The radiant heat flux is then converted to effusion rate (Harris et al., 1998), which is used to model possible lava flow paths using the MAGFLOW (Del Negro et al., 2008; Bilotta et al., 2012) lava flow model (Ganci et al., 2011; 2012b).

## 2.10 Summary

This chapter has identified several unknowns in terms of the study of short-duration volume-limited lava flows. While previous studies have analysed emplacement factors to evaluate their influence on flow length and morphology for long-duration cooling-limited lava flows, no such body of literature exists for short-duration volume-limited flows. As such, current models for lava flow lengths developed based on this information may not be applicable to short-duration volume-limited flows.

One of the reasons for the lack of analysis of volume-limited flows is simply that their short duration has prevented syn-emplacement analysis. Consequently, long-range ground-based visible and thermal time-lapse cameras, deployed for extended periods or permanently installed, can provide a means to capture and study such short-duration volume-limited flows. However, while both visible and thermal cameras have often been used at short-range they are seldom used for quantitative analysis over long viewing distances.

The following three chapters address these issues to meet the objectives and aim of this thesis. Chapter 3 and 4 examine the development of a method for remote analytical study of short-duration volume-limited flows using long-range ground-based visible time-lapse data and the FLOWGO thermo-rheological lava model. Chapter 5 examines improving the application of long-range ground-based thermal cameras for studying lava flows.

# Chapter 3 Using long-range ground-based visible time-lapse imagery to analyse flow emplacement: a study of short-duration volume-limited lava flows at Mt. Etna from 2011 to 2012

## 3.1 Introduction

Understanding the controlling factors of lava flow emplacement can greatly improve lava hazard assessments. Previous studies have shown that flow length positively correlates to effusion rate (Walker 1973; Wadge, 1978; 1979; Kauahikaua et al. 2003) and flow volume (Malin, 1980). Other factors which influence final flow length include the flow cooling rate (e.g. longer flows through cooling rate reductions due to lava tube formation; Swanson, 1973; Greeley, 1976; Greeley et al., 1976; Guest et al., 1980; Pinkerton & Wilson, 1994; Calvari & Pinkerton, 1998,1999; Harris & Rowland, 2009), slope (e.g. Hulme, 1974; Lister, 1992; Pinkerton & Wilson, 1994; Keszthelyi & Self, 1998; Cashman et al., 1999; Polacci & Papale, 1999; Tallarico & Dragoni, 1999; Gregg & Fink, 2000; Kerr et al., 2006; Favalli et al., 2009) and channel morphology (e.g. Macdonald, 1943; Guest et al., 1987; Pinkerton & Wilson, 1994; Dietterich & Cashman, 2014). As discussed in Section 2.4 of Chapter 2, most of these studies focus on long-duration cooling-limited flows, while few studies (Soule et al., 2004) analyse how these factors influence the emplacement and final length of short-duration volume-limited flows.

One of the reasons for this lack of analysis of short-duration flow is simply due to the time constraints imposed on data collection by the duration of these events. One approach to overcome this issue is to employ ground-based time-lapse imagery and photogrammetric techniques to geo-reference the data to a pre-existing DEM (e.g. Moore & Albee, 1980; Chandler & Brunsden, 1995; Lane et al., 2001; James et al., 2006; 2016; Major et al., 2009). In this way, geographic coordinates are obtained for image features such as lava flow fronts

which can then inform estimations of lava flow emplacement properties. Advances in digital camera technology have improved image resolution and decreased camera size, weight and cost. These improved qualities have facilitated the increased use of time-lapse image acquisition and near-real-time monitoring of volcanoes and volcanic activity, both as the sole method of analysis (e.g. Honda & Nagai, 2002; Kerle, 2002; Bluth & Rose, 2004; Herd et al., 2005; James et al., 2006; James et al., 2007; Major et al., 2009; James & Varley, 2012; Orr et al., 2015), and in combination with other methods such as InSAR and GPS surveys (e.g. Zlotnicki et al., 1990; Donnadieu et al., 2003; Pavez et al., 2006; Baldi et al., 2008; Ryan et al., 2010).

This chapter examines the use of long-range ground-based visible time-lapse imagery to better understand the emplacement of short-duration volume-limited lava flows (time-lapse data for all the camera locations is provided in the supplied auxiliary content). The work utilizes visual analysis of flow emplacement using visible time-lapse data and the point feature tracking software Pointcatcher (<http://www.lancaster.ac.uk/staff/jamesm/software/pointcatcher>) and statistical analysis of eruption parameters, topography, and flow/channel complexity to identify the effect and significance of factors on the maximum length attainable by the observed short-duration volume-limited flows.

## 3.2 Volcanic Activity

From January 2011 to April 2012, activity at Mt. Etna consisted of 25 intense, short-duration fire fountaining episodes which resulted in the formation of the New Southeast Crater (NSEC) cone around the former pit crater (Figure 3.1; Behncke et al., 2014). Eruptive vents for all 25 episodes were confined to the NSEC and its southeast, south, and north flanks (Behncke et al., 2014). Each episode rapidly emplaced (< 24 hours) lava flows towards the east-southeast flank of the NSEC, down the headwall of the Valle del Bove, and onto the floor of the valley. Lava flow lengths ranged from 2.1-4.3 km and covered a total area of 3.19 km<sup>2</sup> (Table 3.1; Behncke et al., 2014). Each episode consisted of four main phases: (1) A reactivation phase of small

explosive activity within the crater; (2) a phase of Strombolian-style activity during which explosive activity increased in frequency and intensity; (3) eruption of lava flows, usually preceding the onset of lava fountaining by tens of minutes to several hours, followed by sustained lava fountaining and; (4) waning of explosive activity, draining of channels, and stagnation of lava flows (Table 3.2) (Ganci et al., 2012a; Behncke et al., 2014). The interval time between events varied from 5.5 to 58 days. The total duration of each episode and duration of each phase differed across episodes as well, with total duration of episodes varying from 4 to 309 hours and lava fountaining duration ranging from 0.5 to 5.5 hours (Behncke et al., 2014). Flow fields consisted of 'a'ā lava flows which produced simple volume-limited flow field morphology (Behncke et al., 2014).

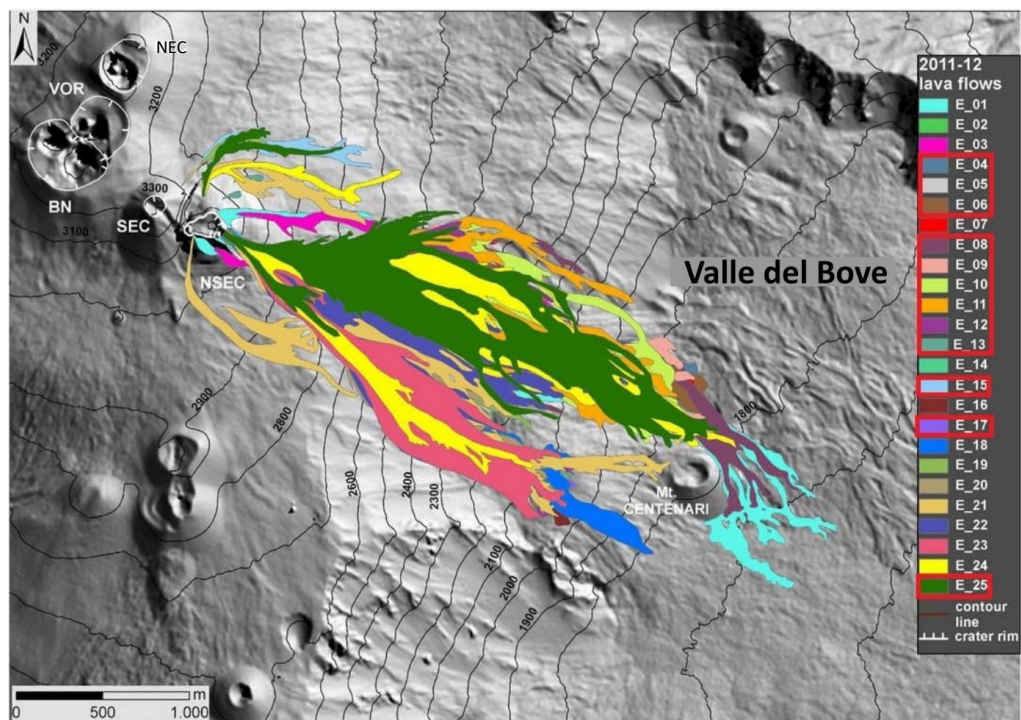


Figure 3.1 – Map of the flow fields emplaced during 2011 to 2012 at Mt. Etna. NEC = Northeast Crater, VOR = Voragine, BN = Bocca Nuova, SEC = Southeast Crater, NSEC = New Southeast Crater. Red boxes identify the episodes examined in this chapter. Figure edited from Behncke et al., 2014.

Table 3.1 – Volcanological parameters of the 25 lava flows from Behncke et al. (2014). Red box identifies episodes captured by time-lapse data. Red text identifies the episodes examined in this chapter.

Date	Episodes	Duration (s)	Length (km)	Area (km <sup>2</sup> )	Min Volume (10 <sup>6</sup> m <sup>3</sup> )	Max Volume (10 <sup>6</sup> m <sup>3</sup> )	Mean Volume (10 <sup>6</sup> m <sup>3</sup> )	Min MOR (m <sup>3</sup> s <sup>-1</sup> )	Max MOR (m <sup>3</sup> s <sup>-1</sup> )	Mean MOR (m <sup>3</sup> s <sup>-1</sup> )
12/01/2011	1	6000	4.3	1.02	1.31	2.33	1.82	219	388	303
18/02/2011	2	3600	3.3	0.45	0.51	0.88	0.7	142	246	194
10/04/2011	3	16,200	2.9	1.32	0.88	1.52	1.2	55	94	74
12/05/2011	4	6000	3.2	0.68	0.77	1.32	1.05	129	220	175
09/07/2011	5	3600	3	0.76	0.84	1.43	1.14	234	398	316
19/07/2011	6	9000	3.3	1.08	0.78	1.35	1.06	87	149	118
25/07/2011	7	7200	3	0.58	0.62	1.08	0.85	86	151	118
30/07/2011	8	7200	3.6	1.2	1.36	2.3	1.83	188	320	254
05/08/2011	9	7200	3.1	0.92	1.04	1.78	1.41	145	247	196
12/08/2011	10	5400	2.9	1.14	1.29	2.2	1.75	240	407	323
20/08/2011	11	1800	2.8	1.18	1.31	2.21	1.76	730	1230	980
29/08/2011	12	2100	2.7	0.65	0.7	1.26	0.98	334	600	467
08/09/2011	13	7200	2.6	0.31	0.34	0.59	0.46	47	82	64
19/09/2011	14	2400	2.2	0.29	0.31	0.55	0.43	131	227	179
28/09/2011	15	1500	2.1	0.29	0.29	0.48	0.38	191	319	255
08/10/2011	16	1200	2.7	0.33	0.37	0.62	0.5	309	519	414

\* Area of the total lava field formed by the overlapping of the 25 single lava flows. **MOR** = mean output rate

Table 3.1 continued

Date	Episodes	Duration (s)	Length (km)	Area (km <sup>2</sup> )	Min Volume (10 <sup>6</sup> m <sup>3</sup> )	Max Volume (10 <sup>6</sup> m <sup>3</sup> )	Mean Volume (10 <sup>6</sup> m <sup>3</sup> )	Min MOR (m <sup>3</sup> s <sup>-1</sup> )	Max MOR (m <sup>3</sup> s <sup>-1</sup> )	Mean MOR (m <sup>3</sup> s <sup>-1</sup> )
23/10/2011	17	7200	2.8	0.39	0.45	0.74	0.59	62	103	82
15/11/2011	18	5400	3.1	0.54	0.61	1.01	0.81	113	187	150
05/01/2012	19	6600	2.4	0.48	0.52	0.86	0.69	78	131	105
09/02/2012	20	7200	2.8	0.6	0.81	1.41	1.11	113	196	154
04/03/2012	21	7200	3.1	1.1	1.15	1.93	1.54	160	268	214
18/03/2012	22	6300	2.7	0.9	0.97	1.75	1.36	154	278	216
01/04/2012	23	5400	2.5	0.67	0.72	1.29	1	133	238	186
12/04/2012	24	2700	3.2	1.05	1.15	1.92	1.54	427	712	570
24/04/2012	25	3000	3.1	1.02	1.14	1.96	1.55	381	652	516
All episodes		138,600	4.3	3.19*	20	35	28	146	251	200

\* Area of the total lava field formed by the overlapping of the 25 single lava flows. **MOR** = mean output rate

Table 3.2 – Temporal eruption data from Behncke et al. (2014) covering the 25 episodes between 2/1/2011 and 24/4/2012, delineating duration of both lava fountaining phases and the full episodes. Red text identifies those episodes examined in this chapter.

Episode	Reactivation	Start Strombolian	Start lava emission	Start fountaining	End fountaining	End episode	Full episode (hh:mm)	Fountaining Duration (hh:mm)
1	02/01/2011 16:00	11/01/2011 08:00	12/01/2011 20:10	12/01/2011 21:50	12/01/2011 23:50	13/01/2011 02:00	42:00	2:00
2	18/02/2011 01:00	18/02/2011 01:45	18/02/2011 12:00	18/02/2011 03:30	18/02/2011 12:30	18/02/2011 13:17	12:20	9:00
3	29/03/2011 08:00	08/04/2011 06:00	09/04/2011 17:55	10/04/2011 08:05	10/04/2011 13:30	10/04/2011 14:03	56:00	5:25
4	08/05/2011 06:00	11/05/2011 17:00	11/05/2011 20:30	12/05/2011 03:20	12/05/2011 05:00	12/05/2011 05:55	96:00	1:40
5	04/07/2011 07:00	07/07/2011 20:00	09/07/2011 12:05	09/07/2011 13:45	09/07/2011 14:45	09/07/2011 15:30	128:30	1:00
6	16/07/2011 08:00	18/07/2011 17:00	19/07/2011 00:00	19/07/2011 00:05	19/07/2011 02:30	19/07/2011 03:00	67:00	2:25
7	24/07/2011 16:00	24/07/2011 18:00	25/07/2011 01:30	25/07/2011 03:00	25/07/2011 05:00	25/07/2011 05:30	13:30	2:00
8	28/07/2011 20:00	30/07/2011 07:50	30/07/2011 17:30	30/07/2011 19:35	30/07/2011 21:30	30/07/2011 22:00	50:00	2:00
9	05/08/2011 16:00	05/08/2011 17:00	05/08/2011 20:15	05/08/2011 21:00	05/08/2011 23:00	06/08/2011 00:15	8:15	2:00

Table 3.2 continued

Episode	Reactivation	Start Strombolian	Start lava emission	Start fountaining	End fountaining	End episode	Full episode (hh:mm)	Fountaining Duration (hh:mm)
10	11/08/2011 03:30	12/08/2011 05:30	12/08/2011 07:50	12/08/2011 08:30	12/08/2011 10:00	12/08/2011 11:00	31:30	1:30
11	19/08/2011 03:36	20/08/2011 02:00	20/08/2011 02:55	20/08/2011 07:00	20/08/2011 07:30	20/08/2011 07:50	28:15	0:30
12	28/08/2011 00:52	28/08/2011 18:00	29/08/2011 03:15	29/08/2011 04:05	29/08/2011 04:40	29/08/2011 05:15	28:30	0:35
13	06/09/2011 12:00	08/09/2011 05:30	08/09/2011 06:50	08/09/2011 06:30	08/09/2011 08:30	08/09/2011 08:45	45:15	2:00
14	16/09/2011 10:27	19/09/2011 02:00	19/09/2011 06:30	19/09/2011 12:20	19/09/2011 13:00	19/09/2011 13:10	74:30	0:40
15	28/09/2011 08:00	28/09/2011 17:30	28/09/2011 19:15	28/09/2011 19:31	28/09/2011 19:55	28/09/2011 20:10	12:10	0:24
16	08/10/2011 11:00	08/10/2011 11:24	08/10/2011 13:30	08/10/2011 14:30	08/10/2011 14:50	08/10/2011 17:45	6:45	0:20
17	23/10/2011 17:13	23/10/2011 17:40	23/10/2011 18:07	23/10/2011 18:30	23/10/2011 20:30	23/10/2011 21:15	4:00	2:00
18	15/11/2011 06:00	15/11/2011 08:00	15/11/2011 06:00	15/11/2011 11:00	15/11/2011 12:29	15/11/2011 13:00	7:00	1:29

Table 3.2 continued

Episode	Reactivation	Start Strombolian	Start lava emission	Start fountaining	End fountaining	End episode	Full episode (hh:mm)	Fountaining Duration (hh:mm)
19	04/01/2012 08:00	04/01/2012 16:00	05/01/2012 02:45	05/01/2012 05:00	05/01/2012 06:50	05/01/2012 08:30	24:30	1:50
20	27/01/2012 11:24	27/01/2012 21:40	08/02/2012 19:00	09/02/2012 00:00	09/02/2012 05:30	09/02/2012 09:00	309:30	5:30
21	16/02/2012 00:00	16/02/2012 20:00	04/03/2012 06:00	04/03/2012 07:30	04/03/2012 09:32	04/03/2012 09:32	417:30	2:02
22	16/03/2012 00:00	17/03/2012 20:00	18/03/2012 05:55	18/03/2012 08:00	18/03/2012 09:45	18/03/2012 10:10	58:10	1:45
23	26/03/2012 00:00	30/03/2012 18:30	01/04/2012 01:00	01/04/2012 02:00	01/04/2012 03:30	01/04/2012 04:30	154:10	1:30
24	10/04/2012 17:50	11/04/2012 19:00	12/04/2012 12:25	12/04/2012 14:30	12/04/2012 15:15	12/04/2012 16:00	46:10	0:45
25	21/04/2012 10:00	23/04/2012 17:00	23/04/2012 00:00	24/04/2012 01:30	24/04/2012 02:20	24/04/2012 02:40	64:20	0:50

## 3.3 Methodology

### 3.3.1 Time-Lapse Data Collection

To obtain wide coverage of the flow field emplacement area, four locations (Mt. Zoccolaro, Serracozza, Schiena dell Asino, and Pizzi Deneri) around the Valle del Bove were selected as installation sites (Figure 3.2). The cameras were deployed from May to October 2011 and then again in April 2012. From May to 13 August 2011 a single camera collected data at each site. After 13 August 2011, an additional camera was installed at two of the sites (Serracozza and Schiena dell Asino). The cameras used were Canon EOS 450D dSLRs, each with a 28 or 50 mm fixed focal length lens, a weather-proof container with an intervalometer (a timer which controls how often an image is taken based on a user-defined interval), and a solar panel and battery. Two different image acquisition intervals were used due to power restrictions caused by limited exposure of the solar panel to the Sun on the south side of the Valle del Bove. The cameras located at Mt. Zoccolaro and Schiena dell Asino were set to record images every 30 minutes while the cameras at Serracozza and Pizzi Deneri were set to record images at 15-minute intervals. Of the 25 fire fountaining episodes that occurred at Mt. Etna from 2011 to 2012, 15 were captured by the time-lapse cameras (Table 3.1).

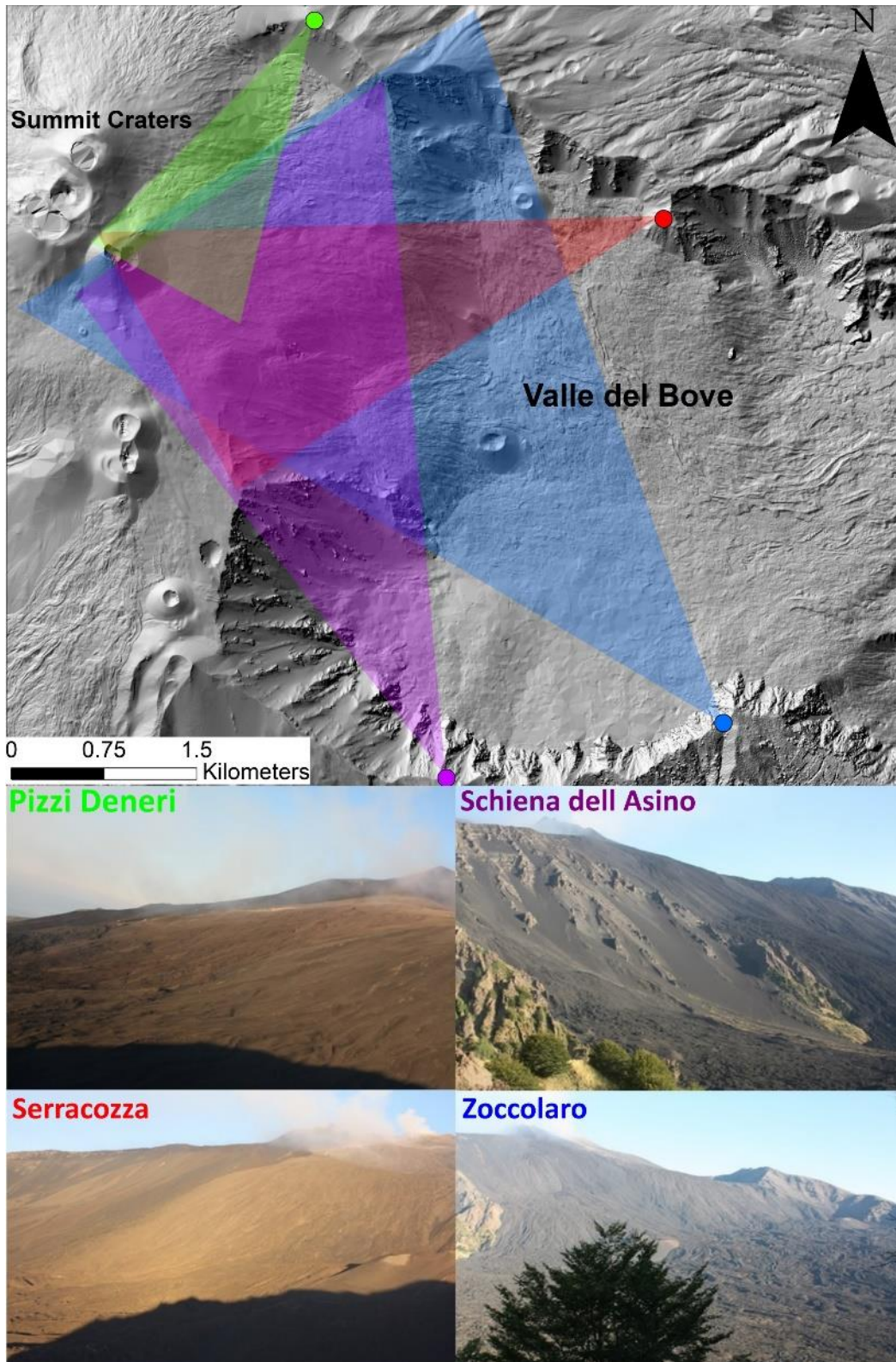


Figure 3.2 – Location and field of view of the four installation sites. Cameras are coded by colour with coloured cones showing the approximate field of view.

### 3.3.2 Lava Flow Emplacement Analysis

The visual analysis of flow emplacement employed the time-lapse data and the freely-available Pointcatcher software (e.g. James et al., 2007; Robson & James, 2007; James et al., 2016). The software allows for the tracking of feature points (specific selected feature or location in the image) manually or automatically using a correlation-based tracking system and can also geo-reference and re-project feature points onto a DEM (James et al., 2016). The geo-referencing and re-projection process requires that the x, y, z position of the camera (i.e. x and y given in Universal Transverse Mercator coordinates and z given in meters) and the camera model (internal optical geometry that defines how an image is created by the camera; James & Robson, 2012) be known. Once these values are input into Pointcatcher, the DEM is projected into the image to assess the camera orientation (Figure 3.3). After the initial orientation, the fit can be manually adjusted to ensure the best alignment of the DEM and reference image (Figure 3.4).

By geo-referencing the images, feature points can be re-projected onto the DEM, thus assigning them real world x, y, and z coordinates (Figure 3.5). The work presented in this chapter employs the Laboratorio di Aerogeofisica-Sezione Roma2 2012 DEM of the Valle del Bove (De Beni et al., 2015).

Calculating the 3-D distance between feature points placed on either side of a flow gives estimates of flow widths. By dividing the horizontal distance between two sequential points by their difference in elevation gives estimates of underlying slope. To estimate flow front advance rates, 3-D displacement between sequential feature points were determined and then divided by the camera's acquisition interval (i.e. 15 or 30 minutes).

Each eruptive episode produced several distinct flow fronts across the flow field. The individual flow which achieved the longest length was identified as the 'primary' flow, and flow front advance rates, width, and underlying slope were estimated by tracking features

points with the Pointcatcher software. The number of bifurcations and confluences were estimated visually using the time-lapse sequences. Flows produced by bifurcation of the primary flow are labelled 'secondary' flows, while flows produced due to bifurcation of secondary flows are labelled 'tertiary' flows.

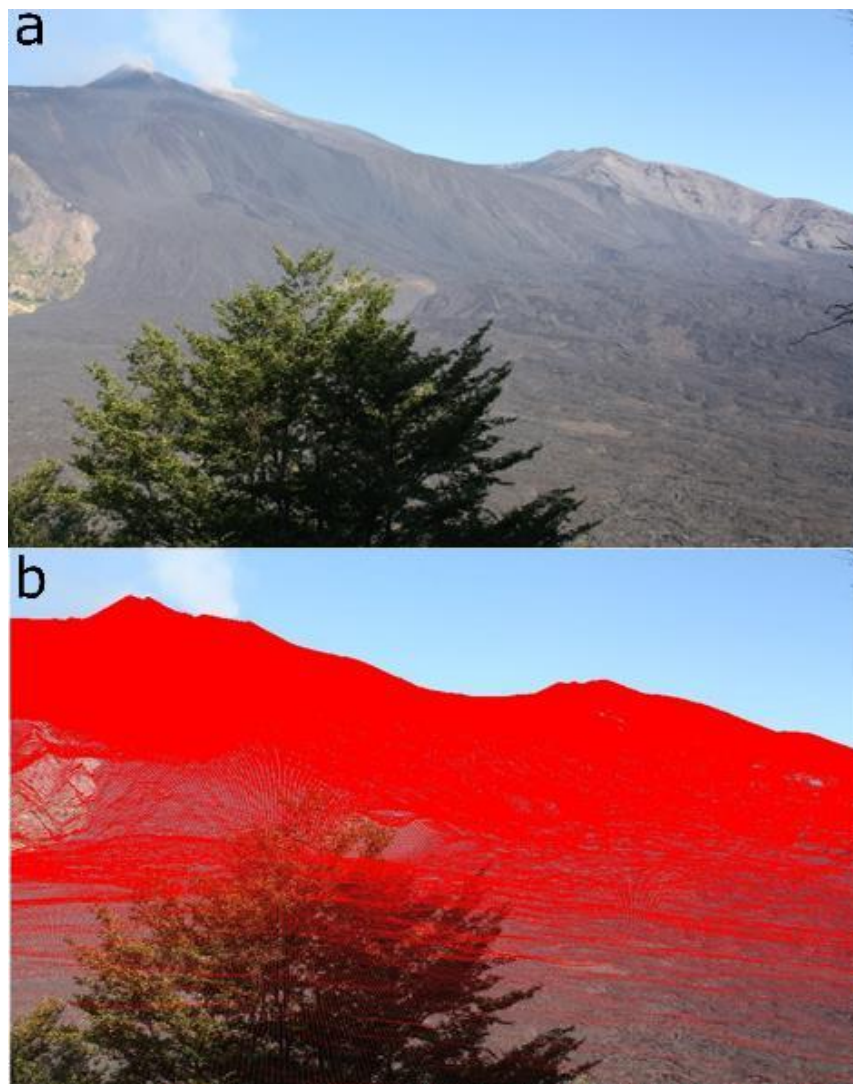


*Figure 3.3 – Selected reference image from the Zoccolaro camera (image taken 13/05/2011 04:33) (a) showing the viewing scene to be geo-referenced to the projected DEM, in red (b).*

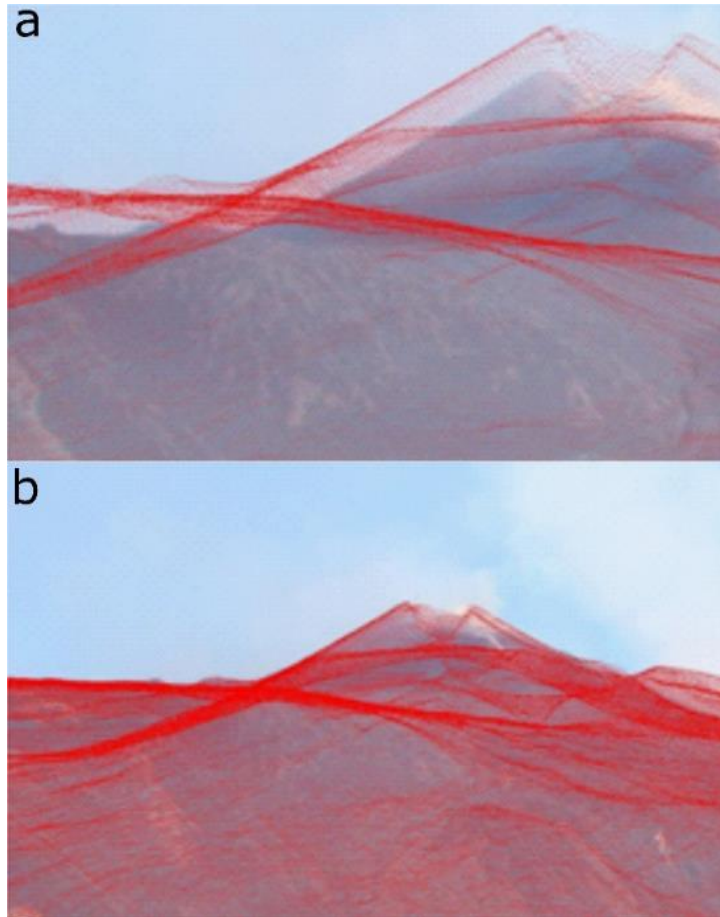


*Figure 3.4 – (a) Initial fit of the DEM to the Zoccolaro reference image done by Pointcatcher. (b) Final fit of DEM to reference image after manual adjustments. For best results the DEM should be matched to stationary image features.*

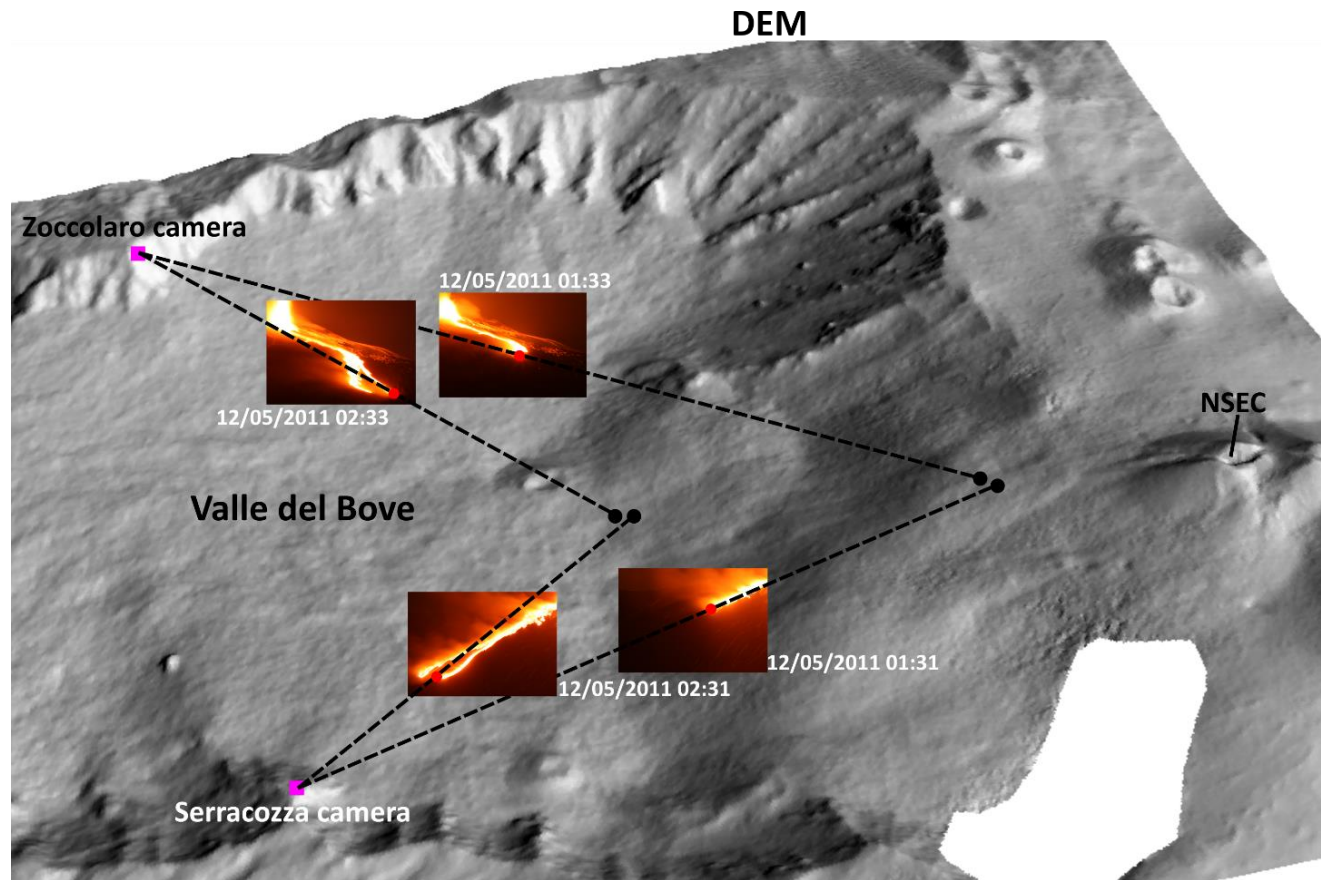


Figure 3.5 – Re-projection methodology used in Pointcatcher for assigning 3D coordinates to a feature point in a time-lapse image sequence (James et al., 2012; 2016). Using two of the cameras employed in this study, observation points are assigned to features in the geo-referenced time-lapse images (red circles in inset images). Using the perspective centre of the camera (purple squares), observation points are given real-world x, y and z coordinates by re-projecting the point from the geo-referenced image onto the surface of the DEM (black circles).

### 3.3.3 Statistical Analysis

Statistical analysis, such as simple correlation relationships and multiple regression, has been employed by previous studies to identify the controlling factors on lava flow length (e.g. Walker 1973; Malin, 1980; Pinkerton & Wilson, 1994), and to identify predictive models for flow length (e.g. Pinkerton & Wilson, 1994; Calvari & Pinkerton, 1998). Prior to any multiple regression analysis, the distribution of data requires examination. For small data sets (< 15 observations) it is important that the data are not highly skewed and follow an approximately normal distribution (e.g. Ghasemi & Zahediasl, 2012; Steele et al., 2016). For these small sample sizes, a non-normal distribution can make statistical significance tests less precise (e.g. Royston, 1991; Elliot & Woodward, 2007; Ghasemi & Zahediasl, 2012). Skewness and non-normality in data can be corrected by applying transformations (e.g. Elliot & Woodward, 2007; Steele et al., 2016). The most commonly used are log transformations, which previous studies (Pinkerton & Wilson, 1994; Calvari & Pinkerton, 1998) have employed to examine lava flow emplacement using multiple regression analysis.

The regression analysis carried out in this chapter uses a log-log transformation, following the method of Pinkerton and Wilson (1994) and Calvari and Pinkerton (1998), to correct the data for non-normal distribution. This method involves transforming both the independent and dependent variables by the natural log, which provides a multiplicative form of the partial least squares regression equation. Using the log transformed data, best subset model selection is employed to identify the best regression models for the given independent variables.

The best subset method used here employs a stepwise variable selection to determine inclusion or removal of a variable by assigning a significance value, known as an alpha, which acts as a cut off value for determining the addition or removal of a variable from a model. The typical alpha value used is 0.05. Any variable with a p-value greater than the alpha value is considered statistically insignificant

and removed (the p-value representing the significance of the variable within a statistical hypothesis test, i.e. the probability of the occurrence of a given event).

Once a set of models has been identified which meet the alpha value, best subset regression compares all models using the Akaike Information Criterion (AIC) (e.g. Akaike, 2011; Steinberg et al., 2011). The formula for calculating AIC is,

$$AIC = n * \log\left(\frac{\sigma^2}{n}\right) + 2 * K \quad 3.1$$

where  $n$  is the sample size,  $\sigma^2$  is the residual sum of squares, and  $K$  is the number of model parameters. The final product of the best subset selection is a list of models which meet the significance threshold and are ordered based on their AIC score. In practice, the smaller the AIC score the better the model is at explaining the relationship between the dependent and independent variables. However, AIC does not account for over-fitting of a model or illustrate the predictive quality of a model. It is therefore necessary to examine additional significance tests to compare the quality of the different models. The following are some of the most commonly-used statistics for evaluating the quality of a regression model:

*Coefficient of determination ( $R^2$ )* – Referred to as the goodness-of-fit,  $R^2$  is a measure of how close a regression model fits the observed values of the dependent variable. It measures the percent of variation in the dependent variable explained by the model. The higher the  $R^2$  the better the model fits the data. However,  $R^2$  increases with every independent variable added to the model and does not identify over-fitted models.  $R^2$  is calculated by dividing the regression sum of squares by the total sum of squares.

*Adjusted coefficient of determination ( $R^2_{adj}$ )* – Adjusted  $R^2$  compares the power of the fit of a regression model that contains different numbers of independent variables. Adjusted  $R^2$  only increases if the new variable added to the model improves the model more than would occur due to chance. Adjusted  $R^2$

decreases when a variable improves the model by less than what is expected due to chance. As a result, adjusted  $R^2$  is a strong indicator of over-fitted models. Over fitting a statistical model results in more parameters being included than can be justified by the data. This results in the model misrepresenting residual variance (i.e. noise) in the data as representing underlying model structure. The equation for calculating  $R^2_{adj}$  is,

$$R^2_{adj} = \left[ \frac{(1-R^2)(n-1)}{n-k-1} \right] \quad 3.2$$

where  $n$  is the number of data observations and  $k$  is the number of independent variables in the model (excluding the constant).

*Predicted coefficient of determination ( $R^2_{pred}$ )* – Predicted  $R^2$  indicates how effective a model is at predicting the dependent variable for new observations. Like adjusted  $R^2$ , predicted  $R^2$  is a strong indicator of over-fitting in models. Predicted  $R^2$  is calculated by systematically removing each observation from the data, fitting a new regression equation to the remaining observations, and determining how well the model predicts the removed observation.

*Standard error of regression (S)* – The standard error of the regression model represents the average distance that observed values are from the regression line. This means that S represents how wrong the model is on average. The smaller the value of S, the closer the observations are to the regression line. S is calculated by taking the square root of the sum of squared errors of the regression.

*Tolerance* – The tolerance statistic is used to identify and quantify how much the variance of a regression coefficient increases due to correlation between independent variables (Hair et al., 2009).

Tolerance of a variable in a regression model is calculated by,

$$Tolerance = 1 - R^2 \quad 3.3$$

where  $R^2$  is calculated by regressing the independent variable of interest by the other independent variables present in the regression model (Hair et al., 2009). For example, an independent variable with a tolerance of 0.6 means that 40 % of the variance of that variable is shared with some other independent variable in the model. The correlation of independent variables in a regression model is referred to as multicollinearity (Hair et al., 2009). Multicollinearity can result in exclusion of significant variables from models due to overestimation of the influence of less significant variables (Hair et al., 2009). Additionally, multicollinearity can affect the relationship of an independent variable to the dependent variable. In a simple linear regression model (where there is only a single independent variable), the regression coefficients will have the same sign (i.e. positive or negative) as the correlation coefficient ( $r$ ) between the independent and dependent variables in the regression model (Mosteller & Tukey, 1977). However, in a multiple regression model (where there is more than one independent variable) the sign of a regression coefficient can become opposite of the  $r$  between the independent and dependent variable. Correlation between independent variables in a model will change the influence that any one independent variable has with the dependent variable (Mosteller & Tukey, 1977; Hair et al., 2009). This effect is known as Simpson's Paradox (Yarnold, 1996; Soltysik & Yarnold, 2010).

*Variance Inflation Factor (VIF)* – VIF is another method for detecting and quantifying how much the variance of a regression coefficient increases if there is correlation between independent variables. VIF is calculated by taking the reciprocal of the tolerance statistic (Hair et al., 2009). For example, taking the reciprocal of a tolerance of 0.6 gives a VIF of 1.7. Taking the square root of the VIF identifies how much the significance of a variable has increased due correlation with the other independent variables in a model. Taking the square root of 1.7 gives a value of 1.3, which means that the standard error of the variable is 1.3 times greater than if it was uncorrelated with any of the other independent variables in the model. A VIF of 1 indicates no correlation between independent variables in the regression

model. A VIF of 1 to 5 (Hair et al., 2009) suggests that moderate correlation exists, and that the relationship of the independent variables should be examined. A VIF greater than five identifies the existence of severe multicollinearity and that corrective measures need to be applied. However, when more than two independent variables have even weak correlation ( $r = 0.25$ ) they can cause significant multicollinearity effects (Vatcheva et al., 2016).

## 3.4 Results

### 3.4.1 Flow Emplacement and Morphology Observations and Correlations

Of the 15 episodes captured by the time-lapse cameras, three had substantial cloud or gas cover obscuring the flow through much of the time-lapse sequence in all four cameras. The remaining 12 episodes had good visibility in two or more cameras and provided good spatial coverage of the flow fields (Table 3.3). The data acquired by the Zoccolaro and Serracozza cameras provided the best combination of spatial and temporal coverage of flow emplacement. All but four of the 12 episodes examined followed the sequence of activity listed in section 3.2. During 12 May 2011 (Episode 4), 20 Aug 2011 (Episode 11), and 24 April 2012 (Episode 25), lava emission began more than 4 hours prior to the start of fire fountaining (Table 3.4). During the 19 July 2011 episode, lava emission occurred  $\sim 5$  minutes prior to the onset of fire fountaining.

Comparing the observed start times for effusive activity and the start and end times of fire fountaining for the 12 episodes with those given by Behncke et al., (2014) in Table 3.2 revealed a discrepancy with Episodes 4 (12/05/2011), 8 (30/07/201), 13 (08/09/2011) and 25 (24/04/2012). In the time-lapse images, the start of lava emission for Episode 4 occurred at 11/05/2011 18:46 and the start and end of fire fountaining was 12/05/2011 01:31 and 12/05/2011 03:31. Behncke et al. (2014) however give the start time of lava emission as 11/05/2011 20:30, and times for the start and end of fire fountaining as 12/05/2011 03:20 and 12/05/2011 05:00. The value reported by Behncke et al., (2014) for the duration

of fire fountaining for Episode 8 appeared to be a rounding issue as Behncke et al., (2014) gave a duration of two hours when in the time-lapse images it was observed as one hour and fifty-five minutes.

Table 3.3 – Visibility and coverage of the 12 selected episodes. Episodes where the entirety of the flow was visible are labelled as “Good,” while episodes where the body of the flow was obscured from view but advancing flow fronts were visible are labelled as “Partial.”

Episode	Zoccolaro		Serracoza		Schiena dell Asino		Pizzi Deneri		Majority of flow emplaced during the day	Majority of flow emplacement during the night	Flow emplacement during both day and night
	Visibility	coverage	Visibility	Coverage	Visibility	Coverage	Visibility	Coverage			
4	Good	Good	Good	Good	Good	Partial	Poor	Poor			√
5	Partial	Good	Partial	Good	Partial	Partial	Good	Poor			√
6	Good	Good	Good	Good	Good	Partial	Good	Poor		√	
8	Good	Good	Good	Good	Partial	Partial	Good	Poor		√	
9	Good	Good	Good	Good	Good	Partial	Good	Poor		√	
10	Partial	Good	Partial	Good	Partial	Partial	Good	Poor	√		
11	Partial	Good	Partial	Good	Partial	Good	Good	Poor	√		
12	Partial	Good	Partial	Good	Partial	Good	Poor	Poor	√		
13	Partial	Good	Partial	Good	Partial	Good	Poor	Poor	√		
15	Good	Good	Good	Good	Good	Good	Poor	Poor		√	
17	Good	Good	Good	Good	Partial	Good	Poor	Poor		√	
25	Good	Good	Good	Good	Good	Partial	Poor	Poor		√	

Table 3.4 – Lava flow emplacement factors for the 12 episodes. Text in red indicate those flows which belong to Group 1.

Episode	4	5	6	8	9	10	11	12	13	15	17	25
	<b>Behncke et al., (2014)</b>											
$L$ (m)	3200	3000	3300	3600	3100	2900	2800	2700	2600	2100	2800	3100
$V_{mean}$ ( $10^6 m^3$ )	1.05	1.14	1.06	1.83	1.41	1.75	1.76	0.98	0.46	0.38	0.59	1.55
$t_{flow}$ (s)	6000	3600	9000	7200	7200	5400	1800	2100	7200	1500	7200	3000
$*MOR_{mean}$ ( $m^3 s^{-1}$ )	176	316	118	254	196	323	980	467	64	255	82	516
$A$ ( $10^6 m^2$ )	0.68	0.76	1.08	1.2	0.92	1.14	1.18	0.65	0.31	0.29	0.39	1.02
<b>Time-lapse</b>												
$adv_{avg\_Z1}$ ( $m s^{-1}$ )	0.04	0.12	0.26	0.12	0.13	0.15	0.05	0.18	0.24	0.57	0.34	0.04
$adv_{max\_Z1}$ ( $m s^{-1}$ )	0.11	0.19	0.28	0.14	0.26	0.23	0.22	0.43	0.34	0.58	0.34	0.13
$adv_{avg\_Z2}$ ( $m s^{-1}$ )	0.16	0.22	0.24	0.36	0.31	0.28	0.34	0.6	0.39	0.35	0.25	0.11
$adv_{max\_Z2}$ ( $m s^{-1}$ )	0.22	0.24	0.33	0.14	0.34	0.29	0.37	0.6	0.42	0.51	0.29	0.4
$adv_{avg\_Z3}$ ( $m s^{-1}$ )	0.04	0.02	0.21	0.1	0.12	0.11	0.06	0.11	0.11	0.03	0.06	0.05

$L$  = length,  $V_{mean}$  = average volume,  $t_{flow}$  = duration of flow,  $MOR_{mean}$  = the mean, mean output rate given by Behncke et al. (2014),  $A$  = area,  $adv_{avg\_Z1}$  = average advance rate in Zone 1,  $adv_{avg\_Z2}$  = average advance rate in Zone 2,  $adv_{avg\_Z3}$  = average advance rate in Zone 3,  $adv_{max\_Z1}$  = maximum advance rate in Zone 1,  $adv_{max\_Z2}$  = maximum advance rate in Zone 2,  $adv_{max\_Z3}$  = maximum advance rate in Zone 3,  $\alpha_{Z1}$  = average slope in Zone 1,  $\alpha_{Z2}$  = average slope in Zone 2,  $\alpha_{Z3}$  = average slope in Zone 3,  $\alpha_{avg\_all}$  = average slope for entire flow length,  $B$  = number of bifurcations,  $B_{Z1}$  = number of bifurcations in Zone 1,  $C$  = number of confluences,  $t_{flow\_time-lapse}$  = duration of flow estimated from time-lapse images (defined as the time between the start of lava emission to the end of fire fountain),  $t_{ff}$  = duration of fire fountain,  $t_{eff\ to\ ff}$  = time between start of emission of lava and start of fire fountain,  $t_{cp}$  = duration of the cooling dominant phase (calculated as the time from the end of fire fountaining to the end of episode),  $W_{max\_Z1}$  = maximum flow field width in Zone 1,  $W_{max}$  = maximum flow field width.

†The timing of fire fountaining start and end and the start of effusion given in Table 3.2 for Episodes 4, 8, 13, and 25 did not match that of the time-lapse data. Values for  $t_{ff}$  and  $t_{eff\ to\ ff}$ , given above are from the time-lapse data.

Table 3.4 continued

Episode	4	5	6	8	9	10	11	12	13	15	17	25
<b>Time-lapse</b>												
$adv_{max\_Z3}$ ( $m\ s^{-1}$ )	0.12	0.13	0.37	0.4	0.33	0.27	0.29	0.53	0.31	0.12	0.17	0.41
$adv_{avg}$ ( $m\ s^{-1}$ )	0.06	0.06	0.23	0.42	0.14	0.16	0.08	0.15	0.23	0.18	0.14	0.06
$adv_{max}$ ( $m\ s^{-1}$ )	0.22	0.24	0.37	0.4	0.34	0.29	0.37	0.6	0.42	0.58	0.34	0.41
$\alpha_{Z1}$ (deg)	19	20	19	19	18	20	20	17	18	21	19	20
$\alpha_{Z2}$ (deg)	25	25	27	22	23	25	25	21	23	23	23	24
$\alpha_{Z3}$ (deg)	16	19	12	15	11	13	21	19	16	10	16	10
$\alpha_{avg\_all}$ (deg)	19	20	19	17	15	18	21	18	19	15	19	17
$B$	8	4	5	11	9	7	6	5	11	8	11	7
$B_{Z1}$	3	3	4	4	5	4	4	2	2	1	2	3
$C$	2	0	2	4	2	0	1	0	0	1	1	3
$t_{flow\_time-lapse}$ (s)	31800	9600	9000	14400	9900	7800	16500	5100	4800	2400	8580	35640
$\dagger t_{ff}$ (s)	7200	3600	8700	6900	7200	5400	1800	2100	3600	1440	7200	3000
$\dagger t_{eff\ to\ ff}$ (s)	24600	6000	300	7500	2700	2400	14700	300	1200	960	1380	32640
$t_{cp}$ (s)	8640	2700	7500	1800	4500	3600	1200	2100	900	900	2700	1200
$W_{max\_Z1}$ (m)	86	170	184	225	234	200	159	111	300	141	93	152
$W_{max}$ (m)	270	470	700	930	730	470	770	570	300	200	300	670

The time given by Behncke et al. (2014) for the start of fire fountaining for episode 13 in Table 3.2 (08/09/2011 06:30) appeared to be a mistake. Examining the time-lapse images for this episode shows no visible activity at this time and shows the start of fire fountaining at 08/09/2011 07:30. Additionally, Behncke et al. (2014) gave the start time for effusive activity for episode 25 as 23/04/2012 00:00. The time-lapse sequence for this episode showed that a small lava flow was emitted during a short sequence of Strombolian-style activity within the NSEC. There was then no activity until 23/04/2012 03:06, when new effusive activity occurred due to a more sustained period of Strombolian-style activity. It was this second period of activity which produced the lava flow field and fire fountaining attributed to episode 25.

Visual analysis of the 12 episodes shows that changes in flow morphology during the emplacement of the flow fields coincide with changes in topography and slope at the boundaries of the Valle del Bove headwall. To examine these changes better, the emplacement area is divided into three zones outlined by the main breaks in slope within the Valle del Bove (Figure 3.6). Zone 1 covers the region from the NSEC to the break in slope that marks the beginning of the headwall of the Valle del Bove. Zone 2 covers the area from the start of the Valle del Bove headwall to the second break in slope at the bottom of the valley headwall and Zone 3 covers the area from the second break in slope extending onto the floor of the Valle del Bove.

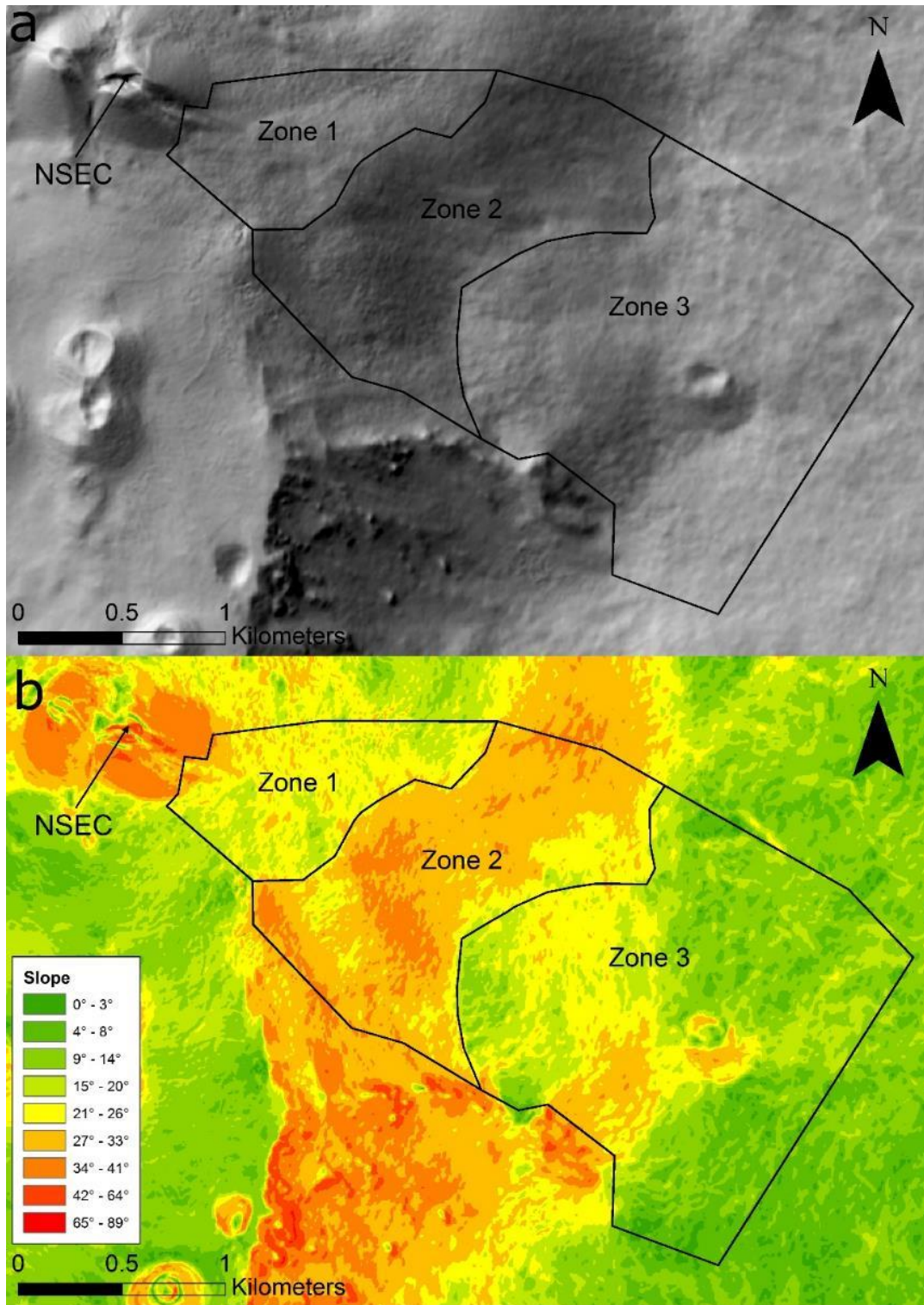


Figure 3.6 – (a) The division of the flow field into three zones based on the slope of the Valle del Bove, where the boundary between Zone 1 and 2 marks the start of the headwall of the Valle del Bove and the boundary between Zone 2 and 3 marks the transition from the headwall to the floor of the Valle del Bove and (b) the slopes within each zone. NSEC = New Southeast Crater.

Episodes 4-11 and 25 emplaced lava flows towards the east of the NSEC while Episodes 12-17 emplaced lavas to the east-southeast of the NSEC. Behncke et al. (2014) attributed this change in flow direction to lava erupted from a short fissure which formed on the south-eastern flank of the NSEC cone (the fissure was not visible in the time-lapse images). Two different flow styles were observed in Zone 1 and classified into two groups (Figure 3.7). Group 1 consists of three episodes (4, 11, and 25) which initially produced one to two unconfined flow lobes advancing at slow rates ( $0.04$  to  $0.05 \text{ m s}^{-1}$ ) until the onset of fire fountaining. Group 2 contains the other nine episodes which produced rapidly advancing ( $0.12$  to  $0.57 \text{ m s}^{-1}$ ) unconfined sheet flows.

For all 12 episodes, flows widened as they advanced through Zone 1, with bifurcations along the advancing flow front producing secondary flows (Figure 3.8). As lava flows crossed the transition point into Zone 2 they became more channelized (Figure 3.8), reaching maximum advance rates of  $0.22$ - $0.6 \text{ m s}^{-1}$ .

Upon transition from Zones 2 to 3, advancing flow fronts widened, with those nearest one another coalescing and advancing through Zone 3 as 1 to 3 broad lava flows. Flow fronts which did not coalesce advanced into Zone 3 as narrow individual lava flows (Figure 3.9). Within Zone 3, advancing flow fronts began to slow, occasionally bifurcating along the flow fronts and producing small lobate lava bodies. Flow field morphology consisted of 'a'ā lava which advanced as either discreet or sheet-like flows within Zone 1, transitioning to semi-channelized 'a'ā flows in Zones 2 and 3 and resulting in overall flow field morphologies which can be described as simple 'a'ā lava flow fields.

Pearson correlation values ( $r$ ) were determined for all of the data listed in Table 3.4 and is given in Table 3.5. For Pearson correlations, an  $r$  value of  $0.1$  to  $0.29$  is considered a weak correlation,  $0.3$  to  $0.49$  a moderate correlation, and  $0.5$  and above a strong correlation (e.g. Kendall & Gibbons, 1990; Chen & Popovich, 2002). Results identified strong correlations

between flow length ( $L$ ) and total volume ( $V_{mean}$ ) ( $r = 0.74$ ), duration given by Behncke et al. (2014) ( $t_{flow}$ ) ( $r = 0.63$ ), duration determined using the time-lapse data ( $t_{flow\_time-lapse}$ ) ( $r = 0.73$ ), and flow field width ( $W_{max}$ ) ( $r = 0.68$ ). Additionally, strong correlations were also found between  $L$  and the number of bifurcations within Zone 1 ( $B_{z1}$ ) ( $r = 0.83$ ), confluences ( $C$ ) ( $r = 0.53$ ), average ( $adv_{avg\_z1}$ ) and maximum ( $adv_{max\_z1}$ ) advance rate within Zone 1 ( $r = -0.55$  and  $-0.66$  respectively), and duration of fire fountaining ( $t_{ff}$ ) ( $r = 0.73$ ) for the 12 examined short-duration volume-limited lava flows. While  $L$  had a strong correlation with both  $V_{mean}$ ,  $t_{flow}$ , and  $t_{flow\_time-lapse}$  results showed a moderate correlation between  $L$  and duration of cooling dominate phase ( $t_{cp}$ ) ( $r = 0.47$ ) and almost no correlation between  $L$  and mean output rate given by Behncke et al. (2014) ( $MOR_{mean}$ ) ( $r = 0.002$ ). Additionally, correlation results identified a strong correlation between  $B_{z1}$ , maximum flow width in Zone 1 ( $W_{max\_z1}$ ) and maximum flow width ( $W_{max}$ ) ( $r = 0.78$  and  $0.61$  respectively).

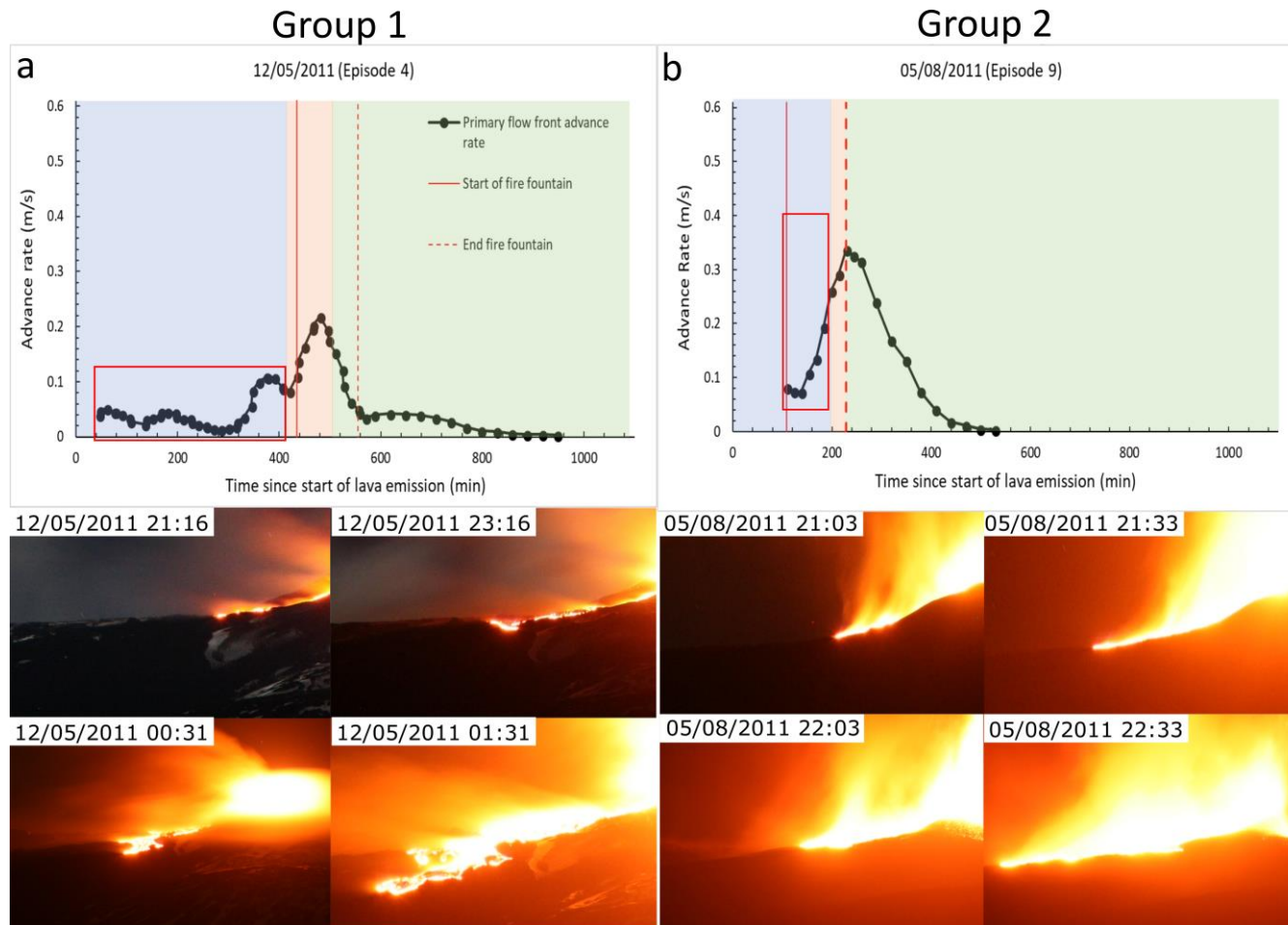
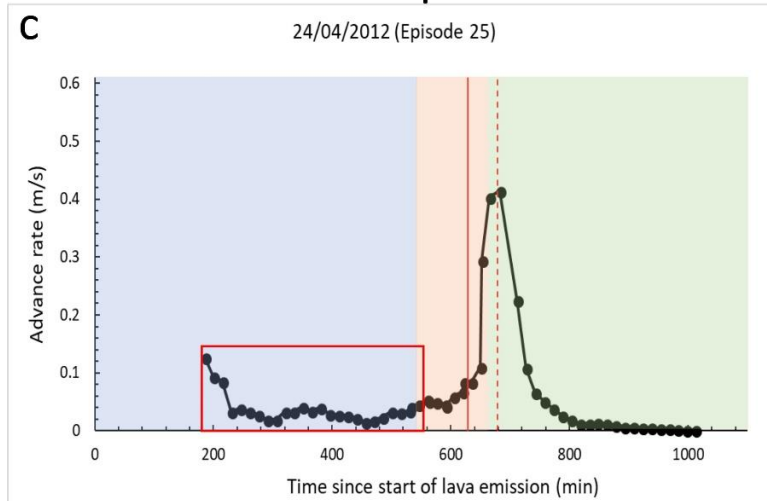
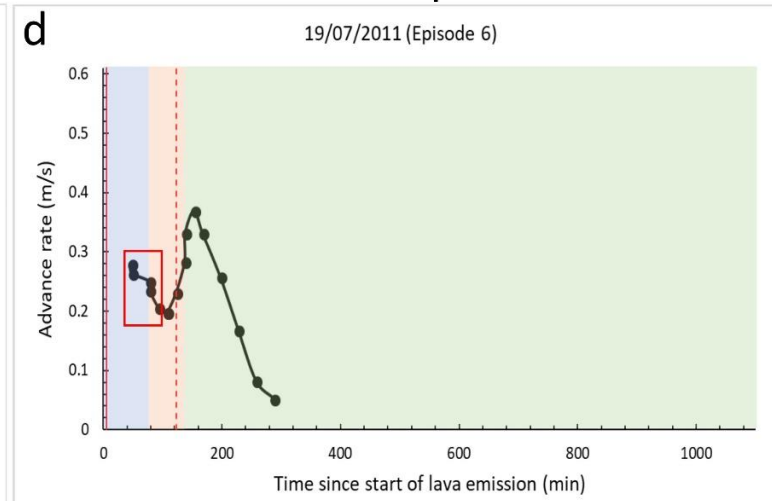


Figure 3.7 – Comparison of the two morphologies observed in Zone 1 and the corresponding advance rates. The 12/05/2011 (a) and 24/04/2012 (c) flows are examples of those belonging to Group 1, while the 05/08/2011 (b) and 19/07/2011 flows (d) represent those flows which belong to Group 2. Red boxes delineate the corresponding period of advance rates to the example images. Images are from the Serracozza camera. Background colours: blue = Zone 1, red = Zone 2, green = Zone 3 (Figure 3.7 continues onto the next page).

### Group 1



### Group 2



25/04/2012 18:06



25/04/2012 00:31



19/07/2011 00:18



19/07/2011 00:33



25/04/2012 01:01



25/04/2012 01:31



19/07/2011 00:48



19/07/2011 01:04



Figure 3.7 continued

a

\* 12/05/2011 flow field evolution (Episode 4)

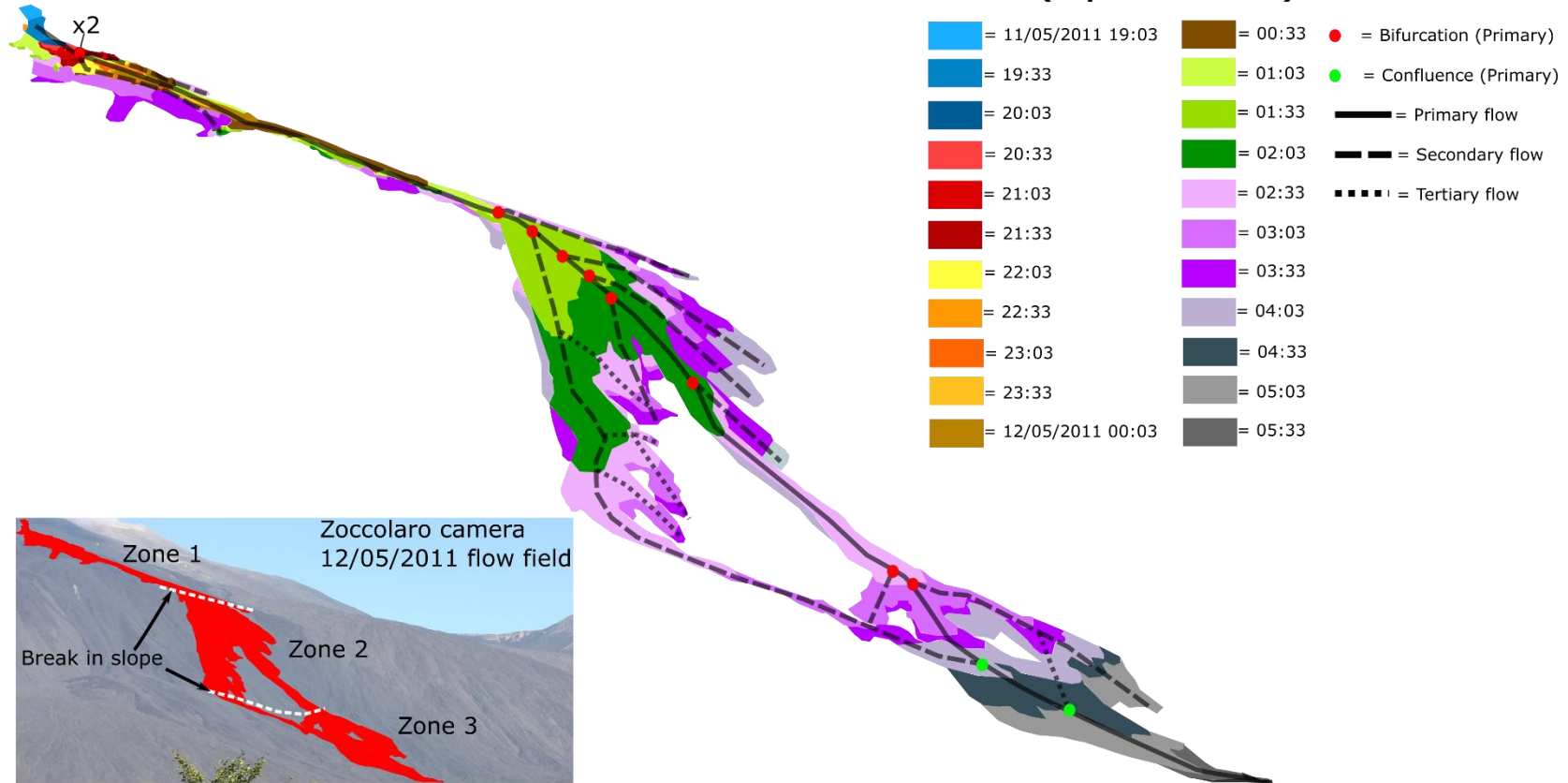


Figure 3.8 – Emplacement of the 12 flow fields (a-m) through time. Flow field outlines were created using images from the Zoccolaro camera as they provided the most complete view of the final flow field. The 24 April 2012 flow field (Episode 25) includes a second emplacement map using the Serracozza camera (l) as the Zoccolaro camera (m) inadequately covered the entire flow field due to a viewing misalignment caused by a rock fall. Solid, dashed, and dotted lines show the direction of flow. \* identifies those flows which belong to Group 1. (Figure 3.8 continues onto the next 11 pages).

b

# 09/07/2011 flow field evolution (Episode 6)

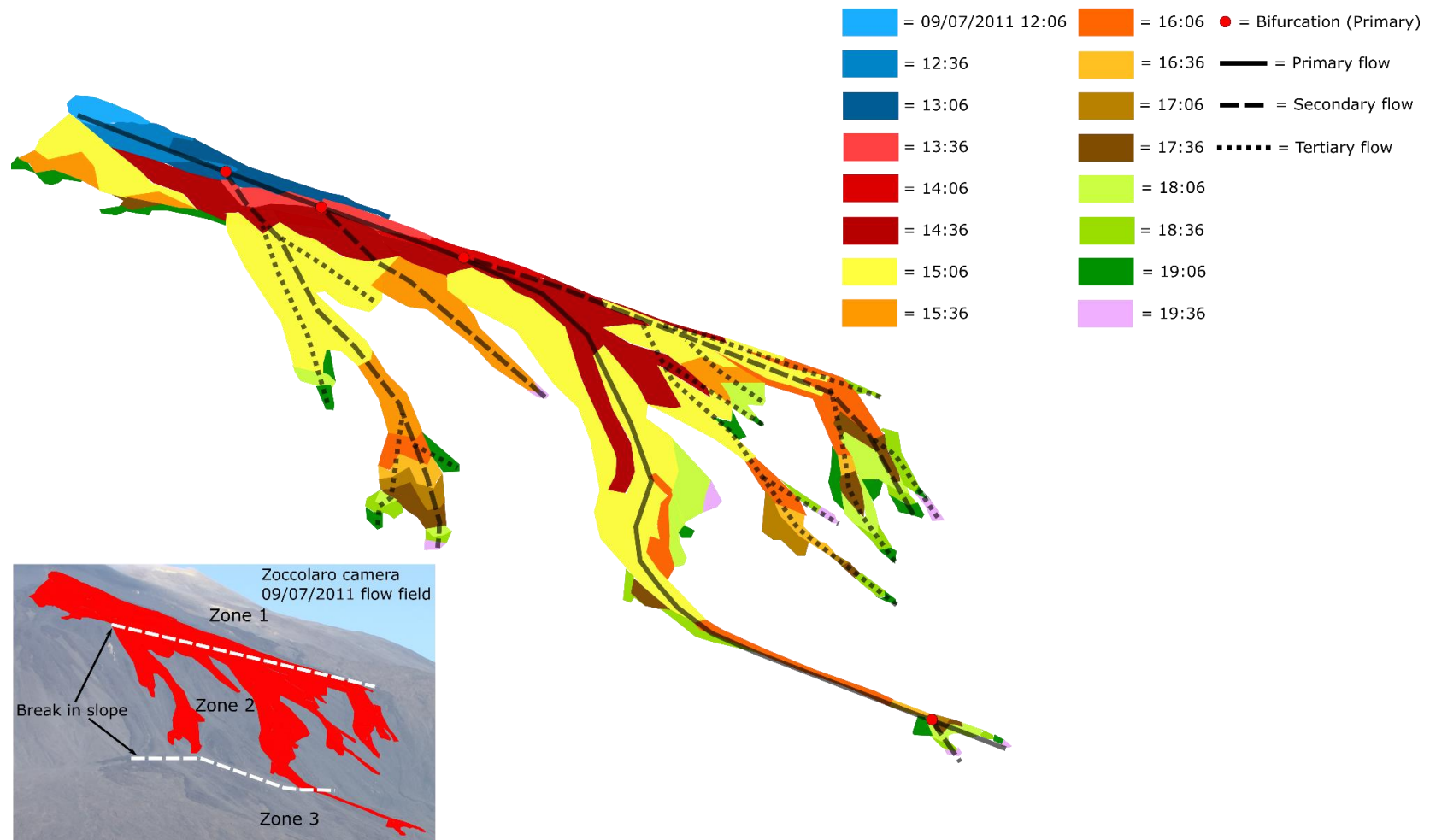


Figure 3.8 continued

C

### 19/07/2011 flow field evolution (Episode 7)

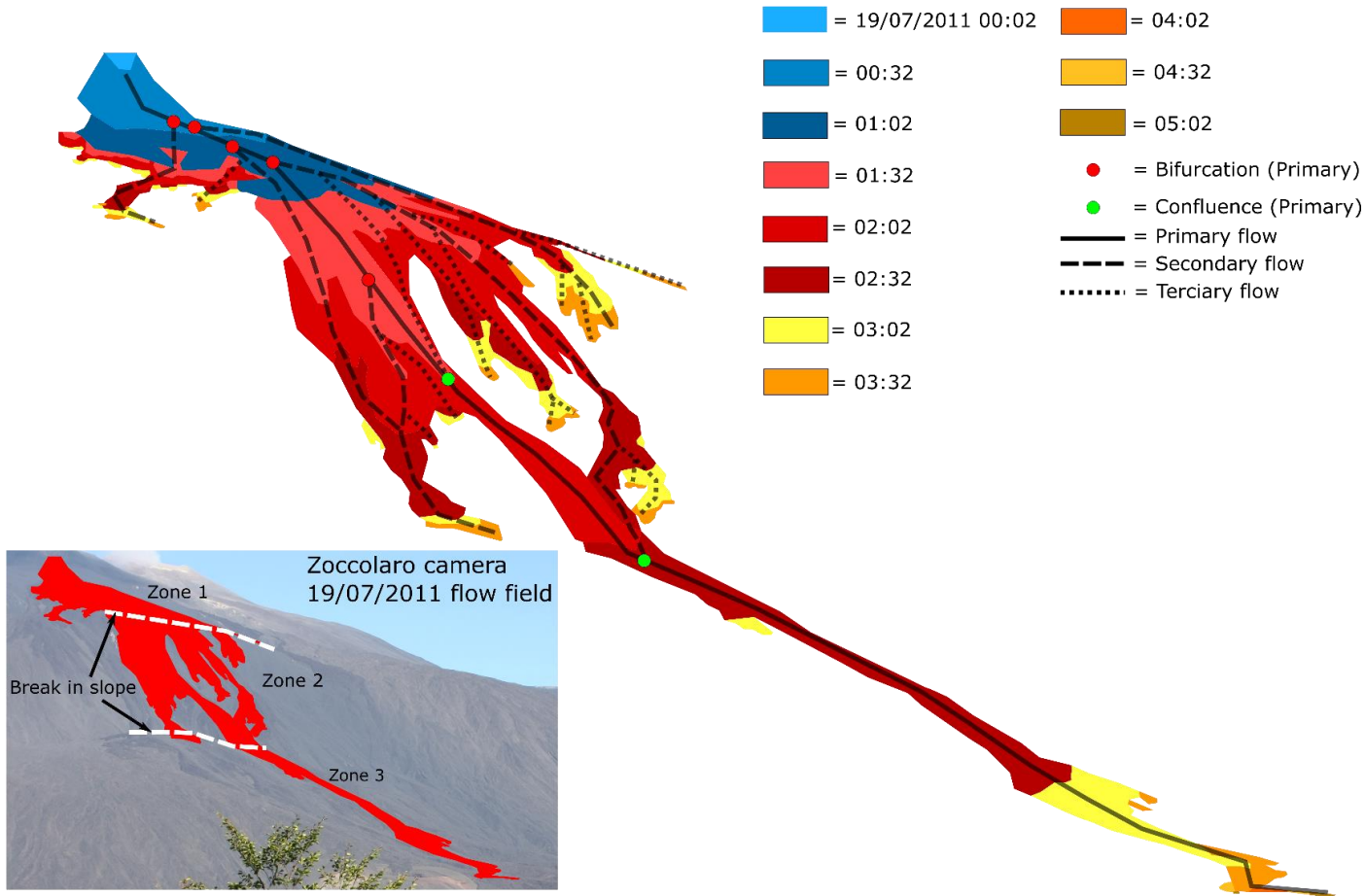


Figure 3.8 continued

d

30/07/2011 flow field evolution (Episode 8)

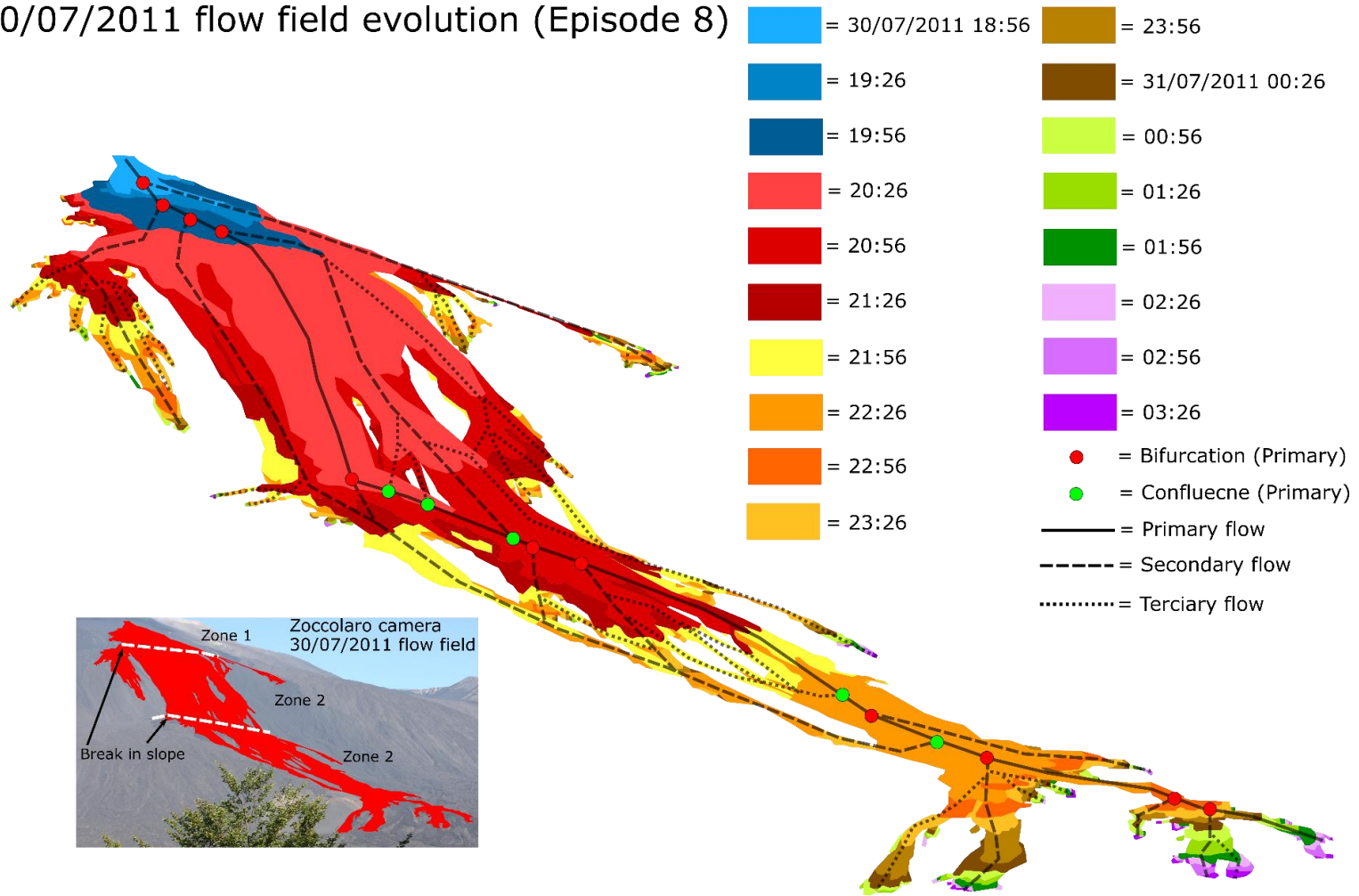


Figure 3.8 continued

e

### 05/08/2011 flow field evolution (Episode 9)

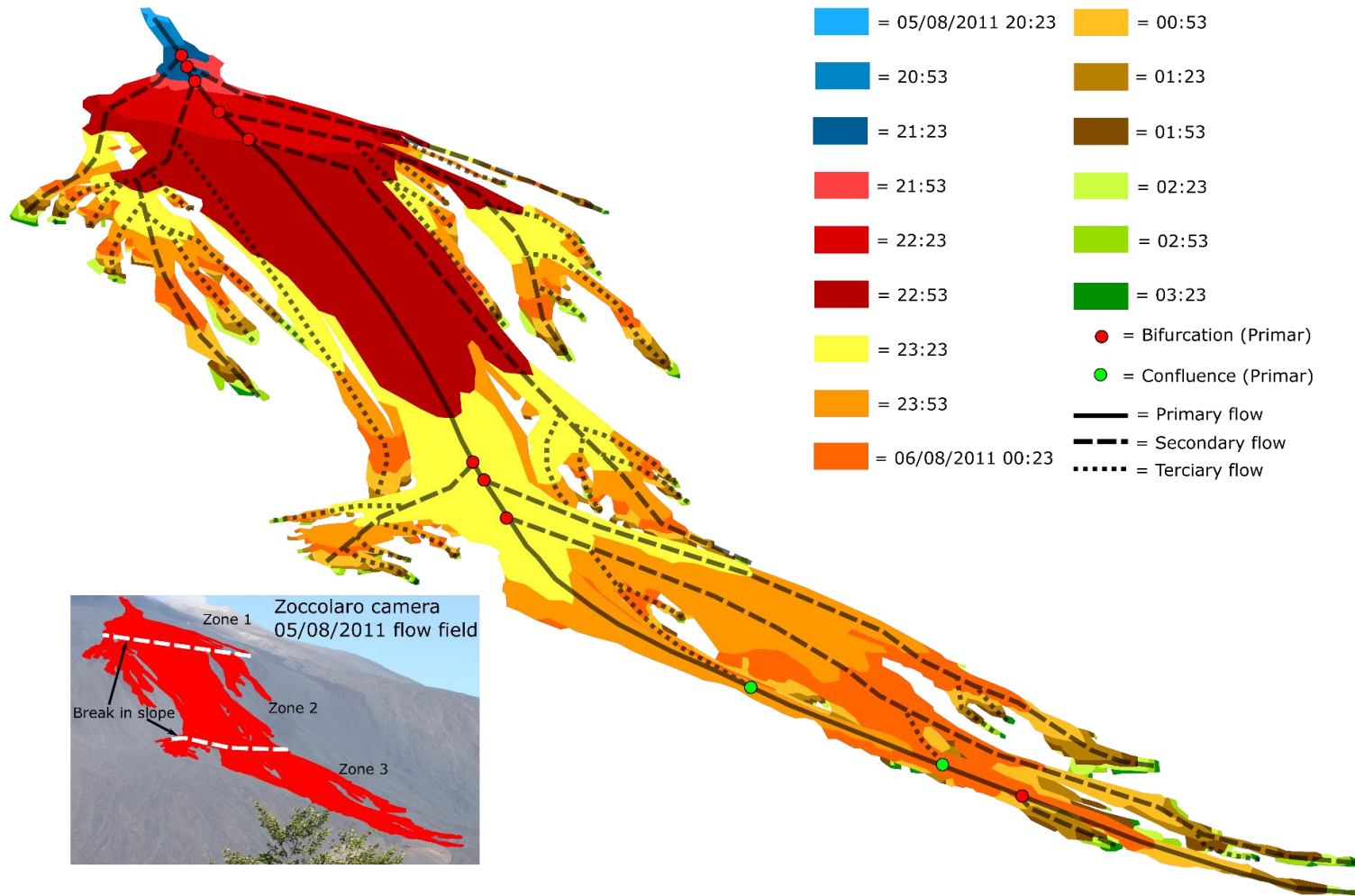


Figure 3.8 continued

f

### 12/08/2011 flow field evolution (Episode 10)

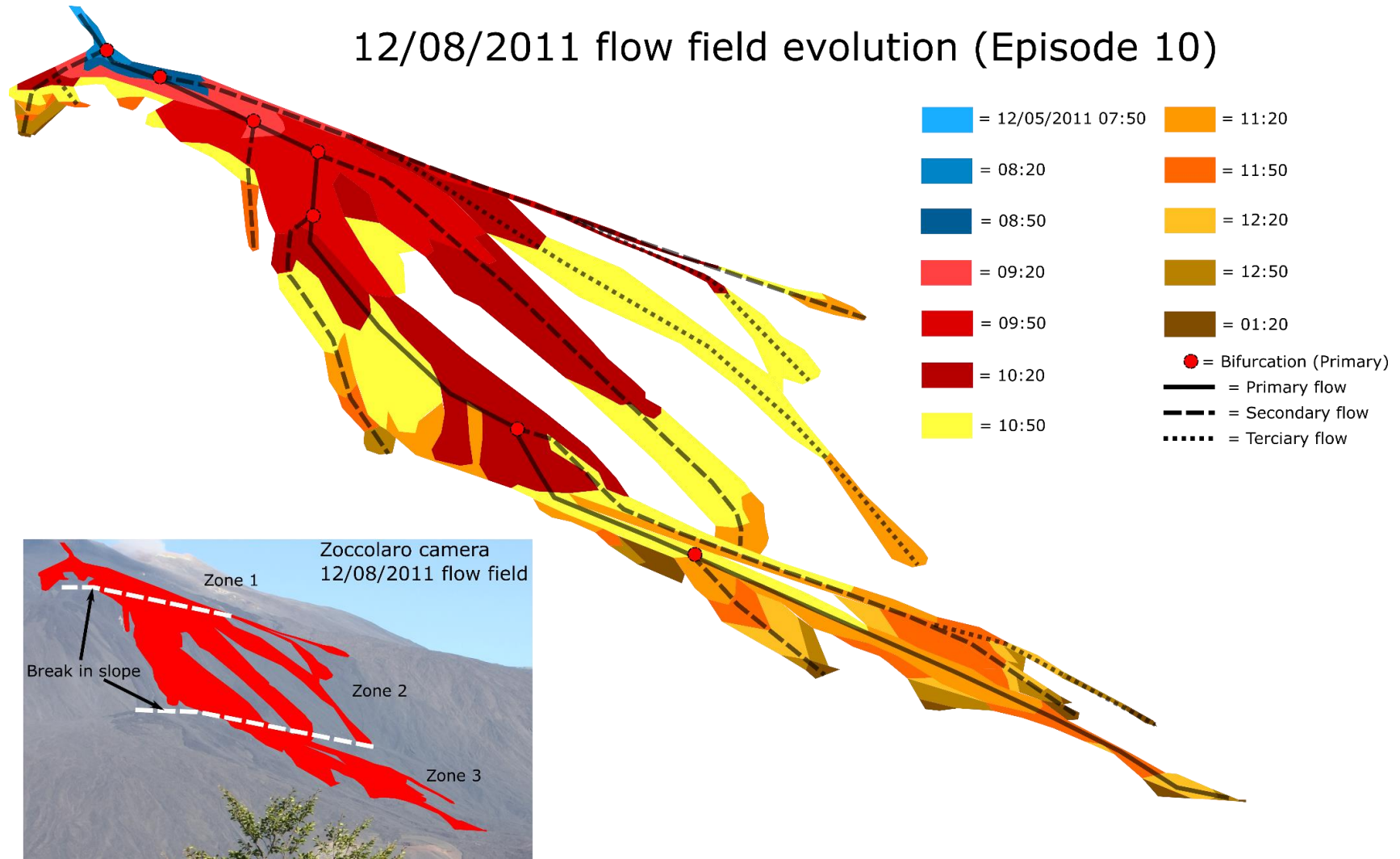


Figure 3.8 continued

\* 20/08/2011 flow field evolution (Episode 11)

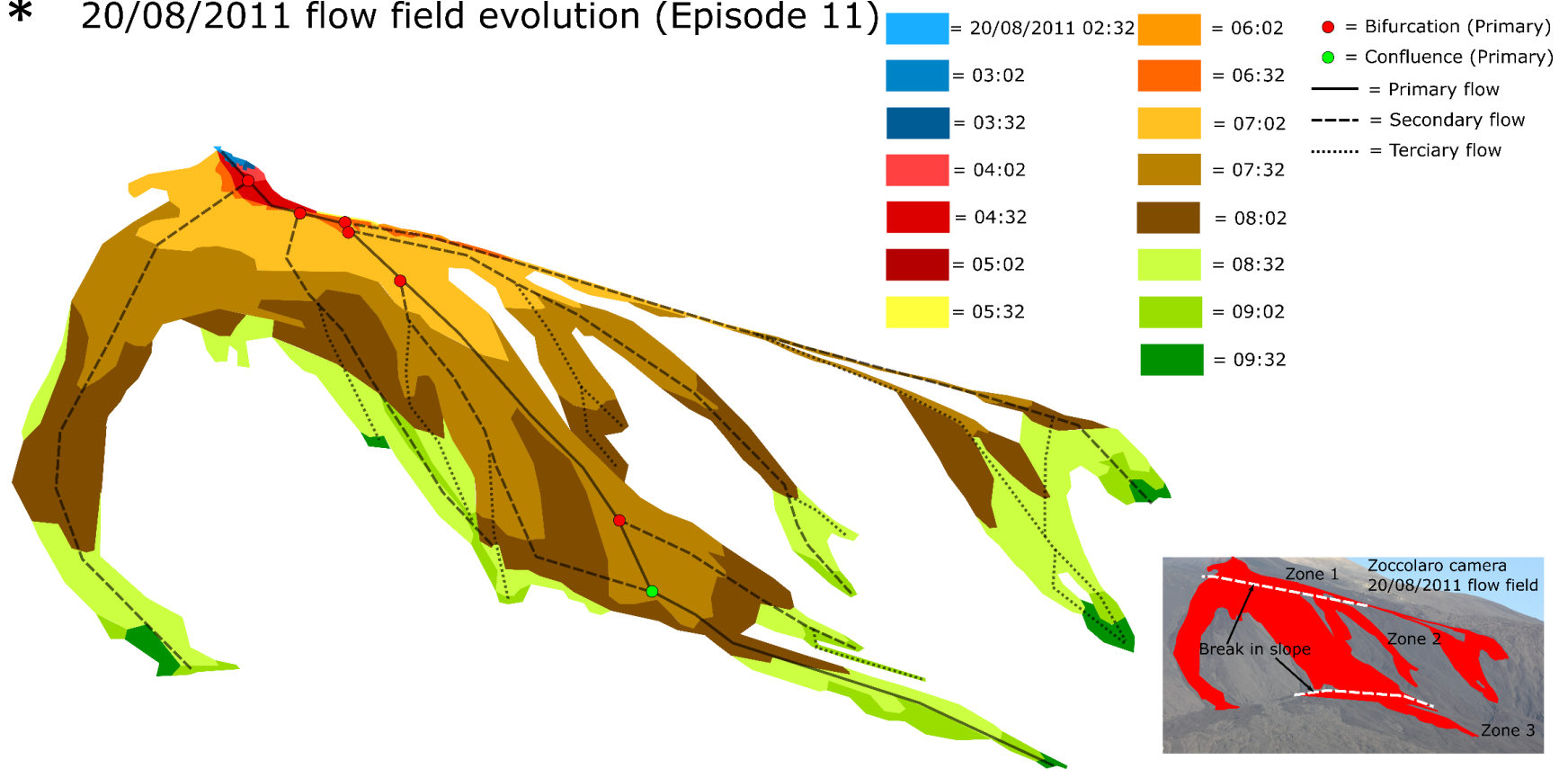


Figure 3.8 continued

h

29/08/2011 flow field evolution (Episode 12)

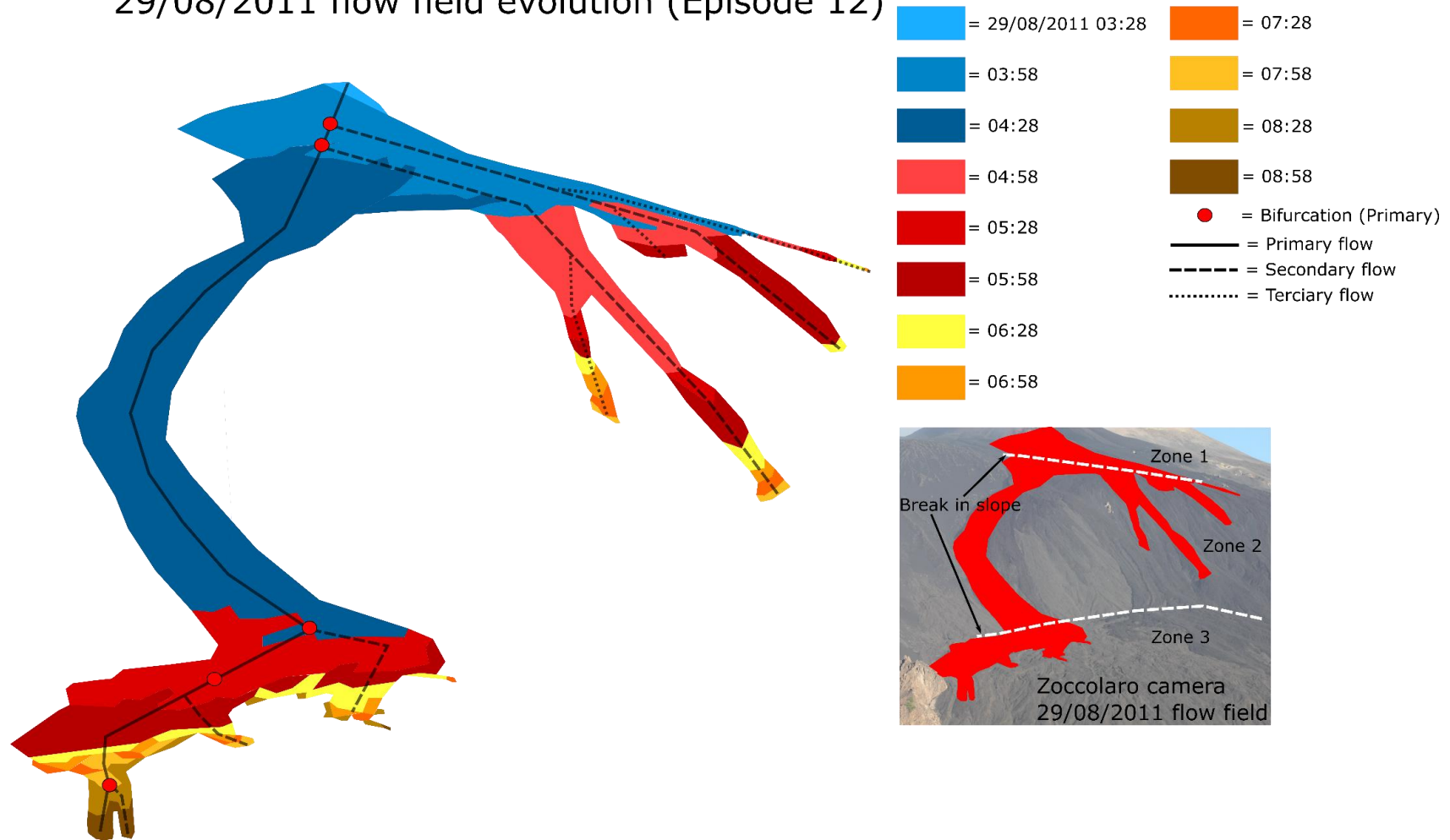


Figure 3.8 continued

i

### 08/09/2011 flow field evolution (Episode 13)

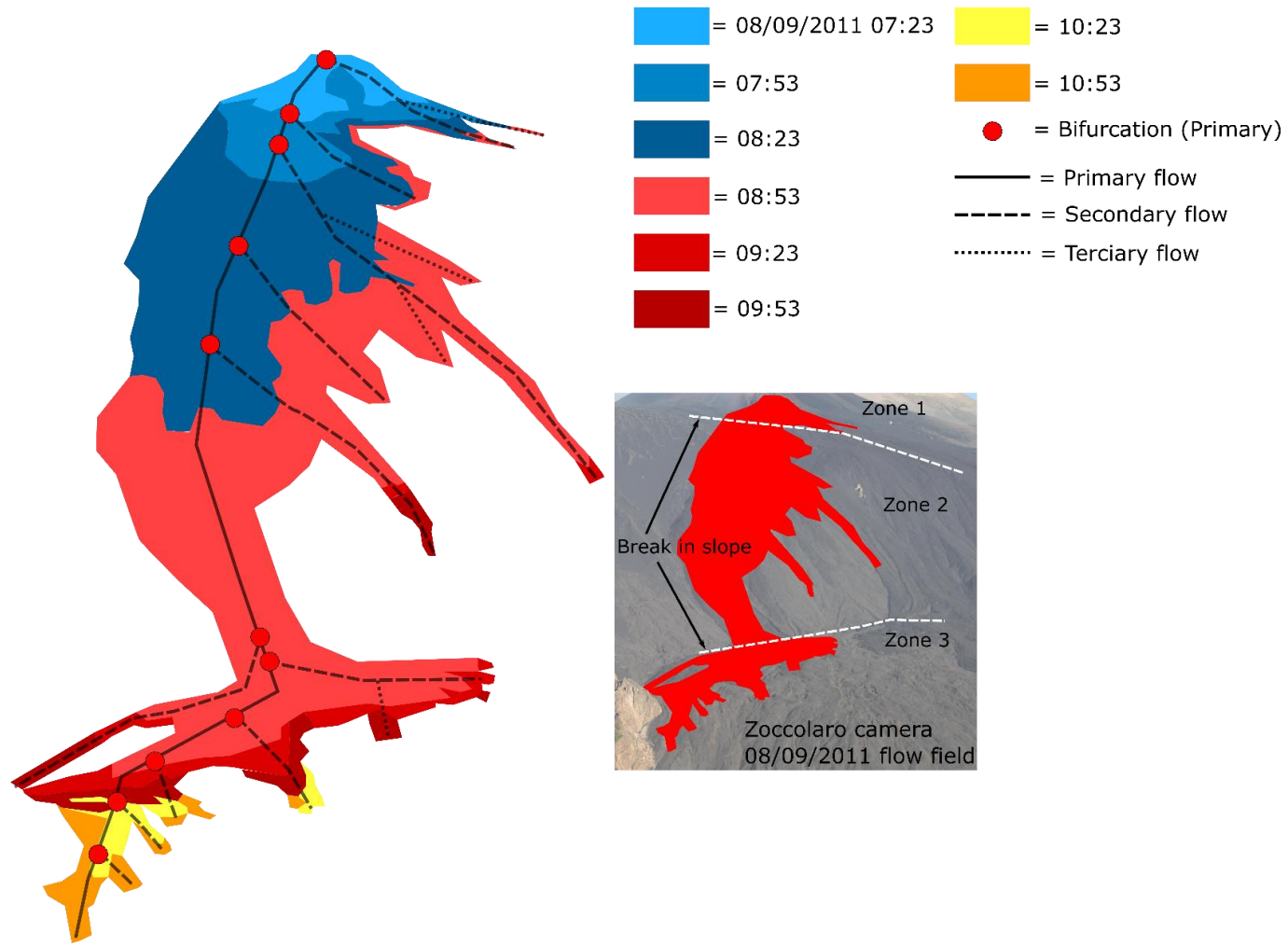


Figure 3.8 continued

j

### 28/09/2011 flow field evolution (Episode 15)

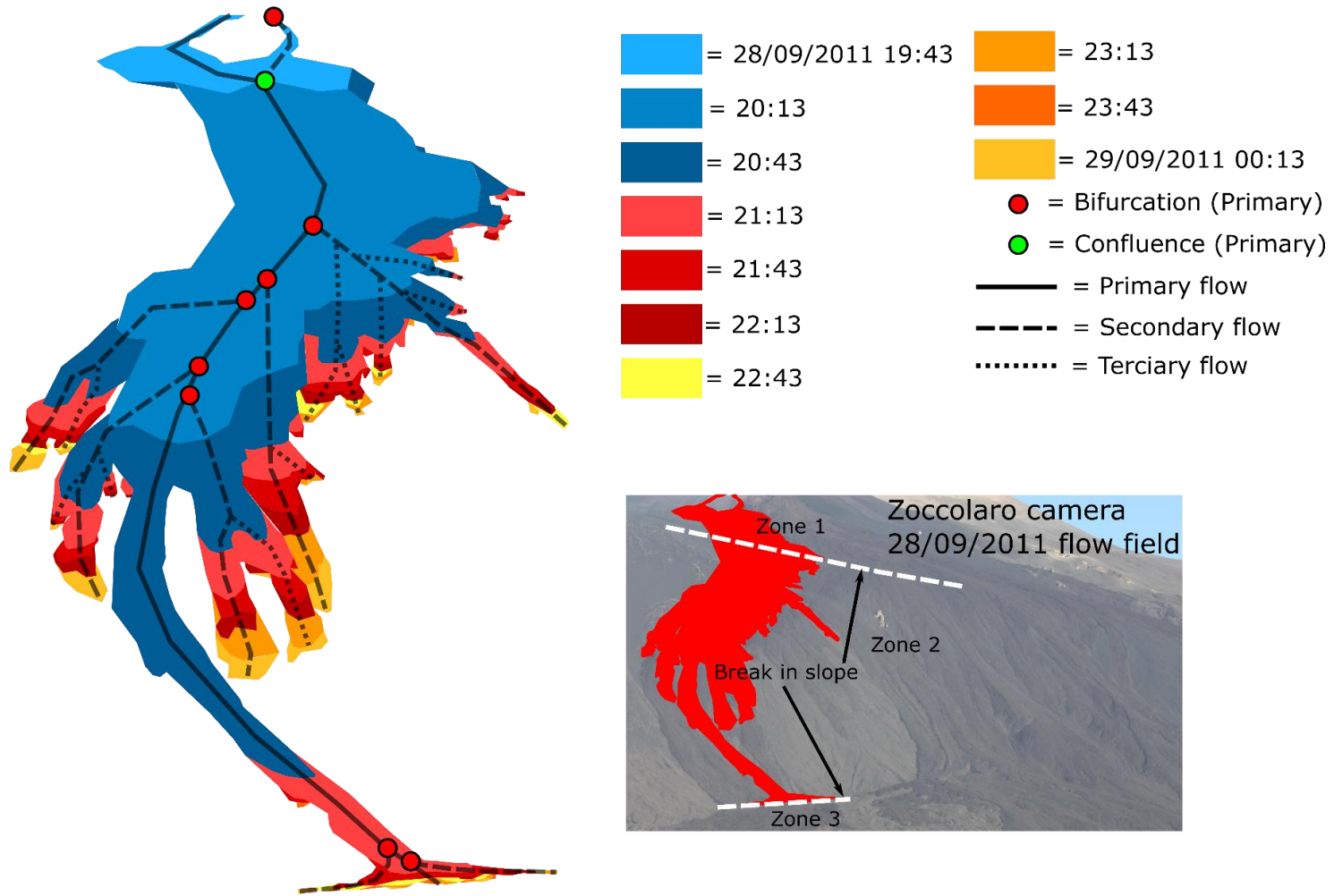


Figure 3.8 continued

k

### 28/10/2011 flow field evolution (Episode 17)

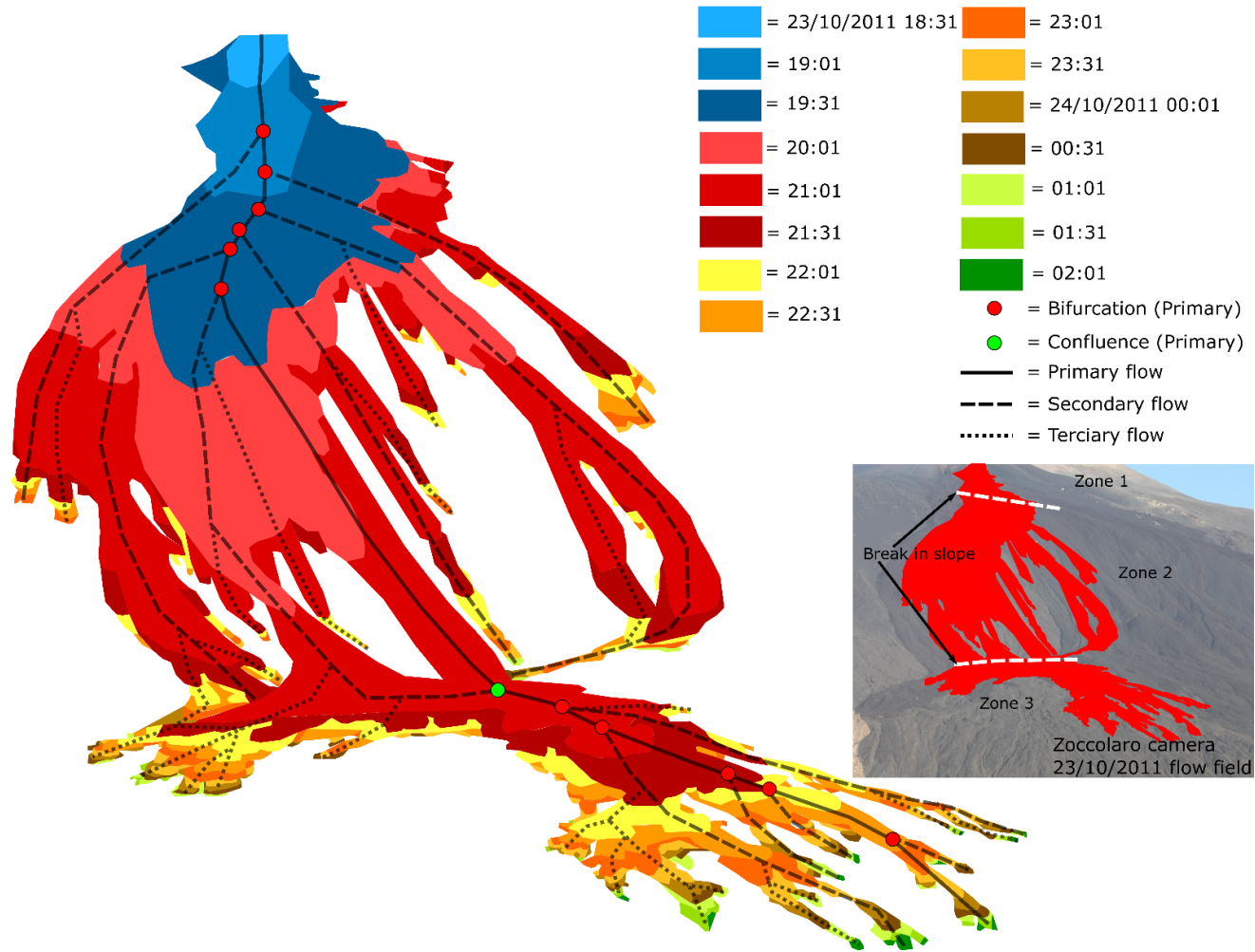


Figure 3.8 continued

\* 24/04/2012 flow field evolution (Episode 25)  
(Serracozzo camera)

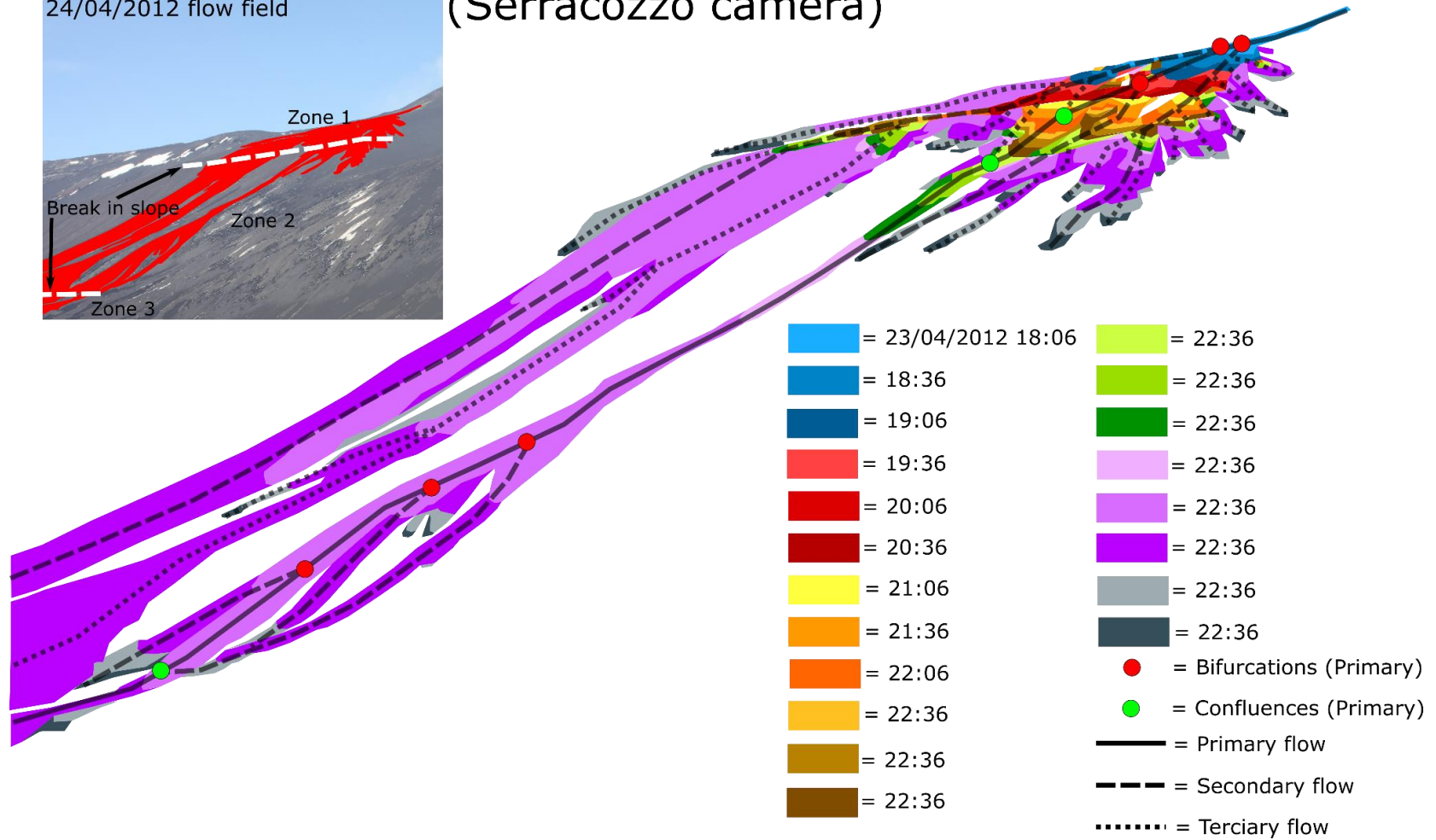


Figure 3.8 continued

m

\* 24/04/2012 flow field evolution (Episode 25)  
(Zoccolaro camera)

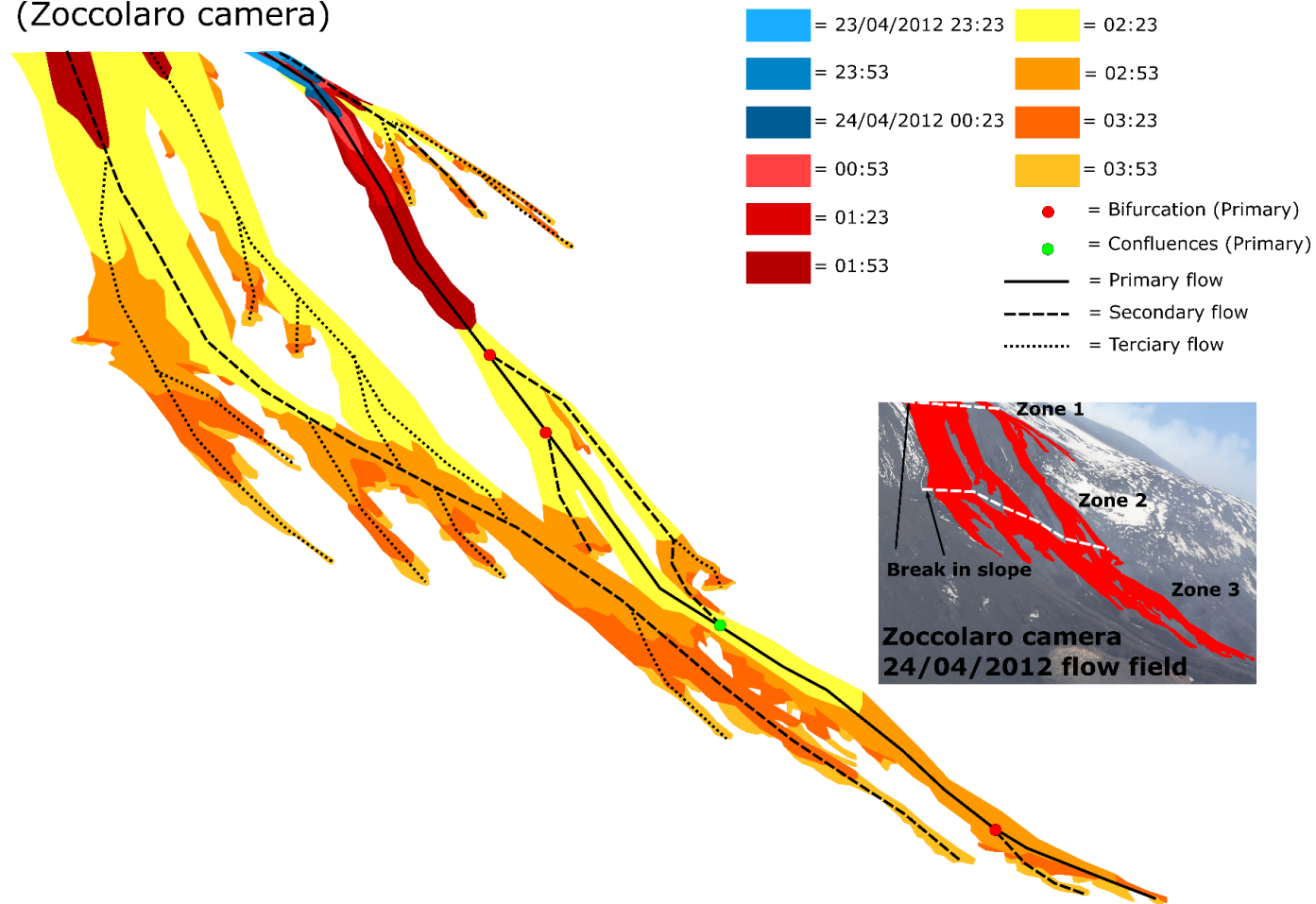


Figure 3.8 continued



Table – 3.5 continued

<b>Factors</b>	<b>adv<sub>avg_Z3</sub></b>	<b>adv<sub>max_Z3</sub></b>	<b>adv<sub>avg</sub></b>	<b>adv<sub>max</sub></b>	<b>α<sub>Z1</sub></b>	<b>α<sub>Z2</sub></b>	<b>α<sub>Z3</sub></b>	<b>α<sub>avg_all</sub></b>	<b>B</b>
<b>adv<sub>avg_Z3</sub></b>	1.00								
<b>adv<sub>max_Z3</sub></b>	0.76	1.00							
<b>adv<sub>avg</sub></b>	0.64	0.39	1.00						
<b>adv<sub>max</sub></b>	0.26	0.47	0.48	1.00					
<b>α<sub>Z1</sub></b>	-0.54	-0.62	-0.28	-0.30	1.00				
<b>α<sub>Z2</sub></b>	-0.09	-0.34	-0.35	-0.53	0.68	1.00			
<b>α<sub>Z3</sub></b>	-0.09	-0.02	-0.16	-0.23	-0.39	-0.16	1.00		
<b>α<sub>avg_all</sub></b>	-0.06	-0.08	-0.36	-0.43	-0.04	0.42	0.73	1.00	
<b>B</b>	0.18	-0.02	0.45	0.10	-0.03	-0.35	-0.24	-0.42	1.00
<b>B<sub>Z1</sub></b>	0.42	0.40	-0.06	-0.54	-0.10	0.31	0.11	0.18	-0.14
<b>C</b>	0.11	0.14	0.10	-0.03	0.20	0.12	-0.46	-0.33	0.34
<b>t<sub>flow_time-lapse</sub></b>	-0.11	0.10	-0.53	-0.56	0.12	0.29	0.06	0.31	-0.02
<b>t<sub>ff</sub></b>	0.43	0.04	0.23	-0.58	-0.12	0.22	-0.11	0.06	0.29
<b>t<sub>eff to ff</sub></b>	-0.46	-0.03	-0.64	-0.33	0.09	-0.08	0.21	0.15	-0.04
<b>t<sub>cp</sub></b>	-0.02	-0.28	-0.31	-0.72	-0.15	0.08	0.15	0.08	-0.03
<b>W<sub>max_Z1</sub></b>	0.26	0.34	0.27	-0.03	0.17	0.14	-0.32	-0.40	-0.18
<b>W<sub>max</sub></b>	0.47	0.74	0.13	0.02	-0.28	-0.02	0.10	0.04	-0.25

Table – 3.5 continued

<b>Factors</b>	<b>B<sub>Z1</sub></b>	<b>C</b>	<b>t<sub>flow_time-lapse</sub></b>	<b>t<sub>ff</sub></b>	<b>t<sub>eff to ff</sub></b>	<b>t<sub>cp</sub></b>	<b>W<sub>max_Z1</sub></b>	<b>W<sub>max</sub></b>
<b>B<sub>Z1</sub></b>	1.00							
<b>C</b>	0.33	1.00						
<b>t<sub>flow_time-lapse</sub></b>	0.61	0.57	1.00					
<b>t<sub>ff</sub></b>	0.57	0.37	0.35	1.00				
<b>t<sub>eff to ff</sub></b>	0.29	0.30	0.79	-0.16	1.00			
<b>t<sub>cp</sub></b>	0.43	0.08	0.39	0.63	0.23	1.00		
<b>W<sub>max_Z1</sub></b>	0.61	0.29	0.05	0.16	-0.05	-0.04	1.00	
<b>W<sub>max</sub></b>	0.78	0.37	0.42	0.19	0.24	-0.03	0.70	1.00



Figure 3.9 – Examples of the changes in morphology as flows transitioned from Zone 2 to Zone 3 and continued into Zone 3 (the floor of the Valle del Bove) (as seen from Zoccolaro). The changes in morphology all occurred over similar slopes (20°-22°). Blue dashed lines mark the transition from Zone 2 to Zone 3, and red arrows identify the advance of lava flows due to coalescing flow fronts at the Zone 2 and 3 boundaries.

### 3.4.2 - Flow Front Advance Rates

Due to the positions of the cameras, the viewing angle to flow fronts was most favourable in the valley headwall region (Zone 2). In Zone 1, where views were oblique and over the greatest distances, the re-projected point coordinates are sensitive to any error in the re-projection onto the DEM (i.e. due to camera misalignment or error in the DEM). As a result, differences between the absolute flow front position ascertained by the Zoccolaro and Serracozza cameras could be large (90-200 m) in the near-vent region (Figure 3.10a). In contrast, for Zones 2 and 3, differences in horizontal position ranged from 1-20 m and in the vertical from 0-15 m. However, despite these differences in absolute position, calculated advance rates from the two cameras were in good agreement (Figure 3.10b). A moving average regression (window span of 5) generated a single advance rate profile using data from both cameras (Figure 3.10b).

Average flow front advance rates for the 12 episodes in Zones 1, 2 and 3 ranged from 0.04-0.57  $\text{m s}^{-1}$ , 0.11-0.60  $\text{m s}^{-1}$ , and 0.02-0.21  $\text{m s}^{-1}$  respectively. Maximum flow front advance rates for the three zones ranged from 0.11-0.58  $\text{m s}^{-1}$ , 0.22-0.60  $\text{m s}^{-1}$ , and 0.12-0.53  $\text{m s}^{-1}$  respectively. The greatest average advance rates occurred within Zone 2 (0.6  $\text{m s}^{-1}$ ), followed by Zone 1 (0.57  $\text{m s}^{-1}$ ) and Zone 3 (0.21  $\text{m s}^{-1}$ ). Advance rates followed a general pattern of increasing with the start of fire fountaining and then decreasing after the termination of fire fountaining (Figure 3.11). All but three of the episodes (6, 15, and 17) rapidly increased their advance rate after the onset of fire fountaining. Five of the episodes (6, 10, 11, 12 and 13) produced continually increasing advance rates for ~40-80 minutes before reaching their peak rates and declining thereafter.

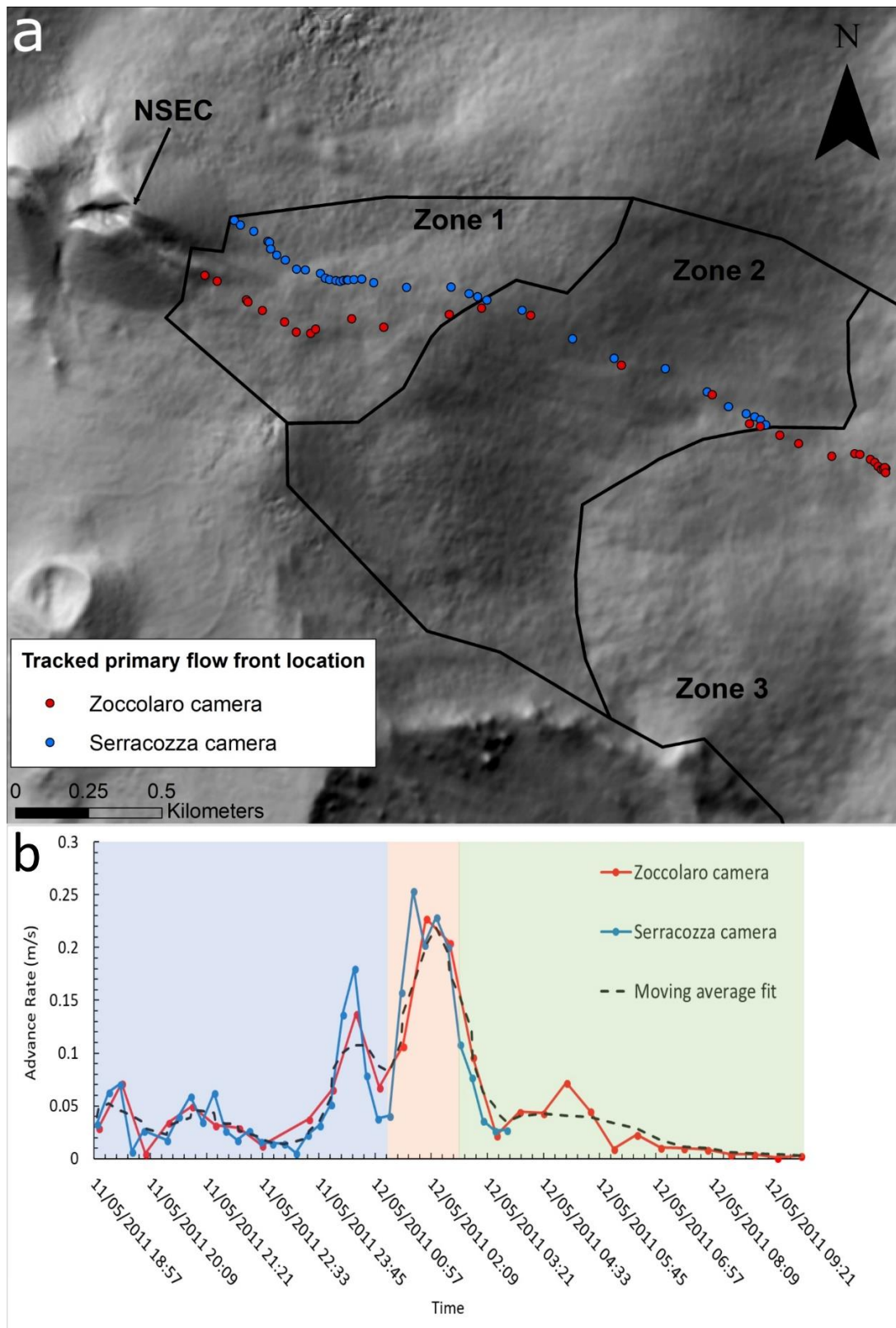


Figure 3.10 – (a) Visualisation of the error in flow front feature point placement for the 12/05/2011 event (episode 4) due to oblique view of the cameras, uncertainties in camera orientation, and error in the DEM. The point locations converge as the flow approaches the top of the headwall (transition from Zone 1 to Zone 2) of the Valle del Bove, where viewing direction becomes more orthogonal. (b) Despite the differences in point locations, calculated advance rates from the two cameras are in good agreement and a combined advance rate profile can be determined using a moving average regression (window span of 5).

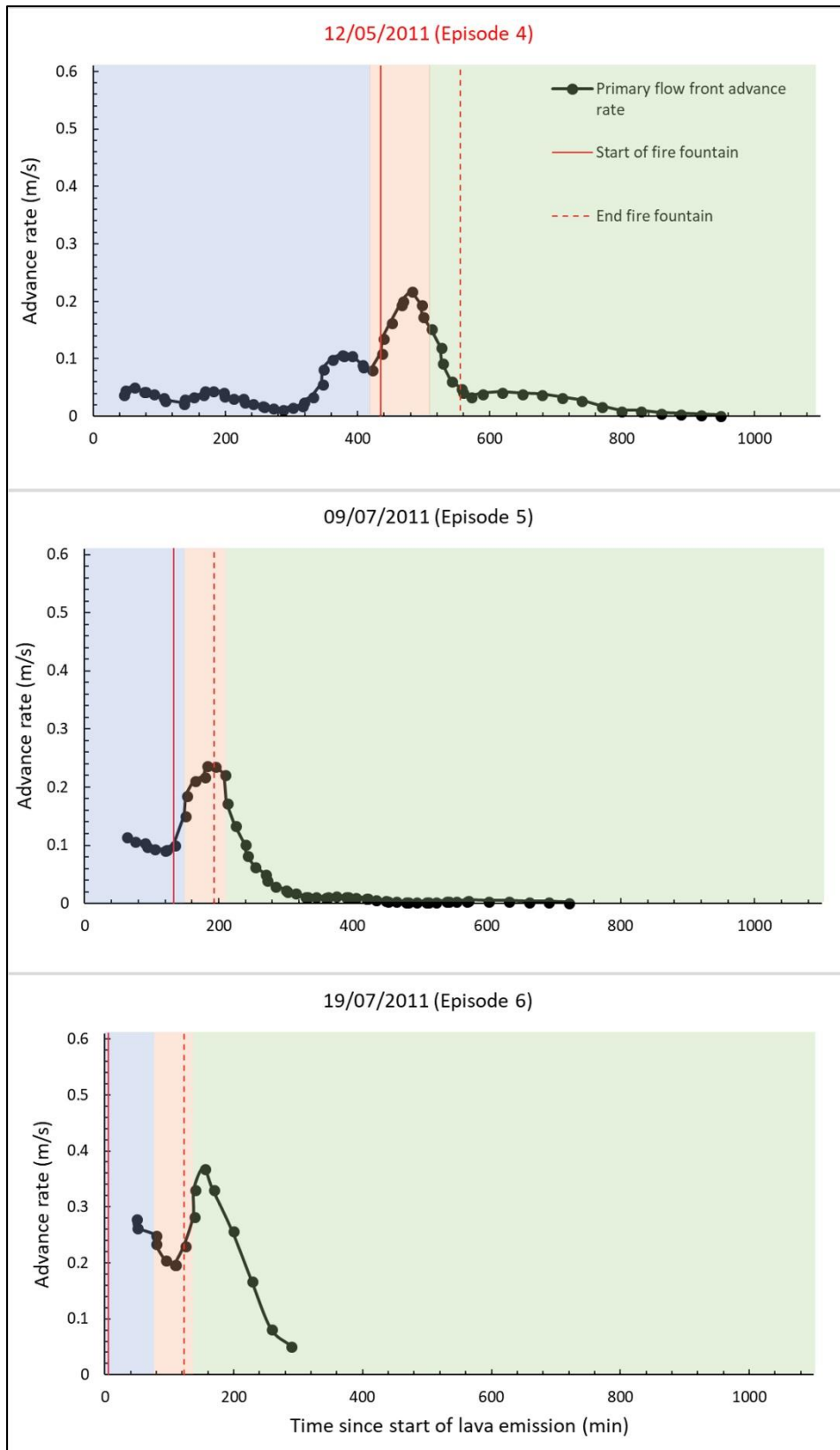


Figure 3.11 – Primary flow front advance rates for the 12 episodes. The timing of the first point represents when an estimate for advance rate was possible after the start of effusive activity. Background colour: blue = Zone 1, red = Zone 2, green = Zone 3. Titles highlighted in red mark those flows belonging to Group 1 (flows which initially advanced as slow moving discrete flows within Zone 1 with average advance rate of 0.05 or less). Figure 3.11 continued on the following three pages.

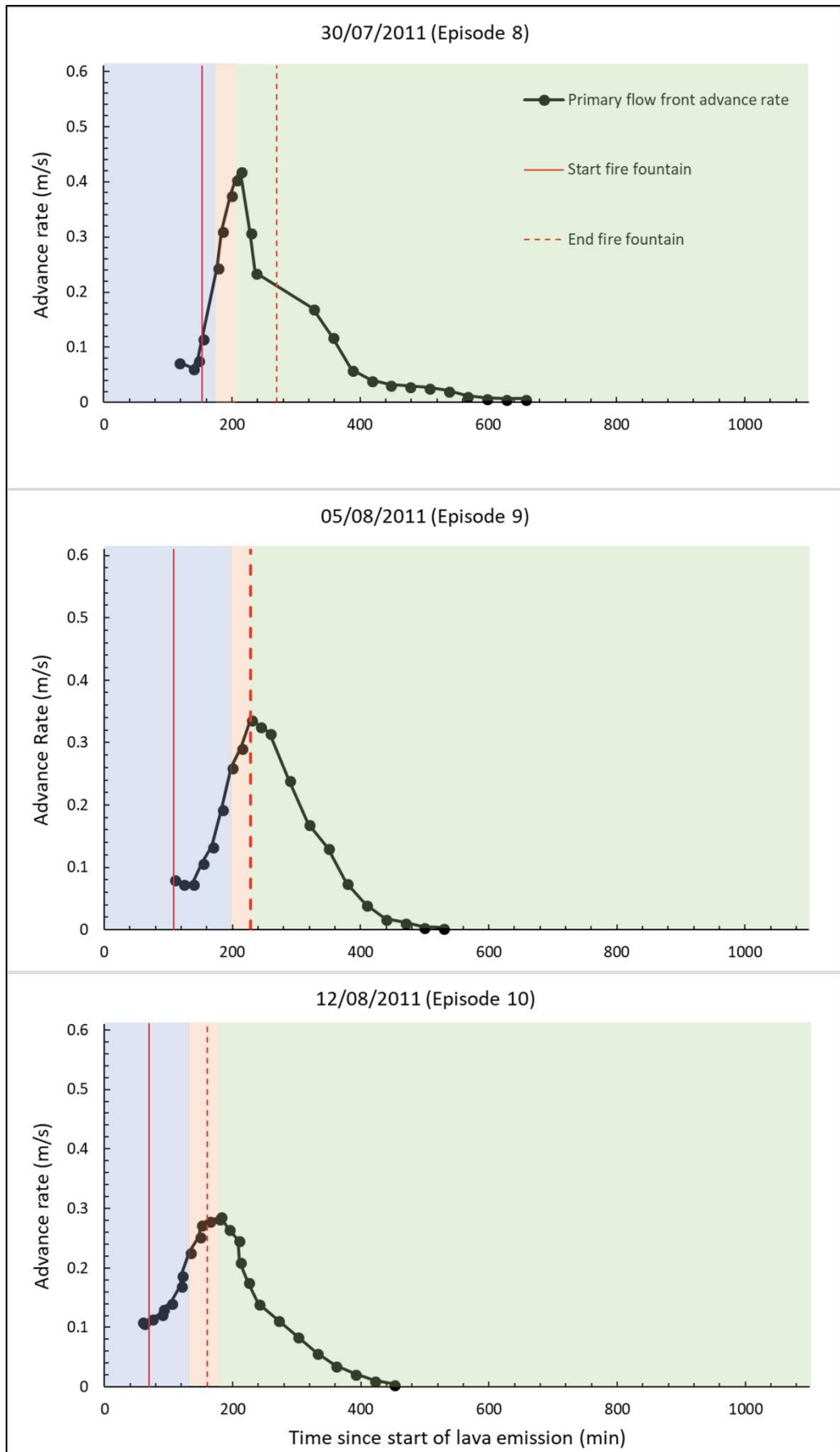


Figure 3.11 continued

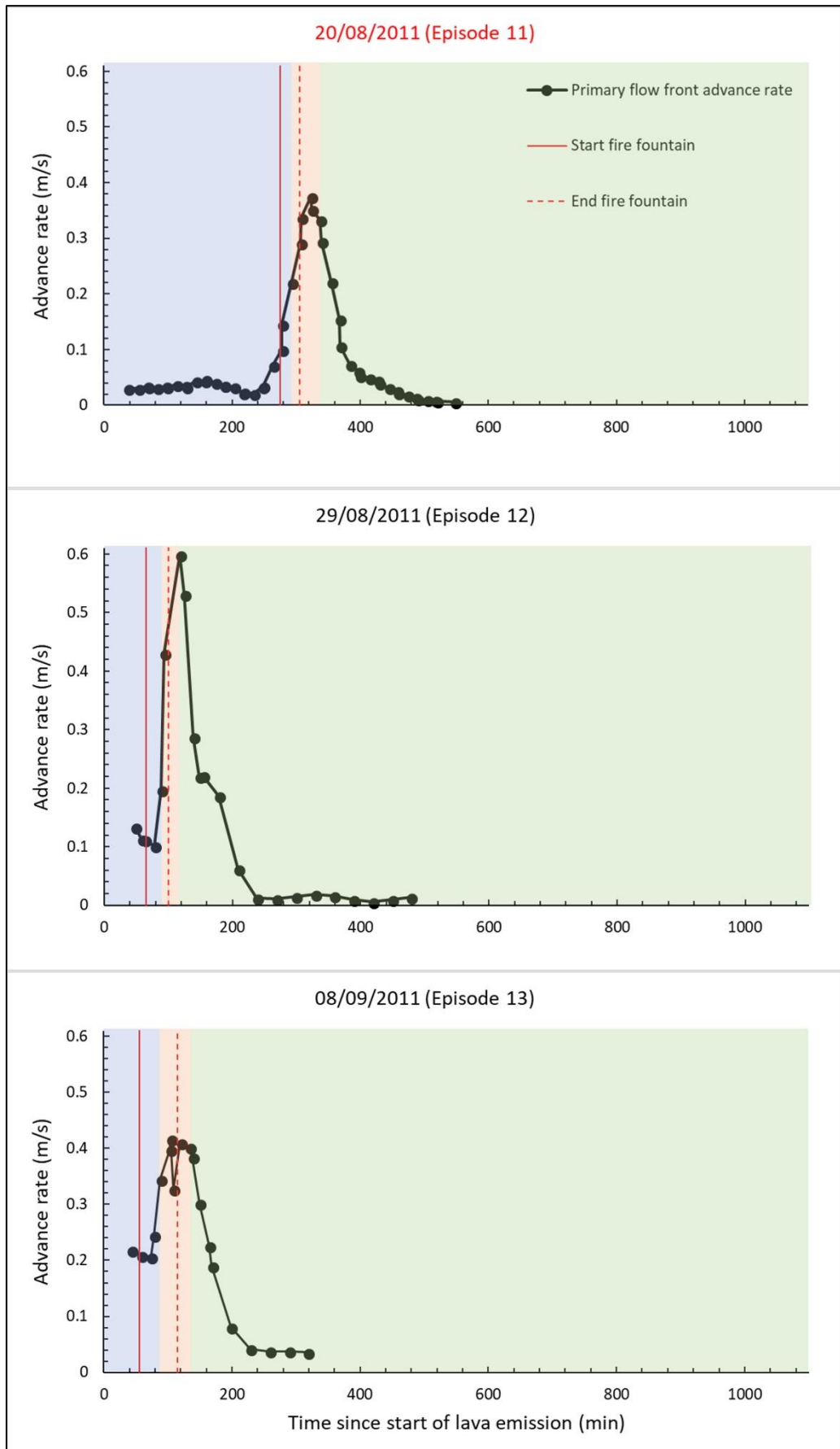


Figure 3.11 continued

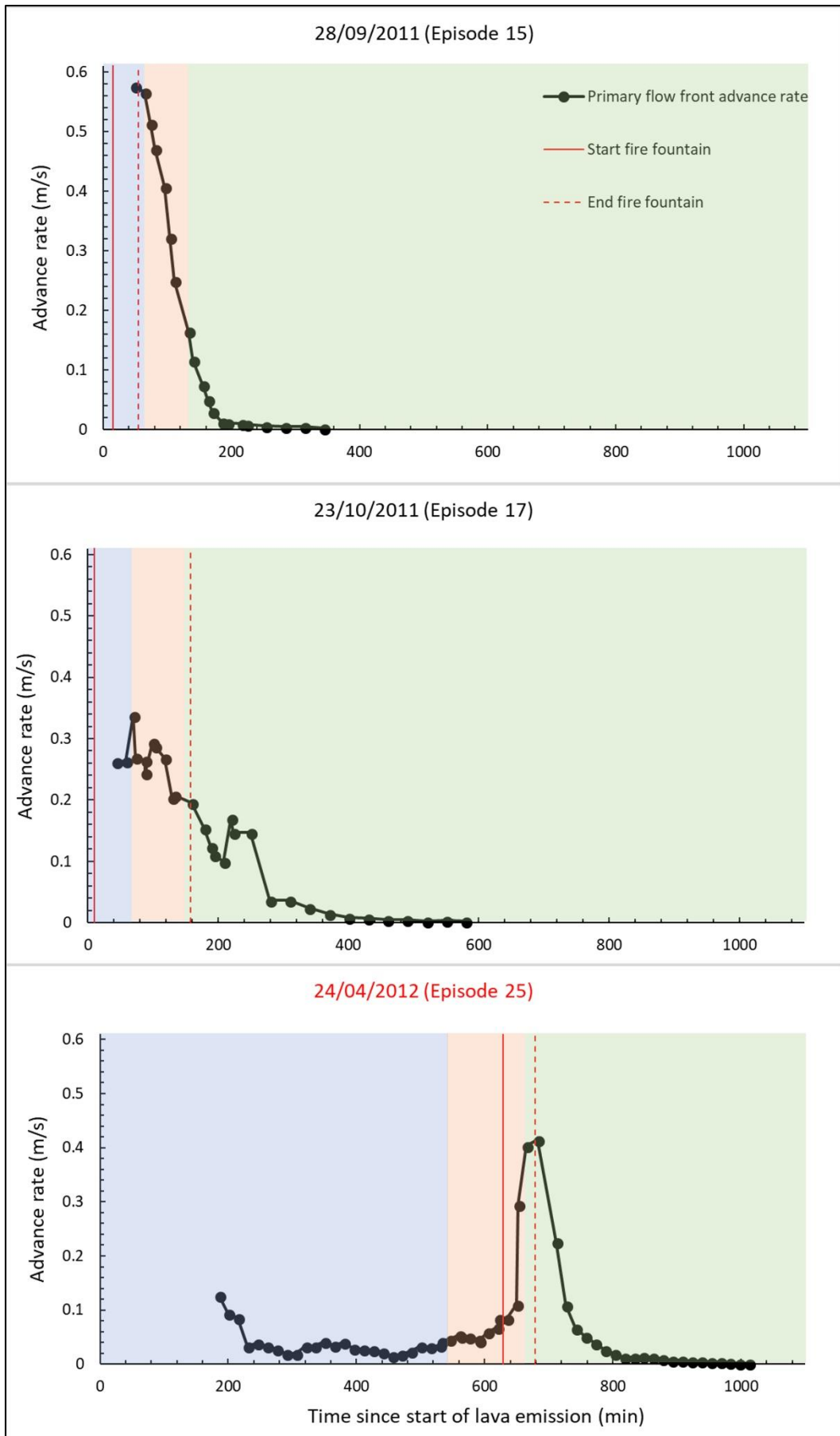


Figure 3.11 continued

### 3.4.3 Regression Analysis for Flow Length

Regression models for flow length for the 12 episodes were generated using the information in Table 3.4 and the best subset selection method with an alpha value of 0.05 (see Section 3.3.3). The ten best-performing models were selected and are listed in Table 3.6. The number of potential models was reduced by eliminating those models which suffered from multicollinearity effects. This was determined by examining the tolerance values and VIF scores of the various models (Table 3.7).

Table 3.6 – Regression models for flow length produced from best subset selection.

Models	Regression equations for length (L)
1†	$201.3 * W_{max}^{0.24} * t_{ff}^{0.14} * B_{Z1}^{-0.13} * adv_{max}^{-0.11} * C^{-0.03}$
2†	$275.3 * W_{max}^{0.21} * t_{ff}^{0.13} * adv_{max\_Z1}^{-0.09} * B_{Z1}^{-0.09}$
3	$431.4 * W_{max}^{0.15} * t_{ff}^{0.1} * adv_{max\_Z1}^{-0.08}$
4	$438.3 * W_{max}^{0.16} * t_{flow}^{0.09} * adv_{max\_Z1}^{-0.09}$
5	$919.7 * W_{max}^{0.23} * adv_{max\_Z1}^{-0.12} * MOR_{mean}^{-0.08}$
6	$291.2 * W_{max}^{0.12} * t_{ff}^{0.12} * t_{flow\_time-lapse}^{0.06}$
7	$121.9 * V_{mean}^{0.15} * t_{ff}^{0.13}$
8	$89.8 * MOR_{mean}^{0.18} * t_{flow}^{0.3}$
9	$90.7 * V_{mean}^{0.18} * t_{flow}^{0.12}$
10	$91.4 * V_{mean}^{0.3} * MOR_{mean}^{-0.12}$

$V_{mean}$  = mean total volume given by Behncke et al. (2014), see Table 3.1,  $MOR_{mean}$  = the mean, mean output rate given by Behncke et al. (2014),  $t_{flow}$  = duration of flow,  $t_{flow\_time-lapse}$  = time-lapse derived duration of flow,  $t_{ff}$  = duration of fire fountain,  $adv_{max\_Z1}$  = maximum advance rate in Zone 1,  $B_{Z1}$  = number of bifurcations in Zone 1,  $C$  = number of confluences,  $W_{max}$  = maximum flow field width. † regression equations in which the sign of the coefficient of a variable was opposite that of its correlation to the dependent variable.

To minimize potential errors caused by multicollinearity, a tolerance threshold of 0.9 and VIF of less than 1.1 were used to identify the best models. These values indicate that a maximum of 10 % of the variance for any one independent variable is shared with the others in the model, and that any inflation of the standard error of the independent variable is not more than 1.1 times what it would be if it were uncorrelated with any other independent variable in the model.

Of the ten selected models, seven of the models (models 1, 2, 3, 5, 6, 8, 10) had two or more independent variables with tolerances  $< 0.9$  and VIFs  $> 1.1$ . Of the remaining three models, model 4 had the lowest standard error of regression ( $S = 0.032$ ) and the best balance of explanatory power ( $R^2 = 0.96$  and  $R^2_{\text{adj}} = 0.94$ ) and predictive power ( $R^2_{\text{pred}} = 0.92$ ) (Table 3.8; Figure 3.12).

Table 3.7 – VIF and p-values for each regression coefficient in each model.

Models	Regression variables	P-value	Tolerance	VIF
1†	$adv_{max\_Z1}$	0.00	0.43	2.33
	$B_{Z1}$	0.01	0.12	8.49
	$C$	0.03	0.51	1.97
	$t_{ff}$	0.0	0.41	2.45
	$W_{max}$	0.00	0.17	6.04
2†	$adv_{max\_Z1}$	0.00	0.61	1.63
	$B_{Z1}$	0.05	0.16	6.4
	$t_{ff}$	0.00	0.52	1.94
	$W_{max}$	0.00	0.25	4.07
3	$adv_{max\_Z1}$	0.00	0.82	1.22
	$t_{ff}$	0.00	0.8	1.25
	$W_{max}$	0.00	0.96	1.04
4	$adv_{max\_Z1}$	0.00	0.91	1.1
	$t_{flow}$	0.00	0.91	1.1
	$W_{max}$	0.00	0.97	1.03
5	$adv_{max\_Z1}$	0.00	0.98	1.02
	$MOR_{mean}$	0.00	0.78	1.28
	$W_{max}$	0.00	0.78	1.28
6	$t_{ff}$	0.00	0.88	1.14
	$t_{flow\_time-lapse}$	0.01	0.75	1.34
	$W_{max}$	0.00	0.82	1.22
7	$V_{mean}$	0.00	0.93	1.07
	$t_{ff}$	0.00	0.93	1.07
8	$MOR_{mean}$	0.00	0.46	2.18
	$t_{flow}$	0.00	0.46	2.18
9	$V_{mean}$	0.00	0.99	1.01
	$t_{flow}$	0.00	0.99	1.01
10	$V_{mean}$	0.00	0.64	1.57
	$MOR_{mean}$	0.00	0.64	1.57

$V_{mean}$  = mean total volume,  $MOR_{mean}$  = the mean, mean output rate given by Behncke et al. (2014),  $t_{flow}$  = duration of flow,  $t_{flow\_time-lapse}$  = time-lapse derived duration of flow,  $t_{ff}$  = duration of fire fountain,  $adv_{max\_Z1}$  = maximum advance rate in Zone 1,  $B_{Z1}$  = number of bifurcations in Zone 1,  $C$  = number of confluences,  $W_{max}$  = maximum flow field width. † regression equations in which the sign of the coefficient of a variable was opposite that of its correlation to the dependent variable.

† regression equations in which the sign of the coefficient of a variable was opposite that of its correlation to the dependent variable.

Table 3.8 – Evaluation statistics for the selected models.

Model	Number of Variables	S	R <sup>2</sup>	R <sup>2</sup> <sub>adj</sub>	R <sup>2</sup> <sub>pred</sub>	AIC
1†	5	0.015	0.99	0.99	0.97	-96.7
2†	4	0.022	0.98	0.98	0.96	-88.6
3	3	0.027	0.97	0.96	0.94	-83.3
4	3	0.032	0.96	0.94	0.92	-79.3
5	3	0.035	0.95	0.93	0.9	-77
6	3	0.039	0.94	0.92	0.86	-74.7
7	2	0.056	0.86	0.83	0.77	-66.7
8	2	0.057	0.86	0.83	0.78	-66.2
9	2	0.057	0.86	0.83	0.78	-66.1
10	2	0.057	0.86	0.83	0.78	-66.1

† Regression equations in which the sign of the coefficient of an independent variable became opposite to its *r* value with the dependent variable (i.e. a regression equation which suffers from Simpson’s Paradox).

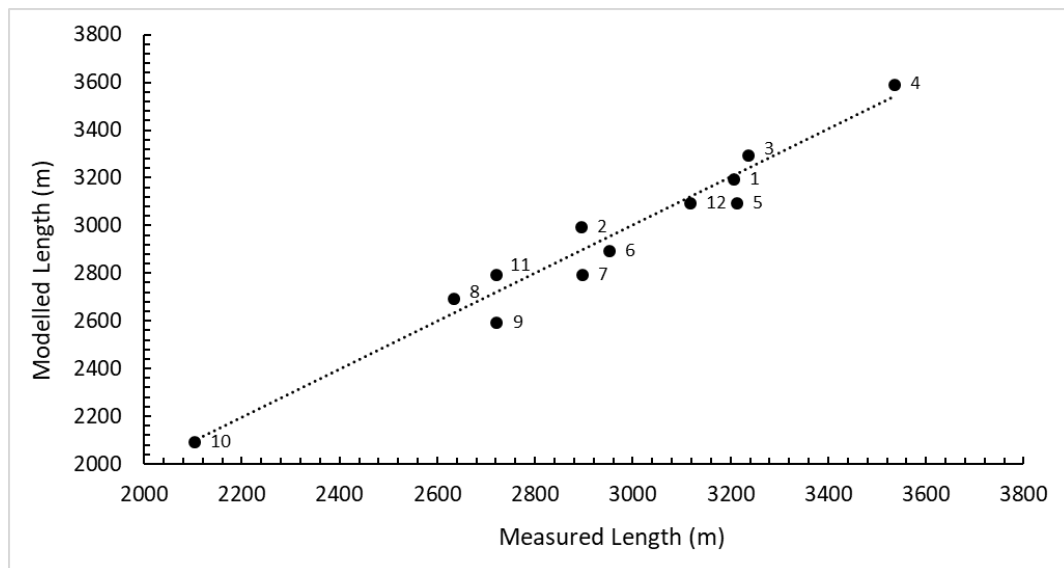


Figure 3.12 – Relationship between measured length and modelled length for the lava flows produced during the 12 episodes using model 4. Markers are labelled with the corresponding episode number.

## 3.5 Discussion

### 3.5.1 Flow Emplacement and Morphology

The emplacement and morphology of the 12 examined flows was influenced by several factors. Visual observation of flow emplacement suggested a strong influence on flow morphology due to pre-existing topography. The topography within Zone 1 consists mainly of small scale surface features, with no large depressions or ridges (Figure 3.13b). The lack of large depressions and ridges allowed flows to advance unconfined and widen as they advanced through Zone 1 (e.g. Hulme, 1974; Lockwood et al., 1987; Kilburn & Lopes, 1988). The topography in Zone 2 consists of large depressions and ridges, formed of older edifice material and levees and flow margins from previous 'a'ā flows (Figure 3.13c). These features captured and confined the advancing flows, causing the transition from unconfined to semi-channelized flows between Zones 1 and 2 observed in the time-lapse images. The steeper slopes within Zone 2 further compounded flow capture and channelling by narrowing and thinning the flow (e.g. Lister 1992). Initially, topography within Zone 3 becomes less confining (Figure 3.13d) and slopes become shallower (Table 3.4), allowing flow fronts to widen and, when in sufficiently close proximity to one another, to coalesce. Further into Zone 3 the topography again contains depression and ridge features comprised of levees and margins from previous 'a'ā flows (Figure 3.13d). These features, combined with flow thinning caused by termination of the supply of material (i.e. the end of effusion marked by the termination of fire fountaining; e.g. Lockwood et al., 1987; Lister 1992) confined the advancing flows, returning them to a more channelized morphology. Additionally, to investigate the effect of confinement on flows the distance for which a primary flow experienced confinement was estimated by measuring the distance from the position where the primary flow reduces in width in Zone 2 and/or Zone 3 for a distance of 100 m or more (Table 3.9). Doing so showed a strong

positive correlation ( $r = 0.63$ ) between final length and length of primary flow confinement for the 12 episodes (Figure 3.14).

Flow widths also effect the thickness of the flow and its susceptibility to interaction with surface features. Wider flows are typically thinner than narrower flows for a given effusion rate, since wider flows distribute their lava volume over a greater area (e.g. Hulme, 1974; List, 1992; Gregg & Fink, 2000). As the thickness of a flow is reduced, it becomes more prone to interaction with topographic features, resulting in flow bifurcations that further reduce the available lava volume of the flow, causing additional thinning (e.g. Lockwood et al., 1987; Dietterich & Cashman, 2014), and also reduces the advance rate of the flow (e.g. Wolfe, 1983; Heliker et al., 2001; Dietterich et al., 2015). Results from this study support these previous observations as  $B_{z1}$  shows a strong positive relationship ( $r = 0.61$ ) with a negative relationship with  $W_{max\_z1}$  and  $adv_{max\_z1}$  and  $adv_{avg\_z1}$  ( $r = -0.48$  and  $-0.58$  respectively) for the 12 episodes (Table 3.5).

Table 3.9 – List of final flow lengths and length of flow confinement to the primary flow for the 12 Episodes.

Episode	Length of flow confinement (m)	Flow length (m)
4	1500	3200
5	1200	3000
6	1900	3300
8	1200	3600
9	800	3100
10	900	2900
11	400	2800
12	200	2700
13	400	2600
15	700	2100
17	800	2800
25	1800	3100

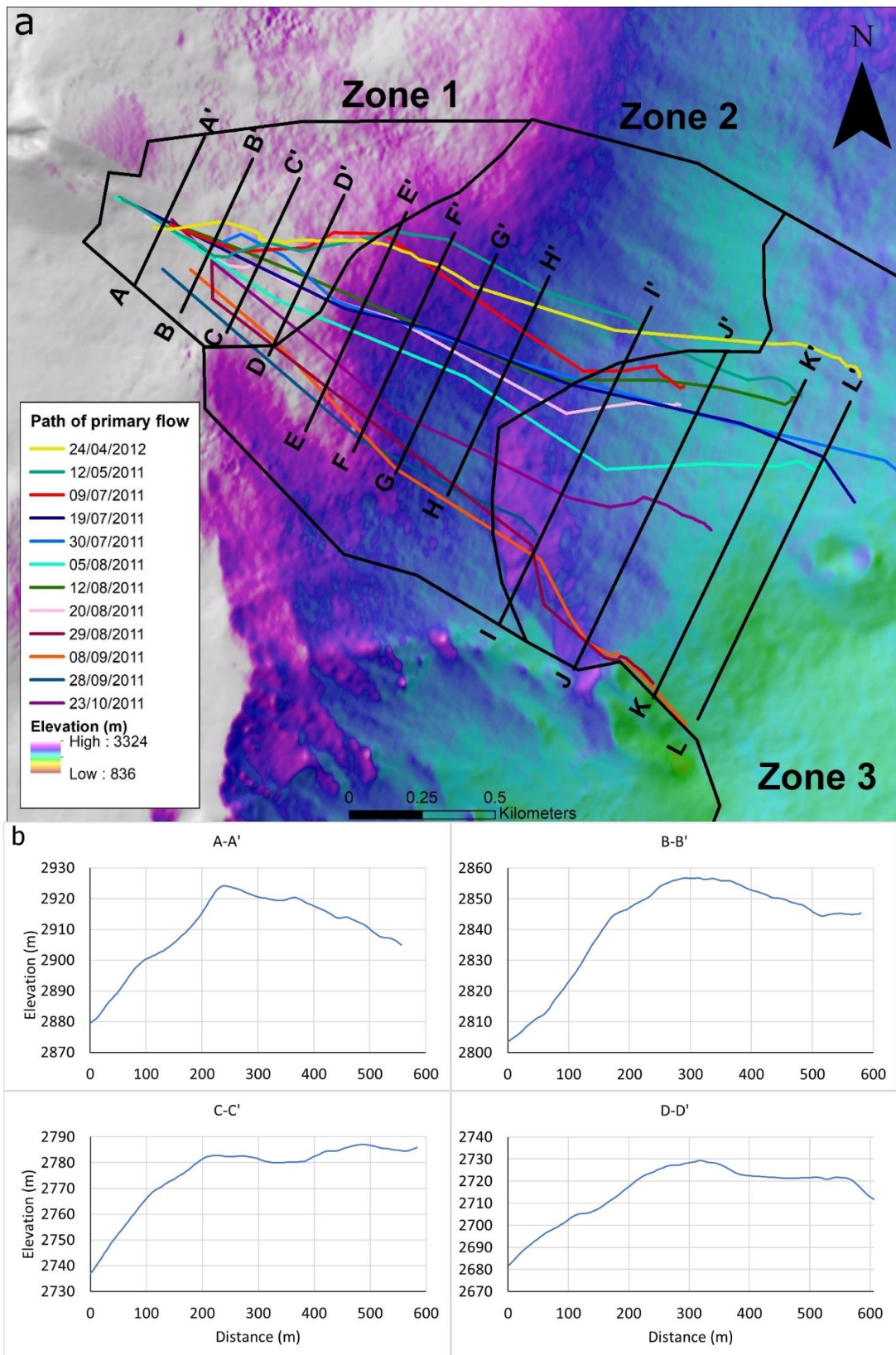


Figure 3.13 – Surface elevation transects (a) for Zone 1 (b), Zone 2 (c), and Zone 3 (d) of the lava flow emplacement area using the Laboratorio di Aerogeofisica-Sezione Roma2 2012 DEM. Figure continues onto the following page.

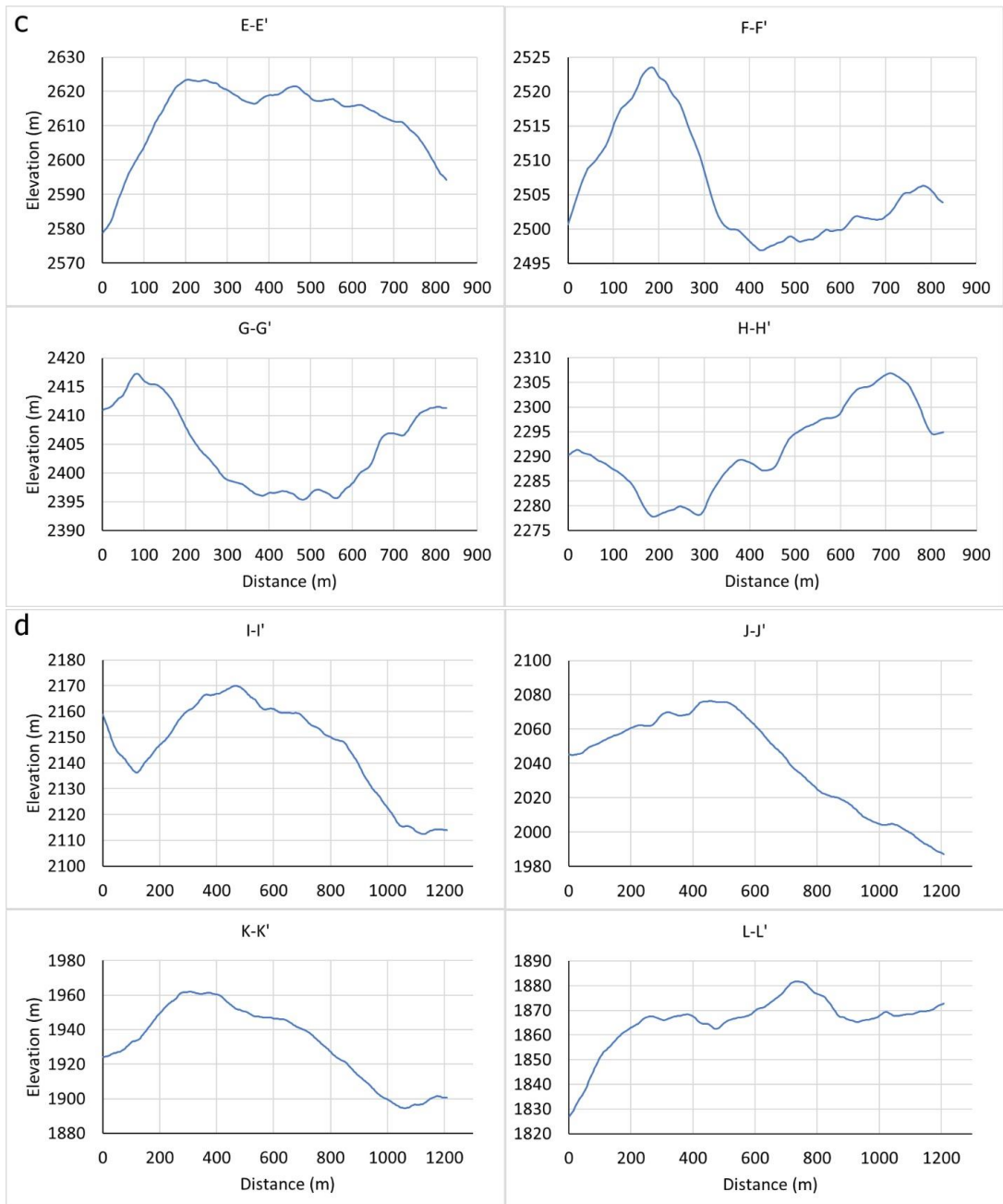


Figure 3.13 continued

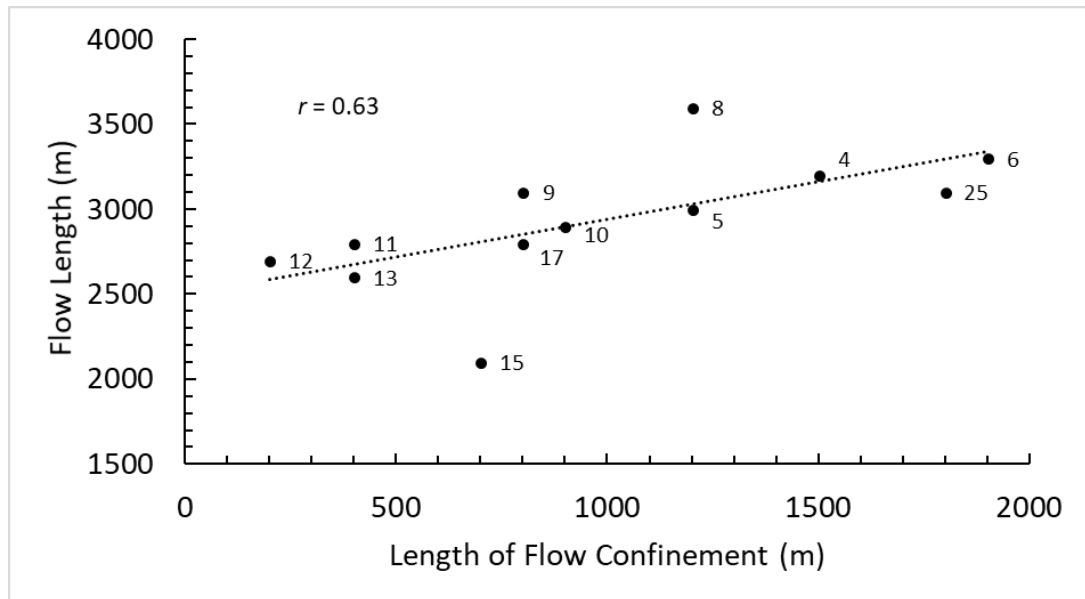


Figure 3.14 – Relationship between final length and length of confinement for the 12 episodes.

In addition to topographic influences, the amount and rate of supply of material also affected flow morphology. The influence of volume and duration on short-duration volume-limited flow morphology is demonstrated in the 12 flows examined here, which show a strong positive correlation (Table 3.5) between  $V_{mean}$ , and  $W_{max}$  and  $L$  ( $r = 0.83$  and  $0.74$  respectively), and a strong positive correlation between  $t_{flow}$ ,  $t_{flow\ time-lapse}$  and  $L$  ( $r = 0.63$  and  $0.73$  respectively). However, examining the influence of mean output rate on flow length and width shows a moderate positive correlation between  $MOR_{mean}$  and  $W_{max}$  ( $r = 0.46$ ) and a weak positive correlation between  $MOR_{mean}$  and  $L$  ( $r = 0.002$ ). The weak relationship between  $MOR_{mean}$  and  $L$  suggests that the mean output rate did not have as significant an impact on the final length of short-duration volume-limited flows as total  $V_{mean}$  and  $t_{flow}$ .

However, while the mean output rate may not have a significant impact on flow length, effusion rates (the rate of supply of erupted lava that is feeding flow at any specific point in time) may have a stronger influence. Previous studies have linked high effusion rates with wider flows (e.g. Walker, 1971; Hulme, 1974; Head & Wilson, 1986; Rowland & Walker, 1990) and higher rates of advance (e.g. Rowland & Walker, 1990; Kauahikaua et al., 2003). Correlation values between maximum advance rate in Zone 1 ( $adv_{max\_z1}$ ) and average advance

rate in Zone 1 ( $adv_{avg\_Z1}$ ) and the time between start of lava emission and onset of fire fountaining ( $t_{eff\ to\ ff}$ ) show strong negative relationships ( $r = -0.7$  and  $-0.89$  respectively) for the 12 short-duration volume-limited flows studied here. Additionally,  $MOR_{mean}$  and  $adv_{avg\_Z1}$  show a negative relationship ( $r = -0.54$ ). Examining  $adv_{max\_Z1}$  and  $adv_{avg\_Z1}$  and  $t_{eff\ to\ ff}$  shows that during Episodes 4, 11, and 25 (Group 1) lava emission began more than four hours prior to the onset of fire fountaining and flows initially advanced slowly (average advance rates of  $0.04$ - $0.05\ m\ s^{-1}$ ) as one or two discrete lobes (Table 3.4). The remaining nine episodes (Group 2) began lava emission 5-120 minutes before fire fountaining and formed broad, rapidly advancing sheets (with average advance rates of  $0.12$ - $0.57\ m\ s^{-1}$ ). The lower advance rates and earlier onset of lava emission prior to fire fountaining, combined with the observed morphologies of Groups 1 and 2 within Zone 1 and the correlations between  $adv_{max\_Z1}$  and  $adv_{avg\_Z1}$  and  $t_{eff\ to\ ff}$ , suggest that the initial effusion rates were lower for Group 1 flows than those of Group 2.

Table 3.10 – Advance rates for Zone 1 and interval between start of lava emission and onset of fire fountaining divided by the two different morphologies observed in Zone 1.

	Episodes	$adv_{max\_Z1}$ (m s <sup>-1</sup> )	$adv_{avg\_Z1}$ (m s <sup>-1</sup> )	$t_{eff\ to\ ff}$ (s)
Group 1	4	0.11	0.04	24600 (410 min)
	11	0.22	0.05	14700 (245 min)
	25	0.13	0.04	32640 (544 min)
Group 2	5	0.19	0.12	6000 (100 min)
	6	0.28	0.26	300 (5 min)
	8	0.14	0.12	7500 (125 min)
	9	0.26	0.13	2700 (45 min)
	10	0.23	0.15	2400 (40 min)
	12	0.43	0.18	3000 (50 min)
	13	0.34	0.24	1200 (20 min)
	15	0.58	0.57	960 (16 min)
	17	0.34	0.34	1380 (23 min)

$adv_{max\_z1}$  = maximum advance rate in Zone 1,  $adv_{avg\_z1}$  = average advance rate in Zone 1,  $t_{eff\ to\ ff}$  = interval between start of lava emission and onset of fire fountaining.

### 3.5.2 Flow length model

As the 12 flows examined here are short-duration and volume-limited in nature, it would follow that the best model for predicting  $L$  should include both  $V_{mean}$  and either  $t_{flow}$  or  $t_{flow\ time-lapse}$ . Model 9 does include both  $t_{flow}$  and  $V_{mean}$  and has low multicollinearity (Table 3.7) but gives a significantly weaker fit than model 4 (Table 3.8). Volume may not have been selected for the best model due to the small sample size (12 flows). Small sample sizes (< 15) reduce the precision of statistical significance tests, such as those used to estimate p-values (e.g. Royston, 1991; Elliot & Woodward, 2007; Ghasemi & Zahediasl, 2012) causing variables to

appear statistically insignificant in small sample sizes, when in a larger set they may be significant.

While model 4 provides strong explanatory and predictive power, caution should be applied when considering its application in other flow scenarios. Model 4 should only be used for flows with similar eruptive and emplacement conditions as those of the 12 flows examined here used to create the regression model. The specific nature and conditions of the emplacement of the 12 flows used to create model 4 means that it would be inadequate at predicting lengths for flows emplaced under different regimes.

As an example, model 4 has been applied to the 19 July and 21 December 1974 short-duration volume-limited flows at Kīlauea volcano, Hawai'i. Applying model 4 to these flows gives lengths of 2260 m and 2790 m respectively. In this instance the model overestimated the length of the 19 July flow by ~200 m (measured length by Moore & Kachadoria (1980) is ~2000 m) and underestimated the length of the 21 December flow by ~9610 m (measured length of 12400 m given by Lockwood et al., (1999)). While both the 19 July and 21 December 1974 flows have similar ranges of advance rates ( $0.1\text{-}2.2\text{ m s}^{-1}$ ), duration (10800-21600 s), and mean output rates ( $150\text{-}275\text{ m}^3\text{ s}^{-1}$ ) to the 12 flows examined here, they vary significantly in other emplacement conditions. Both Hawaiian flows were emplaced on average ground slopes of  $< 5^\circ$ , considerably less than those for the 12 Etnean flows ( $15^\circ\text{-}21^\circ$ ). Likewise, both Hawaiian flows had much larger total erupted volumes ( $3.5\text{ and }5.9 \times 10^6\text{ m}^3$ ) compared to the 12 Etnean flows. Additionally, while the flow length of the 19 July flow was similar to those of the 12 examined Etnean flows (2100-3600 m), the 21 December 1974 flow was significantly longer (12400 m) due to topographic confinement and channelling for a significant portion of its length (e.g. Wilson et al., 1987; Pinkerton & Wilson, 1993; Lockwood et al., 1999; Soule et al., 2004; Dietterich & Cashman, 2014).

### 3.6 Conclusion

Using long-range ground-based visible time-lapse imagery allowed for a detailed visual and statistical analysis of the emplacement and morphology of 12 short-duration volume-limited lava flows which occurred from 2011 to 2012 at Mt Etna. The analysis provided the following results:

- Based on morphology within Zone 1, flows could be divided into two groups, 1) those flows which advanced slowly (average of 0.04-0.05 m s<sup>-1</sup>) as one to two flow lobes, and 2) those flows which rapidly advanced (average of 0.12-0.57 m s<sup>-1</sup>) as broad sheets.
- Advance rates and flow widths within Zone 1, and additionally the interval between the start of lava emission and onset of fire fountaining, indicate that differences in initial instantaneous effusion rate dictated the morphology observed for the two groups.
- Results suggest that the number of bifurcations within Zone 1 was influenced by flow width, with wider flows resulting in a higher number of bifurcations.
- Topographic changes from unconfined flat areas to areas with more confining features resulted in the shifts in flow morphology to semi-channelized in Zones 2 and 3.
- A strong correlation ( $r = 0.63$ ) between final flow length and length of confinement of the primary flow suggests that the length for the 12 Etnean flows is influenced by narrowing and capture due to topography.
- Multiple regression analysis identified maximum flow width ( $W_{max}$ ), duration of flow ( $t_{flow}$ ), and maximum advance rate in Zone 1 ( $adv_{max\_z1}$ ) as producing the best flow length model in terms of explanatory and predictive power ( $R^2 = 0.96$ ,  $R^2_{adj} = 0.94$ , and  $R^2_{pred} = 0.92$ ) for the 12 examined flows.

# Chapter 4 Using time-lapse imagery and FLOWGO to constrain properties of short-duration volume-limited lava flows

## 4.1 Introduction

Lava flows represent the main risk to local populations and infrastructure at many volcanoes. Understanding flow emplacement processes facilitates hazard management and, typically, studies of active lava flows are conducted using field-based surveys which can include sampling for rheological analysis (Cashman et al., 1994; 1999), measurements of flow geometry (Hon et al., 1994; Calvari et al., 2005), temperature measurements using direct (Lipman & Banks, 1987; Pinkerton et al., 2002) and indirect methods, such as ground-based thermal imaging (Calvari et al., 2005; Harris et al., 2005a; Bailey et al., 2006; Spampinato et al., 2011), and short- and long-range observations using ground-based visible photography and laser scanners (Zlotnicki et al., 1990; James et al., 2006, 2007, 2009; Robson & James, 2007; Slatcher et al., 2015).

However, scenarios in which the environment (e.g. steep or rough terrain) or volcanic hazards limit safe access can prevent data collection. Where periods between activity are short, flows can become rapidly buried and even post-emplacement field surveys can be prevented. One solution for overcoming these difficulties is to use ground-based remote time-lapse imagery to record flow emplacement (James et al., 2012; James & Robson, 2014), an approach that has also provided valuable insight into the growth and deformation of lava domes (Sparks et al., 1998; Major et al., 2009; Walter et al., 2013).

The compact size and affordable price of dSLR cameras makes them well-suited for extended field deployments where they can augment or replace other observational methods, depending on the demands of the volcanic and emplacement conditions. These traits make

dSLR time-lapse photography ideal for capturing short-duration volume-limited lava flows. In comparison to longer-duration lava flows, which are usually cooling-limited (e.g. Walker, 1971; Guest et al., 1987), the short-duration of volume-limited lava flows makes capturing and analysing their emplacement difficult.

To explore the emplacement and rheological properties of a short-duration volume-limited lava flow, flow widths and advance rates can be estimated from time-lapse data, which can then be used to estimate thermo-rheological properties using lava flow models such as FLOWGO (Harris & Rowland, 2001; 2015; Harris et al., 2005b; 2007c; 2015; Wantim et al., 2013). Here, estimates of flow properties for two short-duration lava flows at Mt. Etna (emplaced on 12 May 2011 and 19 July 2011) are derived using long-range time-lapse imagery and FLOWGO (Harris et al., 2015).

#### 4.2 The 12 May & 19 July 2011 Fire Fountain Events, Mt. Etna

From 2011 until 2012, eruptive activity at Mt. Etna comprised concurrent short-lived intense fire fountaining episodes with relatively short intervals between episodes (Behncke et al., 2014; Chapter 3, Section 3.2), ranging from 5.5 to 58 days. Emplacement times for lava flows ranged from approximately 20 to 270 minutes (Behncke et al., 2014). These episodes produced simple, volume-limited flow fields (Behncke et al., 2014; Chapter 3, Section 3.4). Of the 25 episodes which occurred in 2011 and 2012, two, on the 12 May and 19 July 2011, have been selected here for detailed analysis. These two episodes have been selected as they are representative of two different lava flow morphologies observed in the proximal region of the flow fields, based on analysis of 12 of the 25 episodes (Chapter 3, Section 3.4.1). The 12 May 2011 episode belongs to a first morphology group (Group 1) which initially advanced as one or two semi-confined flow lobes at low advance rates (average of 0.04 to 0.05 m s<sup>-1</sup>) until the onset of fire fountaining. The 19 July 2011 episode represents the second morphology group

(Group 2) which produced rapidly advancing (average of 0.12 to 0.57 m s<sup>-1</sup>) unconfined sheet flows.

Table 4.1 – Eruption parameters for the 12 May and 19 July 2011 paroxysmal events at Mt. Etna, given by Behncke et al. (2014).

Episode	Date	$t_{flow}$ (s)	$t_{ff}$ (s)	$L$ (km)	$A$ (km <sup>2</sup> )	$V$ (10 <sup>6</sup> m <sup>3</sup> )			* $MOR$ (m <sup>3</sup> s <sup>-1</sup> )		
						Min	Max	Mean	Min	Max	Mean
4	12/05/2011	6000	†7200	3.2	0.68	0.77	1.32	1.05	129	220	175
6	19/07/2011	9000	8700	3.3	1.08	0.78	1.35	1.06	87	149	118

$t_{flow}$  = duration of flow,  $t_{ff}$  = duration of fire fountain,  $L$  = length,  $A$  = lava flow total area,  $V$  = total volume,  $MOR$  = mean output rate.

\*  $MOR$  is given as effusion rate in Behncke et al. (2014).

† Value given in Behncke et al. (2014) does not match with the time-lapse data for the episode (Chapter. 3 Section 3.4.1). The value was therefore replaced with that derived from the time-lapse data.

The eruption parameters and flow characteristics for both the 12 May and 19 July 2011 episodes can be seen in Table 4.1.

### 4.3 FLOWGO Model and Physical Principles

FLOWGO is a one-dimensional lava flow model which simulates changes in basaltic lava rheology and velocity as material advances between set distance intervals along a single, pre-established channel. At each step, estimates for viscosity, yield strength and velocity are calculated based on the temperature and crystallinity conditions of the preceding step and their associated rates of change (Harris et al., 2015). The model is usually initiated using estimated eruption conditions, with the estimates being subsequently refined by comparing model output against available measurements (e.g. channel width and depth, viscosity, yield strength, crystallinity, flow velocity, and lava temperature) in order to evaluate the quality of the model fit (Harris & Rowland, 2001; 2015; Harris et al., 2015).

#### 4.3.1 Velocity and Effusion Rate Calculations

At every location of evaluation down a channel, FLOWGO employs the Jeffrey's equation (Moore, 1987) to derive mean lava flow channel velocity ( $v_{mean}$ ). This can be done using a Bingham fluid modified version of the Jeffrey's equation (Moore, 1987) for either a semi-circular channel or a channel that is wider than it is deep. The following equation is used for a semi-circular channel:

$$v_{mean} = \left( \frac{r^2 p g \sin(\theta)}{8\eta} \right) \left( 1 - \frac{4}{3} \frac{\tau_0}{\tau_b} + \frac{1}{3} \left( \frac{\tau_0}{\tau_b} \right)^4 \right) \quad (m s^{-1}) \quad 4.1$$

where  $r$  is the radius of the channel,  $p$  is the density of the lava,  $g$  is the acceleration due to gravity,  $\theta$  is the underlying slope,  $\eta$  is lava viscosity,  $\tau_0$  is yield strength and  $\tau_b$  is basal shear stress. For a lava channel that is wider than it is deep, the following variant to Equation 1 is used:

$$v_{mean} = \left( \frac{d^2 \rho g \sin(\theta)}{3\eta} \right) \left( 1 - \frac{3\tau_0}{2\tau_b} + \frac{1}{2} \left( \frac{\tau_0}{\tau_b} \right)^3 \right) \quad (m \ s^{-1}) \quad 4.2$$

where  $d$  is the thickness of the lava flow. Next, effusion rate ( $E_r$ ) is calculated by multiplying  $v_{mean}$  by the cross-sectional area (i.e. multiplying by thickness and width) of the flow,

$$E_r = dwv_{mean} \quad (m^3 s^{-1}) \quad 4.3.$$

Note that the calculated channel area will vary depending on the assumed channel-shape.

#### 4.3.2 Mass Conservation

The FLOWGO model assumes that the depth of the lava flow is constant along all points down the channel and that the channel width is variable. For a single channel, this means that the volume flux (rate of supply of material to an individual channel) of lava entering the channel ( $E_{in}$ ) has to be the same as the effusion rate at the vent ( $E_{vent}$ ) (Harris et al., 2015), such that

$$E_{vent} = E_{in} = v_{mean\_head} w_{head} d_{head} \quad (m^3 \ s^{-1}) \quad 4.4$$

where  $v_{mean\_head}$  is the mean velocity of the lava,  $w_{head}$  is the mean channel width and  $d_{head}$  is the channel depth at the head of the channel. Since FLOWGO works on the principle that no volume is lost to the development of levees, the effusion rate ( $E_r$ ) at all points down the channel is equal to the initial effusion rate, or  $E_{vent}$ , such that,

$$E_r = E_{vent} = v_{mean} wd \quad (m^3 \ s^{-1}) \quad 4.5$$

#### 4.3.3 Rheology Calculations

FLOWGO estimates viscosity as a function of crystallinity and temperature by combining the Einstein-Roscoe relationship with the temperature dependent model of Dragoni (1989) (Harris & Rowland, 2001; 2015). The Einstein-Roscoe relationship is defined as:

$$\eta(\phi) = \eta_f (1 - (R\phi))^{-2.5} \quad (Pa \ s) \quad 4.6$$

in which  $\eta_f$  is the dynamic viscosity,  $\phi$  is the crystal content of the lava,  $\phi_{\max}$  is the maximum crystal content a lava can reach before flow is impossible and  $R$  is  $1/\phi_{\max}$  (Pinkerton and Stevenson, 1992; Harris, et al., 2015). The temperature dependent model of Dragoni (1989) is defined as:

$$\eta(T) = \eta_0 \exp^{A(T_0 - T)} \quad (Pa \cdot s) \quad 4.7$$

where  $T$  is the temperature of the lava,  $\eta_0$  is the viscosity of the lava at the liquidus temperature ( $T_0$ ), and  $A$  is a constant related to the composition of the lava (Harris, et al., 2015). Combining the two equations gives the relationship:

$$\eta(T, \phi) = \eta(T)(1 - (R\phi))^{-2.5} \quad (Pa \cdot s) \quad 4.8$$

Additionally, yield strength can also be written as a function of temperature and crystallinity (Dragoni, 1989; Pinkerton & Stevenson, 1992; Harris, et al., 2015):

$$\tau_0(T, \phi) = B[\exp^{C(T_0 - T)} - 1] + [6500\phi^{2.85}] \quad (Pa) \quad 4.9$$

where  $B$  and  $C$  are constants dependent on lava composition.

#### 4.3.4 Thermal Conditions in FLOWGO

FLOWGO uses a two-component model to define the thermal surface of the flow and to calculate the effective radiation temperature of the lava surface ( $T_e$ ), defined by the equation:

$$T_e = [fT_c^4 + (1 - f)T_c^4]^{0.25} \quad (K) \quad 4.10$$

where  $f$  is the fractional crust coverage, defined by the portion of the flow surface occupied by a crust at temperature  $T_c$ , and which is calculated from,

$$f = \exp(av) \quad 4.11$$

where  $a$  is an empirically-derived coefficient which relates  $f$  to  $v$ . It has been postulated that higher velocities are associated with tearing and fracturing of cooled crust, resulting in exposure of the underlying molten core of a flow (Lipman & Banks, 1987; Rowland & Walker, 1990; Cashman et al., 2006) and resulting in a lower value of  $f$ . The loss of an insulating crust and exposure of the hotter core of the flow will increase the rate of temperature loss of the flow (e.g. Flynn and Mouginis-Mark, 1992;1994; Cashman et al., 1999).

The relationship  $1-f$  defines the remaining surface occupied with higher temperature molten material ( $T_h$ ) (Harris & Rowland, 2001). FLOWGO can then calculate heat loss due to radiation ( $Q_{rad}$ ), convection ( $Q_{conv}$ ) and conduction ( $Q_{cond}$ ) using the following:

$$Q_{rad} = \sigma \epsilon T_e^4 w \quad (W m^{-1}) \quad 4.12$$

$$Q_{conv} = h_c (T_{conv} - T_{air}) w \quad (W m^{-1}) \quad 4.13$$

$$Q_{cond} = k \left[ \frac{(T_{core} - T_{base})}{h_{base}} \right] w \quad (W m^{-1}) \quad 4.14$$

where  $\sigma$  is the Stefan-Boltzman constant,  $\epsilon$  is the emissivity of the lava,  $h_c$  is the convective heat transfer coefficient,  $T_{air}$  is the temperature of the air,  $k$  is the thermal conductivity,  $T_{base}$  is the temperature of the lava flow at its base, and  $h_{base}$  is the distance between the core temperature of the lava flow ( $T_{core}$ ) and the location where  $T_{base}$  is reached.  $T_{conv}$  is the surface temperature for convection, and is given by Harris and Rowland (2001) as,

$$T_{conv} = [f T_c^{1.333} + (1 - f) T_h^{1.333}]^{0.75} \quad 4.15.$$

Using Equations 4.10-4.12, FLOWGO is able to calculate the heat lost per defined distance step value as the flow advances, defined as  $\left(\frac{\Delta T}{\Delta x}\right)$  using the following equation:

$$\frac{\Delta T}{\Delta x} = \frac{-Q_{rad} - Q_{conv} - Q_{cond}}{E_r \rho C_L \frac{\Delta \phi}{\Delta T}} \quad (K m^{-1}) \quad 4.16$$

in which  $C_L$  is the latent heat of crystallization and  $\frac{\Delta\phi}{\Delta T}$  is the rate of crystallization, defined as the fraction of crystallization per degree of cooling. Finally, the mass fraction of crystallization per defined distance step can be estimated using the following relationship:

$$\frac{\Delta\phi}{\Delta x} = \left(\frac{\Delta T}{\Delta x}\right)\left(\frac{\Delta\phi}{\Delta T}\right) \quad 4.1$$

#### 4.3.5 Source Terms

Once the temperature, textural and rheological relationships have been initialized, the primary source term required by FLOWGO is a slope profile. A slope profile can be created manually or automatically from a DEM. Once an appropriate slope profile has been made the next two most significant source terms in FLOWGO are channel dimensions (channel width and depth) and effusion rate.

Depending on which of these source terms is known, any unknown term can be adjusted until the modelled output for the known terms equate to observed values. For example, if effusion rate is known, but channel dimensions are not, the channel dimensions can be adjusted until the FLOWGO-modelled effusion rate reflects that the known effusion rate. If effusion rate is unknown but channel dimensions are known, the channel dimensions (width and depth) and slope are used with either equation 4.1 or 4.2 to obtain at-vent mean channel velocity ( $v_{mean}$ ). Mean channel velocity is then used with equation 4.3 to obtain effusion rate (Harris & Rowland, 2001; 2015). Likewise, if effusion rate and one of the channel dimensions is known, the second unknown channel dimension can be obtained by adjusting until the FLOWGO-modelled effusion rate and known channel dimension agree with their observed values.

#### 4.3.6 Stopping Conditions

Once values for channel width and depth, viscosity, effusion rate, yield strength, crystallinity, channel velocity, and lava temperature have been initialized for at-vent conditions (i.e. the starting conditions of the lava flow) FLOWGO loops through all equations, updating them

based on changes to temperature and crystallinity of the flow as it progresses down the channel (Figure 4.1). At each step, the core temperature and crystal content are updated based on the values from the previous step and derived cooling and crystallisation rates, and used to calculate the rheology, flow velocity and depth of the lava flow. The loop is executed until  $T_{core}$  becomes equal to or less than the solidification temperature of the lava, or  $v_{mean}$  becomes 0, meaning that the lava has solidified or that the viscosity and yield strength of the lava have increased to a point where the forward motion of the lava flow has stopped due to cooling.

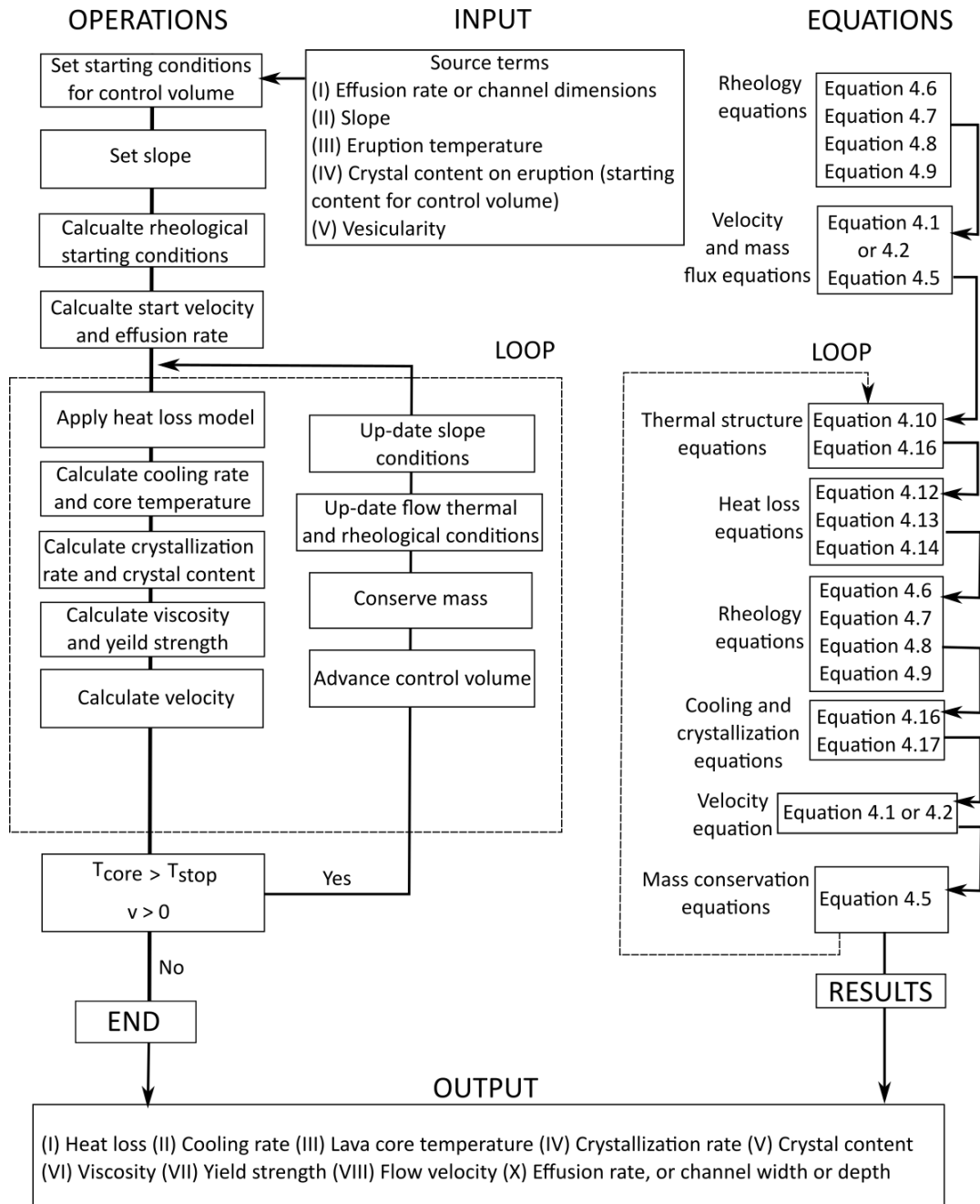


Figure 4.1 – Workflow of the FLOWGO model. Operations are listed on the left-hand side of the figure with equations (listed in sequence) given on the right-hand side (modified from Harris et al., 2015).

## 4.4 Methodology

### 4.4.1 Time-lapse Camera Data

The installation and collection of the time-lapse data used for this study is discussed in detail in Chapter 3, Section 3.3.1. For this work, only time-lapse data from one of the cameras (Monte Zoccolaro), was used because it provided the best spatial coverage of flow emplacement (Figure 4.2).

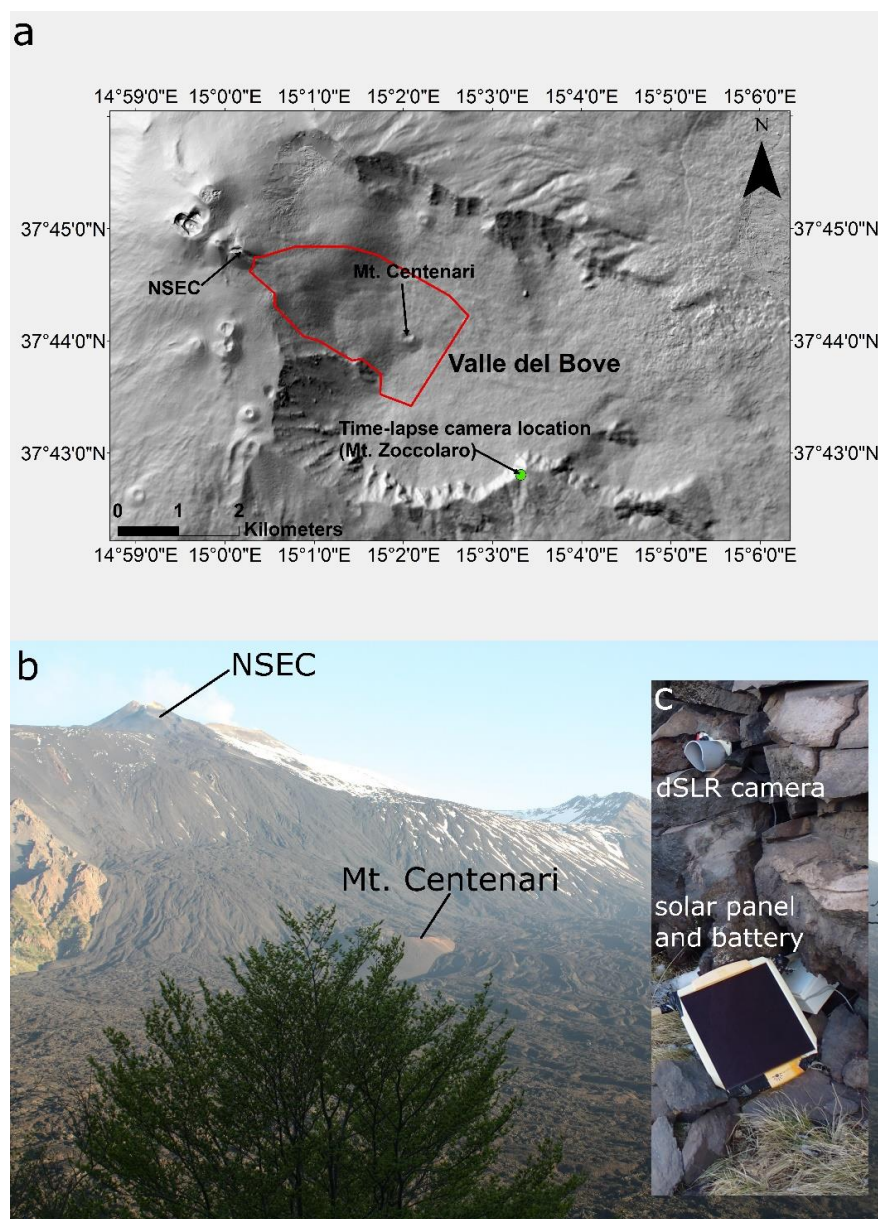


Figure 4.2 – Time-lapse camera installation at Mt. Etna. (a) Shaded relief map of the Valle del Bove created from the Laboratorio di Aerogeofisica-Sezione Roma2 2012 DEM (De Beni et al., 2015), showing the camera location, the New South East Crater (NSEC) which sourced the observed flows, and the area of flow emplacement (outlined in red). (b) An example image from the Zoccolaro time-lapse sequence. (c) A typical camera installation.

#### 4.4.2 Estimating Flow Front Advance Rates and Flow Widths

The 12 May 2011 episode was captured in 24 images, from 11/05/2011 18:33 to 12/05/2011 06:03 and the 19 July 2011 episode was captured in 10 images, from 18/07/2011 23:32 to 19/07/2011 04:02 (both at acquisition intervals of 30 minutes). Advance rates and flow widths were estimated following the method outlined in Chapter 3, Section 3.3.2. Estimates of advance rate and flow width were made for the flow body which reached the greatest length (referred to as the 'primary' flow) and for any new flow produced due to bifurcation of the primary flow (referred to as 'secondary' flows) (Figure 4.3).

To analyse variations in physical and rheological properties throughout the flow fields, the emplacement area was divided into three zones based on the breaks in slope which denote the top of the Valle del Bove headwall and the beginning of the valley floor (Figure 4.4). Flow front advance rates were estimated throughout the three zones as flows were emplaced, while flow widths were estimated once emplacement had predominantly ceased but while there was sufficient incandescence from the flow field to identify individual flow margins. Estimates for flow width were then made every 10 metres along the flow using the Pointcatcher tracking software (e.g. James et al., 2007; Robson & James, 2007; James et al., 2016).

The main source of error in point position occurred due to the oblique viewing angle of the camera. When views are highly oblique, and the viewed surface is located at a great distance from the camera, the projected point coordinates on the DEM surface are highly sensitive to any camera misalignment or to error in the DEM (Chapter 3, Section 3.4.2). For the two events examined here, when point positional errors were determined for the less oblique viewing areas of the image (Zones 2 and 3) errors ranged from 2 to 5 m. For the more oblique areas (Zone 1) errors ranged from 5-100 m. To account for errors in flow width due to point placement errors in the more oblique viewing areas, sections of the flow where width

estimates suddenly increased and decreased width with no corresponding visible change in width were smoothed by extrapolating width values using the points prior to the increase and just after the decrease in flow width (Figure 4.5).

Additionally, for the 19 July 2011 episode, flow width estimates using the time-lapse data could not be acquired in the area from the NSEC cone to the beginning of the Valle de Bove headwall (Zone 1). This was due to difficulty in distinguishing flow margins in this area as a result of the morphology of the flow and the rapid flow advance. To estimate flow widths for the 19 July 2011 episode within Zone 1, a line was extended from the first identifiable flow margin location at the top of the Valle de Bove headwall, back to the earliest flow width estimate possible near the start of the flow (Figure 4.4).

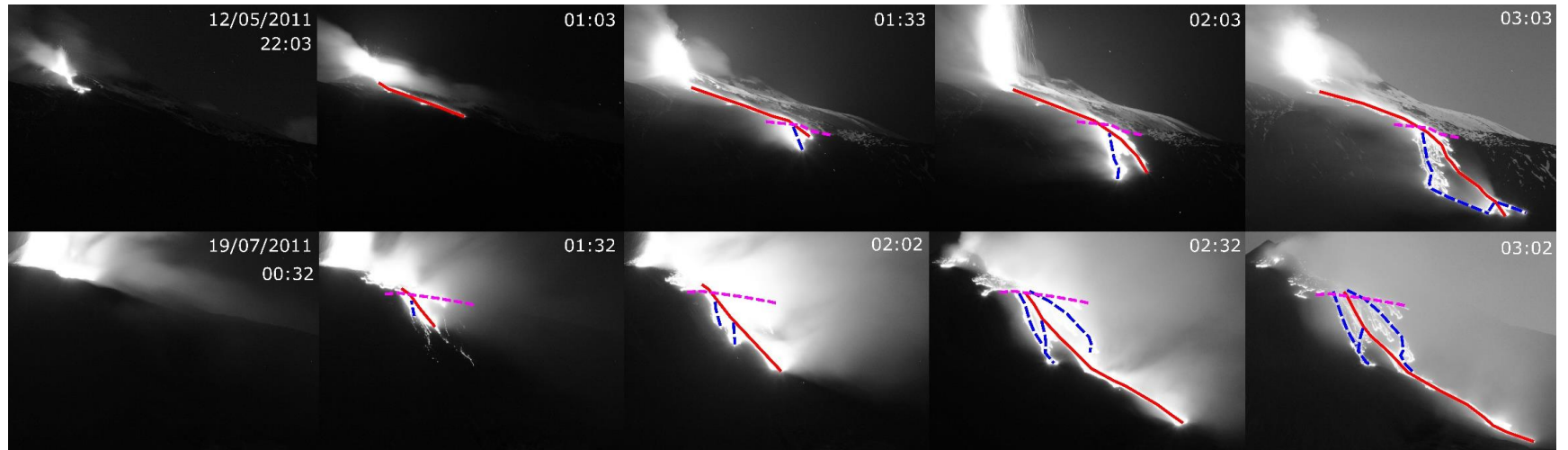


Figure 4.3 – Selection of time-lapse images from Zoccolaro showing the evolution of the flow fields for the 12 May (top sequence) and 19 July 2011 (bottom sequence) episodes. The right-most images were those used for flow width estimates. The red line denotes the primary flow unit with blue dashed lines marking secondary flows produced by bifurcations of the primary flow. Purple dashed line identifies the crest of the Valle del Bove headwall.

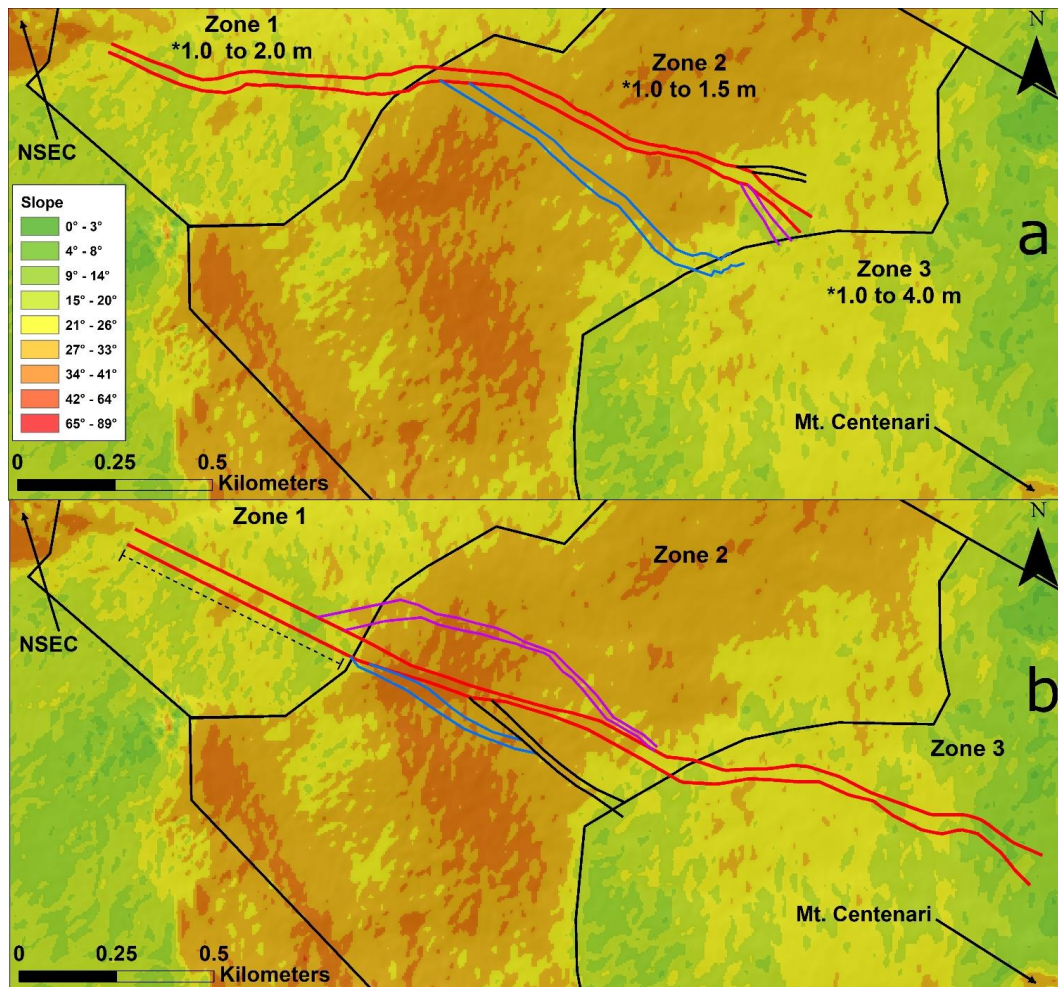


Figure 4.4 – Lava flow outlines for the (a) 12 May and (b) 19 July 2011 episodes examined in this study (solid lines: primary flow unit = red, secondary flows = blue, black, and purple). The flow emplacement area has been divided into three zones defined by the breaks in slope which mark the transition onto the Valle del Bove headwall and the transition onto the valley floor. (b) Dashed line identifies the segment of the 19 July 2011 flow where flow widths could not be estimated using the time-lapse data and were instead estimated by extending a line from the earliest width estimate possible to the first estimate located at the transition from Zone 1 to Zone 2. \*lava flow field thicknesses by zone estimated by Behncke et al. (2014) for the 25 paroxysmal events which occurred in the 2011-2012 period.

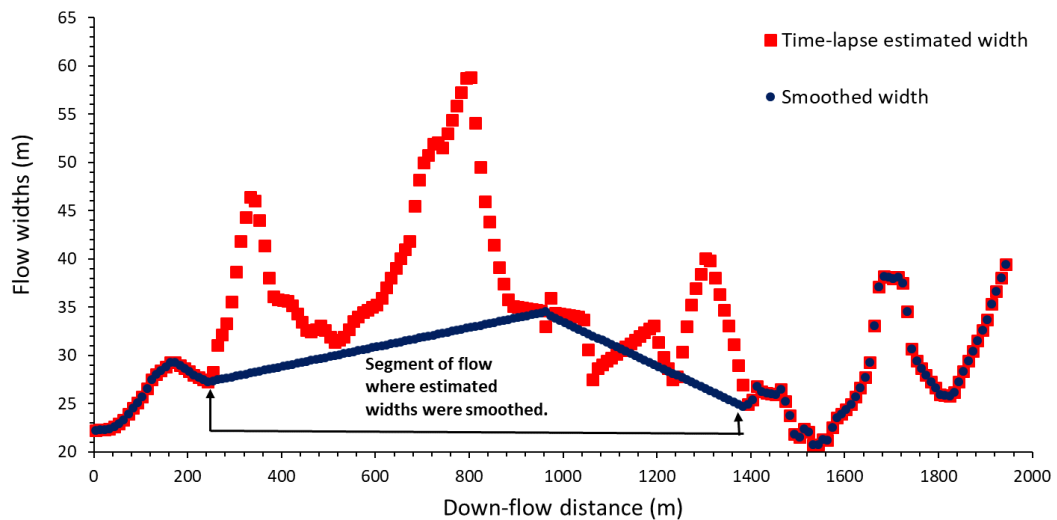


Figure 4.5 – Time-lapse estimated flow widths and the corresponding smoothed widths for the 12 May 2011 primary flow.

#### 4.4.3 FLOWGO Analysis

Identification of channel margins in the time-lapse data was not possible due to the resolution of the images and pixel saturation due to the bright incandescence of the active flow. It was therefore decided to use flow width as a proxy for channel width in FLOWGO since the 2011-2012 Etnean flows were often captured and channelized by pre-existing topographic features (e.g. older flow margins and levees) (Chapter 3). Equation 4.1 was used for the 12 May 2011 flow since its initial morphology was semi-channelized (i.e. Group 1) and Equation 4.2 was used for the 19 July 2011 flows due to its initial broad sheet-like morphology (i.e. Group 2). To estimate the starting parameters for each lava flow, estimated flow widths are compared to modelled flow widths estimated using FLOWGO. Slope values were taken from the DEM at the centre of the flow for each distance interval.

Using measured temperatures and typical phenocryst and vesicularity percentages for Etnean lavas, “hot” and “cold” lava models were created to effectively represent potential end-member starting flow conditions (Table 4.2). Flow widths were then modelled for the primary flow units of the 12 May 2011 and 19 July 2011 flow fields, for each end-member model. Since the 12 May and 19 July 2011 flows had rapid rates of advance (maximum of 0.22 and 0.37 m

s<sup>-1</sup> respectively) and high estimated *MOR* (Table 4.1), the channel velocities can be assumed to be high as well, as higher advance rates require a high rate of supply of material to the flow front (Rowland & Walker, 1990; Kauahikaua et al., 2003). Therefore, a value of -0.16 was used for *a* in equation 4.11 to represent a fractional crust coverage (*f*) of a poorly-insulated lava flow (Harris & Rowland, 2015).

Modelled widths were then compared to measured widths and a sum of squared residuals (SSR) fit was performed between flow widths starting at the top of the Valle del Bove headwall (Zone 2) in order to identify the best-fit channel depth for using both models for each event. The full list of FLOWGO parameters can be seen in Table 4.3.

*Table 4.2 – End-member lava flow models used to best-fit FLOWGO estimated flow widths to measured flow widths. The sources of these values can be seen in Table 4.3.*

Model	Temperature (°C)	Rate of Crystallization ( $\frac{\Delta\phi}{\Delta T}$ )	Viscosity at Eruption (Pa s)	Phenocryst (%)	Vesicularity (%)	Bulk Density (kg m <sup>-3</sup> )
Cold	1065	0.003	667	30	15	2312
Hot	1080	0.004	481	15	29	1931

Table 4.3 – Full list of parameters used in FLOWGO to determine the best fit model for the 12 May and 19 July 2011 episodes.

Input Parameter	Value		Source
	Cold Model	Hot Model	
<b>Channel Dimensions</b>			
Channel width, $w$ , (m)	22.4	44.4	Measured from time-lapse image.
Down-flow increment (m)	10		Selected measurement increment for slope and channel width
<b>Thermal Parameters</b>			
Eruption temperature, $T_{erupt}$ , (°C)	1065	1080	Cold and hot representative temperatures at-vent for active lava flow channels on Mt. Etna (Bailey et al., 2006; Tanguy and Clocchiatti, 1984)
Crust temperature, $T_{crust}$ , (°C)	500		Harris et al., 2015
Temperature buffer, $T_h$ , (°C)	140		Harris & Rowland, 2001
Crust to velocity relationship, $\alpha$	-0.16		Harris & Rowland, 2001
<b>Density and Vesicularity</b>			
Dense rock density, $\rho_{DRE}$ , (kg m <sup>-3</sup> )	2720		Calculated by Harris & Rowland (2015) from compositional data for the 1991-93 eruption at Mt. Etna (Bottinga and Weill, 1970)
Vesicularity, $\phi_b$ , (%)	15	29	Mean vesicularity (22) +/- 7, calculated by Harris et al. (2005)
Bulk density, $\rho$ , (kg m <sup>-3</sup> )	2312	1931	$\rho = (1 - \phi_b) \rho_{DRE}$
<b>Velocity Constants</b>			
Gravity, $g$ , (m s <sup>-2</sup> )	9.8		
Channel shape, $n$	3		Modifier value for different channel geometries for the modified Jeffreys equation for a Bingham fluid (Moore, 1987)
<b>Viscosity and Yield Strength Parameters</b>			
Viscosity at Eruption, $\eta_f(T)$ , (Pa s)	667	481	Calculated using the method of Giordano & Dingwell (2003) using $T_{erupt} = 1065$ & $1080$ °C and $H_2O = 0.1$ wt % ( $H_2O$ value taken from Harris & Allen (2008) for summit eruptions at Mt. Etna)
Constant A, (K <sup>-1</sup> )	0.04		Dragoni, 1989
Constant B, (Pa)	0.01		Dragoni, 1989
Constant C, (K <sup>-1</sup> )	0.08		Dragoni, 1989
<b>Radiation Parameters</b>			
Stefan-Boltzman, $\sigma$ , (W m <sup>2</sup> K <sup>-4</sup> )	5.67 x 10 <sup>-8</sup>		
Emissivity, $\epsilon$	0.98		Ball & Pinkerton, 2006

Table 4.3 continued

Input Parameter	Value		Source
<b>Conduction Parameters</b>			
Thermal conduction, $K$ , (W m K)	Cold Model	Hot Model	Given by Harris et al. (2007) as calculated following Peck (1978). (Wooster et al., 1997) (Harris and Rowland, 2001)
Basal temperature, $T_{base}$ , (°C)	2.5	500	
Core to base distance (%)	19		
Distance from base to core temp, $h_{base}$ , (m)	Calculated in model		
<b>Convection Parameters</b>			
Wind speed, $U$ , (m s <sup>-1</sup> )	3.3	3.1	Average monthly value for the Mt. Etna area (www.yr.no)
Air temperature, $T_{air}$ , (°C)	25	32	Average monthly value for the Mt. Etna area (www.yr.no)
Convective heat transfer coefficient, $C_h$	0.0036		Given by Harris and Rowland (2001) from Greeley and Iverson (1987)
Air density, $\rho_{air}$ , (kg m <sup>3</sup> )	0.4412		
Air specific heat capacity, $cp_{air}$ , (J kg K)	1099		
<b>Crystal Parameters</b>			
Crystal content, $\phi$ , (%)	15	30	Range of values from petrological analysis of lava flows during 2011-2013 (Viccario et al., 2015)
Cooling range, $\Delta T$ , (K)	150		Harris et al., 2015
Rate of crystallization, $\Delta\phi/\Delta T$	0.003	0.004	Harris et al., 2015
Latent heat of crystallization, $L$ , (J kg)	3.50 x 10 <sup>5</sup>		Harris et al., 2015
R ( $1/\phi_{max}$ )	1.51		Pinkerton and Stevenson, 1992; Harris and Rowland, 2001; Harris et al., 2015

With FLOWGO being a single-channel model, to model bifurcated flows, additional models were required. Outputs for the first model (of the parent flow) were used to provide the initial conditions for the second model, representing the new flow produced at the bifurcation. A sum of squared residuals (SSR) fit was performed on the secondary models to estimate the best-fit channel depth and volume flux for the new flow.

The volume flux of the bifurcated flow was then subtracted from the volume flux of the parent flow for distances greater than the bifurcation distance and a new sum of least squares fit was performed on the parent flow using the reduced volume flux to estimate the new channel depth due to the reduction in supply.

## 4.5 Results

Flow emplacement was only visible up to an emplacement length of 1890 m for the 12 May 2011 flow field and to 2540 m for the 19 July 2011 flow field, which accounted for approximately 59 % and 77 % of the actual final length reached by each event. This limited visibility was due to an inability to distinguish the active lava flow fronts from the image background during day-light hours. In images which occurred at night, the incidences of the active flow fronts make them easily identifiable. In day-light images this incidence is not visible. Additionally, as a flow cools the intensity of the incidences decreases. For the 19 July 2011 flow, FLOWGO-modelled estimates were only carried out to a flow length of 2310 m, because after this distance, modelled values increased exponentially causing FLOWGO to crash.

Time-lapse estimated flow front advance rates and FLOWGO-outputs using the “cold” and “hot” lava models for the primary flow in each zone and for each episode can be seen in Table 4.4. FLOWGO-estimated flow widths using both lava models starting at Zone 2 were similar to those widths estimated with the time-lapse data, with a difference in SSR of ~1.0 % for the 12 May and ~8.0 % for the 19 July 2011 flows (Figure 4.6).

Overall, FLOWGO-modelled widths for the 12 May 2011 flow were more in line with time-lapse estimated widths than those of the 19 July 2011 flow. However, for both flows, the FLOWGO-modelled widths in Zone 1 (outlined in Figure 4.6 by the dashed red boxes) covered a wide range and were not in agreement with either the smoothed time-lapse estimated widths for the 12 May 2011 flow or the interpolated width estimates for the 19 July 2011 flow (Figure 4.6).

FLOWGO's model-estimated average primary flow channel depths for the 12 May and 19 July 2011 flows were  $1.6 \pm 0.2$  m and  $1.3 \pm 0.2$  m, respectively. Modelled channel velocities ranged from 0.8 to 6.0  $\text{m s}^{-1}$  for the 12 May 2011 flow and from 0.2 to 4.1  $\text{m s}^{-1}$  for the 19 July 2011 flow. FLOWGO estimated effusion rate for the 12 May and 19 July primary flow units were  $140.5 \pm 10.5 \text{ m}^3 \text{ s}^{-1}$  and  $105.5 \pm 6.5 \text{ m}^3 \text{ s}^{-1}$ , respectively. Multiplying these values by the duration of flow ( $t_{flow}$ ) for both episodes gives volumes of  $1.01 \times 10^6 \pm 0.07 \times 10^6 \text{ m}^3$  for the 12 May episode and  $0.95 \times 10^6 \pm 0.06 \times 10^6 \text{ m}^3$  for the 19 July episode.

While FLOWGO functioned properly when estimating properties for the primary flows in both the 12 May and 19 July 2011 flows, estimating changes in flow depth caused by bifurcations to the primary flow succeeded only when applied to the 12 May 2011 flow. In the case of the 19 July flow, division by zero errors in the processing loop caused FLOWGO to crash. As a result, FLOWGO-modelled estimates for only the primary flow were made for the 19 July 2011 flow.

Table 4.4 – FLOWGO-modelled flow properties for the “cold” and “hot” models, and time-lapse estimated advance rates for the 12 May and 19 July 2011 primary flow units. Mean values are in brackets.

Episode	Time-lapse Estimated Advance Rate (m s <sup>-1</sup> )	Flow Velocity (m s <sup>-1</sup> )		Viscosity (Pa s)		Channel Depth (m)		Effusion Rate (m <sup>3</sup> s <sup>-1</sup> )		<sup>1</sup> Volume (10 <sup>6</sup> m <sup>3</sup> )	
		Cold	Hot	Cold	Hot	Cold	Hot	Cold	Hot	Cold	Hot
12/05/11											
Zone 1	0.01-0.11 (0.04)	2.0-3.8 (2.9)	3.2-6.0 (4.5)	3020-3570 (3280)	910-1080 (990)	1.8	1.4	130	151	0.78	0.91
Zone 2	0.08-0.22 (0.16)	0.8-3.5 (1.9)	2.0-5.4 (3.5)	3570-5050 (4200)	1080-1400 (1230)	1.3-1.8 (1.5)	1.2-1.4 (1.2)				
<sup>2</sup> Zone 3	0.003-0.12 (0.04)	No Data	No Data	No Data	No Data	No Data	No Data				
19/07/11											
Zone 1	0.24-0.28 (0.26)	0.9-2.5 (1.9)	1.4-3.9 (2.8)	3020-3680 (3320)	910-1120 (1010)	1.5	1.1	99	112	0.89	1.01
Zone 2	0.2-0.33 (0.24)	1.3-2.7 (2.0)	2.0-4.1 (3.1)	3690-4760 (4170)	1120-1450 (1270)	1.5	1.1				
Zone 3	0.05-0.37 (0.21)	0.2-1.4 (1.0)	0.4-2.2 (1.5)	4780-8040 (5960)	1460-2390 (1810)	1.5	1.1				

<sup>1</sup>Volume calculated by multiplying the duration of flow given in Table 4.1 by the FLOWGO-modelled effusion rate for the primary flow. <sup>2</sup>No values are available due inability to identify advancing flow fronts during day-light hours.

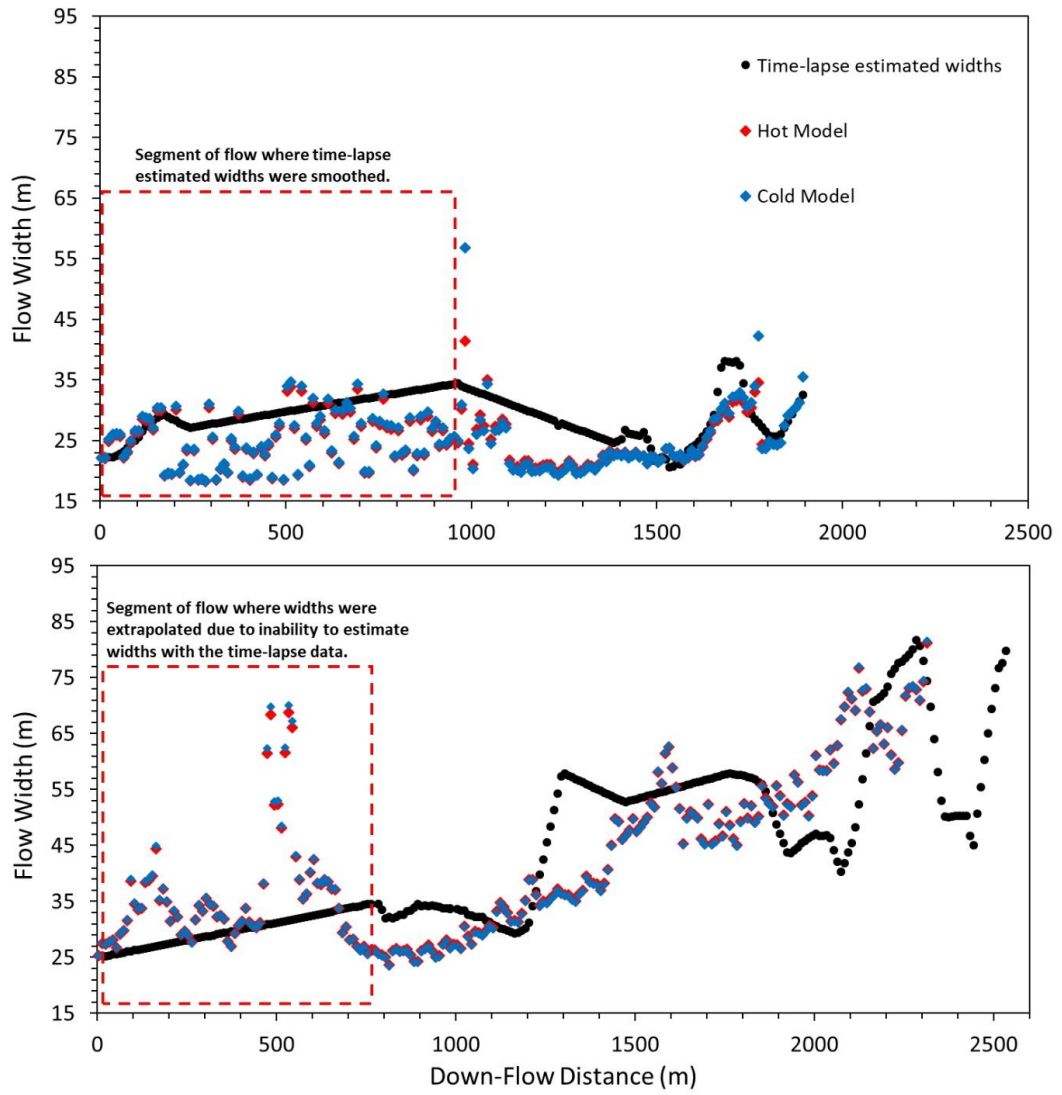


Figure 4.6 – Modelled widths for the 12 May (top) and 19 July (bottom) primary flows. Dashed red box outlines the proximal section of the flows (i.e. the segment of the flows within Zone 1).

## 4.6 Discussion

### 4.6.1 Flow Thickness

FLOWGO was designed to model lava flow within a single channel, with the assumption that channel width is variable and channel depth is constant. This assumption results in a single FLOWGO-channel depth value for the entire flow. While the FLOWGO-estimated flow thicknesses of 0.59 to 1.82 m for the cold model and 0.4 to 1.36 m for the hot model for the 12 May and 19 July 2011 primary flows are in the range of field-based estimates (1.0 to 4.0 m) made by Behncke et al. (2014) using GPS surveys and laser rangefinder measurements for the 25 episodes which occurred from 2011-2012 at Mt. Etna (Figure 4.7), it is recognized that depth will vary down flow.

While small scale down-flow variations in channel depth cannot be determined using FLOWGO, by modelling secondary flows produced due to bifurcation of the primary flow and subtracting their FLOWGO-estimated volume flux from that of the primary flow and then re-running FLOWGO with the reduced volume flux past the distance of the bifurcation, changes in channel depth can be estimated (Figure 4.7). Doing this with the 12 May 2011 flow provided zone-based thickness ranges and average thicknesses per zone which were more in line with field-based estimates made by Behncke et al. (2014) than by using FLOWGO to only model the primary flow unit. However, applying this method to the 19 July 2011 primary flow caused FLOWGO to crash.

The failure of FLOWGO to model secondary flows and their effect on the primary flow for the 19 July 2011 episode can be attributed to the use and interpolation of flow widths within Zone 1 and that FLOWGO is designed to model channelized flow. The 19 July 2011 flow initially advanced rapidly (average rates of 0.12 to 0.57 m s<sup>-1</sup>) as an unconfined, broad sheet-like flow. This made it very difficult to get accurate flow width estimates within Zone 1 using the time-lapse data and necessitated the use of linear interpolation to estimate flow widths within this

zone. However, by estimating the widths in this way, a channelized morphology is assumed for the 19 July 2011 flow, when in reality the morphology is that of a non-channelized sheet flow. In contrast to the 19 July 2011 flow, the 12 May 2011 flow initially advanced slowly (average of 0.04 to 0.05 m s<sup>-1</sup>) as a single flow lobe with a more channelized nature. As a result, flow width estimates were much easier to attain using the time-lapse images as flows advanced slower and had better identifiable margins.

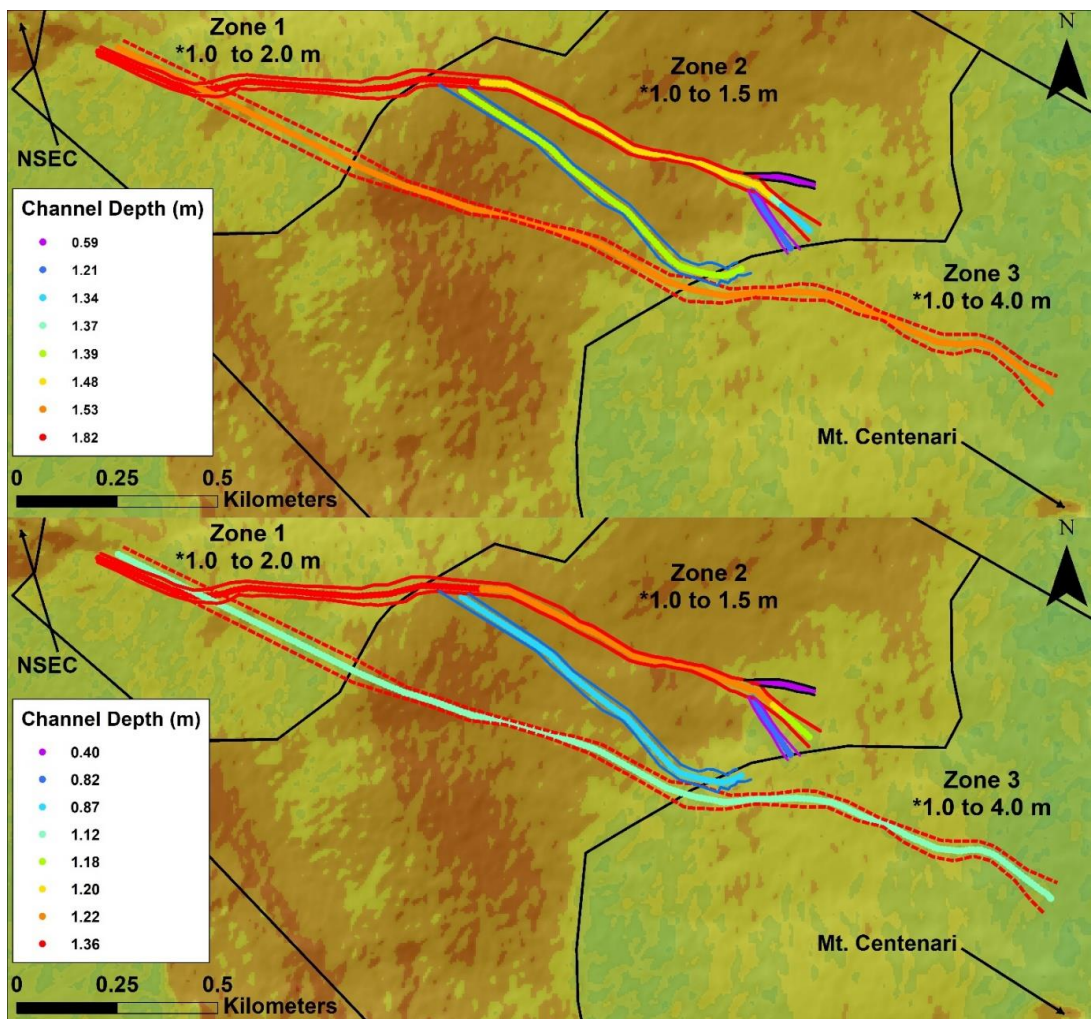


Figure 4.7 – FLOWGO-estimated channel depths for the “cold” lava model (top) and “hot” lava model (bottom) for the 12 May (solid lines: primary flow unit = red, secondary flows =, blue, black, and purple) and 19 July 2011 (dashed line: primary flow unit = red) flows. \*Field-based thickness estimates for each Zone given by Behncke et al. (2014).

#### 4.6.2 Effusion Rate and Total Volume

FLOWGO-derived effusion rates and subsequent estimates for volume using the primary flow units of the 12 May and 19 July 2011 events agree with the range of mean output rates (*MOR*) estimated by Behncke et al. (2014) (Table 4.1). For the 12 May 2011 primary flow unit, the FLOWGO-estimated effusion rate was  $141 \pm 11 \text{ m}^3 \text{ s}^{-1}$  (with the error estimate defined by the difference between the cold and hot model), compared to the Behncke et al., (2014) *MOR* estimate of 129-220  $\text{m}^3 \text{ s}^{-1}$ . Similarly, FLOWGO estimated an effusion rate of  $105.5 \pm 6.5 \text{ m}^3 \text{ s}^{-1}$  for the 19 July 2011 primary flow unit which compares to the Behncke et al. (2014) estimated *MOR* for the whole flow field of 87-149  $\text{m}^3 \text{ s}^{-1}$ .

Multiplying the FLOWGO-estimated effusion rate for the 12 May and 19 July 2011 primary flow units by the flow emplacement durations given in Table 1, a total volume of  $1.01 \times 10^6 \pm 0.07 \times 10^6 \text{ m}^3$  and  $0.95 \times 10^6 \pm 0.06 \times 10^6 \text{ m}^3$  was calculated for each episode respectively. These values are within the range of total volume estimated by Behncke et al. (2014) for both episodes (Table 4.1). These results suggest that a reliable estimate for effusion rate and volume can be made using only the primary flow unit for the 12 May and 19 July 2011 flows.

Comparing effusion rates from SEVIRI-based data (Ganci, et al., 2012) with those of this study and from Behncke et al. (2014) show that the SEVIRI-estimated effusion rate for the 12 May 2011 event ( $43.1 \text{ m}^3 \text{ s}^{-1}$ ) is significantly lower than estimates by either FLOWGO or by Behncke et al. (2014). SEVIRI-estimated effusion rates for the 19 July 2011 event ( $148.5 \text{ m}^3 \text{ s}^{-1}$ ) match the maximum effusion rate estimated by Behncke et al. (2014).

However, the FLOWGO and Behncke et al. (2014) volume estimates for the 12 May and 19 July primary flow units are considerably smaller than the respective values of  $1.47 \times 10^6 \text{ m}^3$  and  $2.14 \times 10^6 \text{ m}^3$ , derived from SEVIRI data by Ganci et al. (2012a). From these volumes, Ganci et al. (2012a) estimated effusion rates by dividing the total volume by the duration of activity defined as the first two of three eruption phases, derived from the measured radiant intensity

profile for each event. The durations used by Ganci et al. (2012a) for the 12 May (255 min) and 19 July 2011 (240 min) episodes are considerably greater than that estimated by Behncke et al. (2014) (Table 4.1) and include the period of increasing activity leading to fire fountaining as well as the duration of fountaining itself. In contrast, the flow duration estimates given by Behncke et al. (2014) are the same as, or very similar to, the duration of fire fountaining. Dividing the SEVIRI-estimated volumes by the Behncke et al. (2014) (Table 4.1) durations of the 12 May and 19 July 2011 episodes gives effusion rates of  $204 \text{ m}^3 \text{ s}^{-1}$  and  $238 \text{ m}^3 \text{ s}^{-1}$  respectively. It is therefore possible that SEVIRI-based volume estimates represent the maximum bound and can be used to estimate the upper limit for effusion rate for the 12 May and 19 July 2011 flows.

#### 4.6.3 Limitations and Errors

FLOWGO is designed to model the thermo-rheological change of a lava flow within a channel. Here, an attempt was made to apply FLOWGO to model volume-limited semi-channelized flow and unconfined sheet flow and use their flow margin widths as a proxy for channel width. While doing so for the primary flow for each episode produced reasonable results, caution is advised on their interpretation.

Errors in the estimated flow width due to model assumptions (i.e. flow width as a proxy for channel width), point placement, smoothing (in the case of the 12 May 2011 flow), or interpolated estimates (the 19 July 2011 flow), can affect the best fit channel depth, with wider flow widths producing shallower channel depths and narrower flow widths producing deeper flow depths. Since equation 4.1 and 4.2 in FLOWGO rely on channel depth to calculate channel velocity, and equation 4.4 uses channel velocity, flow depth, and flow width to estimate effusion rate, any error in the best-fit depth or in the flow width estimates will affect these and other model-outputs.

An example of such errors can be seen in the FLOWGO-derived channel velocities and effusion rate for the 12 May 2011 primary flow unit within Zone 1 (Table 4.4). Examining the FLOWGO-estimated average channel velocities for the May 12 and 19 July 2011 primary flows showed that the 12 May flow had the higher value within Zone 1. However, looking at the time-lapse estimated flow front advance rates for the 12 May and 19 July 2011 primary flows showed that the 19 July flow had the higher advance rate within Zone 1 (average of  $0.04 \text{ m s}^{-1}$  compared to an average of  $0.26 \text{ m s}^{-1}$ ). Remembering that higher rates of effusion produce higher flow front advance rates (e.g. Rowland & Walker, 1990; Kauahikaua et al., 2003), with higher rates of flow front advance requiring greater channel velocities to supply the material needed to maintain the rate of advance, the 19 July 2011 primary flow is expected to have had the higher channel velocities. It is also important to remember that FLOWGO-estimated velocities are for lava flowing in a channel. As such, these values do not represent flow front advance rates, which can be an order of magnitude lower than channel velocities (Lipman & Banks, 1987).

## 4.8 Conclusion

By using FLOWGO with lava flow widths measured from time-lapse data with typical rheological and textural properties for 'a'ā lavas at Mt. Etna, estimates for flow properties for the 12 May and 19 July 2011 episodes were possible and provided the following results:

- Using flow widths estimated from the time-lapse data for the 12 May and 19 July 2011 flows in place of channel widths in FLOWGO gave estimates for effusion rate and total volume which were in agreement with field-based estimates from previous literature.
- Modelling the effects of bifurcations on primary flows using flow widths in FLOWGO provided flow thickness estimates which agreed with previous literature. However, this only worked when applied to the more channelized 12 May flow and failed, due to the extrapolation of flow width and the insufficient accuracy of the channelized flow assumption, when applied to the unconfined 19 July 2011 flow.

# Chapter 5 Improving long-range ground-based thermal remote sensing of lava flows.

## 5.1 Introduction

Ground-based thermal remote sensing has become a valuable tool for the study and monitoring of volcanoes and their hazards (Calvari et al., 1994; Crisci et al., 2003; Del Negro et al., 2008; Harris & Maciejewski, 2000; Harris et al., 2007a; 2007b; Pinkerton & Wilson, 1994; Ramsey & Harris, 2012; Spampinato et al., 2011). Ground-based data are regularly used to estimate volume of lava flows for determining mean output rates, and effusion rates from radiant heat flux (Harris et al., 2007; Harris et al., 2005; Harris & Neri, 2002; Ganci et al., 2012; Ganci et al., 2013; Harris et al., 2011). This is important as effusion rate is a dominant factor in controlling the final shape and lengths of flows (e.g. Walker, 1973; Hulme, 1974; Wadge, 1978; Malin, 1980; Pieri & Baloga, 1986; Pinkerton & Wilson, 1994; Harris & Rowland, 2009), and thus measurements are vital for constraining flow models and for hazard assessment (e.g. Del Negro et al., 2008; Ganci et al., 2011; Ganci et al., 2012).

Unlike satellite-based sensors, ground-based thermal cameras can be placed and operated as situations demand, covering restricted areas in high detail, or enabling broader but continuous monitoring of activity. Collecting ground-based data from long ranges (e.g. greater than 1 km away) can enable calculation of volumes and effusion rates using the radiant heat flux estimated from corrected surface temperatures (Ganci et al., 2011a; 2013) and allows access to locations suitable for safe, sustained, long-term monitoring. Nevertheless, such long-range deployments are often avoided due to factors such as atmospheric attenuation and across-image variations in the target path-length resulting in substantial uncertainty in the derived surface temperatures (Ball & Pinkerton, 2006; James et al., 2006).

To derive an apparent surface temperature from an at-sensor measured temperature the transmittance (fraction of radiant energy that is passed through the atmosphere from the emitting body), upwelling radiance (the radiance emitted by the atmosphere) and reflected radiance (radiance reflected by the Earth's surface) is required, which varies with atmospheric temperature ( $T_a$ ), relative humidity ( $RH$ ), the presence of aerosols, viewing geometry and viewing distance. For volcanological measurements taken with a broadband TIR thermal camera (with a spectral window of 7.5-13  $\mu\text{m}$ ) the contribution of reflected radiance to the measured signal is generally negligible and can be ignored (Harris, 2013; Chapter 2, Section 2.4.2).

Commonly, atmospheric corrections are carried out with dedicated software from the camera manufacturer (such as FLIR's ThermaCam Researcher and Researcher IR) which applies a single path-length correction derived from a horizontal viewing path of user-defined atmospheric temperature, relative humidity, and path length (Sawyer, 2002; Calvari & Pinkerton, 2004; Calvari et al., 2004). Corrections carried out using this software are calculated using the low resolution atmospheric transmission radiative transfer model (LOWTRAN 7) (personal communication, FLIR support), although LOWTRAN has now been generally superseded by the moderate resolution atmospheric transmission radiative transfer model (MODTRAN) (Anderson et al., 1996; Abreu & Anderson, 1996; Berk et al., 1999; 2005; 2009; Spampinato et al., 2011). Additionally, FLIR's ThermaCam Researcher software comes with a calibration appropriate for short-range imagery, which implements a minimum allowed transmittance value of 0.4 for atmospheric corrections.

Additionally, FLIR's ThermaCam Researcher software assumes a single transmittance value for the entire image. However, range variations across oblique long-range images are likely to be greater than in short-range images and, as a result, transmittance values will vary greatly across the image. James et al. (2006) showed that, for a thermal image with horizontal viewing

distances of ~100-400 m, corrections to emissive power were  $\pm 3\%$  compared to those calculated using a uniform viewing distance across the entire image. The work done by James et al. (2006) used short-range ground-based thermal images. Typical horizontal viewing distances and distance differences within an image for long-range ground-based thermal cameras will be significantly greater than those used by James et al. (2006). For example, typical distance variation in thermal images taken with the INGV-Catania fixed ground-based thermal camera, located at Mount Cagliato, range from ~3.0 to 8.7 km.

Another limitation when using the FLIR software is that it only uses a horizontal-path geometry when applying atmospheric corrections. While a horizontal-path may be suitable for short-distance observations, in most monitoring-style deployments the actual viewing geometry of the sensor will be inclined (i.e. a slant-path) (Figure 5.1).

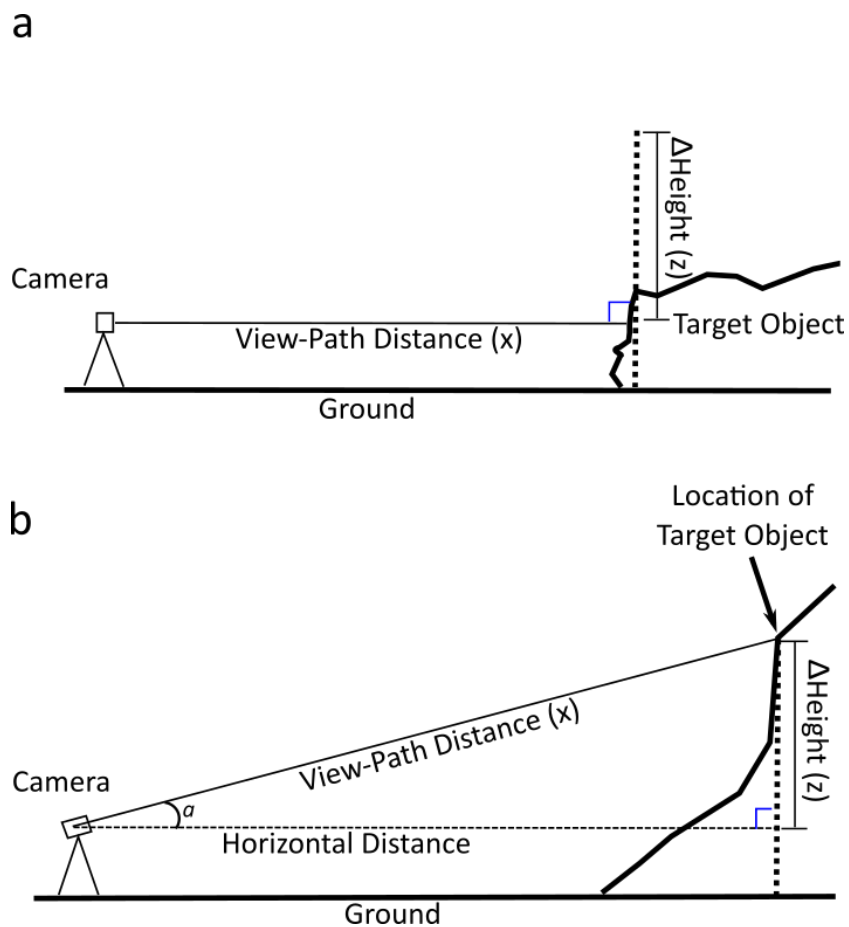


Figure 5.1 – Typical viewing scenarios for ground-based thermal cameras: (a) horizontal view-path and (b) slant view-path, where  $a$  is the viewing angle and  $\Delta\text{Height}$  is the difference in height between the target and the camera.

In MODTRAN, users have the option to select either a horizontal or a slant-path viewing geometry and, to employ slant-path, an atmospheric model is used (or supplied) to describe the atmospheric pressure, temperature and relative humidity for two or more layers of given thickness. This can represent a more realistic scenario for most volcano monitoring setups but requires the number and thickness of the atmospheric layers to be defined (along with their associated properties).

Here, to overcome the common limitations in processing software (e.g. maximum allowed transmittance, horizontal viewing geometries and a single transmissivity value per image), a workflow is explored for correcting and analysing long-range ground-based thermal data on a pixel by pixel basis. This workflow uses average transmittance and upwelling radiance values calculated for the spectral window of the sensor for path-lengths 0.1-10 km by MODTRAN 4.0. First, the sensitivity of the derived temperatures to path characteristics of viewing distance, atmospheric temperature, relative humidity, pressure and viewing angle is assessed.

For this study ground-based time-lapse thermal camera data from the 29 August 2011 fire fountaining episode at Mt. Etna (time-lapse thermal data is provided in the supplied auxiliary content) are used because this event was well documented using ground survey techniques (e.g. Kinematic GPS mapping of lava flows, measurements of flow thickness using laser rangefinders) (Behncke et al., 2014), and also by SEVIRI data (Ganci et al., 2012). Using the proposed workflow with the time-lapse thermal camera data from the 29 August episode, lava flow area, flow volume, mean output rate (*MOR*), and radiant heat flux are estimated and compared to results for each determined using ground survey techniques (Behncke et al., 2014) and from SEVIRI data (Ganci et al., 2012a).

Comparison with SEVIRI-based data is particularly significant as INGV-Catania currently utilize SEVIRI-based estimates for flow area, volume, mean output rate, and radiant heat flux to drive the MAGFLOW lava flow model which is used for flow hazard modelling (e.g. Del Negro et al.,

2008; Ganci et al., 2011; 2012b; 2015). However, while SEVIRI data provide an almost continuous temporal coverage of Mt. Etna (acquisition interval of 15 minutes), they cannot observe activity through cloud cover and suffer from low spatial resolution (~3 km at nadir) which means that the thermal contribution of other concurrent activity (such as fire fountaining or exposed versus covered lava channels) cannot be distinguished within the overall thermal output. This can lead to radiant heat flux estimates representing the total contribution of activity in an area instead of that of a specific flow, which can cause issues when used to drive lava flow models for hazard evaluation.

## 5.2 Workflow for Processing Long-Range Ground-Based Thermal Data

To process ground-based thermal data collected at long-range, an automated workflow implemented in Matlab was constructed which corrects each thermal image for atmospheric and viewing effects, on a pixel-by-pixel basis (Figure 5.2, Appendix 6). This can be accomplished by calculating transmittance and upwelling radiance values over different path lengths and for different atmospheric conditions (Appendix 1) for atmospheric correction using the MODTRAN atmospheric model (e.g. Harris, 2013).

Transmittance and upwelling radiance values for a horizontal- and slant-path viewing geometry were pre-computed using MODTRAN. For a horizontal-path viewing geometry, average atmospheric transmittance,  $\tau_{avg\ trans}$ , and upwelling radiance,  $L_{integrated\ UpRad}$ , values were computed for ranges of  $RH$  and  $T_a$  of 0.0-100 % (in 1.0 % intervals) and 10-35 °C (at 1.0° intervals) respectively, for viewing distances of 0.0 to 10.0 km (in 0.1 km intervals), a target emissivity of 0.98, and at the altitude of the sensor (Appendix 2). The results were then parameterised by fitting equations

$$\tau_{avg\ trans}(T_a, RH) = a_1 e^{a_2 x} + a_3 e^{a_4 x} \quad 5.1$$

and

$$L_{integrated\ UpRad}(T_a, RH) = b_1 e^{b_2 x} + b_3 e^{b_4 x} \quad 5.2$$

where  $x$  is the path-length distance in meters and  $a_{1-4}$  and  $b_{1-4}$  are constants derived for any combination of  $T_a$  and  $RH$  and stored in a look-up table (Appendix 3). Equations 5.1 and 5.2 fitted the MODTRAN results with  $r^2$  values  $>0.99$ .

For the slant-path option in MODTRAN, due to the complexity of the model atmosphere needed (i.e. two or more atmospheric layers), a look-up table of all combinations of  $T_a$  and  $RH$ , equivalent to the one created for the horizontal-path, was not created due to the difficulty in programming and time required to do so. Instead, transmittance and upwelling radiance values were computed on an image-by-image basis, using the specific atmospheric conditions present to create the model atmosphere (Appendix 4).

To determine the appropriate transmissivity and upwelling radiance for any pixel within an image for a horizontal-path, the path-length and atmospheric parameters ( $T_a$  and  $RH$ ) are required. Given  $T_a$  and  $RH$  values appropriate to the time of image acquisition, values of  $a_{1-4}$  and  $b_{1-4}$  are retrieved from the look-up tables. The viewing distance can be derived from a distance map (Appendix 5) calculated by geo-referencing the image to a DEM (James et al., 2006). Using the viewing distance maps with Equations 5.1 and 5.2, maps of transmittance and upwelling radiance for pixels within the target area can be derived.

To correct a thermal image using the transmittance map, the image is first converted from temperature to radiance using the FLIR-supplied equation

$$L_{at-sensor} = \frac{5.57033 \times 10^{-8}}{\pi} T^4 \quad 5.3$$

(which is derived by integrating the Planck equation for the spectral window of the sensor, personal communication, FLIR Support), where  $L_{total}$  is the total at-sensor radiance and  $T$  is temperature in Kelvin. The radiance image is then corrected for transmittance,  $\tau$ , upwelling radiance,  $L_{integrated\ UpRad}$  and emissivity,  $\epsilon$ ,

$$L_{corrected} = \frac{L_{at-sensor} - L_{integrated\ UpRad}}{\epsilon * \tau} \quad 5.4$$

to give  $L_{corrected}$ , the atmospherically corrected radiance, and where transmittance and upwelling radiance values are taken from the appropriate maps. Finally, the image is georectified (James et al., 2006; James et al., 2007) by projecting onto the DEM, and a cosine correction is applied to each pixel to account for the angles between the viewing direction and the DEM normal (Ganci et al., 2013).

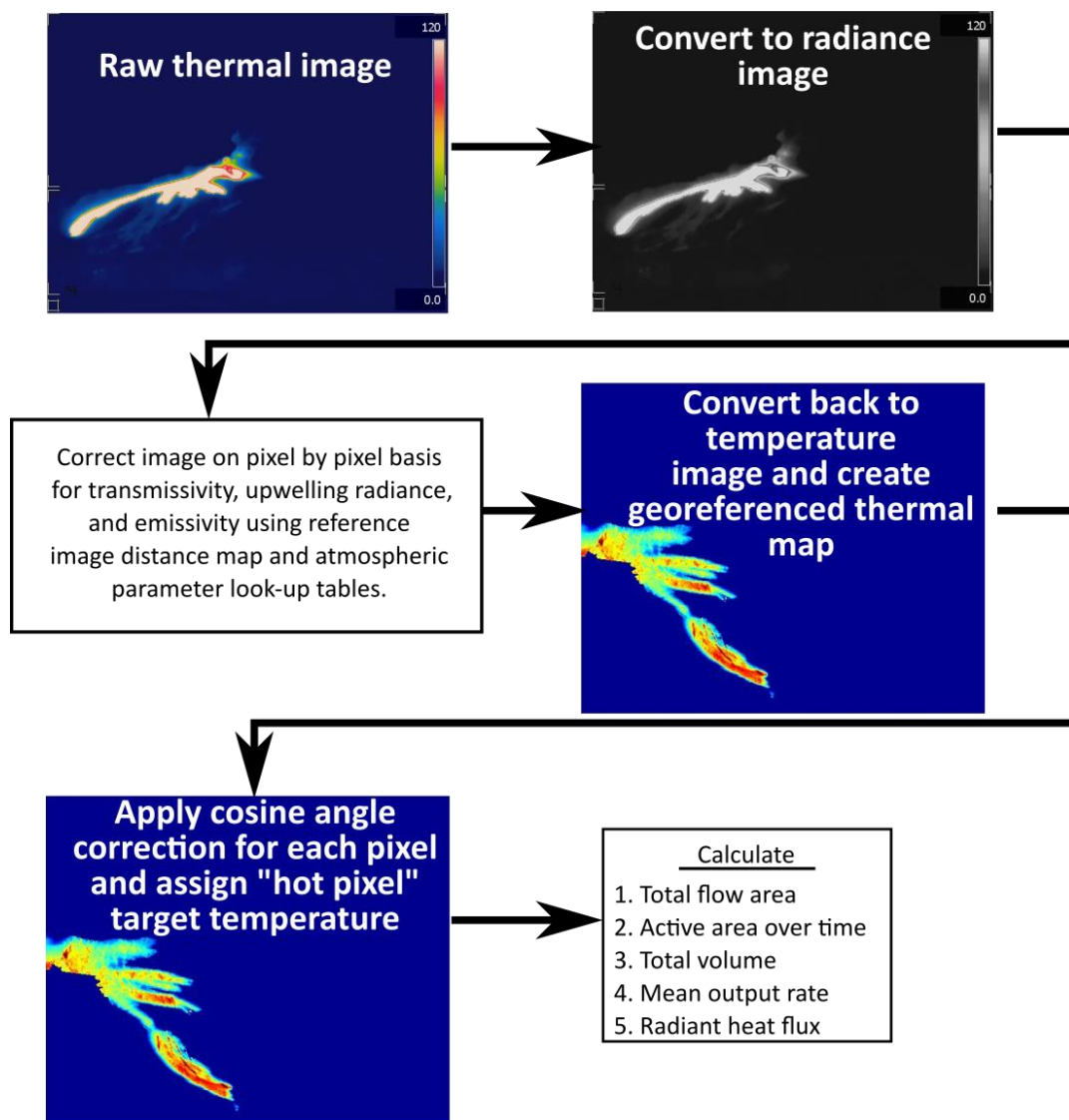


Figure 5.2 – Outline of the processing workflow used in this study to correct long-range ground-based thermal time-lapse data on a pixel-by-pixel basis.

### 5.3 Sensitivity to Atmospheric Conditions

Sensitivity tests were carried out to determine the effect of variations in path-length, atmospheric pressure,  $T_a$  and  $RH$ , and the presence of aerosols on calculated surface temperatures. Three at-sensor apparent temperatures were selected to represent generic low (400 K), medium (500 K) and high (600 K) values. Surface temperatures were calculated using a target emissivity of 0.98 along a horizontal path-length of 0.1-10 km at an altitude of 1.0 km, at atmospheric pressures from 850-1000 mb,  $T_a$  ranging from 15-25 °C, and an  $RH$  of 40-60 %.

The presence and effect of volcanic aerosols on calculating surface temperatures of volcanic domes has previously been studied by Sawyer and Burton (2006). In their study, Sawyer and Burton (2006) found that the presence of volcanic aerosols, particularly  $SO_2$  and  $H_2O$ , underestimated surface temperatures by ~400 K for an actual source temperature of 1200 K. However, these effects should be negligible when observing lava flows, unless the flow is obscured by a volcanic plume, as lava flows quickly lose most of their gas (Burton et al., 2003). However non-volcanic aerosols can provide a non-negligible effect over long path lengths. To assess the impact of non-volcanic aerosols along the path length on the calculation of surface temperatures, we compare results produced using an aerosol-free atmospheric model to those derived when using MODTRAN's 'Rural, Visibility = 23 km' aerosol model.

### 5.4 Case Study: 29 Aug 2011 Event, Mt. Etna

The 29 August 2011 episode was the 12<sup>th</sup> of 25 fire fountaining events which occurred at Mt. Etna between January 2011 and April 2012 (Ganci et al., 2012; Behncke et al., 2014). The episode had a total duration of 28.5 hours, which comprised an initial period of Strombolian style activity, leading into a period of sustained activity which produced a lava flow and sustained fire fountaining (fire fountaining duration of 35 min) (Behncke et al., 2014). For this study, thermal data covering the period of active lava flows and fire fountaining (between

02:00 and 08:00) were used (Figure 5.3). The INGV-Catania fixed ground-based thermal camera is located at Mount Cagliato (507943.99 E 4176495.18 N UTM) at an elevation of 1.154 km (Figure 5.4). The path-length to target for the camera is ~3.0-8.7 km with a target altitude of ~1.9-3 km and a nominal pixel area of 25 m<sup>2</sup> on the ground (Ganci et al., 2013). The DEM used for georeferencing images and to create the distance map was the 2005 DEM from the V3-LAVA project database.

Horizontal and slant path-length viewing geometries were used along with the inclusion of the MODTRAN 'Rural, Visibility = 23 km' aerosol model to calculate transmittance and upwelling radiance values. Values were calculated at 100-m-intervals over a path-length range of 0.0-10.0 km for horizontal-path viewing geometries, and 2.0-10.0 km for slant-path viewing geometries using recorded  $T_a$  and  $RH$  over the spectral window of the sensor (7.5-13  $\mu\text{m}$ ). A path-length distance of 2.0 km was used for the slant-path viewing geometry as this met the geometry requirements (range > height difference) to complete the operation in MODTRAN (Chapter 2, Section 2.4.4).

For the horizontal-path, transmittance and upwelling radiance look-up tables were calculated over ranges of  $RH$  and  $T_a$  of 0.0-100 % (in 1.0 % intervals) and 10-35 °C (at 1.0° intervals) respectively. Hourly recorded meteorological data (taken at the INGV-Palermo meteorological station at Primoti, located ~1 km NE of EMCT) between 02:00 and 08:00 (M. Liuzzo, personal communication, 2012) were used, as this was the nearest meteorological station to the EMCT camera, and interpolated to estimate  $T_a$  and  $RH$  for each image to account for changes in atmospheric temperature and relative humidity throughout the time-lapse sequence (Appendix 7). The  $T_a$  and  $RH$  values for each image in the sequence were then used to select the appropriate lookup table for transmittance and upwelling radiance.

For the slant-path, a 3-layer atmospheric model was created using NECP/NCAR Reanalysis 1 meteorological data (provided by the NOAA/OAR/ESRL PSD, Boulder, Colorado, USA, from

their Web site at <http://www.esrl.noaa.gov/psd/>) which provides averaged values for different elevations at four times per day (00:00, 06:00, 12:00, 18:00) for a 276 km x 276 km area (Appendix 8). From these,

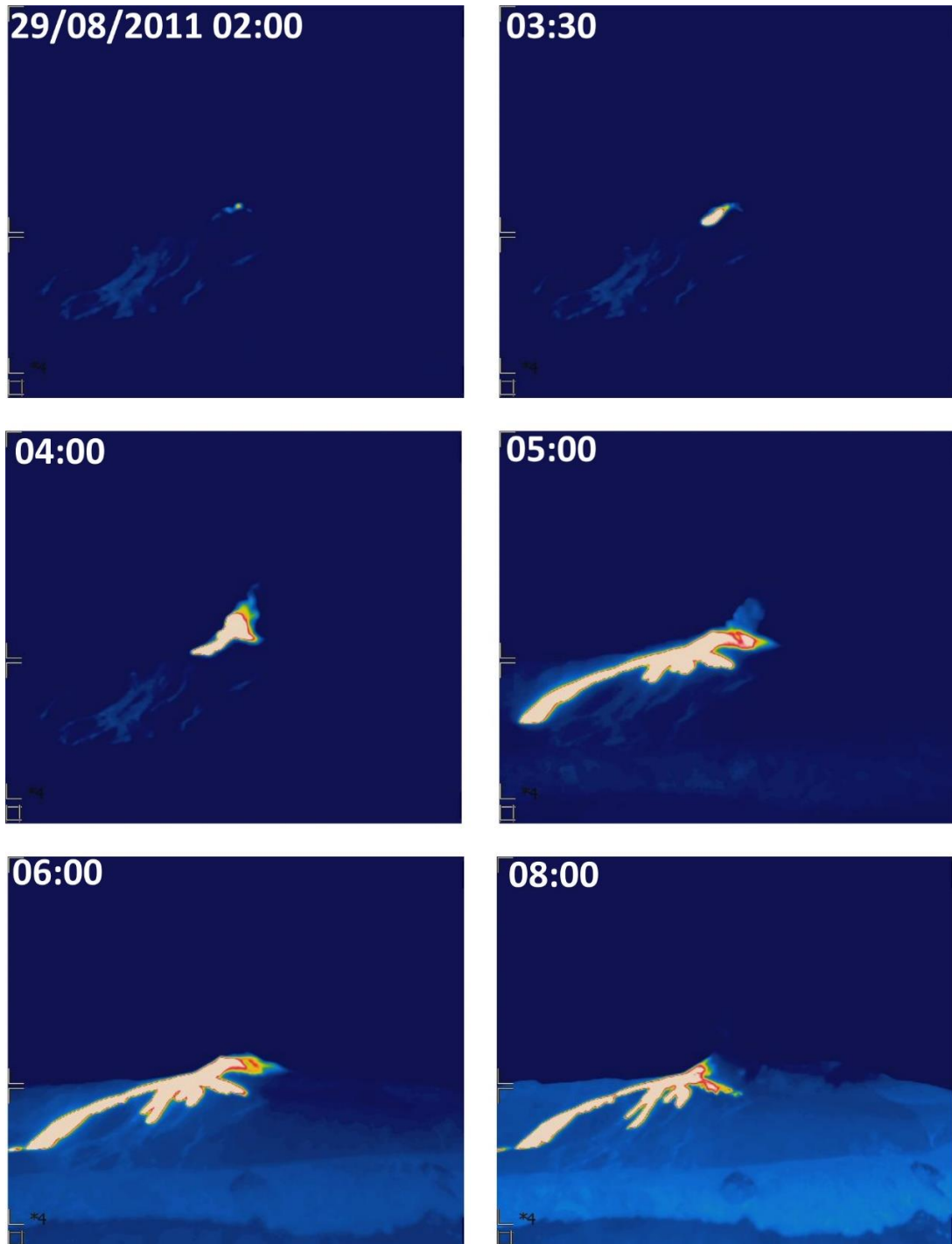


Figure 5.3 – Selection of thermal images from the time-lapse sequence of the 29 August 2011 episode.

$T_a$  and  $RH$  values were interpolated for layer boundary altitudes of 1.154, 2.077 and 3.00 km, at the image acquisition times throughout the time-lapse sequence.

Lower (400 K) and upper (1300 K) temperature bounds were selected to identify the temperature range for target pixels (Harris et al., 2005b), and an emissivity of 0.98 for rough Etnean basalts (Ball & Pinkerton, 2006) was used. Additionally, the “Rural, Visibility = 23 km” aerosol model was also included in the corrections for both viewing geometries. A time series was then produced of total pixels in the target temperature range, and this was used to produce a time series of total radiant heat flux by summing the heat flux values for pixels identified as hot lava (i.e. pixels within the target temperature range).

Using these temperature ranges and emissivity, calculations for total lava flow area, volume, and maximum radiant heat flux were carried out. The total area of the lava flow was calculated by summing all pixels identified within the target temperature range in at least one image. To obtain total flow volume, thickness values of 1 and 2 m were applied uniformly to the calculated total area to determine a minimum and maximum value for volume. These values for thickness were selected based on field observations of lava flows associated with fire fountaining events at Mt. Etna (Harris & Neri, 2002; Calvari et al., 2011; Vicari et al., 2011).

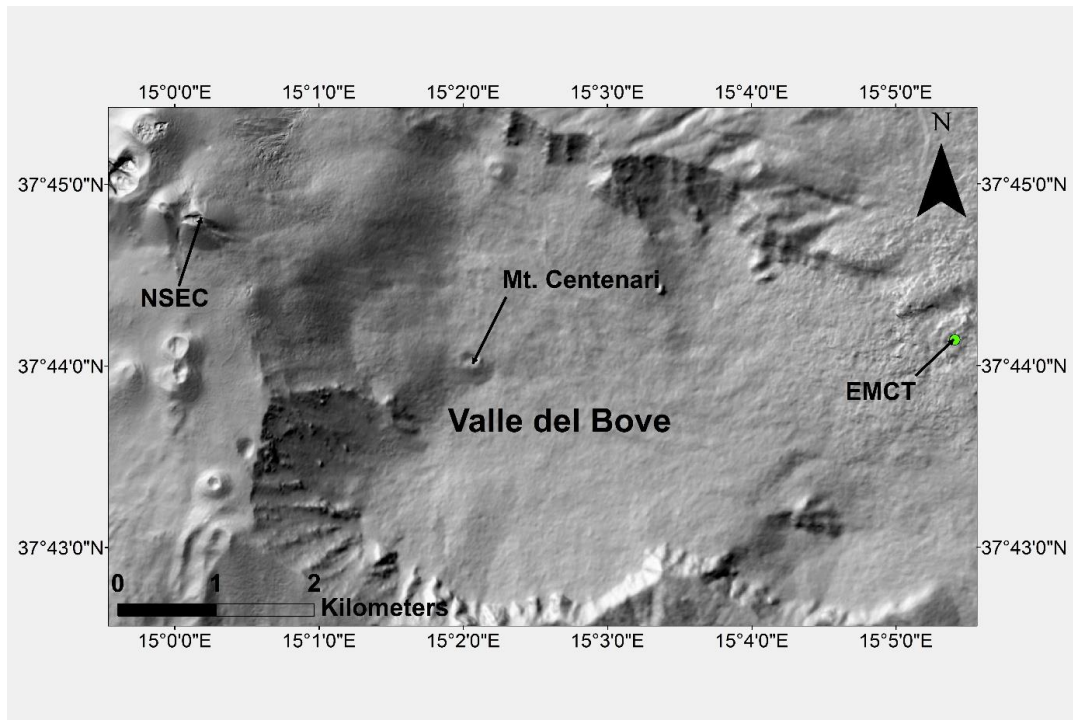


Figure 5.4 – A hill-shaded DEM (2005 DEM from the V3-LAVA project database) of Mt. Etna, showing the location of the INGV-Catania fixed ground-based thermal camera (EMCT) at Mount Cagliato to the east of the Valle del Bove.

## 5.6 Results

### 5.6.1 Sensitivity to Atmospheric Conditions

The simulations demonstrated that, for a horizontal path, changes in  $T_a$  produced greater increases in calculated surface temperature (up to 85 K for an at-sensor temperature of 600 K) than changes in  $RH$  (up to 63 K for an at-sensor temperature of 600 K) (Figure 5.5a). Changes in calculated surface temperatures with atmospheric pressure were negligible (e.g. < 2 K for all tested temperatures, Figure 5.5c). However, inclusion of the aerosol model resulted in increased calculated surface temperatures of up to 94.0 K (for an at-sensor temperature of 600 K, Figure 5.5d).

### 5.6.2 Case Study

For this study, a 3-layer model atmosphere for the slant-path viewing geometry was used because it provided the best option in terms of creation time and computational speed, and because only an insignificant difference in calculated surface temperature was seen when

more complex atmospheric models were used (Appendix 9). For example, Figure 5.6 shows the calculated surface temperature for an apparent temperature of 500 K using a 3, 5, 8, and 15-layer model atmosphere created using the NECP/NCAR Reanalysis 1 meteorological data. The 3, 8, and 15-layer models produced very similar calculated surface temperatures, with a difference of  $\sim 0.71$  K between the 3, 8, and 15-layer models at 10.0 km. However, calculated surface temperatures created using the 5-layer model were significantly lower than those produced by the 3, 8, and 15-layer models. This was due to an error in the setup of the atmospheric conditions for the 5-layer atmosphere model in the MODTRAN LTN run file used to execute the slant-path geometry.

Of the two viewing geometries, the slant-path viewing geometry produced the highest values for total area, volume, mean output rate, and radiant heat flux (Table 5.1). Differences in calculated surface temperatures between the horizontal- and slant-path viewing geometries ranged between 15-22 K at the active margins of the flow and from 21-29 K within the active portions of the body of the flow (Figure 5.7). A comparison of the two viewing geometries showed that the slant-path geometry also returned a greater number of pixels in the target temperature range, i.e.  $> 400$  K and  $< 1300$  K (Figure 5.8).

Additionally, the range of surface temperatures calculated using the workflow and employing both the horizontal- and slant-path viewing geometries (400-1263 K) agree with surface temperature ranges measured by Harris et al. (2005b) using a hand-held thermal camera at ranges of 0-70 m for an active lava channel at Mt. Etna (493-1253 K). However, the average surface temperature recorded by Harris et al. (2005b) was 962 K, while the average surface temperature found using the horizontal- and slant-path viewing geometries was 593 K and 609 K respectively.

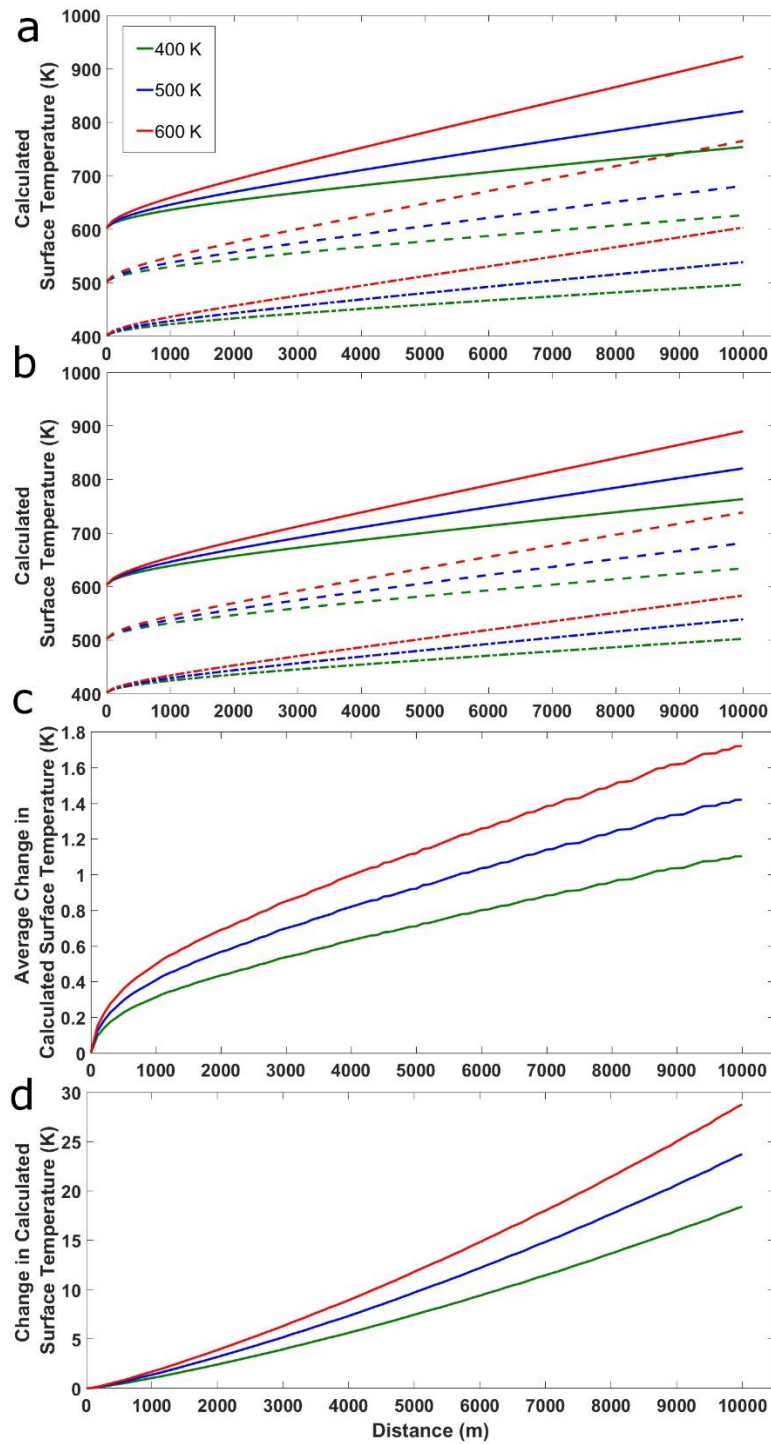


Figure 5.5 – Calculated surface temperatures for apparent temperatures of 400 K, 500 K, and 600 K plotted against viewing distance for (a) atmospheric temperature (5 °C steps from 15-25 °C at 50 % relative humidity), (b) relative humidity (steps of 10 from 40-60 % relative humidity at 20 °C), (c) atmospheric pressure (steps of 50 mb from 1000-800 mb at 20 °C and 50 % relative humidity), and (d) with and without aerosols ('Rural, Visibility = 23 km' aerosol model at 20 °C 50% relative humidity). Dot-dash line = lowest range for atmospheric conditions, dash line = middle range for atmospheric conditions, solid line = highest range for atmospheric conditions.

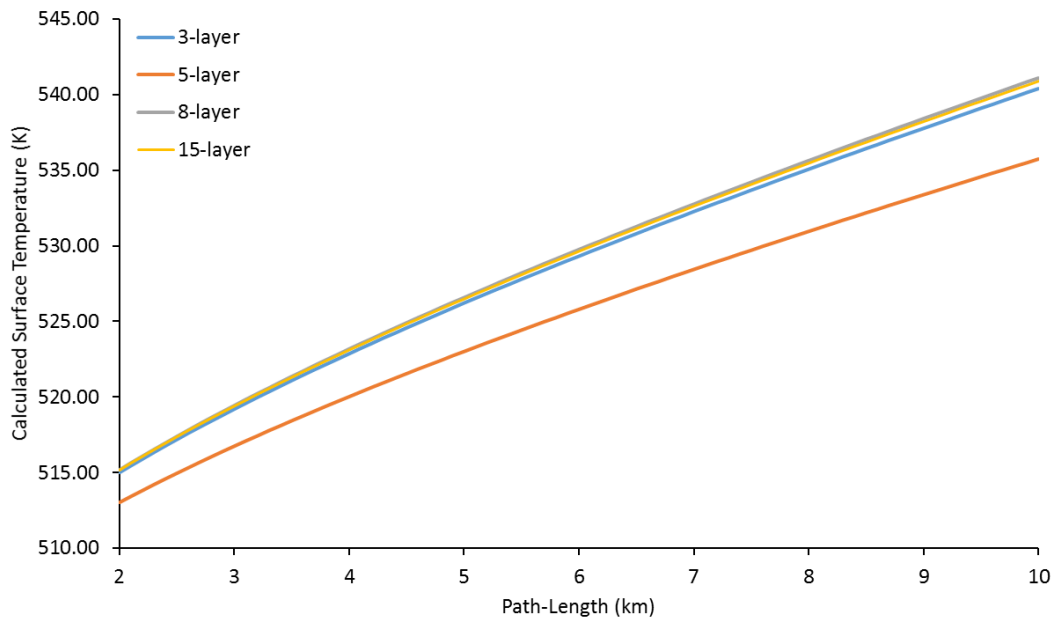


Figure 5.6 – Difference in surface temperatures calculated for an apparent temperature of 500 K for a 3, 5, 8, and 15-layer model atmosphere created using the NCEP/NCAR Reanalysis 1 data and INGV-Catania fix ground-based thermal camera viewing geometry. The 5 and 8-layer models accounted for the minimum and maximum calculated surface temperature of all the models tested. For more information on the models tested and the calculated surface temperatures for each see Appendix 3 & 4.

Table 5.1 – Calculated values for flow area, volume and maximum radiant heat flux for the 29 Aug 2011 fire fountaining episode.

Methodology	Total Detected Pixels	Total Flow Area (km <sup>2</sup> )	Min Volume (10 <sup>6</sup> m <sup>3</sup> )	Max Volume (10 <sup>6</sup> m <sup>3</sup> )	Mean Volume (10 <sup>6</sup> m <sup>3</sup> )	†Min MOR (m <sup>3</sup> s <sup>-1</sup> )	†Max MOR (m <sup>3</sup> s <sup>-1</sup> )	†Mean MOR (m <sup>3</sup> s <sup>-1</sup> )	Maximum Radiant Heat (GW)
Horizontal-Path	31887	0.58	0.58	1.16	0.87	276	552	414	3.4
Slant-Path	34155	0.65	0.65	1.3	0.97	310	619	517	4.2
Behncke et al. (2014)	n/a	0.65	0.7	1.26	0.98	334	600	467	n/a
Ganci et al. (2012a) *	n/a	0.87	n/a	n/a	1.74	114	n/a	n/a	19.9

\*Values calculated using SEVIRI satellite data. †Calculated by dividing the volume by duration (given by Behncke et al. (2014) as 2100 s or 35 min). Ganci et al. (2012a) use a duration determined with the SEVIRI data.

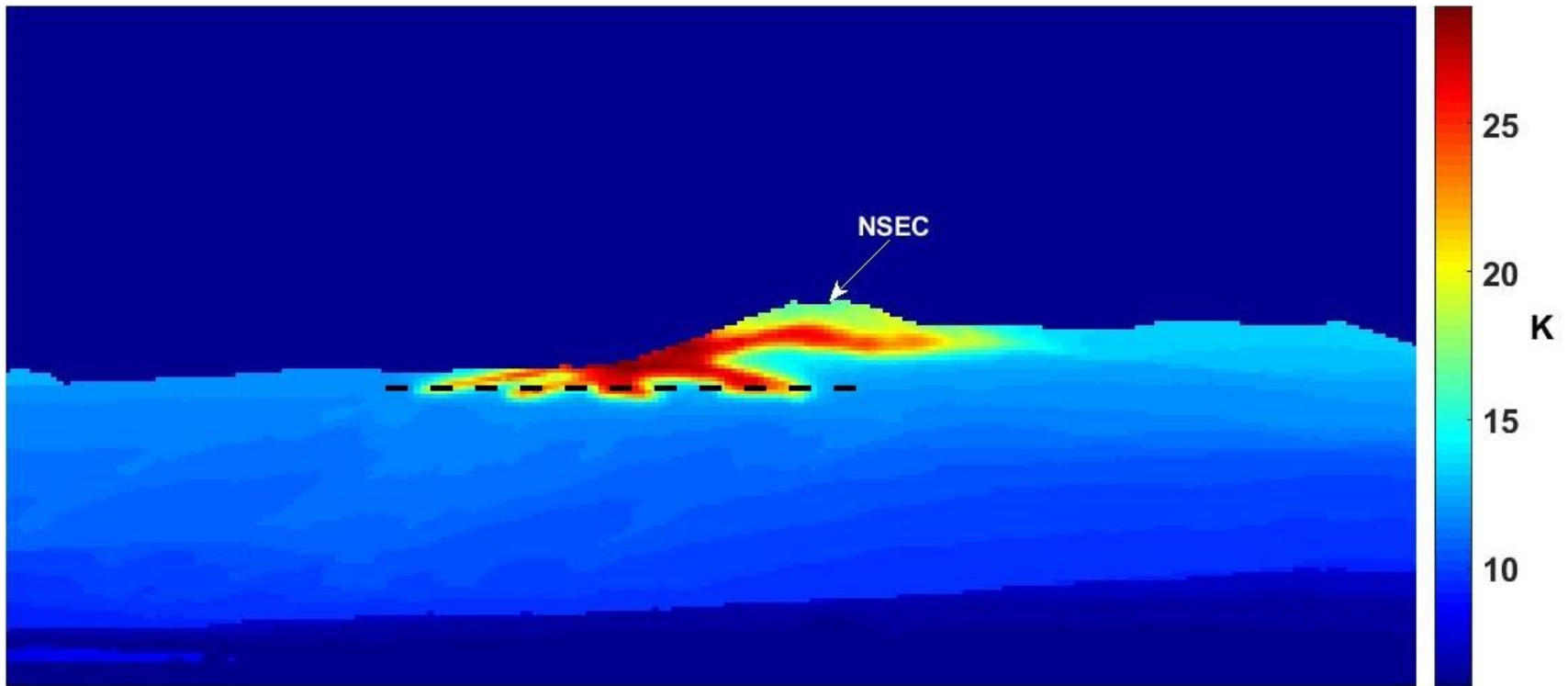


Figure 5.7 – Differences in atmospherically corrected surface temperature between the horizontal and slant-path viewing geometry for the 29/08/2011 lava flow at 04:35. Dashed black line shows the approximate location of start of the Valle del Bove headwall.

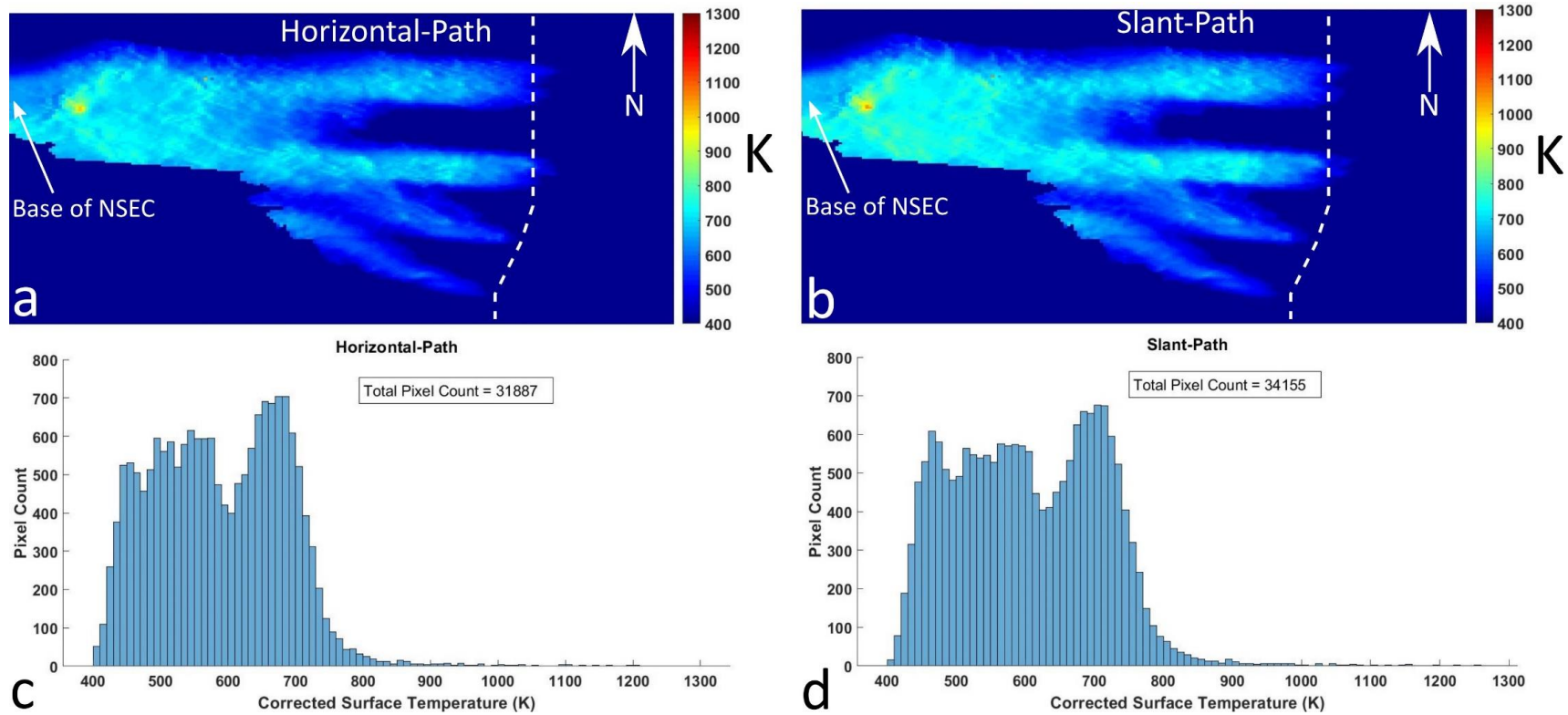


Figure 5.8 – 29 Aug 2011 04:35 corrected and georeferenced temperature map and associated histogram for a target temperature range of 400-1350 K using a horizontal (a & c) and slant-path (b & d) viewing geometry. The thermal image and associated histogram represents the maximum radiant heat flux produced during the duration of the eruption. Dashed white line show approximate location of the start of the Valle del Bove headwall.

## 5.7 Discussion

### 5.7.1 Sensitivity

The inclusion of the 'Rural, Visibility = 23 km' aerosol model when calculating transmittance and upwelling radiance using MODTRAN resulted in a significant increase of calculated surface temperatures with distance. The effect of aerosols when calculating surface temperature observed in this study and by previous studies (e.g. Sawyer & Burton, 2006; Patrick et al., 2014) shows that it is important to account for the presence of aerosols when calculating surface temperatures. When using MODTRAN to compute transmittance and upwelling radiance the user has the option of selecting from a list of included aerosol models or manually creating their own. For most applications, the MODTRAN rural aerosol models (visibility = 5 km and visibility = 25 km) are suggested as these models represent non-industrial/non-urban environments (Kneizys et al., 1996). However, it should be noted that the MODTRAN rural aerosol models provide an approximation of non-volcanic aerosols. If volcanic aerosols are present then they needed to be manual defined, either by direct measurement (Sawyer & Burton, 2006) or using estimates based on typical values for the location, to assure minimal error when calculating surface temperatures.

### 5.7.2 Case Study

Calculated total area, volume, and *MOR* using the horizontal and slant-path methods agreed well with the field-based measurements of Behncke et al. (2014), with the slant-path results producing the closest fit. However, when compared to results derived from SEVIRI data by Ganci et al. (2012a), calculated total area and volume were lower and *MOR* was higher using the ground-based data. The higher *MOR* values for the ground-based data are due to the duration used to divide total volume being shorter (35 min) than that used by Ganci et al. (2012a) for the SEVIRI data (255 min). In terms of overall radiant heat flux trend both the

ground-based and the SEVIRI data produced similar results, with the major peaks in both coinciding at the same times (Figure 5.9).

However, radiant heat flux profiles calculated from the EMCT thermal camera produced a single sharp peak, compared with the two sharp peaks produced from the SEVIRI data by Ganci et al. (2012a). Also, the second peak in the SEVIRI profile represents the maximum radiant heat flux calculated for the event, while the maximum value corresponds with the first peak in the EMCT data. Additionally, radiant heat flux intensity calculated for the SEVIRI data was up to five times greater than that calculated for the ground-based data.

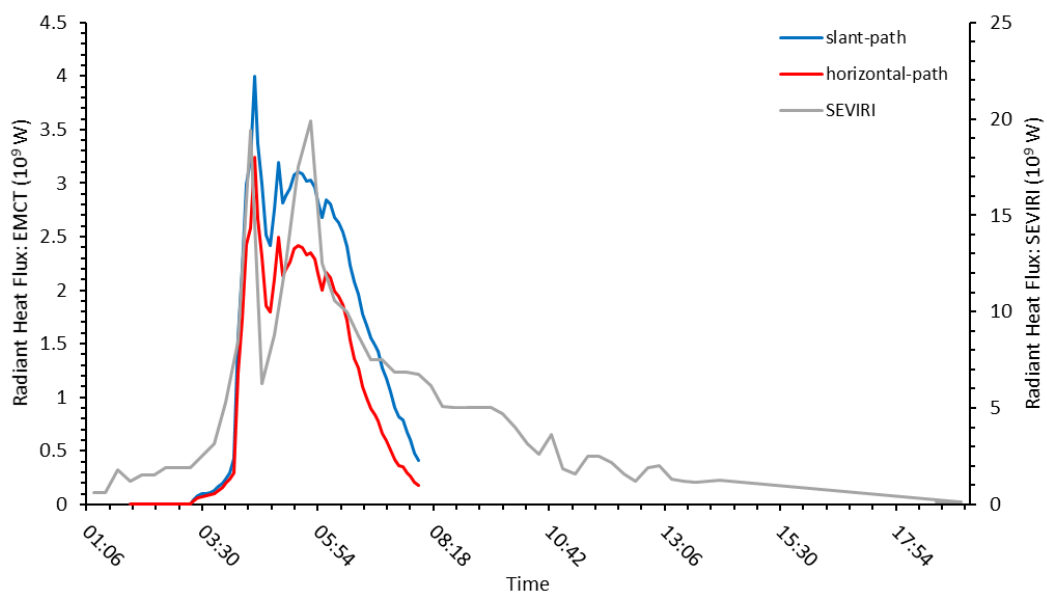


Figure 5.9 – Comparison of radiant heat flux profiles for the 29 Aug 2011 event calculated using the EMCT data with a horizontal and slant-path viewing geometry and SEVIRI data.

These disagreements are likely due to the difference in viewing angle between the ground-based camera and the SEVIRI satellite (Appendix 10). Ball and Pinkerton (2006) examined the effect of viewing angle on measurements taken using a handheld thermal camera for rough lava flows typical of Mt. Etna. They found that as the viewing angle approached 90 degrees from the horizontal (equivalent to the nadir view of SEVIRI satellite), apparent surface temperatures increased. Ball and Pinkerton (2006) attributed this increase in apparent surface

temperature to the camera's increasing ability to detect depressions in the surface of the lava as the viewing angle became closer to 90 degrees.

These depressions, likely caused by fracturing and cracking in the crust of the flow, expose the hotter interior of the flow and thus radiate at greater temperatures than the surrounding, cooler flow surface. As viewing angles become closer to 0° (i.e. more horizontal), less radiance is observed due to the obscuring of these depressions by the roughness of the surface of the lava. While a cosine angle correction was applied to the thermal data to account for the effects of viewing angle, such corrections do not account for a reduction in observed radiance due to obstruction of a radiating body.

The differences in the overall radiant heat flux profiles between the ground-based camera and SEVIRI could also be from obscuration of the lava flow from cloud cover or ash from the fire fountaining. Ganci et al. (2012a) reported that the SEVIRI data for the 29 August 2011 event suffered from obscuration by ash during the fountaining and possibly from cloud cover due to the cloudy conditions during the event.

### 5.7.3 Viewing Geometries

While calculated surface temperature ranges for both the horizontal- and slant-path viewing geometries were similar to short-range (0-70 m) measurements made by Harris et al. (2005b) for an active flow on Mt. Etna, a difference of ~353 K exists between the average surface temperatures calculated here and those measured by Harris et al. (2005b). This difference can be attributed to the effects of pixel resolution (i.e. the surface area covered by each pixel) and how pixel temperature is recorded by the thermal camera. Thermal cameras give a pixel temperature by integrating the temperature across an entire pixel (Ball & Pinkerton, 2006; Harris et al., 2005b; Harris, 2013; Personal communication, FLIR support). As viewing distance increases, the area covered per pixel increases, resulting in temperatures being integrated over a larger area reducing the maximum temperature recorded. At the distance used by

Harris et al. (2005b) the pixel area would be less than a square metre (Harris 2013), while the viewing distances used here (up to 8 km) has a pixel area of 25 m<sup>2</sup>. The difference in average surface temperature of ~353 K seen here is similar to that found by Ball and Pinkerton (2006), who observed a decrease in surface temperature of ~468 K due to changes in pixel resolution for viewing distances > 250 m.

In terms of the viewing geometries, both ground-based camera and satellite-based approaches produced comparable results for flow area and volume to those derived using field-based methods. The values produced by the slant-path geometry were slightly greater than those using a horizontal-path. This difference is due to the slightly higher number of pixels within the target temperature range produced by the slant-path geometry, which resulted from a difference in  $T_a$  and  $RH$  between the NCEP/NCAR Reanalysis 1 data and the Primoti data. After 04:50 values begin to diverge, with  $RH$  values for the interpolated NCEP/NCAR Reanalysis 1 data increasing by as much as 87 % greater than the corresponding Primoti value (Appendix 7). These increases in  $T_a$  and  $RH$  resulted in higher calculated surface temperatures being returned. However, prior to 04:50 the interpolated  $T_a$  and  $RH$  values for the Primoti meteorological data, used for the horizontal-path, and the NCEP/NCAR Reanalysis 1 data, used for the slant-path, were in close agreement.

#### 5.7.4 Limitations and Application

The complexity of the model atmospheres needed for the slant-path geometry does not allow for the creation of look-up tables for transmittance and upwelling radiance using a typical range of atmospheric temperatures and relative humidity for the viewing scene. Without such look-up tables, the correctional values must be calculated on an image by image basis, thus making processing very labour intensive and difficult to automate.

However, while results using the horizontal viewing geometry produced the lowest values for area, volume,  $MOR$ , and radiant heat flux (Table 5.1), employing a horizontal-path viewing

geometry allows a look-up table which covers all possible combinations of atmospheric temperature and relative humidity for an area of interest to be created. This would then allow for the implementation of a fully automated correctional process. In terms of Mt. Etna, results produced using such a process would allow for real-time/near real-time information on lava flow emplacement and could act as a lower bound on lava flow area, volume, and *MOR* to those derived from SEVIRI data. Additionally, using the presented workflow with a horizontal-viewing geometry allows it to be easily modified for use in other locations. To do this, all that is needed is a DEM of the area of interest, a sample image from the camera to be used, generation of appropriate distance maps, and creation of look-up tables for transmissivity and upwelling radiance using Equations 5.1 and 5.2 for  $T_a$  and  $RH$  ranges appropriate for the target location.

## 5.8 Conclusions

The workflow presented here provides a means of processing long-range ground-based thermal data for atmospheric and viewing effects using either a horizontal- or slant-path viewing geometry. From this work the following results were found:

1. Results from the sensitivity test using the workflow agreed with previous studies (e.g. Sawyer, 2002; Calvari & Pinkerton, 2004; Harris 2013) in emphasising the effect of changes in atmospheric temperature and relative humidity on calculated surface temperatures, especially at long viewing distances (1-10 km).
2. Changes in atmospheric pressure had a negligible effect on calculated surface temperatures (< 2 K), while the presences of aerosols resulted in a difference of ~94 K at a viewing distance of 10 km.
3. Comparing the two viewing geometries (horizontal- and slant-path) showed that both produced values for lava flow area, volume, and *MOR* which were similar to values estimated

from ground-based survey techniques, with the slant-path geometry returning values which were in closer agreement.

4. The calculated surface temperature ranges agreed with those measured at short-range by Harris et al. (2005b) for an active lava flow at Mt. Etna. However, a difference of  $\sim 353$  K was seen in the average surface temperature measured here compared to that measured by Harris et al (2005b). This difference is likely due to the larger pixel area ( $25 \text{ m}^2$ ) present in the EMCT camera data used here, resulting in a greater area of temperature integration.

5. SEVIRI-derived values for lava flow area, volume, and radiant heat flux were greater than those produced by either the horizontal- or slant-path viewing geometries. Additionally, the maximum radiant heat flux calculated from the ground-based data was up to five times lower than that derived from SEVIRI data. This suggests that the oblique viewing angle of the ground-based camera may be preventing detection of more radiant areas of the lava flow surface due to obstruction of the radiating surface. However, the overall radiant heat flux profiles produced from the ground-based data was in agreement with the SEVIRI-derived profile.

6. While the slant-path viewing geometry better represents the actual viewing scenario of the INGV-Catania EMCT camera, and produced values for flow area, volume, *MOR*, and radiant heat flux which were in closer agreement to those found by previous ground-based studies, the complexity of the atmospheric model needed to use a slant-path geometry is very time consuming to set up and makes it impossible to automate. However, employing the workflow presented here with a horizontal-viewing geometry would allow for an automated, near real-time estimate of lava flow area, volume, and *MOR* which could be used as a lower bound to satellite-derived values.

## Chapter 6 Discussion and Conclusions

### 6.1 Emplacement of Short-Duration Volume-Limited Lava Flows at Mt. Etna: 2011 and 2012

This thesis has analysed the emplacement of short-duration volume-limited flows at Mt. Etna through long-range ground-based visible time-lapse imagery and statistical analysis (Chapter 3). The results showed strong correlations between flow length and total volume ( $r = 0.74$ ), duration ( $r = 0.63$  and  $0.73$ ), and flow field width ( $r = 0.68$ ) for the 12 short-duration volume-limited Etnean flows studied. Results also identified strong correlations between length and the number of bifurcations within Zone 1 ( $r = 0.83$ ), confluences ( $r = 0.53$ ), average and maximum advance rate within Zone 1 ( $r = -0.55$  and  $-0.66$ ), and duration of fire fountaining ( $r = 0.73$ ) for the 12 examined short-duration volume-limited lava flows.

Previous studies have shown a similarly strong correlation for length and morphology with effusion rate (e.g. Walker 1973; Wadge, 1978, 1979; Rowland & Walker, 1990; Kauahikaua et al. 2003) and volume (Malin, 1980). Lower effusion rates are typically associated with longer durations and narrow flows while higher effusion rates are associated with shorter durations and wider flows (e.g. Walker, 1971; Hulme, 1974; Head & Wilson, 1986; Kilburn & Lopes, 1988; Rowland & Walker, 1990; Kauahikaua et al., 2003; Kerr et al., 2006). Higher effusion rates also produce faster flow advance (Rowland & Walker, 1990; Kauahikaua et al., 2003). However, for a volume-limited flow, the total available supply and duration of supply rather than the effusion rate have the greatest influence on flow length and morphology (e.g. Walker, 1971; Guest et al., 1987; Wilson et al., 1993).

As discussed in Chapter 3 Section 3.5.1, pre-existing topography also affected the emplacement and morphology of the studied flows. If topography within the flow emplacement area is relatively smooth (does not contain any depressions or large linear

ridges) flows can advance unconfined, allowing them to spread laterally and widen until they reach their Bingham fluid dependent width, as described by Hulme (1974). This lack of confinement and allowed flow widening is reflected in the advance and morphology of the Group 2 flows, which advanced through Zone 1 as a broad sheet, continuing to widen until transitioning from Zone 1 to Zone 2. While Group 1 flows initially advanced as one to three discrete flow lobes within Zone 1, they widened after the onset of fire fountaining as they advanced through the remaining area of Zone 1. If the topography contains depressions (defined by pre-existing flow margins) or ridges (such as those formed due to fault scarps or channel levees), they can capture and channelize flows (e.g. Wilson et al., 1987; Wilson et al., 1993; Soule et al., 2004). This capturing and channelizing of flows was evident in both Groups 1 and 2 as flows transitioned from Zone 1 into Zone 2, where they went from being unconfined to semi-channelized in morphology.

Flow confinement results in the concentration of material into a single flow (Wilson et al., 1993; Dietterich & Cashman, 2014) thus increasing the available volume of the flow. For a volume-limited flow this would then mean that the flow has the potential to reach a greater final length due to the increase in available volume (e.g. Walker, 1971; Guest et al., 1987; Wilson et al., 1993). The effect of flow confinement on flow length can be examined for other short-duration volume-limited flows with similar durations, mean output rate, and volumes as the 12 Etna flows studied here. Four such examples are the Episode 40 and 43 of the 1983-1986 Pu'u 'O'o eruptions and the 19 July and 21 December 1974 flows at Kilauea volcano, Hawai'i. Episode 40 and 43 had durations of 14 hours and 12 hours respectively. Additionally, mean output rates for the two Episodes were roughly identical ( $\sim 230 \text{ m}^3 \text{ s}^{-1}$ ) and total flow volumes were  $11.6 \times 10^6 \text{ m}^3$  and  $12.1 \times 10^6 \text{ m}^3$  respectively. However, the Episode 40 lava flow was confined within a topographic depression. As a result, the Episode 40 lava flow attained a length of 8.4 km in 14 hours, while the unconfined Episode 43 lava flow reached a length of 5.3 km in 12 hours (Heliker et al., 2001; 2003).

Similarly, the 19 July 1974 eruption at Kilauea volcano lasted for 3-5 hours with an estimated mean output rate of  $150\text{-}275\text{ m}^3\text{ s}^{-1}$  and produced a flow volume of  $\sim 3.5 \times 10^6\text{ m}^3$  (Soule et al., 2004), and the 21 December 1974 eruption at Kilauea volcano lasted  $\sim 6$  hours, with a mean output rate of  $270\text{ m}^3\text{ s}^{-1}$  and flow volume of  $\sim 5.9 \times 10^6\text{ m}^3$  (Soule et al., 2004). While both the 19 July and 21 December 1974 flows had similar durations, mean output rates, and total volumes, the 21 December 1974 lava flow experienced confinement due to topographic influences and was focused into a single channel for a significant portion of the distance of the lava flow resulting in a final length of 12.1 km compared to a final length of 2 km attained by the 19 July 1974 flow (Soule et al., 2004).

As at Hawaii, confinement of the Etnean primary flows suggests that those confined over a greater distance resulted in a longer final flow length ( $r = 0.63$ ). The effect of confinement on flows can be further examined by comparing flows with similar total volumes, slopes and durations. Episodes 4, 5, and 6 all produced similar final flow lengths (3200, 3000, and 3300 respectively) and were emplaced under similar conditions. Episodes 4 and 6 had total volumes of  $1.05 \times 10^6\text{ m}^3$  and  $1.06 \times 10^6\text{ m}^3$  respectively, while Episode 5 had a total volume of  $1.14 \times 10^6\text{ m}^3$ . Episodes 4 and 6 were emplaced on an average slope of 19 degrees and Episode 5 was emplaced on an average slope of 20 degrees. Episodes 4 and 6 had durations of 1.6 h and 2.5 hours respectively, while Episode 5 had a duration of 1 h. Because of the strong correlation between length and total volume ( $r = 0.74$ ) and duration ( $r = 0.63$ ) it would be expected that Episode 5 would have achieved the longest final length. Additionally, Episode 5 had the least number of bifurcations to the primary flow (four) and had the highest mean output rate ( $316\text{ m}^3\text{ s}^{-1}$ ) compared to Episodes 4 and 6, which had eight and five bifurcations respectively, and mean output rates of  $176\text{ m}^3\text{ s}^{-1}$  and  $118\text{ m}^3\text{ s}^{-1}$  respectively. However, examining the total distance over which the primary flows were confined shows that Episode 6 was confined over a longer distance (1900 m) than Episode 4 (1500 m) and Episode 5 (1200 m), thus suggesting that confinement resulted in the longer final flow length of Episode 6.

Flow confinement has also been directly related to increased advance rates. Field measurements of the 1983-1986 episodes of the Pu'u 'O'o eruption at Kilauea volcano made by Wolf (1988) and Heliker et al. (2001; 2003), and laboratory experiments using both syrup and molten basalt carried out by Dietterich et al. (2015), found that flow advance rate accelerated due to topographic confinement. Higher advance rates due to confinement are reflected by the higher advance rates of the Episode 40 and 21 December 1974 Hawaiian flows over the Episode 42 and 19 July 1974 flow. Likewise, the increase in flow front advance due to confinement was also observed in flow front advance rates estimated for the 12 short-duration volume-limited lava flows analysed in Chapter 3 at Mt. Etna. For 10 of the episodes maximum advance rates increased between 33-85 % from Zone 1 to Zone. In general, results identified that the highest maximum advance rates occurred within Zones 2 ( $0.22\text{-}0.60\text{ m s}^{-1}$ ) and 3 ( $0.12\text{-}0.53\text{ m s}^{-1}$ ) where flows had become captured and confined.

While all four Hawaiian flows were short-duration volume-limited flows and had mean output rates ( $150\text{-}280\text{ m}^3\text{ s}^{-1}$ ) which fall within the range of those estimated for the 12 Etnean flows ( $64\text{-}980\text{ m}^3\text{ s}^{-1}$ ) by Behncke et al. (2014), they differ regarding duration, total volume, and advance rate ( $0.1\text{-}2.2\text{ m s}^{-1}$  compared to  $0.06\text{-}0.42\text{ m s}^{-1}$ ). While all are classified as short-duration flows, the duration of the 12 Etnean flows (0.5-2.5 h) was less than those of the Hawaiian flows (3-14 h). So, while mean output rates were comparable to the range estimated for the 12 Etnean flows, the longer durations of the Hawaiian flows resulted in a greater erupted volume ( $3.5\text{-}21.1 \times 10^6\text{ m}^3$ ) compared to that of the 12 Etnean flows ( $0.38\text{-}1.83 \times 10^6\text{ m}^3$ ). As a result, the Hawaiian flows would have the potential to attain a greater length due to a larger available supply of material (e.g. Walker, 1971; Guest et al., 1987).

Like flow confinement, underlying slope will affect the advance rate of a lava flow, which has the potential to affect flow length. Lava flows emplaced on steep slopes will have a higher advance rate than those on shallower slopes (e.g. Hulme, 1974; Gregg & Fink, 2000). However,

examining the advance rates for the four Hawaiian flows ( $0.1\text{-}2.2\text{ m s}^{-1}$ ) shows that advance rates were of a similar range to the 12 Etnean flows ( $0.06\text{-}0.42\text{ m s}^{-1}$ ), except for the 21 December 1974 flow, which was higher (Table 6.1), despite the higher underlying slopes of the 12 Etnean flows (average of 15-21 degrees) compared to the Hawaiian flows (average of < 5 degrees). One reason for the difference in advance rates could be the number of flow bifurcations caused by flow thinning due to the higher underlying slopes of the 12 Etnean flows. Changes in slope can affect the thickness of a flow with flows emplaced on steeper slopes being thinner than those emplaced on shallower slopes (e.g. Hulme, 1974; Lister, 1992; Kerr, et al., 2006; Gregg & Fink, 2000). As discussed in Chapter 3 Section 3.5.1, reducing the thickness of a lava flow will make it more prone to interaction with topographic features, thus increasing the chance of flow bifurcation which reduces the available volume of the flow, resulting in further flow thinning (e.g. Lockwood et al., 1987; Dietterich and Cashman, 2014; Dietterich et al., 2015). Flow bifurcation also effects flow advance rate, reducing advance rates by as much as ~50 % (Wolfe, 1988; Heliker et al., 2001; Dietterich & Cashman, 2014; Dietterich et al., 2015). The negative correlation between average and maximum advance rate within Zone 1 and bifurcations in Zone 1 ( $r = -0.58$  and  $-0.48$  respectively) indicates that bifurcations in Zone 1 are associated with lower advance rates. Likewise, results also show a strong correlation between flow length and number of bifurcations within Zone 1 ( $r = 0.83$ ).

The 12 Etnean flows and four Hawaiian flows also differ in terms of their eruptive temperature. Typically, lava flows with higher temperatures will be less viscous than flows with lower temperatures (e.g. Shaw, 1969; McBirney & Murase, 1984; Pinkerton & Norton, 1995; Cashman et al., 1999; Chapter 2, section 2.3.1). Typical Hawaiian lava is erupted at temperatures of  $1150\text{-}1170\text{ }^{\circ}\text{C}$  (Cashman & Mangan, 2014) while typical eruptive temperatures for Etnean flows range from  $1065\text{-}1120\text{ }^{\circ}\text{C}$  (e.g. Tanguy & Clocchiatti, 1984; Pinkerton & Norton, 1995; Bailey et al., 2006, Harris et al, 2007b). The higher temperatures of Hawaiian lava flows mean they are less viscous than their Etnean counterparts, giving them

the potential to attain a longer maximum length. Additionally, Lombardo (2016) and Tarquini & Coppola (2018) showed that heat loss of a flow increases with steeper slopes. As the 12 Etnean flows were emplaced on steeper slopes (average of 15-21 degrees) compared to the Hawaiian flows (average slopes of < 5 degrees), suggests that the Etnean flows could have experienced a higher rate of cooling, thus effecting their potential final length.

Using multiple regression analysis to model flow length for the 12 short-duration volume-limited Etnean flows identified that maximum flow width, duration of flow, and maximum advance rate in Zone 1 provided the model (Model 4) with the best combination of explanatory and predictive power ( $R^2 = 0.96$ ,  $R^2_{\text{adj}} = 0.94$ , and  $R^2_{\text{pred}} = 0.92$ ) for the 12 short-duration volume-limited flows examined in this thesis. This model can be compared to the regression model of Calvari and Pinkerton (1998), produced by analysing 17 Etnean lava flows. Their model identified mean discharge rate, duration of flow, and the average ground slope as significant factors influencing final lengths of Etnean lava flows.

Unlike the 12 short-duration volume-limited Etnean flows examined here, the 17 Etnean flows analysed by Calvari and Pinkerton (1998) were cooling-limited flows with longer durations (1-12 days) and lower mean output rates ( $0.2\text{-}60 \text{ m}^3 \text{ s}^{-1}$ ). Since the 12 flows analysed for this study are short-duration and volume-limited in nature, meaning their final lengths should be dictated by the available supply of material and the duration of supply (Walker, 1973; Guest et al., 1987; Wilson et al., 1993), it is reasonable to assume that mean discharge rate would play a less significant role than either duration or total volume when modelling the lengths of this style of flow.

The correlations between length and mean output rate, total volume, and duration of flow support this assumption and the observations of previous studies on volume-limited flows (e.g. Guest et al., 1987; Wilson et al., 1993), as length shows a weak correlation to mean output

rate ( $r = 0.002$ ) but a strong positive correlation to total volume and duration of flow ( $r = 0.73$  and  $0.63$  respectively) for the 12 short-duration volume-limited flows examined here.

Table 6.1 – Emplacement data on 12 Etnean flows and four Hawaiian short-duration volume-limited flows.

Lava Flow	Duration (s)	Mean output rate ( $\text{m}^3 \text{s}^{-1}$ )	Volume ( $10^6 \text{ m}^3$ )	Average Slope (Degrees)	Length (m)	Average Advance Rate ( $\text{m s}^{-1}$ )	Eruption Temperature ( $^{\circ}\text{C}$ )	Study
12 Etnean flows examined in Ch. 3	1800-9000 (0.5-2.5 h)	64-980	0.38-1.83	15-21	2100-3600	0.06-0.42	N/A	Chapter 3, Behncke et al., (2014)
Episode 40, 1983-1986 Pu'u 'O'o eruption, Kilauea	50400 (14 h)	230	11.6	~3	8400	0.17	N/A	Wolfe (1988), Heliker et al., (2001; 2003), Dietterich & Cashman (2014)
Episode 43, 1983-1986 Pu'u 'O'o eruption, Kilauea	43200 (12 h)	280	12.1	~3	5300	0.12	N/A	Wolfe (1988), Heliker et al., (2001; 2003), Dietterich & Cashman (2014)
19 Jul 1974, Kilauea	10800-18000 (3-5 h)	150-275	3.5	< 5	2000	0.1-1.6	1150	Moore & Kachadoria (1980), Soule et al. (2004)
21 Dec 1974, Kilauea	21600 (6 h)	270	5.9	< 5	12400	1.4-2.2	1168	Lockwood et al. (1999), Soule et al. (2004)

## 6.2 Comparison to Long-Duration Cooling-Limited Flows at Mt. Etna

Using FLOWGO to model the primary flows of the 12 May and 19 July episodes provided estimates for emplacement (e.g. effusion rate, total volume, flow velocities) and thermo-rheological (e.g. viscosity) properties which can be compared with other lava flows at Mt. Etna. By comparing flow properties between different lava flows, individual flows can be evaluated to see which flow regime they reflect, i.e. volume-limited or cooling-limited. This information can then inform decisions on selecting appropriate models to estimate flow properties, such as run out lengths.

FLOWGO estimates for channel velocity and effusion rate for both the 12 May ( $1.9\text{--}4.5\text{ m s}^{-1}$  and  $141 \pm 11\text{ m}^3\text{ s}^{-1}$ ) and 19 July ( $1.0\text{--}3.1\text{ m s}^{-1}$  and  $106 \pm 7\text{ m}^3\text{ s}^{-1}$ ) 2011 flows are greater than channel velocities and effusion rates measured during other Etnean eruptions, such as the 1991-1993 eruption ( $0.02\text{--}1.5\text{ m s}^{-1}$  and  $5.8\text{ m}^3\text{ s}^{-1}$ ; Calvari et al., 1994) and the September 2004 eruption ( $\sim 1\text{ m s}^{-1}$  and  $2.2 \pm 0.8\text{ m}^3\text{ s}^{-1}$ ; Global Volcanism Network, 2004; Mazzarini et al., 2005). This difference reflects that the former were short-duration events (1.6 h and 2.5 h respectively) while the latter were long-duration events (33 days and 473 days respectively). Long-duration events typically have lower rates of effusion which produce lower flow velocities (both channel and advance) while short-duration events are associated with higher effusion rates and higher flow velocities (e.g. Walker, 1971; Hulme, 1974; Rowland & Walker, 1990; Kauahikaua et al., 2003; Kerr et al., 2006). At Mt. Etna, long-duration events produce effusion rates of  $0.2\text{--}60\text{ m}^3\text{ s}^{-1}$  (e.g. Guest et al., 1987; Calvari et al., 1994; Calvari & Pinkerton, 1998; Mazzarini et al., 2005; Favalli et al., 2010; Lombardo, 2016). As such, applying a flow length model that has been developed using data, such as effusion rate, from long-duration events to short-duration would not necessarily provide accurate estimates for final flow length. Calvari and Pinkerton (1998) caution the use of applying models to data that is outside

the range of the training data. The results of such an application can be illustrated by applying the model of Calvari and Pinkerton (1998) to the 12 May and 19 July 2011 flows. The model of Calvari and Pinkerton (1998) was developed using data for flows at Mt. Etna which had durations of 24 h to 288 h, average ground slopes between 2 and 20 degrees, and time-averaged effusion rates of 0.2 to 60 m<sup>3</sup> s<sup>-1</sup>. Applying the model gives a final length of 138 m for the 12 May and 137 m for the 19 July 2001 flows, which is considerably lower than the actual lengths for the two flows (3200 m 3300 m respectively). Comparing the ranges of the data used by Calvari and Pinkerton (1998) and the 12 May and 19 July 2011 flows shows that average ground slopes for the 12 May and 19 July 2011 flows (19 degrees respectively) is within the range for slope used in the Calvari and Pinkerton (1998) model. However, effusion rates for the 12 May and 19 July (141 ± 11 m<sup>3</sup> s<sup>-1</sup> and 106 ± 7 m<sup>3</sup> s<sup>-1</sup> respectively) are greater, and durations (1.6 h and 2.5 h respectively) are lower than the ranges of the Calvari and Pinkerton (1998) data, suggesting that effusion rate and duration are the sources of error when using the Calvari and Pinkerton (1998) model with the two short-duration volume-limited flows discussed here. The considerations discussed above are important when using or selecting a model to obtain accurate estimates for potential lava flow runout length as inaccurate estimates can cause issues when performing lava flow hazard assessment.

### 6.3 Long-Range Ground-Based Visible Time-Lapse Data – Monitoring Applications

The time-lapse data collection methods and analysis methodologies used in Chapters 3 and 4 could be employed at other volcanoes as an inexpensive option for capturing and analysing lava flow emplacement. By performing multiple regression analysis from information derived from long-range ground-based visible time-lapse data (Chapter 4), a simple robust model for flow length can be created for other volcanoes. The results in Chapter 4 showed that by using estimated flow widths for the primary channel from time-lapse images and typical rheological

and textural properties for Etnean basalts, reasonable estimates for effusion rate and total volume can be attained from FLOWGO.

Additionally, average flow thicknesses were estimated for the more channel-like 12 May 2011 flow by using FLOWGO to model secondary flows caused by bifurcation of the primary flow unit. While estimated flow thicknesses for the 12 May 2011 flow were within the ranges of field-based estimated thickness (Behncke et al., 2014), no estimates were possible for the unconfined sheet-like 19 July 2011 flow due to the method causing FLOWGO to crash when applied to this flow. This suggests that the use of flow width as a substitute for channel width for unconfined flows, even when using Equation 4.2, is not appropriate and is only usable with flows that have a more channel-like morphology, such as those belonging to Group 1.

Implementation of the techniques presented in Chapter 3 and 4 at other highly active basaltic volcanoes, such as Piton de la Fournaise and Mt. Cameroon, could further our understanding of flow emplacement processes for volume-limited lava flows and also act as rapid, inexpensive methods of estimating flow volume, output rates, and flow thickness. However, certain considerations need to be taken into account, depending on the deployment style and the kind of information required from time-lapse data.

The first consideration is the acquisition interval of the images. While the 15- and 30-minute acquisition intervals used in this research proved adequate for identifying flow fronts and margins and in estimating flow front advance rates and widths, a smaller acquisition interval would be needed to capture and track the development of flow bifurcations and confluences. In terms of the lava flows analysed, bifurcations and confluences developed sufficiently quickly that the 15- and 30-minute image interval would only capture the interaction after it had occurred. By reducing the acquisition interval to 5- or 10-minutes it may be possible to track these features through their development. The ability to accurately locate and identify bifurcations and confluences would improve estimates on the number of such features

present in a flow field. More accurate estimates of the number of bifurcations and confluences could improve the assessment of their effect on flow emplacement following the methods used in Chapter 3.

A shorter acquisition interval would have also provided a better constraint on the calculated advance rates throughout the emplacement. Because of the rapid emplacement of these flows, Zones 1 and 2 were often traversed in < 30 min (one to two image acquisition periods). Using a smaller acquisition interval would increase the number of calculable advance rates throughout the emplacement of the lava flow and could capture variations in advance rate better. By examining flow front advance rates and tracking the development of bifurcations and confluences, interactions between advancing flow fronts and surface topographic features could be better studied. Furthering our understanding of how interactions affect advance rate and volumetric flow rate and how these influence final flow lengths can help to improving lava flow models used to predict potential flow paths and inundation for hazard assessment.

The acquisition interval available will be limited by power and the amount of data storage available for images. Permanent installations, which are telemetered, would be able to make use of small acquisition intervals since this style of installation can transmit images to large-storage-capacity data devices located at observatories or research institutions. However, these permanent-style installations require a sufficient source of power to operate both the sensor and the telemetered signalling device (Harris, 2013; Patrick et al., 2014). Many such installations rely on installed solar panels to provide this power. In locations where there is significant cloud cover through part or all the year, solar panels can struggle to generate the power level needed to keep the instruments operating. Focal length of the lens should also be considered depending on the application of the time-lapse data and the style of installation. Depending on the pixel size of the camera and the viewing distance from the camera to the

target, different focal lengths need to be used. For path lengths similar to those used in this research (~3.5-4.5 km), focal lengths of 28-50 mm provided images with spatial resolutions of approximately 1 m, and allowed for the capture, analysis, and mapping of flow emplacement. The main limitation when using long-range ground-based visible time-lapse data (Chapters 3 and 4) during this research was the inability to distinguish the active lava flow from the background in images which occurred during day-light hours or when cloud cover obscured the lava flow. This loss of visibility made measurements of flow advance rates and observations of emplacement processes difficult, and often resulted in analysis only being possible for part of the emplacement of the lava flows. However, this could be remedied by pairing the time-lapse camera with a thermal camera which could help augment the visible images during daylight and cloudy conditions. Another option could be to replace or pair visible dSLR cameras with infrared (IR) modified dSLR cameras (Figure 6.1). IR-modified dSLR cameras are cameras that have had the IR blocking filter, which sits in front of the cameras sensor, removed and replaced with a filter which only allows IR light through it.



Figure 6.1 – Examples of the same viewing scene taken using a visible and an IR-modified dSLR camera at night (top) and obscured by clouds (bottom).

### 6.3 Long-Range Ground-Based Thermal Data

A similar processing method for correcting long-range ground-based data as that employed in Chapter 5 was presented by Ganci et al. (2013). However, subsequent investigation into the method of Ganci et al., (2013) carried out as part of the research for this thesis identified a bug in FLIR's ThermaCam Researcher which resulted in atmospheric temperature and relative humidity values being held at constant values of 25 °C and 50 %. Examining the effect of this bug on the method of Ganci et al., (2013) showed that it resulted in an over-estimate of calculated surface temperatures and radiant heat. The workflow presented in Chapter 5 avoids this issue by using MODTRAN-calculated transmittance and upwelling radiance values for a range of atmospheric temperatures and relative humidity for path-lengths up to 10 km.

As a result, a reliable, rapid, semi-automated processing workflow for correcting long-range ground-based thermal data was developed using Matlab. Using the workflow, estimated lava flow area, volume, and mean output rate for the case-study examined in Chapter 5 were in good agreement with field-based estimates (Behncke et al., 2014). The workflow presented in Chapter 5 has the potential to correct long-range ground-based thermal data for rapid estimations of lava flow area, volume, and mean output rates in near real-time and can be applied to constrain estimates for these values made using other methods (e.g. satellite-based, ground-survey mapping done with GPS or laser rangefinders). Radiant heat flux estimates made from data corrected using the workflow presented in Chapter 5 showed a disparity between long-range ground-based and satellite-based thermal data, with ground-based results being up to five times lower than satellite-based results. This difference indicates that the oblique viewing angle of the ground-based camera prevented detection of the more radiant areas of the lava flow surface. Until an adequate correction method can be developed to account for this effect, the viewing-angle from a potential installation site needs to be considered based on what type of data is desired. For example, for the EMCT camera used

here, the viewing angle did not have a significant effect on estimations for flow area, volume, or mean output rate. However, if effusion rate estimates are desired using the radiant heat flux, then the effects of the oblique viewing angle need to be considered as they would result in inaccurate results. Flow hazard modelling carried out using unreliable effusion rate values can result in inept planning and hazard assessment.

Another benefit of the workflow is the ease at which it can be adapted to other geographic locations. To do this, all that is needed is a DEM, the location (x and y in UTM coordinates and z in m) of the thermal camera, and a camera model. Once the image has been aligned to the DEM, the path-length from the camera to each DEM cell can be calculated and a distance map of the viewed scene is generated. MODTRAN can then be used to generate lookup tables of transmittance and upwelling radiance for the range of typical atmospheric conditions in the study area for the full range of path-lengths present within images.

However, for best results it is advantageous that the thermal camera is either installed next to or as close as possible to a meteorological sensor, to provide an accurate record of atmospheric temperature and relative humidity. Sensitivity results from Chapter 5 highlighted the effect of increased water vapour content in the air on calculated surface temperatures. The greatest difference in calculated surface temperature occurred when atmospheric temperature was increased while relative humidity was held constant (from 15-25 °C in 5 °C steps at 50 %), producing a difference of 85 K for an apparent temperature of 600 K at 10 km (Chapter 5). When relative humidity was increased while atmospheric temperature was held constant (from 40-60 % in steps of 10 at 20°) a difference of 63 K for an apparent temperature of 600 K at 10 km was determined.

While the workflow presented in Chapter 5 works for imaging lava flows at long-ranges, additional considerations will be needed if the path-length passes through dense volcanic gas plumes (Sawyer and Burton, 2006; Patrick et al., 2014; 2016). In this situation, additional

information about the amounts and types of gas present in the plume will need to be included when running MODTRAN. Additionally, some situations will allow the processing to be simplified. For example, in situations where very short-ranges are used, simple path-length corrections, such as that provided by the ThermaCam Researcher software can be used (Chapter 5). Additionally, FLIR's new Researcher IR software has a built-in calibration tool which allows the user to create custom calibrations, for either short or long ranges, that can be applied to data. If the user has access to MODTRAN and a calibrated blackbody source the tool allows for the input of user-calculated MODTRAN total transmission and path radiance.

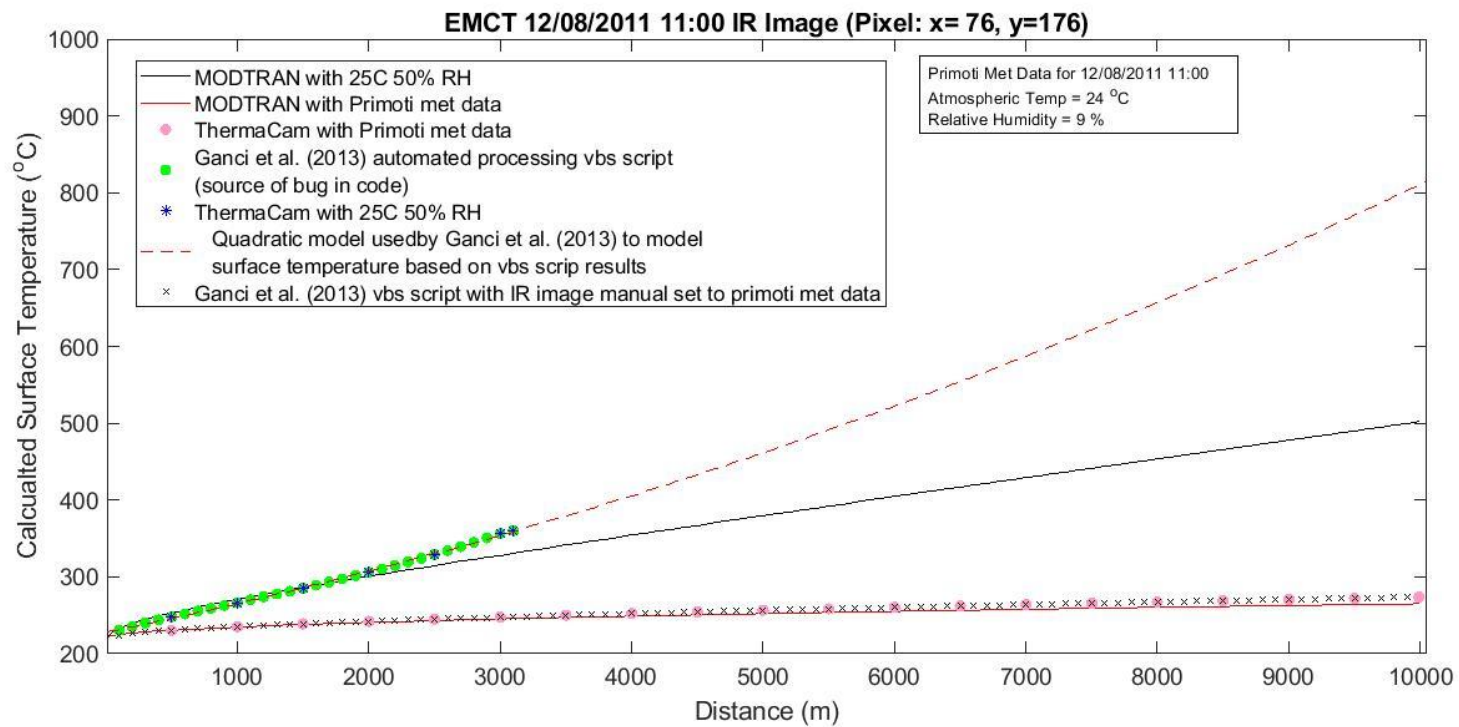


Figure 6.2 – Effect of the bug discovered when using the Ganci et al. (2013) automated processing visual basic (vbs) script with ThermaCam Researcher.

## 6.4 Future Work

While the work carried out in this thesis has provided insights into the emplacement of short-duration volume-limited lava flows, further investigation into how these different factors influence the final length achievable by this style of lava flow are required. As mentioned in section 6.1, surface roughness may have a significant effect on flow length. As such, the development of a reliable and practical measurement of surface roughness as it pertains to linear topographic features such as pre-existing flow levees and drained channels could help improve the determination of flow lengths by lava flow models used for hazard assessment. Additional time-lapse investigations at Mt. Etna and other volcanoes using smaller acquisition intervals to help track changes in flow front advance rate and bifurcations due to interactions with topography could also help to improve flow length modelling. Future time-lapse investigations could also include additional analysis of lava flow emplacement and flow thickness variability, through the use of lava flow models. For this work, FLOWGO was used because of the ease of setup and flexibility of the model; however, to use FLOWGO, a constant value for flow thickness has to be assumed in order to conserve volume. By using FLOWGOW to model new flows created by bifurcations to the parent flow, a better estimate of flow thickness throughout the flow was possible.

Furthermore, these additional investigations could also be used to assess the use of IR-modified dSLR cameras to augment or replace visible dSLR cameras for capturing lava flow emplacement. Preliminary tests of IR-modified dSLR cameras at Mt. Etna during 2008-2009 suggest that a tandem deployment with visible dSLR cameras could greatly improve the tracking of lava flows during daylight hours or when the lava flows are obscured by cloud. However, at night and when high reflective surfaces (such as snow) are present, images from the IR-modified dSLR cameras suffered from significant ghost and halo effects. By deploying both cameras to cover a scene, each can be used to account for the limitations in the other.

The visible dSLR images can be used to track flows at night while the IR-modified images can be used to track the flows during the day or in hazy conditions.

The discrepancy between radiant heat flux calculated using long-range ground-based and satellite-based thermal data also requires further investigation. By comparing per-pixel calculated radiant heat from a sensor looking vertically down at a lava surface to that of a ground-based sensor, it may be possible to develop a correction to apply to ground-based thermal data to account for the radiance lost due to viewing angle. This could be carried out by revisiting the work of Ganci et al. (2013) employing the workflow presented in Chapter 3 or through the use of a drone-based thermal sensor. By correcting long-range ground-based data for this effect, more accurate surface temperatures could be obtained. The improved accuracy of surface temperatures calculated from long-range ground-based thermal data could then be used to help constrain thermal areas for mixed-pixel corrections using satellite-based data.

## 6.5 Conclusions

Understanding how different factors affect the emplacement of lava flows is vital in mitigating the risk posed. While a significant amount of work has been carried out on the emplacement of long-duration cooling-limited lava flows, the short-duration and speed at which many volume-limited flows are emplaced has limited volcanologists' ability to analyse their emplacement. It is the aim of this thesis to improve understanding of how short-duration volume-limited lava flows are emplaced by analysing examples from Mt. Etna during 2011 and 2012. To achieve this aim, the following objectives were addressed:

- (1) Develop a method for remote analytical study of short-duration volume-limited flows using long-range ground-based visible time-lapse data and 2) thermo-rheological modelling.
- (2) Improve the application of long-range ground-based thermal cameras for studying lava flows.

Results from Chapter 3 showed that a strong correlation exists between final flow length and total volume, duration, flow field width, number of bifurcations in the proximal zone of the flow, number of confluences, average and maximum advance rate in the proximal zone, and duration of fire fountaining. However, unlike previous studies, no correlation was found between final length and mean output rate for the 12 short-duration volume-limited flows examined. Results also showed that based on morphology within the proximal zone of the flow (Zone 1), flows could be divided into two groups, (1) those flows which advanced slowly (average of 0.04-0.05 m s<sup>-1</sup>) as one to two flow lobes, and (2) those flows which rapidly advanced (average of 0.12-0.57 m s<sup>-1</sup>) as broad sheets. Additionally, advance rates and flow widths within Zone 1, and the interval between the start of lava emission and onset of fire fountaining, indicated that differences in at-vent initial supply rate dictated the morphology observed for the two groups.

Topographic changes within the flow emplacement area from unconfined flat areas to areas with more confining features resulted in variation in flow morphology from non-channelized to semi-channelized in Zones 2 and 3. Further examination of the effects of flow confinement for three of the 12 flows examined here and at other short-duration volume-limited flows suggests that flow length for the 12 studied Etnean flows is influenced by such confinement or capture. Performing multiple regression analysis on the 12 studied Etnean flows identified maximum flow width, duration of flow, and maximum advance rate in Zone 1 as producing the best flow length model in terms of explanatory and predictive power ( $R^2 = 0.96$ ,  $R^2_{\text{adj}} = 0.94$ , and  $R^2_{\text{pred}} = 0.92$ ) for the 12 examined flows.

Results from Chapter 4 show how using flow widths derived from time-lapse images in place of channel width, in combination with typical rheological and textural properties for Etnean lavas, estimates for effusion rate, flow thickness, and total volume can be made using the FLOWGO thermo-rheological lava model. By modelling only the primary flow for both the 12

May and 19 July 2011 episodes FLOWGO-provided estimates for effusion rate and total volume which agreed with field-based estimates for mean output rate and total volume made by Behncke et al. (2014) using GPS surveys and laser rangefinder measurements.

Additionally, using FLOWGO to model changes in flow thickness due to bifurcations of the primary flows produced average flow thickness estimates for the more channel-like 12 May 2011 flow which were within the range of field-based estimates made by Behncke et al. (2014). However, no thickness estimates were possible using this method for the unconfined 19 July flow, suggesting that substituting flow width for channel width in FLOWGO for unconfined flows is inappropriate. As such, this method should only be applied to flows with a more channel-like morphology.

Chapter 5 discusses the development of a semi-automated workflow for processing long-range ground-based thermal data for atmospheric and viewing effects using two different viewing geometries. Comparing the two viewing geometries (horizontal- and slant-path) showed that both produced values for lava flow area, volume, and mean output rate which were similar to values estimated from ground-based survey techniques. However, of the two, the slant-path geometry returned values which were in closer agreement. Calculated surface temperature ranges agreed with those measured at short-range by Harris et al. (2007) for an active lava flow at Mt. Etna. However, a difference of  $\sim 353$  K was seen in the average surface temperature measured here compared to that measured by Harris et al (2007). This difference is caused by the larger pixel area ( $25 \text{ m}^2$ ) present in the EMCT camera data used here and this resulted in a greater area of temperature integration per pixel.

SEVIRI-derived values for lava flow area, volume, and radiant heat flux were greater than those produced by either the horizontal- or slant-path viewing geometries. Additionally, the maximum radiant heat flux calculated from the ground-based data was up to five times lower than that derived from SEVIRI data. However, the overall radiant heat flux trends produced

from the ground-based data were in agreement with the SEVIRI-derived profile. This difference in power suggests that the oblique viewing angle of the ground-based camera may be preventing detection of more radiant areas of the lava flow surface.

While the slant-path viewing geometry better represents the actual viewing scenario of the INGV-Catania EMCT camera, and produced values for flow area, volume, mean output rate, and radiant heat flux which were in closer agreement to those found by Ganci et al. (2011) and Behncke et al. (2014), the complexity of the atmospheric model needed to use a slant-path geometry is very time consuming to set up and makes it very difficult to automate. However, employing the workflow presented here with a horizontal-viewing geometry would allow for an automated, near real-time estimate of lava flow area, volume, and mean output rate which could be used as a lower bound to satellite-derived values.

The methodologies presented in this thesis have the potential to be applied in situations where conditions in the lava emplacement area limit traditional field-based surveys or at volcanoes where limited monitoring using cameras is in place. Additionally, the low cost and ease with which long-range ground-based visible cameras can be set makes them a viable option for rapid monitoring at volcanoes which may have little to no monitoring systems in place. The methods presented here could also be used in situations which call for rapid deployment and analysis of lava flow activity. Additionally, further development of the thermal data processing workflow could enable volcanologists to perform quantitative studies on other volcanic phenomena using similar long-range ground-based thermal camera deployments and could increase the analytical potential of current permanently installed thermal cameras used by volcano observatories. Long-range ground-based thermal data could be used to help constrain measurements from satellite-based sensors and to create multi-component thermal models for more accurate surface temperature calculations.

Further research into addressing the current limitations (e.g. visibility issues with long-range ground-based visible time-lapse data during daylight hours and in hazy conditions, effect of viewing angle on radiant heat flux calculations for long-range ground-based thermal data) of the methodologies used in this thesis would allow the full potential of these methods to be realised. By improving estimates for radiant heat flux using long-range ground-based thermal cameras, real-time effusion rate estimates can be made. Having access to such information can allow lava flow hazard models, such as HOTSAT (Ganci et al., 2011a), to be run in real time, allowing concurrent mitigation decisions to be made. Additionally, improving the accuracy of estimates for lava flow area, volume, and effusion rate by using long-range ground-based thermal cameras or thermo-rheological models can help in validating values derived from satellite-based sensors or from ground-based surveys (e.g. GPS mapping and laser rangefinder and LiDAR measurements).

Long-range ground-based visible cameras can be employed to capture and analyse lava flow emplacement at low cost at other volcanoes, enabling volcanologists to perform similar visual and statistical analysis of lava flow emplacement. Furthermore, long-range ground-based visible data can be used to perform multiple regression analysis to develop volcano-specific flow length models. These models can provide information as to the significance of different factors that influence flow length for different flow types. As a result, more accurate models for predicting flow lengths for specific flow types can be created, reducing the likelihood of incompatible models being used and resulting in more accurate flow length estimates for flow hazard assessment.

## Works Cited

- Abreu, L. and Anderson, G. (1996) *The MODTRAN 2/3 Report and LOWTRAN 7 Model*, North Andover: Ontar Corporation.
- Acocella, V. and Neri, M. (2003) 'What makes flank eruptions? The 2001 Etna eruption and its possible triggering mechanisms', *Bulletin of Volcanology*, vol. 65, no. doi: 10.1007/s00445-003-0280-3, pp. 517-529.
- Akaike, H. (2011) 'Akaike's Information Criterion', in Lovric, M. (ed.) *International Encyclopaedia of Statistical Science*, Berlin, Heidelberg: Springer.
- Alparone, S., Andronico, D., Lodato, L. and Sgroi, T. (2003) 'Relationship between tremor and volcanic activity during the Southeast Crater eruption on Mount Etna in early 2000', *Journal of Geophysical Research*, vol. 108, no. B5, p. 2241.
- Anderson, G.P., Kneizys, F.X., Chetwynd, J.H., Rothman, L.S., Hoke, M.L., Berk, A., Berstein, L.S., Acharya, P.K., Snell, H.E., Mlawer, E., Clough, S.A., Wang, J., Lee, S., Revercomb, H.E., Yokota, T., Kimball, L.M., Shettle, E.P., Abreu, L.W. and Selby, J. (1996) 'Reviewing atmospheric radiative transfer modelling: new developments in high- and moderate-resolution FASCODE/FASE and MODTRAN', *Optical Spectroscopic Techniques and Instrumentation for Atmospheric and Space Research II*, Denver, 10.1117-12.256105.
- Andronico, D., Branca, S., Calvari, S., Burton, M., Caltabiano, T., Corsaro, R.A., Del Carlo, P., Garfi, G., Lodato, L., Miragila, L., Mure, F., Neri, M., Pecora, E., Pompilio, M., Salerno, G. and Spampinato, L. (2005) 'A multi-disciplinary study of the 2002-03 Etna eruption: insight into a complex pluming system', *Bulletin of Volcanology*, vol. 67, pp. 314-330.
- Applegarth, L., Pinkerton, H., James, M. and Calvari, S. (2010) 'Morphological complexities and hazards during the emplacement of channel-fed 'a'a lava flow fields: A study of the 2001 lower flow field on Etna', *Bulletin of Volcanology*, vol. 72, pp. 641-656.
- Aspinall, J.R., Marcus, W.A. and Boardman, J.M. (2002) 'Considerations in collecting, processing, and analysing high spatial resolution hyperspectral data for environmental investigation', *Journal of Geographical Systems*, vol. 4, pp. 15-29.
- Avolio, M., Crisi, G., Di Gregorio, S., Rongo, R., Spataro, W. and Trunfio, G. (2006) 'SCIARA y2: An improved cellular automata model for lava flows and applications to the 2002 Etnean crisis', *Computers and Geoscience*, vol. 32, pp. 876-889.
- Badalamenti, B., Capasso, G., Carapezza, M.L., D'Alessandro, W., Di Gangi, F. and Diliberto, I. (1994) 'Soil gas investigations during the 1991-1993 Etna eruption', *Acta Vulcanologica*, vol. 4, pp. 135-141.
- Bailey, J., Harris, A., Dehn, J., Calvari, S. and Rowland, S. (2005) 'The changing morphology of an open lava channel on Mt. Etna', *Bulletin of Volcanology*, vol. 68, no. 6, pp. 497-515.
- Bailey, J.E., Harris, A.J.L., Dehn, J., Calvari, S. and Rowland, S.K. (2006) 'The changing morphology of an open lava channel on Mt. Etna', *Bulletin of Volcanology*, vol. 68, pp. 497-515.

- Baldi, P., Coltelli, M., Fabris, M., Marsella, M. and Tommasi, P. (2008) 'High precision photogrammetry for monitoring the evolution of the NW flank of Stromboli volcano during and after the 2002-2003 eruption', *Bulletin of Volcanology*, vol. 70, pp. 703-715.
- Ballestracci, R. and Nougier, J. (1984) 'Detection by infrared thermography and modelling of an icecapped geothermal system in Kerguelen Archipelago', *Journal of Volcanology and Geothermal Research*, vol. 20, pp. 85-100.
- Ball, M. and Pinkerton, H. (2006) 'Factors affecting the accuracy of thermal imaging cameras in volcanology', *Journal of Geophysical Research*, vol. 11, p. B11203.
- Ball, M., Pinkerton, H. and Harris, A. (2008) 'Surface cooling, advection and the development of different surface textures on active lavas on Kilauea, Hawai'i', *Journal of Volcanology and Geothermal Research*, vol. 173, no. 1-2, pp. 148-156.
- Barberi, F., Brondi, F., Carapezza, M., Cavarra, L. and Murgia, C. (2003) 'Earthen barriers to control lava flows in the 2001 eruption of Mt. Etna', *Journal of Volcanology and Geothermal Research*, vol. 123, pp. 231-243.
- Barberi, F., Carapezza, M., Valenza, M. and Villari, L. (1993) 'The control of lava flow during the 1991-1992 eruption of Mt. Etna', *Journal of Volcanology and Geothermal Research*, vol. 56, pp. 1-34.
- Barberi, F., Civetta, L., Rosi, M. and Scandone, R. (2009) 'Chronology of the 2007 eruption of Stromboli and the activity of the Scientific Group', *Journal of Volcanology and Geothermal Research*, vol. 182, no. 3-4, pp. 123-130.
- Behncke, B. *INGV - Sezione di Catania*, [Online], Available: <http://www.ct.ingv.it/en/component/content/article/2-uncategorised/355-the-etnean-observatory-of-the-ingv.html> [12 July 2018].
- Behncke, B., Branca, S., Corsaro, R.A., De Beni, E., Miraglia, L. and Proietti, C. (2014) 'The 2011-2012 summit activity of Mount Etna: Birth, growth and products of the new SE crater', *Journal of Volcanology and Geothermal Research*, vol. 270, pp. 10-21.
- Behncke, B., Neri, M. and Nagay, A. (2005) 'Lava flow hazard at Mount Etna (Italy): new data from a GIS-based study', in Manga, M. and Ventura, G. (ed.) *Kinematics and dynamics of lava flows: Geological Society of America, special paper 396*.
- Behncke, B., Neri, M., Pecora, E. and Zanon, V. (2006) 'The exceptional activity and growth of the Southeast Crater, Mount Etna (Italy), between 1996 and 2011', *Bulletin of Volcanology*, vol. 69, pp. 149-173.
- Berk, A. (1989) *A Moderate Resolution Model for LOWTRAN 7*, Burlington: Spectral Sciences, Inc.
- Berk, A., Acharya, P., Anderson, G. and Gossage, B. (2009) 'Recent development in the MODTRAN atmospheric model and implications for hyperspectral compensation', *Geoscience and Remote Sensing Symposium*, Cape Town, 262-265.
- Berk, A., Anderson, G.P., Acharya, P.K., Bernstein, L.S., Muratov, L., Lee, J., Fox, M., Adler-Golden, S.M., Chetwynd, J.H., Hoke, M.L., Lockwood, R.B., Gardner, J.A., Cooley, T.W., Borel, C.C. and Lewis, P.E. (2005) 'MODTRAN 5: a reformulated atmospheric band model with auxiliary species and practical multiple scattering options: update', *Algorithms and*

Technologies for Multispectral, Hyperspectral, and Ultraspectral Imagery XI, Orlando, 10.1117-12.606026.

Berk, A., Anderson, G.P., Bernstein, L.S., Acharya, P.K., Dothe, H., Matthew, M.W., Adler-Golden, S.M., Chetwynd, H., Richtsmeier, S.C., Pukall, B., Allred, C.L., Jeong, L.S. and Hoke, M.L. (1999) 'MODTRAN4 radiative transfer modelling for atmospheric correction', *Optical Spectroscopic Techniques and Instrumentation for Atmospheric and Space Research III*, Denver, 10.1117-12.366388.

Bianchi, R., Casacchia, R., Coradini, A., Duncan, A., Guest, J., Kahle, A., Lanciano, P., Pieri, D. and Poscolieri, M. (1990) 'Remote sensing of Italian volcanos', *EOS Transactions, American Geophysical Union*, vol. 71, no. 46, pp. 1789-1791.

Bilotta, G., Cappello, A., Herault, A., Vicari, A., Russo, G. and Del Negro, C. (2012) 'Sensitivity analysis of the MAGFLOW Cellular Automaton model for lava flow simulation', *Environmental Modelling and Software*, vol. 35, pp. 122-131.

Bisson, M., Behncke, B., Fornacia, A. and Neri, M. (2009) 'LiDAR-based digital terrain analysis of an area exposed to the risk of lava flow invasion: the Zafferana Etnea territory, Mt. Etna (Italy)', *Natural Hazards*, vol. 50, pp. 321-334.

Blackett, M. (2017) 'An overview of infrared remote sensing of volcanic activity', *Journal of Imaging*, vol. 3, no. 13.

Bluth, G. and Rose, W. (2004) 'Observations of eruptive activity at Santiaguito volcano, Guatemala', *Journal of Volcanology and Geothermal Research*, vol. 136, pp. 297-302.

Bohren, C.F. and Clothiaux, E.E. (2006), in *Fundamentals of Atmospheric Radiation*, Wiley-VCH verlag GmbH & Co. KgaA.

Bonaccorso, A., Bonforte, A., Camvari, S., Del Negro, C., Di Grazia, G., Neri, M., Vicari, A. and Boschi, E. (2011) 'The initial phases of the 2008-2009 Mount Etna eruption: A multidisciplinary approach for hazard assessment', *Journal of Geophysical Research*, vol. 116, pp. DOI: 10.1029/2010JB007906.

Bonaccorso, A., Calvari, S., Linde, A., Sacks, S. and Boschi, E. (2012) 'Dynamics of the shallow plumbing system investigated from borehole strainmeters and cameras during the 12 March 2007 Vulcanian paroxysm at Stromboli volcano', *Earth and Planetary Science Letters*, no. 357-358, pp. 249-256.

Bonneville, A. and Gouze, P. (1992) 'Thermal survey of Mount Etna Volcano from space', *Geophysical Research Letters*, vol. 19, no. 7, pp. 725-728.

Bottinga, Y. and Weill, D.F. (1970) 'Densities of liquid silicate systems calculated from partial molar volumes of oxide components', *American Journal of Science*, vol. 269, pp. 169-182.

Bousquet, J. and Lanzafame, G. (2004) 'The tectonics and geodynamics of Mt. Etna: Synthesis and interpretation of geological and geophysical data', *Washington DC American Geophysical Union Geophysical Monograph Series*, vol. 143, pp. 29-47.

Branca, S., Coltelli, M., Groppelli, G. and Lentini, F. (2011) 'Geological map of Etna volcano, 1:50,000 scale', *Italian Journal of Geoscience*, vol. 130, pp. 265-291.

- Burton, M., Allard, P., Mure, F. and Oppenheimer, C. (2003) 'FTIR remote sensing of fractional magma degassing at Mount Etna, Sicily', *Geological Society, London, Special Publication*, vol. 213, pp. 281-293.
- Burton, M., Neri, M., Andronico, D., Branca, S., Caltabiano, T., Calvari, S., Corsaro, R., Carlo, P., Lanzafame, G., Lodato, L., Miraglia, L., Salerno, G. and Spampinato, L. (2005) 'Etna 2004-2005: An archetype for geodynamically-controlled effusive eruptions', *Geophysical Research Letters*, vol. 32, p. L09303.
- Calvari, S., Bonaccorso, A., Madonia, P., Liuzzo, M., Salerno, G., Behncke, B., Caltabiano, T., Cristaldi, A., Giuffrida, G., La Spina, A., Marotta, E., Ricci, T. and Spampinato, L. (2014) 'Major eruption style changes induced by structural modifications of a shallow conduit system: the 2007-2012 Stromboli case', *Bulliten of Volcanology*, vol. 76, no. 841, pp. 3-15.
- Calvari, S., Coltelli, M., Neri, M., Pompilio, M. and Scribano, V. (1994) 'The 1991-1993 Etna eruption: chronology and lava flow-field evolution', *Acta Vulcanologica*, vol. 4, pp. 1-14.
- Calvari, S. and Pinkerton, H. (1998) 'Formation of lava tubes and extensive flow field during the 1991-1993 eruption of Mount Etna', *Journal of Geophysical Research*, vol. 103, pp. 27291-27301.
- Calvari, S. and Pinkerton, H. (2004) 'Birth, growth and morphologic evolution of the 'Laghetto' cinder cone during the 2001 Etna eruption', *Journal of Volcanology and Geothermal Research*, vol. 132, no. 2-3, pp. 225-239.
- Calvari, S., Spaminato, L., Lodato, L., Harris, A., Patrick, M., Dehn, J., Burton, M. and Andronico, D. (2005) 'Chronology and complex volcanic processes during the 2002-2003 flank eruption at Stromboli volcano (Italy) reconstructed from direct observations and surveys with a handheld thermal camera', *Journal of Geophysical Research*, vol. 110, p. B02201.
- Calvari, S.A.G., Spampinato, L., Gouhier, M., La Spina, A., Pecora, E., Harris, A., Labazuy, P., Biale, E. and Boschi, E. (2011) 'An unloading foam model to constrain Etna's 11-13 January 2011 lava fountaining episode', *Journal of Geophysical Research*, vol. 116, p. B11207.
- Cannata, A., Montalto, E. and Gresta, S. (2009) 'Tracking eruption phenomena by infrasound: May 13, 2008 eruption at Mt. Etna', *Geophysical Research Letters*, vol. 36.
- Carling, G., Radebaugh, J., Saito, T., Lorenz, R., Dangerfield, A., Tingey, D., Keith, J., South, J., Lopes, R. and Diniega, S. (2015) 'Temperatures, thermal structure, and behaviour of eruptions at Kilauea and Erta Ale volcanoes using a consumer digital camcorder', *GeoResJ*, vol. 5, pp. 47-56.
- Cashman, K., Kerr, R. and Griffiths, R. (2006) 'A laboratory model of surface crust formation and distribution on lava flows through non-uniform channels', *Bulletin of Volcanology*, vol. 68, pp. 753-770.
- Cashman, K.V., Mangan, M.T. and Newman, S. (1994) 'Surface degassing and modifications to vesicle size distribution in active basalt flows.', *Journal of Volcanology and Geothermal Research*, vol. 61, pp. 45-68.

- Cashman, K.V., Thornber, C. and Kauahikaua, J.P. (1999) 'Cooling and crystallization of lava in open channels, and the transition of Pahoehoe Lava to 'A'a', *Bulletin of Volcanology*, vol. 61, pp. 306-323.
- Castruccio, A. and Contreras, M.A. (2016) 'The influence of effusion rate and rheology on lava flow dynamics and morphology: A case study from the 1971 and 1988-1990 eruptions at Villarrica and Lonquimay volcanoes, Southern Andes of Chile', *Journal of Volcanology and Geothermal Research*, vol. 327, pp. 469-483.
- Chandler, J. and Brunnsden, D. (1995) 'Steady state behaviour of the black ven mudslide: The application of archival analytical photogrammetry to studies of landform change', *Earth Surface Processes*, vol. 20, pp. 255-275.
- Chen, P.Y. and Popovich, P.M. (2002) *Quantitative Application in the Social Sciences: Correlation*, Thousand Oaks: Sage.
- Coppola, D., James, M.R., Staudacher, T. and Cigolini, C. (2010) 'A comparison of field- and satellite-derived thermal flux at Piton de la Fournaise: implications for the calculation of lava discharge rate', *Bulletin of Volcanology*, vol. 72, no. 341.
- Coppola, D., Staudacher, T. and Cigolini, C. (2005) 'Volume, effusion rates, and emplacement mechanisms inferred from thermal imaging and global positioning systems (GPS) survey', in Manga, M. and Ventura, G. (ed.) *Kinematics and dynamics of lava flows: Geological Society of America Special Paper 396*.
- Coppola, D., Staudacher, T. and Cigolini, C. (2007) 'Field thermal monitoring during the August 2003 eruption at Piton de la Fournaise (La Reunion)', *Journal of Geophysical Research*, vol. 112, no. B05215.
- Corradini, S., Pugnaghi, S., Teggi, S., Buongiorno, M.F. and Bogliolo, M.P. (2003) 'Will ASTER see the Etna SO<sub>2</sub> plume?', *International Journal of Remote Sensing*, vol. 14, no. 6, pp. 1207-1218.
- Corsaro, R.A. and Miraglia, L. (2005) 'Dynamics of 2004-2005 Mt. Etna effusive eruption as inferred from petrologic monitoring', *Geophysical Research Letters*, vol. 32, no. L13302.
- Cosentino, M., Lombardo, G., Paterne, G., Schick, R. and Sharp, A.D.L. (1982) 'Seismological research on Mount Etna: state-of-the-art and recent trends', *Memorie della Societa Geologica Italiana*, vol. 23, pp. 159-202.
- Crisci, G.M., Di Gregorio, S., Nicoletta, F., Rongo, R. and Spataro, W. (1999) 'Analysing Lava Risk for the Etnean Area: Simulations by Cellular Automata Methods', *Natural Hazards*, vol. 20, pp. 215-229.
- Crisci, G.M., Di Gregorio, S., Rongo, R., Scarpello, M., Spataro, W. and Calvari, S. (2003) 'Revisiting the 1669 Etnean eruptive crisis using a cellular automata model and implications for volcanic hazard in the Catania area.', *Journal of Volcanology and Geo thermal Research*, vol. 123, pp. 211-230.
- Crisp, J. and Baloga, S. (1994) 'Influence of crystallization and entrainment of cooler material on the emplacement of basaltic aa lava flows', *Journal of Geophysical Research*, vol. 99, no. 0148-0227.

- Crisp, J., Cashman, K.V., Bonini, J.A., Houghton, S.B. and Pieri, D.C. (1994) 'Crystallization history of the 1984 Mauna Loa lava flow', *Journal of Geophysical Research*, vol. 99, no. B4, pp. 7177-7198.
- Cristofolini, R., Ghisetti, F., Scrope, R. and Vezzani, L. (1985) 'Character of the stress field in the Calabrian Arc and Southern Apennines (Italy) as deduced by geological, seismological and volcanological information', *Tectonophysics*, vol. 117, pp. 39-58.
- Cristofolini, R. and Romano, R. (1982) 'Petrologic features of the etnean volcanic rocks', *Memorie della Societa Geologica Italiana*, vol. 23, pp. 99-115.
- D'Ambrosio, D., Filippone, G., Marocco, D., Rongo, R. and Spataro, W. (2013) 'Efficient application of GPGPU for lava flow hazard mapping', *Journal of Supercomputing*, vol. 65, no. doi: 10.1007/s11227-013-0949-0, pp. 630-644.
- D'Ambrosio, D., Spataro, W., Parise, R., Rongo, R., Filippone, G., Spataro, D., Iovine, G. and Marocco, D. (2014) 'Lava flow modelling by the Sciara-fv3 parallel numerical code'.
- Dana, C.E. (1981) *Characteristics of volcanoes with contributions of facts and principles from the Hawaiian Islands*, New York: Dodd, Mead and Company.
- De Beni, E., Behncke, B., Branca, S., Nicolosi, I., Carluccio, R., Caracciolo, F. and Chiappini, M. (2015) 'The continuing story of Etna's New Southeast Crater (2012-2014): Evolution and volume calculations based on field surveys and aero photogrammetry', *Journal of Volcanology and Geophysical Research*, vol. 303, pp. 175-186.
- Dehn, J., Dean, K.G., Engle, K. and Izbekov, P. (2002) 'Thermal precursors in satellite images of the 1999 eruption of Shishaldin Volcano', *Bulletin of Volcanology*, vol. 64, pp. 525-534.
- Del Negro, C., Cappello, A., Neri, M., Bilotta, G., Herault, A. and Ganci, G. (2013) 'Lava flow hazards at Mount Etna: constraints imposed by eruptive history and numerical simulations', *Scientific Reports*, vol. 3, no. 3493.
- Del Negro, C., Foruna, L., Herault, A. and Vicari, A. (2008) 'Simulations of the 2004 lava flow at Etna volcano using magflow cellular automata model', *Bulletin of Volcanology*, vol. 70, no. doi: 10.1007/s00445-007-0168-8, pp. 805-812.
- Di Grazia, G., Cannata, A., Montalto, P., Patane, D., Privitera, E., Zuccarello, L. and Boschi, E. (2009) 'A multiparameter approach to volcano monitoring based on 4D analyses of seismic-volcanic and acoustic signals: The 2008 Mt. Etna eruption', *Geophysical Research Letters*, vol. 36, no. L18307.
- Dietterich, H.R. and Cashman, K.V. (2014) 'Channel networks within lava flows: Formation, evolution, and implications for flow behaviour', *Journal of Geophysical Research: Earth Surface*, vol. 119, pp. 1704-1724.
- Dietterich, H., Cashman, K., Rust, A. and Lev, E. (2015) 'Diverting lava flows in the lab', *Nature Geoscience*, vol. 8, pp. 494-496.
- Donnadieu, F., Kelfoun, K., van Wyk de Vries, B., Cecchi, E. and Merle, O. (2003) 'Digital photogrammetry as a tool in analogue modelling: applications to volcano instability', *Journal of Volcanology and Geothermal Research*, vol. 123, pp. 161-180.

- Dragoni, M. (1989) 'A dynamical model of lava flows cooling by radiation ', *Bulletin of Volcanology*, vol. 51, pp. 88-95.
- Dutton, C.E. (1883) *Hawaiian volcanoes*, 2005<sup>th</sup> edition, Honolulu: University of Hawaii Press.
- Dzurisin, D., Moran, S.C., Lisowski, M., Schilling, S.P., Anderson, K.R. and Cynthia, W. (2015) 'The 204-2008 dome-building eruption at Mount St. Helens, Washington: epilogue', *Bulletin of Volcanology*, vol. 77, no. 89, pp. 1-17.
- Edner, H., Ragnarson, P., Svanberg, S., Wallinder, E., Derrara, R., Cioni, R., Raco, B. and Taddeucci, G. (1994) 'Total fluxes of sulphur dioxide from the Italian volcanoes Etna, Stromboli, and Vulcano measured by differential absorption lidar and passive differential optical absorption spectroscopy', *Journal of Geophysical Research*, vol. 99.
- Ellis, W. (1825) *A narrative of an 1823 tour through Hawaii with remarks on the history, traditions, manners, customs and language of the inhabitants of the South Sandwich Islands*, 2004<sup>th</sup> edition, Honolulu: Mutual.
- Emerson, O.H. (1926) 'The formation of a'a and pahoehoe', *American Journal of Science*, vol. 5, pp. 109-114.
- Favalli, M.A., Fornaciai, F., Mazzarin, A., Harris, A., Neri, M., Behncke, B., Pareschi, M.T., Tarquini, S. and Boschi, E. (2010) 'Evolution of an active lava flow field using a multitemporal LIDAR acquisition', *Journal of Geophysical Research*, vol. 115, no. B11203.
- Favalli, M., Mazzarini, F., Pareschi, M.T. and Boschi, E. (2009) 'Topographic controls on lava flow paths at Mount Etna, Italy: Implications for hazard assessment', *Journal of Geophysical Research*, vol. 114, pp. 1-13.
- Ferrucci, F., Dogano, C. and Pino, N.A. (1990) 'Approach to the volcanic tremor by covariance analysis: Application to the 1989 eruption of Mt. Etna (Sicily) ', *Geophysical Research Letters*, vol. 17, no. 13, pp. 2425-2428.
- Flyne, L.P. and Mougini-Mark, P.J. (1992) 'Cooling rate of an active Hawaiian lava flow from nighttime spectroradiometer measurements', *Geophysical Research Letters*, vol. 19, no. 17, pp. 1783-1786.
- Flyne, L.P. and Mougini-Mark, P.J. (1994) 'Temperature of an active lava channel from spectral measurements, Kilauea Volcano, Hawaii', *Bulletin of Volcanology*, vol. 56, no. 4, pp. 297-301.
- Flynn, L.P., Wright, R., Garbeil, H., Harris, A.J.L. and Pilger, E. (2002) 'A global thermal alert using MODIS: initial results from 2000-2001', *Advancements in Environmental Monitoring and Modelling*, vol. 1, pp. 37-69.
- Francis, P., Burton, M.R. and Oppenheimer, C. (1998) 'Remote measurements of volcanic gas compositions by solar occultation spectroscopy', *Nature*, vol. 396, pp. 567-570.
- Frazzetta, G. and Romano, R. (1984) 'The 1983 Etna Eruption: Event Chronology and Morphological Evolution of the Lava Flow', *Bulletin of Volcanology*, vol. 2, pp. 1079-1096.
- Fujita, E., Hidaka, M., Goto, A. and Umino, S. (2009) 'Simulations of measures to control lava flows', *Bulletin of Volcanology*, vol. 71, pp. 401-408.

- Fujita, E. and Nagai, M. (2016) 'LavaSIM: its physical basis and applicability', *Geological Society, London Special Publication*, vol. 426, no. doi: 10.1144/SP426.14, pp. 375-386.
- Gabrieli, F., Corain, L. and Vettore, L. (2016) 'A low-cost landslide displacement activity assessment from time-lapse photogrammetry and rainfall data: Application to the Tessina landslide site', vol. 269, pp. 56-74.
- Ganci, G., Harris, A.J.L., Del Negro, C., Guehenneux, Y., Cappello, A., Labazuy, P., Calvari, S. and Gouhier, M. (2012a) 'A year of lava fountaining at Etna: Volumes from SEVRI', *Geophysical Research Letters*, vol. 39, p. L06305.
- Ganci, G., James, M.R., Calvari, S. and Del Negro, C. (2013) 'Separating the thermal fingerprints of lava flows and simultaneous lava fountaining using ground-based thermal camera and SEVRI measurements', *GEOPHYSICAL RESEARCHER LETTERS*, vol. 40, pp. 1-6.
- Ganci, G., Vicari, A., Cappello, A. and Del Negro, C. (2012b) 'An emergent strategy for volcano hazard assessment: From thermal satellite monitoring to lava flow modeling', *Remote Sensing the Environment*, vol. 119, pp. 197-207.
- Ganci, G., Vicari, A., Fortuna, L. and Negro, C.D. (2011) 'The HOTSAT volcano monitoring system based on combined use of SEVRI and MODIS multispectral data', *Annals of Geophysics*, vol. 54, pp. 544-550.
- Garcia, M., Pietruszka, A., Rhodes, J. and Swanson, K. (2000) 'Magmatic Processes During the Prolonged Pu'u' O'o Eruption of Kilauea Volcano, Hawaii', *Journal of Petrology*, vol. 41, pp. 967-990.
- Gemmellaro, C. (1857) *La Vulcanologia dell'Etna: la Topografia, la Geologia, la Storia delle sue Eruzioni, la Descrizione e lo Esame de Fenomeni Vulcanici*, 1989<sup>th</sup> edition, Catania: Atti Accad Gioco 14.
- Ghasemi, A. and Zahediasl, S. (2012) 'Normality Tests for Statistical Analysis: A Guide for Non-Statisticians', *International Journal of Endocrinology & Meabolism*, vol. 10, no. 2, pp. 486-489.
- Giordano, D. and Dingwell, D. (2003) 'Viscosity of hydrous Etna basalts: Implications for Plinian-style basaltic eruptions', *Bulletin of Volcanology*, vol. 65, pp. 8-14.
- Goetz, A.F.H., Boardman, J.W., Kinderland, B. and Heidebrecht, K.B. (1997) 'Atmospheric correction: On deriving surface reflectance from hyperspectral images.', *Proceedings SPIE*, vol. 3118, pp. 14-22.
- Greeley, R. (1976) 'Modes of emplacement of basalt terrains and an analysis of mare volcanism in the Orientale Basin', *Seventh Lunar Science Conference*, vol. 3, pp. 2747-2759.
- Greeley, R. and Iverson, D.J. (1987) 'Measurements of wind friction speeds over lava surfaces and assessment of sediment transport', *Geophysical Research Letters*, vol. 14, pp. 925-928.
- Greenley, R., Wilbur, C. and Storm, D. (1976) 'Frequency distribution of lava tubes and channels on Mauna Loa Volcano, Hawaii', *Geological Society of America Abstracts*, vol. 8, p. 892.
- Gregg, T.K.P. and Fink, J.H. (2000) 'A laboratory investigation into the effects of slope on lava flow morphology', *Journal of Volcanology and Geothermal Research*, vol. 96, pp. 145-159.

- Griffiths, R.W. (2000) 'The Dynamic of Lava Flows', *Annual Review Fluid Mechanics*, vol. 32, pp. 477-518.
- Guest, J.E., Kilburn, C.R.J., Pinkerton, H. and Duncan, A. (1987) 'The evolution of flow fields: observations of the 1981 and 1983 eruptions of Mount Etna, Sicily', *Bulletin of Volcanology*, vol. 49, pp. 527-540.
- Guest, J.E., Underwood, J.R. and Greeley, R. (1980) 'Role of lava tubes in flows from the Observatory Vent, 1971 eruption on Mount Etna', *Geological Magazine*, vol. 117, no. 6, pp. 604-606.
- Hair, J.F., Black, W.C., Babin, B.J. and Anderson, R.E. (2009) *Multivariate data analysis*, Upper Saddle River: Prentice Hall.
- Harris, A. (2013) *Thermal Remote Sensing of Active Volcanoes: A User's Manual*, New York: Cambridge University Press.
- Harris, A. and Allen, J.S. (2008) 'One-, two- and three-phase viscosity treatments for basaltic lava flows', *Journal of Geophysical Research*, vol. 113, pp. doi:10.1029/2007JB005035.
- Harris, A., Bailey, J., Calvari, S. and Dehn, J. (2005b) 'Heat loss measured at a lava channel and its implications for down-channel cooling and rheology', *Geological Society of America Special Publication*, vol. 396, pp. 125-146.
- Harris, A.J.L., Blake, S., Rothery, D.A. and Stevens, N.F. (1997a) 'A chronology of the 1991 to 1993 Etna eruption using advanced very high-resolution radiometer data: implications for real-time thermal volcano monitoring', *Journal of Geophysical Research*, vol. 102, pp. 7985-8003.
- Harris, A.J.L., Dehn, J. and Calvari, S. (2007a) 'Lava effusion rate definition and measurement: a review', *Bulletin of Volcanology*, vol. 70, pp. 1-22.
- Harris, A., Dehn, J., Patrick, M., Calvari, S., Ripepe, M. and Lodato, L. (2005a) 'Lava effusion rates from hand-held thermal infrared imagery: an example from the 2003 effusive activity at Stromboli', *Bulletin of Volcanology*, vol. 68, pp. 107-117.
- Harris, A., Favalli, M., Mazzarini, F. and Pareschi, M. (2007c) 'Best-fit results from application of a thermo-rheological model for channelized lava flow to high spatial resolution morphological data', *Geophysical Research Letters*, vol. 34, no. doi:10.1029/2006GL028126.
- Harris, A.J.L., Keszthelyi, L., Flynn, L.P., Mougini-Mark, P.J., Thornber, C., Kauahikaua, J., Sherrod, D., Trusdell, F., Sawyer, M.W. and Flament, P. (1997b) 'Chronology of the Episode 54 eruption at Kilauea Volcano, Hawaii, from GOES-9 satellite data', *Geophysics Research Letter*, vol. 24, pp. 3281-3284.
- Harris, A.J.L. and Maciejewski, A.J.H. (2000) 'Thermal surveys of the Vulcano Fossa fumarole field 1994-1999: evidence for fumarole migration and sealing', *Journal of Volcanology and Geothermal Research*, vol. 102, pp. 119-147.
- Harris, A.J.L. and Neri, M. (2002) 'Volumetric observations during paroxysmal eruptions at Mount Etna: pressurized drainage of a shallow chamber or pulsed supply?', *Journal of Volcanology and Geothermal Research*, vol. 57, pp. 79-95.

- Harris, A.J.L., Rhety, M., Gurioli, L., Villeneuve, N. and Paris, R. (2015) 'Simulating the thermo-rheological evolution of channel-contained lava: FLOWGO and its implementation in EXCEL', *Geological Society of London*, vol. 426.
- Harris, A. and Rowland, S. (2001) 'FLOWGO: a kinematic thermo-rheological model for lava flowing in a channel', *Bulletin of Volcanology*, vol. 63, pp. 20-44.
- Harris, A.J.L. and Rowland, S.K. (2009) 'Effusion rate controls on lava flow length and the role of heat loss: a review', *Studies in Volcanology: The Legacy of George Walker*, vol. 2, pp. 33-51.
- Harris, A. and Rowland, S. (2015) 'FLOWGO 2012: An updated framework for thermo-rheological simulations of channel-contained lava', in *Hawaiian Volcanoes: From Source to Surface*, 1<sup>st</sup> edition, John Wiley & Sons, Inc.
- Harris, A., Steffke, A., Calvari, S. and Spampinato, L. (2011) 'Thirty years of satellite-derived lava discharge rates at Etna: Implications for steady volumetric output', *Journal of Geophysical research*, vol. 116, p. B08204.
- Head, J.W. and Wilson, L. (1986) 'Volcanic processes and landforms on Venus: theory, predictions, and observations', *Journal of Geophysical Research*, vol. 91, no. B9, pp. 9407-9446.
- Heliker, C.K.J., Sherrod, D.R., Lisowski, M. and Cervelli, P. (2003) 'The rise and fall of Pu'u 'O'o cone 1983-2002', in Heliker, C., Swanson, D.A. and Takahashi, T.J. (ed.) *The Pu'u 'O'o-Kupaianaha eruption of Kilauea Volcano Hawaii: The first 20 years*, U.S. Geological Survey Professional paper 1676.
- Heliker, C., Ulrich, G.E., Margriner, S.C. and Hoffmann, J.P. (2001) *Maps showing the development of the Pu'u 'O'o-Kupaianaha flow fields, June 1984-February 1987, Kilauea Volcano, Hawaii*, Washington, D.C.: United States Geological Survey.
- Herault, A., Vicari, A., Ciaudo, A. and Del Negro, C. (2009) 'Forecasting lava flow hazards during the 2006 Etna eruption: Using the MAGFLOW cellular automata model', *Computers and Geoscience*, vol. 35, pp. 1050-160.
- Herd, R.A., Edmonds, M. and Bass, V.A. (2005) 'Catastrophic lava dome failure at Soufriere Hills Volcano, Montserrat, 12-13 July 2003', *Journal of Volcanology and Geothermal Research*, vol. 148, pp. 234-252.
- Hidaka, M., Goto, A., Umno, S. and Fujita, E. (2005) 'VTFS project: Development of the lava flow simulation code LavaSIM with a model for three-dimensional convection, spreading, and solidification', *Geochemistry, Geophysics, Geosystems*, vol. 6, pp. doi: 10.1029/2004GC000869.
- Hitchcock, C.H. (1909) *Hawaii and its volcanoes*, Honolulu: The Hawaiian Gazette Company.
- Honda, K. and Nagai, M. (2002) 'Real-time volcano activity mapping using ground-based digital imagery', *Journal of Photogrammetry & Remote Sensing*, vol. 57, pp. 159-168.
- Hon, K.A., Gansecki, C. and Kauahikaua, J. (2003) 'The transition from 'a'ā to pāhoehoe crust on flows emplaced during the Pu'u 'O'o-Kupaianaha eruption', in Heliker, C., Swanson, D.A. and Takahashi, T.J. (ed.) *The Pu'u 'O'o-Kupaianaha eruption of Kilauea volcano, Hawai'i: The first 20 years*, U.S. Geological Survey Professional Paper 1676.

- Hon, K., Kauahikaua, J., Denlinger, R. and Mackay, K. (1994) 'Emplacement and inflation of pahoehoe sheet flows: Observations and measurements of active lava flows on Kilauea Volcano, Hawaii', *Geological Society of America Bulletin*, vol. 106, pp. 351-370.
- Hon, K., Kauahikaua, J.P. and Machay, K. (1993) 'Inflation and cooling data from pahoehoe sheet flows on Kilauea volcano', *U.S Geological Survey Professional Paper*, no. 93-342.
- Hoover, S.R., Cashman, K.V. and Manga, M. (2001) 'The yield strength of subliquidus basalts - experimental results', *Journal of Volcanology and Geothermal Research*, vol. 107, pp. 1-18.
- Hulme, G. (1974) 'The Interpretation of Lava Flow Morphology', *Geophys. J. R. astr. Soc.*, vol. 39, pp. 361-383.
- Jagger, T.A. (1930) 'Distinction between pahoehoe and aa or block lava', *Volcano Letters*, vol. 281, pp. 1-3.
- James, M.R., Applegarth, L.J. and Pinkerton, H. (2012) 'Lava channel roofing, overflow, breaches and switching: insights from the 2008-2009 eruption of Mt. Etna', *Bulletin of Volcanology*, vol. 74, pp. 107-117.
- James, M.R., How, P. and Wynn, P.M. (2016) 'Pointcatcher software: analysis of glacial time-lapse photography and integration with multitemporal digital elevation models', *Journal of Glaciology*, vol. 62, no. 231, pp. 159-169.
- James, M.R., Pinkerton, H. and Applegarth, L.J. (2009) 'Detecting the development of active lava flow fields with a very-long-range terrestrial laser scanner and thermal imagery', *Geophysical Research Letters*, vol. 36, p. L22305.
- James, M.R., Pinkerton, H. and Ripepe, M. (2010) 'Imaging short period variations in lava flux', *Bulletin of Volcanology*, vol. 72, pp. 671-676.
- James, M.R., Pinkerton, H. and Robson, S. (2007) 'Image-based measurement of flux variation in distal regions of active lava flows', *Geochemistry, Geophysics, Geosystems*, vol. 8, p. Q03006.
- James, M. and Robson, S. (2012) 'Straightforward reconstruction of 3D surfaces and topography with a camera: Accuracy and geosciences applications', *Journal of Geophysical Research*, vol. 117.
- James, M.R. and Robson, S. (2014) 'Sequential digital elevation models of active lava flows from ground-based stereo time-lapse imagery', *ISPRS Journal of Photogrammetry and Remote Sensing*, vol. 97, pp. 160-170.
- James, M.R., Robson, S., Pinkerton, H. and Ball, M. (2006) 'Oblique photogrammetry with visible and thermal images of active lava flows', *Bulletin of Volcanology*, vol. 69, pp. 105-108.
- James, M. and Varley, N. (2012) 'Identification of structural controls in an active lava dome with high resolution DEMs: Volcan de Colima, Mexico', *Geophysical Research Letters*, vol. 39, pp. 223-303.
- Jolly, G. (2015) 'The role of volcano observatories in risk reduction', in Loughlin, S., Sparks, R., Brown, S., Jenkins, S. and Vye-Brown, C. (ed.) *Global Volcanic Hazards and Risk*, Cambridge: Cambridge University Press.

- Jones, A.E. (1937) 'The formation of basaltic lava flows', *The Journal of Geology*, vol. 45, no. 8, pp. 872-880.
- Jones, A.E. (1943) 'Classification of lava surfaces', *Trans American Geophysics Union*, vol. 1, pp. 265-286.
- Kaneko, K., Munekane, H. and Wooster, M. (2002) 'Monitoring eruption plumes at Usu Volcano (Japan) using thermal infrared camera imagery broadcast via the internet', *Advances in Environmental Monitoring and Modeling*, vol. 1, no. 3, pp. 153-166.
- Kauahikaua, J., Sherrod, D.R., Cashman, K.V., Heliker, C., Hon, K., Mattox, T.N. and Johnson, J.A. (2003) 'Hawaiian lava-flow dynamics during the Pu'u 'O'o-Kupaianaha eruption: a tale of two decades', *U.S. Geological Survey Professional paper*, no. 1676.
- Kendall, M.G. and Gibbons, J.D. (1990) *Rank Correlation Methods*, 5<sup>th</sup> edition, London: Edward Arnold.
- Kendrick, J.E., Lavalley, Y., Ferk, A., Perugini, D., Leonhardt, R. and Dingwell, D.B. (2012) 'Extreme frictional processes in the volcanic conduit of Mount St. Helens (USA) during the 2004–2008 eruption', *Journal of Structural Geology*, vol. 38, pp. 61-76.
- Kereszturi, G., Nemeth, K., Moufti, M., Cappello, A., Murcia, H., Ganci, G., Del Negro, C., Procter, J. and Zahran, H. (2016) 'Emplacement conditions of the 1256 AD Al-Madinah lava flow field in Harrat Rahat, Kingdom of Saudi Arabia - Insights from surface morphology and lava flow simulations', *Journal of Volcanology and Geothermal Research*, vol. 309, pp. 14-30.
- Kerle, N. (2002) 'Volume estimations of the 1998 flank collapse at Casita volcano, Nicaragua: a comparison of photogrammetric and conventional techniques', *Earth Surface Processes and Landforms*, vol. 27, pp. 759-772.
- Kerr, R., Griffiths, R. and Cashman, K. (2006) 'Formation of channelized lava flows on an unconfined slope', *Journal of Geophysical Research*, vol. 111, no. doi:10.1029/2005JB004225, p. B10206.
- Keszthelyi, L. (1995) 'A preliminary thermal budget for lava tubes on the Earth and planets', *Journal of Geophysical Research*, vol. 100, no. B10, pp. 20411-20420.
- Keszthelyi, L., Harris, A.J.L. and Dehn, J. (2003) 'Observations of the effect of wind on the cooling of active lava flows', *Geophysical Research Letters*, vol. 30, no. 19.
- Keszthelyi, L. and Self, S. (1998) 'Some physical requirements for the emplacement of long basaltic lava flows', *Journal of Geophysical Research*, vol. 103, pp. 27,447-27,464.
- Kilburn, C.R.J. (1981) 'PAHOEHOE AND AA-LAVAS - A DISCUSSION AND CONTINUATION OF THE MODEL OF PETERSON AND TILLING', *Journal of Volcanology and Geothermal Research*, vol. 11, no. 2-4, pp. 373-382.
- Kilburn, C.R.J. (1996) 'Patterns and predictability in the emplacement of subaerial flows and flow fields', in Scarpa, R. and Tilling, R.I. (ed.) *Monitoring and mitigation of volcano hazards*, Berlin: Springer.
- Kilburn, C. (2000) 'Lava flows and flow fields', in Sigurdsson, H. (ed.) *Encyclopedia of Volcanoes*, San Diego: Academic Press.

- Kilburn, C.R.J. and Lopens, R.M.C. (1988) 'The growth of aa lava flow fields on Mount Etna, Sicily', *Journal of Geophysical Research*, vol. 93, no. B12, pp. 14759-14772.
- Kneizys, F., Shettle, E., Abreu, L., Chetwynd, J., Anderson, G., Gallery, W., Selby, J. and Clough, S. (1988) *Users Guide to LOWTRAN 7*, Hanscom AFB: Air Force Geophysics Laboratory.
- Kouchi, A., Tsuchiyama, A. and Sunagawa, I. (1986) 'Effects of stirring on crystallization kinetics of basalt: texture and element partitioning', *Contributions to Mineralogy and Petrology*, vol. 93, no. 4, pp. 429-438.
- Kruse, A.F. (1994) 'Imagin Spectrometer Data Analysis - A Tutorial ', *Proceedings of the International Symposium on Spectral Sensing Research*, vol. 1, pp. 44-54.
- Lane, S.N., Chandler, J.H. and Porfiri, K. (2001) 'Monitoring River Channel and Flume Surfaces with Digital Photogrammetry', *Journal of Hydraulic Engineering*, vol. 127, no. 10.
- Lautze, N.C., Harris, A.J.L., Bailey, J.E., Ripepe, M., Calvari, S., Dehn, J., Rowland, S.K. and Evans-Jones, K. (2004) 'Pulsed lava effusion at Mount Etna during 2001', *Journal of Volcanology and geothermal Research*, vol. 137, pp. 231-246.
- Lewis, A., Hilley, G.E. and Lewicki, J.L. (2015) 'Integrated thermal infrared imaging and structure-from-motion photogrammetry to map apparent temperature and radiant hydrothermal heat flux at Mammoth Mountain, CA, USA', *Journal of Volcanology and Geothermal Research*, vol. 303, pp. 16-24.
- Lipman, P.W. and Banks, N.G. (1987) 'Aa flow dynamics, Mauna Loa 1984', *U.S. Geological Survey Professional Paper 1350*, vol. 2.
- Lister, J. (1992) 'Viscous flows down an inclined plane from point and line sources', *Journal of Fluid Mechanics*, vol. 242, no. doi:10.1017/S0022112092002520, pp. 631-653.
- Lockwood, J.P., Dvorak, J.J., English, T.T., Koyanagi, R.Y., Okamura, A.T., Summers, M.L. and Tanigawa, W.R. (1987) 'Mauna Loa 1974–1984: a decade of intrusive and extrusive activity', *U.S. Geological Survey Professional Paper*, vol. 1350, pp. 537-570.
- Lockwood, J.P., Holcomb, R.T., Klein, F., Okamura, A.T. and Peterson, D.W. (1999) 'Magma migration and resupply during the 1974 summit eruptions of Kilauea Volcano, Hawaii', *US Geological Survey Professional Paper*, vol. 1613.
- Lodato, L., Spampinato, L., Harris, A., Calvari, S., Dehn, J. and Patrick, M. (2007) 'The morphology and evolution of the Stromboli 2002-2003 lava flow field: an example of basaltic flow field emplaced on a steep slope', *Bulliten of Volcanology*, vol. 69, pp. 661-679.
- Lombardo, V. (2016) 'Influence of pre-existing topography on downflow lava discharge', *Geophysical Journal International*, vol. 205, pp. 122-133.
- Lyman, A.W., Kerr, R.C. and Griffiths, R.W. (2005) 'Effects of internal rheology and surface cooling on the emplacement of lava flows', *Journal of Geophysical Research*, vol. 110, p. B08207.
- Lyons, J.J., Waite, G.P., Rose, W.I. and Chigna, G. (2010) 'Patterns in open vent, strombolian behavior at Fuego volcano', *Bulliten of Volcanology*, vol. 72, no. 1.
- Macdonald, G.A. (1953) 'Pahoehoe, aa, and block lava', *American Journal of Science*, vol. 251, pp. 169-191.

- Macdonald, G.A. (1972) *Volcanoes*, New Jersey: Prentice Hall.
- Major, J.J., Dzurisin, D., Schilling, S.P. and Poland, M.P. (2009) 'Monitoring lava-dome growth during the 2004-2008 Mount St. Helens, Washington eruption using oblique terrestrial photography', *Earth and Planetary Science Letters*, vol. 286, pp. 243-254.
- Malin, M.C. (1980) 'Lengths of Hawaiian lava flows', *Geology*, vol. 8, pp. 306-308.
- Malinconico Jr., L. (1979) 'Fluctuations in SO<sub>2</sub> emission during recent eruptions of Etna', *Nature*, vol. 278, pp. 43-45.
- March, B.D. (1981) 'On the crystallinity, probability of occurrence, and rheology of lava and magma', *Contributions to Mineralogy and Petrology*, vol. 78, pp. 85-98.
- Massonnet, D., Briole, P. and Arnaud, A. (1995) 'Deflation of Mount Etna monitored by spaceborne radar interferometry', *Nature*, vol. 375, pp. 567-570.
- Mazzarini, F., Pareschi, M.T., Favalli, M., Isola, I., Tarquini, S. and Boschi, E. (2005) 'Morphology of basaltic lava channels during the Mt. Etna September 2004 eruption from airborne laser altimeter data', *Geophysical Research Letters*, vol. 32, pp. DOI: 10.1029/2004GL021815.
- McBirney, A.R. and Murase, T. (1984) 'Rheological properties of magma', *Annual Review Earth Science*, vol. 12, pp. 337-357.
- McGimsey, R.G., Schnieder, D.J., Neal, C.A. and Roach, A.L. (1999) 'Use of FLIR observations during eruptive repose at two Alaskan volcanoes', *Annual American Geophysical Union Meeting*, , vol. V32-07.
- Mercalli, G. (1907) *I Vulcani Attivi della Terra*, Milano: Ulrico Hoepli.
- Metzner, A.B. (1985) 'Rheology of suspensions in polymeric liquids', *Journal of Rheology*, vol. 29, pp. 739-775.
- Moore, H. (1987) 'Preliminary Estimates of the rheological properties of 1984 Mauna Loa Lava', in Decker, R., Wright, T. and Stauffer, P. (ed.) *Volcanism in Hawaii*, Washington, D.C.: United States Government Printing Office.
- Moore, J. and Albee, W. (1980) 'Topographic and structural changes, March-July 1980-photogrammetric data', in Litman, P.W. and Mullineaux, D.R. (ed.) *The 1980 eruptions of Mount St. Helens, Washington, U.S.*
- Moore, H.J. and Kachadoorian, R. (1980) 'Estimates of lava-flow velocities using lava trees', *Reports of Planetary Geology Program 1979-1980: national Aeronautics and Space Administration*, vol. 81776, pp. 201-203.
- Mosteller, F. and Tukey, J.W. (1977) *Data analysis and regression: a second course in statistics*, Reading: Addison-Wesley Publishing Co.
- Moxham, R. (1971) *Thermal Surveillance of Volcanoes*, Paris: Unesco.
- Murray, J.B. (1997) 'Deformation mega-network at Mt Etna Volcano', *Journal of Conference Abstracts*, vol. 2, no. 1, p. 53.
- Murray, J.B. and Guest, J.E. (1982) 'Vertical ground deformation on Mount Etna, 1975-1980', *GSA Bulletin*, vol. 93, no. 11, pp. 160-1175.

- Nahar, A.A. and Mahmud, A. (2015) 'InSAR Observation for the Surface Displacements at Mt. Etna between 2003 and 2007', *International Journal of Geosciences*, vol. 6, pp. 159-171.
- Neri, M., Guglielmino, F. and Rust, D. (2007) 'Flank instability on Mount Etna: Radon, radar interferometry and geodetic data from the southern boundary of the unstable sector', *Journal of Geophysical Research*, vol. 112, no. B04410.
- Nichols, R.L. (1936) 'Flow units in basalt', *Journal of Geology*, vol. 44, pp. 617-630.
- Nichols, R.L. (1939) 'Viscosity of lava', *Journal of Geology*, vol. 47, no. 3, pp. 290-302.
- Nye, C.J., Keith, T.E.C., Eichelberger, J., Miller, T., McNutt, S., Mran, S., Schneider, D., Dehn, J. and Schaefer, J. (2002) 'The 1999 eruption of Shishaldin Volcano, Alaska: monitoring a distant eruption', *Bulliten of Volcanology*, vol. 64, no. 8, pp. 507-519.
- Ohba, T., Hiromitsu, T., Oshima, H., Yoshida, M. and Goto, A. (2002) 'Effect of explosion energy and depth on the nature of explosion cloud A field experimetal study', *Journal of Volcanology nd Geothermal Research*, vol. 115, pp. 33-42.
- Oliverio, M., Spataro, W., D'Ambrosio, D., Rongo, R., Spingola, G. and Trunfio, G. (2011) 'OpneMP parallelization of the SCIARA Cellular Automata lava flow model: peromance analysis on shared-memory computers', *Procedia Computer Science*, vol. 4, no. doi: 10.1016/j.procs.2011.04.029, pp. 271-280.
- Oppenheimer, C. and Yirgu, G. (202) 'Thermal imaging of an active lava lake: Erta 'Ale volcano, Ethiopia', *International Journal of Remote Sensing*, vol. 23, pp. 4777-4782.
- Orr, T., Bleacher, J., Partick, M. and Wooten, K. (2015) 'A sinuous tumulus over an active lava tube at Kilauea Volcano: Evolution, analogs, and hazard forecasts', *Journal of Volcanology and Geothermal Research*, vol. 291, pp. 35-48.
- Orr, T.R. and Rea, J.C. (2012) 'Time-lapse camera observations of gas piston activity at Pu'u'O'o, Kilauea volcano, Hawai'i', *Bulletin of Volcanology*, vol. 74, no. 10, pp. 2353-2362.
- Palacci, M. and Papale, P. (1999) 'The Development of Compound Lava Fields at Mount Etna', *Physics and Chemistry of the Earth*, vol. 24, pp. 949-952.
- Patrick, M.R. (2007) 'Strombolian explosive styles and source conditions: Insights from thermal (FLIR) video', *Bulliten of Volcanology*, vol. 69, pp. 769-784.
- Patrick, M., Orr, T., Antolik, L., Lee, L. and Kamibayashi, K. (2014) 'Continuous monitoring of Hawaiin volcanoes with thermal cameras', *Journal of Applied Volcanology*, vol. 3:1.
- Patrick, M.R., Swanson, D. and Orr, T. (2016) 'Automated tracking of lava lake level using thermal images at Kilauea Volcano, Hawai'i', *Journal of Applied Volcanology*, vol. 5, no. 6.
- Pavez, A., Remy, D., Bonvalot, S., Diamet, M., Gabalda, G., Froger, J.-L., Julien, P., Legrand, D. and Mosset, D.. (2006) 'Insight into ground deformations at Lascar volcano (Chile) from SAR interferometry, photogrammetry and GPS data: Implications on volcano dynamics and future space monitoring', *Remote Sensing of the Environment*, vol. 100, pp. 307-320.
- Peck, D.L. (1978) 'Cooling and vesiculation of Alae lava lake, Hawaii', *US Geologic Survey Professional Paper*, vol. 935, pp. B:1-59.

- Peterson, D.W. and Tilling, R.I. (1980) 'Transition of basaltic lava from pahoehoe to aa, Kilauea Volcano, Hawaii: Field observations and key factors', *Journal of Volcanology and Geothermal Research*, vol. 7, no. 3-4, pp. 271-293.
- Pieri, D.C. and Baloga, S.M. (1986) 'Eruption rate, area, and length relationships for some Hawaiian lava flows', *Journal of Volcanology and Geothermal Research*, vol. 30, pp. 29-45.
- Pinkerton, H., James, M. and Jones, A. (2002) 'Surface Temperature Measurements of Active Lava Flows on Kilauea Volcano, Hawaii', *Journal of Volcanology and Geothermal Research*, vol. 113, pp. 159-176.
- Pinkerton, H. and Norton, G.E. (1995) 'Rheological properties of basaltic lavas at sub-liquidus temperatures: laboratory and field-measurements on lavas from Mount Etna', *Journal of Volcanology and Geothermal Research*, vol. 68, no. 4, pp. 307-323.
- Pinkerton, H. and Sparks, R.S.J. (1978) 'Field measurements of the rheology of lava', *Nature*, vol. 276, pp. 383-385.
- Pinkerton, H. and Stevenson, R. (1992) 'Methods of determining the rheological properties of magmas at sub-liquidus temperatures', *Journal of Volcanology and Geothermal Research*, vol. 53, pp. 47-66.
- Pinkerton, H. and Wilson, L. (1994) 'Factors controlling the lengths of channel-fed lava flows', *Bulletin of Volcanology*, vol. 56, pp. 108-120.
- Poland, M.P., Dzurisin, D., LaHusen, R.G., Major, J.J., Lapcewich, D., Endo, E.T., Gooding, D.J., Schilling, S.P. and Janda, C.G. (2008) 'Remote camera observations of lava dome growth at Mount St. Helens, Washington, October 2004 to February 2006', in Serrod, D.R., Scott, W.E. and Stauffer, P.H. (ed.) *A volcano rekindled: the renewed eruption of Mount St. Helens, Washington, October 2004 to February 2006*, U.S. Geological Survey.
- Power, J.A., Nye, C.J., Coombs, M.L., Wessels, R.L., Cervelli, P.F., Dehn, J., Wallace, K.L., Freymueller, J.T. and Doukas, M.P. (2006) 'The reawakening of Alaska's Augustine volcano', *EOS*, vol. 87, no. 37, pp. 373-377.
- Proietti, C., Coltelli, M., Marsella, M. and Fujita, E. (2009) 'A quantitative approach for evaluating lava flow simulation reliability: LavaSIM code applied to the 2001 Etna eruption', *Geochemistry, Geophysics, Geosystems*, vol. 10, pp. doi: 10.1029/2009GC002426.
- Pugnaghi, S., Gangale, G., Corradini, S. and Buongiorno, M.F. (2006) 'Mt. Etna sulfur dioxide flux monitoring using ASTER-TIR data and atmospheric observations', *Journal of Volcanology and Geothermal Research*, vol. 152, no. 1-2, pp. 74-90.
- Ramsey, M.S. and Harris, A.J.L. (2012) 'Volcanology 2020: How will thermal remote sensing of volcanic surface activity evolve over the next decade?', *Journal of Volcanology and Geothermal Research*, vol. 249, pp. 217-233.
- Rees, W.G. (2001) *Physical Principles of Remote Sensing*, 2<sup>nd</sup> edition, Cambridge: Cambridge University Press.
- Riker, J., Cashman, K., Kauahikaua, J. and Montierth, C. (2009) 'The length of channelized lava flows: Insight from the 1859 eruption of Mauna Loa Volcano, Hawaii', *Journal of Volcanology and Geothermal Research*, vol. 183, pp. 139-156.

- Ripepe, M., Delle Donne, D., Lacanna, G., Marchetti, E. and Ulivieri, G. (2009) 'The onset of the 2007 Stromboli effusive eruption recorded by an integrated geophysical network', *Journal of Volcanology and Geothermal Research*, vol. 182, pp. 131-136.
- Robert, B., Marris, A., Gurioli, L., Medard, E., Sehlke, A. and Whittington, A. (2014) 'Textural and rheological evolutions of basalt flowing down a lava channel ', *Bulletin of Volcanology* , vol. 76, no. doi./10.1007/s00445-014-0824-8.
- Robson, S. and James, M.R. (2007) 'Photogrammetric image sequence processing to determine change in active lava flows', Proc. Remote Sensing and Photogrammetry Society Ann. Conf., Newcastle upon Tyne, 321-322.
- Rothery, D.A., Borgia, A., Carlton, R.W. and Oppenheimer, C. (1992) 'The 1992 Etna lava flow imaged by Landsat TM', *International Journal of Remote Sensing*, vol. 13, pp. 2759-2763.
- Rowland, S.K., Barbel, H. and Harris, A.J.L. (2005) 'Lengths and hazards from channel-fed lava flows on Mauna Loa, Hawai'i, determined from thermal and downslope modeling with FLOWGO', *Bulliten of Volcanology*, vol. 67, no. 7, pp. 634-647.
- Rowland, S., Garbeil, H. and Harris, A. (2005) 'Lenghts and hazards form channel-fed lava flows on Mauna Loa, Hawai'i, determined from thermal and downslope modelling with FLOWGO', *Bulletin of Volcanology*, vol. 67, no. doi: 10.1007/s00445-004-0399-x, pp. 634-647.
- Rowland, S. and Harris, A. (2015) 'Lava Flows and Rheology', in *Encyclopedia of Volcanoes*, Oxford: Elsevier Science & Technology.
- Rowland, S.K. and Walker, G.P.L. (1990) 'Pahoehoe and aa in Hawaii: volumetric flow rate controls the lava structure', *Bulliten of Volcanology*, vol. 52, no. 8, pp. 615-628.
- Royston, P. (1991) 'Estimating departure from normality', *Statistics in Medicine*, vol. 10, pp. 1283-1293.
- Ryan, G.A., Loughlin, S.C., James, M.R., Jones, L.D., Calder, E.S., Christopher, T., Strutt, M.H. and Wadge, G. (2010) 'Growth of the lava dome and extrusion rates at Soufrière Hills Volcano, Montserrat, West Indies: 2005–2008', *Geophysical Research Letters*, vol. 37, no. L00E08.
- Ryerson, F.J., Weed, H.C. and Piwinski, A.J. (1988) 'Rheology of subliquidus magmas: 1. Picritic compositions', *Journal of Geophysical Research*, vol. 93, no. B4, pp. 3421-3421.
- Sawyer, G. (2002) *Atomspheric Correction of FLIR Thermal Imagery*, Istituto Nazionale di Geofisica e Vulcanologia, Sezone di Catania, Internal Report.
- Sawyer, G.M. and Burton, M.R. (2006) 'Effects of a volcanic plume on thermal imaging data', *Geophysical Research Letters*, vol. 33, no. L14311.
- Scrope, G.P. (1858) *The geology and extinct volcanoes of Central France*, London: John Murray.
- Shaw, H.R. (1969) 'Rheologyof basalt in the melting range', *Journal of Petrology*, vol. 10, pp. 510-535.
- Shaw, G.A. and Burke, H.K. (2003) 'Spectral Imaging for Remote Sensing', *Lincoln Labratory Journal*, vol. 14, pp. 3-28.

- Shaw, H.R., Wright, T.L., Peck, D.L. and Okamura, R. (1968) 'The viscosity of basaltic magma: an analysis of field measurements in Makopuhi lava lake, Hawaii', *American Journal of Science*, vol. 266, pp. 225-264.
- Shimozuru, D. and Kagiya, T. (1978) 'A newly devised infra-red ground scanner and its application to geothermal research in volcanoes', *Journal of Volcanology and Geothermal Research*, vol. 4, pp. 251-264.
- Slatcher, N., James, M., Calvari, S., G, G. and Browning, J. (2015) 'Quantifying Effusion Rates at Active Volcanoes through Integrated Time-lapse Laser Scanning and Photography', *Remote Sensing*, vol. 7, no. doi:10.3390/rs71114967, pp. 14967-14987.
- Smets, B., d'Oreye, N., Kervyn, M. and Kervyn, F. (2017) 'Gas piston activity of the Nyiragongo lava lake: first insights from a stereographic time-lapse camera system', *Journal of African Earth Science*, vol. 134, pp. 874-887.
- Soltysik, R.C. and Yarnold, P.R. (2010) 'The use of unconfounded climatic data improves atmospheric prediction', *Optimal Data Analysis*, vol. 1, pp. 67-100.
- Soule, S.A., Chasman, K.V. and Kauahikauam, J.P. (2004) 'Examining flow emplacement through the surface morphology of three rapidly emplaced, solidified lava flows, Kilauea Volcano, Hawaii', *Bulletin of Volcanology*, vol. 66, pp. 1-14.
- Spampinato, L., Calvari, S., Oppenheimer, C. and Boschi, E. (2011) 'Volcano surveillance using infrared cameras', *Earth-Science Review*, vol. 106, pp. 63-91.
- Spampinato, L., S, C., Oppenheimer, C. and Lodato, L. (2008) 'Shallow magma transport for the 2002-3 Mt. Etna eruption inferred from thermal infrared surveys', *Journal of Volcanology and Geothermal Research*, vol. 177, no. doi: 10.1016/j.jvolgeores.2008.05.013, pp. 301-312.
- Sparks, R.S.J., Pinkerton, H. and Hulme, G. (1976) 'Classification and formation of lava levees on Mt Etna, Sicily', *Geology*, vol. 4, pp. 269-271.
- Sparks, R.S.J., Young, S.R., Barclay, J., Calder, E.S., Cole, P., Darroux, B., Davies, M.A., Druitt, T.H., Harford, C., Herd, R., James, M., Lejeune, A.M., Loughlin, S., Norton, G. and Watts, R. (1998) 'Magma production and growth of the lava dome of the Soufriere Hills Volcano, Montserrat, West Indies: November 1995 to December 1997', *Geophysics Research Letters*, vol. 25, pp. 3421-3424.
- Staudacher, T. (2010) 'Field observations of the 2008 summit eruption at Piton de la Fournaise (Ile de La Réunion) and implications for the 2007 Dolomieu collapse', *Journal of Volcanology and Geothermal Research*, vol. 191, no. 1-2, pp. 60-68.
- Steele, B., Chandler, J. and Reddy, S. (2016) *Algorithms for data science*, Berlin: Springer.
- Steinberg, P.D., Brett, M.T., Bechtold, J.S., Richey, J.E., Porensky, L.M. and Smith, S.N. (2011) 'The influence of watershed characteristics on nitrogen export to and marine fate in Hood Canal, Washington, USA', *Biogeochemistry*, vol. 106, pp. 415-433.
- Stumpf, A., Malet, J.P., Allemand, P., Pierrot-Deseilligny, M. and Skupin-ski, G. (2015) 'Ground-based multi-view photogrammetry for the monitoring of landslide deformation and erosion', *Geomorphology*, vol. 321, pp. 130-145.

- Suh, C.E., Stansfield, S.A., Sparks, R.S.J., Njome, M.S., Wantim, M.N. and Ernst, G.G.J. (2011) 'Morphology and structure of the 1999 lava flows at Mount Cameroon Volcano (West Africa) and their bearing on the emplacement dynamics of volume-limited flows', *Geology Magazine*, vol. 148, pp. 22-34.
- Swanson, D.A. (1973) 'Pahoehoe flows from the 1969-1971 Mauna Ulu eruptions, Kilauea Volcano, Hawaii', *Geologic Society of America Bulliten*, vol. 84, pp. 615-626.
- Taddeucci, J., Pompilio, M. and Scarlato, P. (2002) 'Monitoring the explosive activity of the July–August 2001 eruption of Mt. Etna (Italy) by ash characterization', *Geophysical Research Letters*, vol. 29, no. 8.
- Tallarico, A. and Dragoni, M. (1999) 'Viscous Newtonian laminar flow in a rectangular channel: application to Etna lava flows', *Bulliten of Volcanology*, vol. 61, pp. 40-47.
- Tanguy, J.-C. and Clocchiatti, R. (1984) 'The Etnean lavas, 1977-1983: petrology and minerology', *Bulletin of Volcanology*, vol. 47, pp. 879-894.
- Tanguy, J.C., Condomines, M. and Kieffer, G. (1997) 'Evolution of the Mount Etna magma: constraints on the present feeding system and eruptive mechanism', *Journal of Volcanology and Geothermal Research*, vol. 75, pp. 221-250.
- Tarquini, S. and Coppola, D. (2018) 'Combined morphological and thermal analysis of lava flows: A way to boost understanding of emplacement dynamics', *Terra Nova*, vol. 30, pp. 215-221.
- Travelletti, J., Delacourt, C., Allemand, P., Malet, J.-P., Schmittbuhl, J., Toussaint, R. and Bastard, M. (2012) 'Correlation of multi-temporal ground-based optical images for landslide monitoring: Application, potential and limitations', *ISPRS Journal of Photogrammetry and Remote Sensing*, vol. 70, pp. 39-55.
- Vatcheva, K.P., Lee, M.-J., McCormick, J.B. and Rahbar, M.H. (2016) 'Multicollinearity in Regression Analyses Conducted in Epidemiologic Studies', *Epidemiology*, vol. 227, no. 2.
- Vicari, A., Alexis, H., Del Negro, C., Coltelli, M., Marsella, M. and Proietti, C. (2007) 'Modeling of the 2001 lava flow at Etna volcano by Cellular Automata approach', *Environmental Modelling and Software*, vol. 22, pp. 1465-1471.
- Vicari, A., Ganci, G., Behncke, B., Cappello, A., Neri, M. and Del Negro, C. (2011) 'Near-real-time forecasting of lava flow hazards during the 12-13 January 2011 Etna eruption', *Geophysical Research Letters*, vol. 38, p. L13317.
- Viccaro, M., Calcagno, R., Garozzo, I., Giuffrida, M. and Nicotra, E. (2015) 'Continuous magma recharge at Mt. Etna during the 2011-2013 period controls the style of volcanic activity and composition of erupted lavas', *Mineralogy and Petrology*, vol. 109, pp. 67-83.
- Volcano.oregonstate.edu *Lava Flows*, [Online], Available: <http://volcano.oregonstate.edu/book/export/html/131> [10 July 2018].
- von Buch, L. (1836) *Description physique des Iles Canaries*, Paris: F.G. Levrault.
- Wadge, G. (1976) 'The deformation of Mount Etna 1971-1974', *Journal of Volcanology and Geothermal Research*, vol. 1, pp. 237-263.

- Wadge, G. (1978) 'Effusion rate and the shape of aa lava flow fields on Mount Etna', *Geology*, vol. 6, pp. 503-506.
- Wadge, G. (1979) 'Storage and release of magma on Mount Etna: reply to a discussion by J.C. Tanguy', *Journal of Volcanology and Geothermal Research*, vol. 6, pp. 189-195.
- Wadge, G., Young, P. and McKendrick, I. (1994) 'Mapping lava flow hazards using computer simulations', *Journal of Geophysical Research*, vol. 99, pp. 489-504.
- Walker, G.P.L. (1967) 'Thickness and viscosity of Etnean lavas', *Nature*, vol. 213, pp. 484-485.
- Walker, G. (1971) 'Compound and simple lava flows and flood basalts', *Bulletin of Volcanology*, vol. 35, no. 3, pp. 579-590.
- Walker, G.P.L. (1973) 'Lengths of Lava Flows ( and Discussion)', *Philosophical Transactions of the Royal Society*, vol. 274, pp. 107-188.
- Walter, T.R., Ratdomopurbo, A., Subandriyo, Aisyah, N., Brotopuspito, K.S., Salzer, J. and Luhr, B. (2013) 'Dome growth and coulée spreading controlled by surface morphology, as determined by pixel offset in photographs of the 2006 Merapi eruption', *Journal of Volcanology and Geothermal Research*, vol. 261, pp. 121-129.
- Wantim, M., Kervyn, M., Ernst, G., del Marmol, M., Suh, C. and Jacobs, P. (2013) 'Numerical experiments on the dynamics of channelised lava flows at Mount Cameroon volcano with the FLOWGO thermo-rheological model', *Journal of Volcanology and Geothermal Research*, vol. 253, pp. 35-53.
- Wessels, R.L., Vaughan, R.G., Patrick, M.R. and Coombs, M.L. (2013) 'High-resolution satellite and airborne thermal infrared imaging of precursory unrest and 2009 eruption at Redoubt Volcano, Alaska', *Journal of Volcanology and Geothermal Research*, vol. 259, pp. 248-269.
- Wilson, L., Pinkerton, H., Head, J.W. and Magee-Roberts, K. (1993) 'A classification scheme for the morphology of lava flow fields', *Lunar and Planetary Science*, vol. 24, no. 3, pp. 1527-1528.
- Witter, J.B. and L, H.A.J. (2007) 'Field measurements of heat loss from skylights and lava tube systems', *Journal of Geophysical Research*, vol. 112, no. B01203.
- Wolfe, E.W. (1988) 'The Puu Oo eruption of Kilauea Volcano, Hawaii: Episodes 1 through 20, January 8, 1983, through June 8, 1984', *United States Geological Survey Professional Paper*, vol. 1463.
- Wooster, M.J., Wright, R., Blake, S. and Rothery, D.A. (1997) 'Cooling mechanisms and an approximate thermal budget for the 1991-1993 Mount Etna lava flow', *Geophysical Research Letters*, vol. 24, pp. 3277-3280.
- Wright, R. and Flynn, L.P. (2003) 'On the retrieval of lava-flow surface temperatures from infrared satellite data', *Geology*, vol. 31, pp. 893-896.
- Wright, R., Flynn, L.P., Garbeil, H., Harris, A.J.L. and Pilger, E. (2002) 'Automated volcanic eruption detection using MODIS', *Remote Sensing the Environment*, vol. 82, pp. 135-155.

Wright, R., Gabriel, H. and Harris, A. (2008) 'Using infrared satellite data to drive a thermo-rheological /stochastic lava flow emplacement model: a method for near-real time volcanic hazard assessment', *Journal of Geophysical Research*, vol. 35, pp. <http://doi.org/10.1029/2008GL035228>.

Yarnold, P.R. (1996) 'Characterizing and circumventing Simpson's Paradox for ordered bivariate data', *Educational and Psychological Measurement*, vol. 56, no. 3.

Young, P. and Wadge, G. (1990) 'FLOWFRONT: SIMULATION OF A LAVA FLOW', *Computers and Geoscience*, vol. 16, pp. 1171-1191.

Yr, [Online], Available: [www.yr.no](http://www.yr.no) [15 May 2016].

Yuhara, L., Ehara, S. and Tagomori, K. (1981) 'Estimations of heat discharge rates using infrared measurements by a helicopter-borne thermocamera over the geothermal areas of Unzen volcano, Japan', *Journal of Volcanology and Geothermal Research*, vol. 9, pp. 99-109.

Zlotnicki, J., Ruegg, J.C., Bachelery, P. and Blum, P.A. (1990) 'Eruptive mechanism on Piton de la Fournaise volcano associated with the December 4, 1983, and January 18, 1984 eruptions from ground deformation monitoring and photogrammetric surveys', *Journal of Volcanology and Geothermal Research*, vol. 40, pp. 197-217.

# Appendix 1 – MODTRAN output file of transmittance and upwelling radiance calculated from LTN file at 100 m steps for a range of 0-100 km using a horizontal-path geometry

**For this study, one such output was needed for every set of atmospheric temperature and relative humidity (e.g. 2500 files to generate the look-up tables for a horizontal-path geometry for ATM T of 10-35 °C at RH of 0-100 %) Typical file size is 600,000-800,000 KB depending on the complexity of the atmospheric model used.**

\*\*\*\*\*

```
*
*
* MODTRAN4: Official Version 1.1 Apr 2000 *
*
*
* Developed in a collaborate effort between *
* SPECTRAL SCIENCES, INC. (www.spectral.com) *
* and the AIR FORCE RESEARCH LABORATORY *
* (www-vsbn.plh.af.mil). *
*
*
```

\*\*\*\*\*

CARD 1 \*\*\*\*\*T 0 1 1 0 0 0 0 0 0 0 0 1 0 0.000 0.02

CARD 1A \*\*\*\*\*FF 0T 5 380.00000 0.000

MOLECULAR BAND MODEL DATA FILE: DATA/BMP99\_01.BIN

CARD 2 \*\*\*\*\* 1 0 0 0 0 0 0.00000 0.00000 0.00000 0.00000 1.15400



IV1 = 765 CM-1 ( 13.07 MICRONS)

IV2 = 1335 CM-1 ( 7.49 MICRONS)

IDV = 1 CM-1

IFWHM = 1 CM-1

1 ATMOSPHERIC PROFILES

I	Z	P	T	N2	CNTMSLF	CNTMFRN	MOL SCAT	N-1	O3 (UV)	O2 (UV)	WAT
DROP	ICE	PART	RAIN	RATE							
(KM)	(MB)	(K)		( MOL/CM2 KM )	(-)	(-)	( ATM CM/KM )		(GM/M3)		
(GM/M3)	(MM/HR)										

1	1.1540	954.000	292.5	7.090E-01	3.415E+20	2.738E+22	8.793E-01	2.523E-04	0.000E+00	0.000E+00	0.000
				0.000	0.000	0.000					

1 ATMOSPHERIC PROFILES

I	Z	P	T	AEROSOL 1	AEROSOL 2	AEROSOL 3	AEROSOL 4	AER1*RH	RH (%)	RH
(%)	CIRRUS	WAT	DROP	ICE	PART					
(KM)	(MB)	(K)	(-)	(-)	(-)	(-)	(-)	(BEFORE H2O SCALING)	(AFTER)	(-)
(550nm VIS [KM-1])										

1	1.1540	954.000	292.5	1.580E-01	0.000E+00	0.000E+00	0.000E+00	6.105E-01		
				5.236E+01	5.236E+01	0.00000	0.00000	0.00000		

1 ATMOSPHERIC PROFILES (AFTER COLUMN SCALING)

I Z P H2O O3 CO2 CO CH4 N2O O2 NH3 NO NO2  
 SO2 HNO3

(KM) (MB) ( ATM CM / KM )

1 1.1540 954.000 1.08E+03 0.00E+00 0.00E+00 0.00E+00 0.00E+00 0.00E+00 0.00E+00 0.00E+00  
 0.00E+00 0.00E+00 0.00E+00 0.00E+00 0.00E+00

1 ATMOSPHERIC PROFILES

I Z CFC-11 CFC-12 CFC-13 CFC-14 CFC-22 CFC-113 CFC-114 CFC-115 CLONO2  
 HNO4 CHCL2F CCL4 N2O5

(KM) ( ATM CM/KM )

1 1.1540 0.00E+00 0.00E+00 0.00E+00 0.00E+00 0.00E+00 0.00E+00 0.00E+00 0.00E+00 0.00E+00  
 0.00E+00 0.00E+00 0.00E+00 0.00E+00 0.00E+00

HORIZONTAL PATH AT ALTITUDE = 1.154 KM WITH RANGE = 0.000 KM, MODEL = 0

TOTAL COLUMN ABSORBER AMOUNTS FOR THE LINE-OF-SIGHT PATH:

HNO3 O3 UV CNTMSLF1 CNTMSLF2 CNTMFRN N2 CONT MOL SCAT

(ATM CM) (ATM CM) (MOL CM-2) (MOL CM-2) (MOL CM-2) (550 NM EXT)

0.0000E+00 0.0000E+00 0.0000E+00 0.0000E+00 0.0000E+00 0.0000E+00  
 0.0000E+00

AER 1 AER 2 AER 3 AER 4 CIRRUS WAT DROP ICE PART MEAN AER

RH

(KM GM/M3) (KM GM/M3) (PRCNT)

0.000000 0.000000 0.000000 0.000000 0.000000 0.000000 0.000000  
0.00

H2O O3 CO2 CO CH4 N2O  
( ATM CM )  
0.0000E+00 0.0000E+00 0.0000E+00 0.0000E+00 0.0000E+00 0.0000E+00

O2 NH3 NO NO2 SO2  
( ATM CM )  
0.0000E+00 0.0000E+00 0.0000E+00 0.0000E+00 0.0000E+00

CFC-11 CFC-12 CFC-13 CFC-14 CFC-22 CFC-113 CFC-114  
( ATM CM )  
0.0000E+00 0.0000E+00 0.0000E+00 0.0000E+00 0.0000E+00 0.0000E+00  
0.0000E+00

CFC-115 CLONO2 HNO4 CHCL2F CCL4 N2O5  
( ATM CM )  
0.0000E+00 0.0000E+00 0.0000E+00 0.0000E+00 0.0000E+00 0.0000E+00

1 RADIANCE(WATTS/CM2-STER-XXX)  
0 FREQ WAVLEN DIREC PATH THERMAL SCAT PART SURFACE EMISSION SURFACE  
REFLECTED TOTAL RADIANCE INTEGRAL TOTAL  
(CM-1) (MICRN) EMIS (CM-1) (MICRN) (CM-1) (CM-1) (MICRN) (CM-1) (MICRN)  
(CM-1) (MICRN) TRANS

765. 13.072 0.980 0.00E+00 0.00E+00 0.00E+00 0.00E+00 0.00E+00 0.00E+00  
0.00E+00 0.00E+00 0.00E+00 0.00E+00 1.00000

766. 13.055 0.980 0.00E+00 0.00E+00 0.00E+00 0.00E+00 0.00E+00 0.00E+00  
0.00E+00 0.00E+00 0.00E+00 0.00E+00 1.00000

767. 13.038 0.980 0.00E+00 0.00E+00 0.00E+00 0.00E+00 0.00E+00 0.00E+00  
0.00E+00 0.00E+00 0.00E+00 0.00E+00 1.00000

768. 13.021 0.980 0.00E+00 0.00E+00 0.00E+00 0.00E+00 0.00E+00 0.00E+00  
0.00E+00 0.00E+00 0.00E+00 0.00E+00 1.00000

.  
. .  
. .  
. .

1332. 7.508 0.980 0.00E+00 0.00E+00 0.00E+00 0.00E+00 0.00E+00 0.00E+00 0.00E+00  
0.00E+00 0.00E+00 0.00E+00 1.00000

1333. 7.502 0.980 0.00E+00 0.00E+00 0.00E+00 0.00E+00 0.00E+00 0.00E+00  
0.00E+00 0.00E+00 0.00E+00 0.00E+00 1.00000

1334. 7.496 0.980 0.00E+00 0.00E+00 0.00E+00 0.00E+00 0.00E+00 0.00E+00  
0.00E+00 0.00E+00 0.00E+00 0.00E+00 1.00000

1335. 7.491 0.980 0.00E+00 0.00E+00 0.00E+00 0.00E+00 0.00E+00 0.00E+00  
0.00E+00 0.00E+00 0.00E+00 0.00E+00 1.00000

INTEGRATED ABSORPTION FROM 765 TO 1335 CM-1 = 0.0000 CM-1

AVERAGE TRANSMITTANCE = 1.0000

INTEGRATED TOTAL RADIANCE = 0.000000E+00 WATTS CM-2 STER-1 (FROM 765 TO 1335  
CM-1 )

MINIMUM SPECTRAL RADIANCE = 0.000000E+00 WATTS CM-2 STER-1 / CM-1 AT 1335 CM-  
1

MAXIMUM SPECTRAL RADIANCE = 0.000000E+00 WATTS CM-2 STER-1 / CM-1 AT 1335  
CM-1

TARGET-PIXEL (H2) SURFACE TEMPERATURE [K] = 0.000

AREA-AVERAGED GROUND TEMPERATURE [K] = 292.490

TARGET-PIXEL (H2) DIRECTIONAL EMISSIVITY = 0.980

AREA-AVERAGED GROUND EMISSIVITY = 0.980

SPECTRUM WILL BE CONVOLVED USING A TRIANGULAR SLIT

CONVOLVED SPECTRA ARE IN FILES PLTOUT.SCN AND TAPE7.SCN

BANDPASS FOR CONVOLVING = 769. TO 1333. CM-1.

UNCONVOLVED INTEGRATED RADIANCE: 0.00000E+00 WATTS CM-2 STER-1

CONVOLVED INTEGRATED RADIANCE: 0.00000E+00 WATTS CM-2 STER-1

## Appendix 2 – Excerpt from MODTRAN LTN file for a horizontal-path viewing geometry

**Highlighted values indicate those which had to be changed by hand for each iteration (e.g. for ATM T of 10-35 °C for RH of 0-100 % means 2500 iterations).**

T 0 1 0 0 0 0 0 0 0 0 0 0 1 0 0.000 0.00

F OF 0 365.000

0 0 0 0 0 0 0.000 0.000 0.000 0.000 1.158

1 0 0Aug12

1.158 9.540E+02 **1.000E+01 0.000E+00** 0.000E+00 0.000E+00ABH6A666666666

1.158 0.000 0.000 0.001 0.000 0.000 0 0.000

769.000 1333.000 1.000 2.000RN 1 A

[START\_INC]

range 0.000000 10.000000 0.100000

[END\_INC]

1

## Appendix 3 – Matlab code for extracting transmittance and upwelling radiance from MODTRAN outputs

### Transmittance Extraction code

```
x = find(strncmp(US1976layer10, ' AVERAGE TRANSMITTANCE', 21));
a = US1976layer10((x(:, :)), 1);
US1976layer10 = a;
for i = 1:length(US1976layer10)
    Trans_ATMT = US1976layer10{i};
    US1976layer10{i} = (Trans_ATMT(end-6:end));
end

%Convert cell/string to numbers
US1976layer10 = cell2mat(US1976layer10);
US1976layer10 = str2num(US1976layer10);

% %Divide AvgTrans into constituent parts
US1976layer10_trans = reshape(US1976layer10, 81, 1);

%generate coeff for look up

a1_coeff = NaN(1, size(US1976layer3, 2));
a2_coeff = NaN(1, size(US1976layer3, 2));
a3_coeff = NaN(1, size(US1976layer3, 2));
a4_coeff = NaN(1, size(US1976layer3, 2));
for iRH = 1:size(US1976layer3)

    [f, gof, output] = fit(distance2, US1976layer3(:, iRH), 'exp2');
    a1_coeff(iRH) = f.a1;
    a2_coeff(iRH) = f.a22;
    a3coeff(iRH) = f.a3;
    a4_coeff(iRH) = f.a4;

    % Note that row 1 = a_coeff and row 2 = b_coeff
    Aug29slant_trans_abcd = [a1_coeff; a2_coeff; a3_coeff; a4_coeff];
    all_f(iRH) = f;

    plot(f, Distance, x15C_RadTemp(:, 1))
end
```

### Upwelling radiance extraction code

```
x = find(strncmp(Aug29slant, ' INTEGRATED TOTAL RADIANCE', 25));
a = Aug29slant((x(:, :)), 1);

Aug29slant_rad = a;
for i = 1:length(Aug29slant_rad)
```

```

    Uprad = Aug29slant_rad{i};
    Aug29slant_rad{i} = (Uprad(end-57:end-46));
end
%Convert cell/string to numbers
Aug29slant_rad = cell2mat(Aug29slant_rad);
Aug29slant_rad = str2num(Aug29slant_rad);
Aug29slant_rad = Aug29slant_rad*100*100;
%Divide AvgTrans into constituent parts
Aug29slant_rad = reshape(Aug29slant_rad,81,73);

%generate coeff for look up
a1_coeff = NaN(1, size(Aug29slant_rad, 2));
a2_coeff = NaN(1, size(Aug29slant_rad, 2));
a3coeff = NaN(1, size(Aug29slant_rad, 2));
a4_coeff = NaN(1, size(Aug29slant_rad, 2));
for iRH = 1:size(Aug29slant_rad)

    [f, gof, output] = fit(distance2, Aug29slant_rad(:,iRH), 'exp2');

    a1_coeff(iRH) = f.a1;
    a2_coeff(iRH) = f.a2;
    a3_coeff(iRH) = f.a3;
    a4_coeff(iRH) = f.a4;

% Note that row 1 = a_coeff and row 2 = b_coeff
Aug29slant_rad_abcd = [a1_coeff;a2_coeff;a3_coeff;a4_coeff];
% all_f(iRH) = f;

% plot(f,Distance,x15C_RadTemp(:,1))
end

```

## Appendix 4 – Excerpt from MODTRAN LTN file for a slant-path viewing geometry

Highlighted values have to be edited by hand for every set of atmospheric temperature and relative humidity (e.g. changed for 74 inputs for the 29 Aug 2011 case-study).

```
T 7 2 1 0 0 0 0 0 0 0 0 1 0 0.000 0.02
FT 2T 5 380.000
1 0 0 0 0 0 0.000 0.000 0.000 0.000 1.154
3 0 0*
1.154 9.070E+02 2.924E+02 4.990E+01 0.000E+00 0.000E+00AAH
2.077 8.260E+02 2.877E+02 3.140E+01 0.000E+00 0.000E+00AAH
3.000 7.530E+02 2.831E+02 1.940E+01 0.000E+00 0.000E+00AAH
1.154 3.150 0.000 2.000 0.000 0.000 0 0.000
769.000 1333.000 1.000 1.000 W1
[START_INC]
range 2.000000 10.000000 0.100000
[END_INC]
1
```

## Appendix 5 – Matlab code for generating viewing distance map from DEM

### Code supplied by Dr. Mike James (Lancaster University)

```
% Georegistering the Mt Cagliato camera in WGS84 UTM (meters)

%% Import the DEM
% Original DEM used...
% dem = dlmread('..\Downloads\12August2011\dem_2007_10m_xyz');
% step = 10;
Big_dem =
dlmread('C:\Users\anson_000\Documents\MATLAB\bove_2005_5m');
dem = Big_dem( Big_dem(:,1)>499100, :);
dem = dem( dem(:,1)<505000, :);
step = 5;
%% Cameras and imagery
campos = [ 507943.99 4176495.18 1158];
campoint = [144.7759 71.8155 -52.0706]; (updated for no PO)

% Read a representative image
% im = imread('..\Downloads\12August2011\Thermal
Camera\EMCT\EMCT_20110812-051500.bmp');
im = imread('Emct_20110812-051500.tif');
im = im(:, :, 1:3);

% Use VMS model (for compatibility with Tania), but set unjustified
% parameters to zero. Update the pd for her camera
EMCTcam = VMS_camera('flirs40');
EMCTcam.pd = 33.7625;
EMCTcam.po = [0 0]; % No justification for po
EMCTcam.a1 = 0; % No justification for a1
EMCTim = R3_image(im, EMCTcam, campos, campoint);

% Carry out the data overlay to check or refine the orientation
EMCTim = dataoverlay_gui(EMCTim, dem);

%% So now have the dem and the oriented image

% Viewing distance calculation
im_pts = EMCTim.project_to_image('cdem');
% Calculate the distance to camera for each DEM point
dist = sqrt( sum( (dem - repmat(EMCTim.sensor_position, size(dem, 1),
1)).^2, 2 ) ));

dist_im = NaN*zeros(npY, npX);
for i = 1:size(im_pts, 2)
    x = round(im_pts(1, i)); y = round(im_pts(2, i));
    if ~isnan(x*y) && x > 0 && y > 0 && x <= npX && y <= npY
        if ( isnan(dist_im(y, x)) || dist_im(y, x) > dist(i) )
            dist_im(y, x) = dist(i);
        end
    end
end
end

imagesc(dist_im);
```

## Appendix 6 – Matlab code for thermal data processing workflow

```
% Work flow for image correction
working_folder =
'C:\Users\anson_000\Documents\MATLAB\Correction_Aug12_29';
cd( working_folder )

% Load distance map
distance_map = dlmread('rangemap3.txt');
% distance_map_km = distance_map./1000;

% Load reprojection and registration lookup table
% A matrix the size of the cropped DEM in which each 'pixel' is
stored the
% index to a pixel in the image

% Load transmittance coeff tables
% load('x10C_abcd.mat');
% load('x11C_abcd.mat');
% load('x12C_abcd.mat');
% load('x13C_abcd.mat');
% load('x14C_abcd.mat');
% load('x15C_abcd.mat');
% load('x16C_abcd.mat');
% load('x17C_abcd.mat');
% load('x18C_abcd.mat');
% load('x19C_abcd.mat');
% load('x20C_abcd.mat');
% load('x21C_abcd.mat');
% load('x22C_abcd.mat');
% load('x23C_abcd.mat');
% load('x24C_abcd.mat');
% load('x25C_abcd.mat');
% load('x26C_abcd.mat');
% load('x27C_abcd.mat');
% load('x28C_abcd.mat');
% load('x29C_abcd.mat');
% load('x30C_abcd.mat');
% load('x31C_abcd.mat');
% load('x32C_abcd.mat');
% load('x33C_abcd.mat');
% load('x34C_abcd.mat');
% load('x35C_abcd.mat');
%Uprad coeffs
% load('x10C_rad_abcd.mat');
% load('x11C_rad_abcd.mat');
% load('x12C_rad_abcd.mat');
% load('x13C_rad_abcd.mat');
% load('x14C_rad_abcd.mat');
% load('x15C_rad_abcd.mat');
% load('x16C_rad_abcd.mat');
% load('x17C_rad_abcd.mat');
% load('x18C_rad_abcd.mat');
% load('x19C_rad_abcd.mat');
% load('x20C_rad_abcd.mat');
% load('x21C_rad_abcd.mat');
% load('x22C_rad_abcd.mat');
% load('x23C_rad_abcd.mat');
% load('x24C_rad_abcd.mat');
```

```

% load('x25C_rad_abcd.mat');
% load('x26C_rad_abcd.mat');
% load('x27C_rad_abcd.mat');
% load('x28C_rad_abcd.mat');
% load('x29C_rad_abcd.mat');
% load('x30C_rad_abcd.mat');
% load('x31C_rad_abcd.mat');
% load('x32C_rad_abcd.mat');
% load('x33C_rad_abcd.mat');
% load('x34C_rad_abcd.mat');
% load('x35C_rad_abcd.mat');
% % Load atmospheric parameters time series
% load('atmosT_Aug29');
% load('image_times_Aug29');
% load('RH_Aug29');
    load ('Aug29slant_trans_abcd');
    load('Aug29_slant_rad_abcd');
% Load files required for rectification
load('EMCTim.mat') % Oriented R3_image
load('cdem') % cropped dem per Tania's specifications
step = 5;

% Load emissivity value
load('Emissivity');

% Extract FLIR camera coordinates
x0=EMCTim.sensor_position(1); % 507943.99;
y0=EMCTim.sensor_position(2); % 4176495.18;
z0=EMCTim.sensor_position(3); % 1160;

im_files = dir( fullfile(working_folder, 'Image_files_csv', '*.csv')
);
im_files = {im_files.name};
% im_files = im_files(97);
% trans_files = trans_files(97);
% % Correct all files for pathlength (transmissivity correction)
for transID = 1:length(Aug29slant_trans_abcd)
    ATM_file_Trans_coeff = Aug29slant_trans_abcd(:,transID);
    transm_map =
(ATM_file_Trans_coeff(1)*exp(ATM_file_Trans_coeff(2)*distance_map))+
(ATM_file_Trans_coeff(3)*exp(ATM_file_Trans_coeff(4)*distance_map));
end

for radID = 1:length(Aug29slant_rad_abcd)
    ATM_file_rad_coeff = Aug29slant_rad_abcd(:,radID);
    UpRad_map
=(ATM_file_rad_coeff(1)*exp(ATM_file_rad_coeff(2)*distance_map))+
(ATM_file_rad_coeff(3)*exp(ATM_file_rad_coeff(4)*distance_map)) ;
end

for fileID = 1:length(im_files)
    im_file = im_files{fileID};

    % Extract time
    % hrs = str2double(im_file(15:16));
    % mins = str2double(im_file(17:18));
    % hrs = hrs+mins/60;

```

```

% Use hrs to index into the array of atmospheric temperatures and RH
values
    % calculate atmosT and RH at a given hrs
%   atmosT = interp1(image_times_Aug29,atmosT_Aug29,hrs);
%   atmosT_rad = interp1(image_times_Aug29,atmosT_Aug29,hrs);
%   RH = interp1(image_times_Aug29,RH_Aug29,hrs);
%
%   % Form the matrix name which requires the atmosT to the
nearest
%   % degr. Copy the appropriate matrix into ambient_T
%   round_atmosT = round(atmosT);
%   round_atmosT_rad = round(atmosT_rad);

% Trans and UpRad Map Createion
%   trans_coeffs = round_atmosT;
%   rad_coeffs = round_atmosT_rad;

% Use extracted RH value as an index into the trans_coeffs
% Note - values range from 1 to 101 (with 1 = to 0RH and 101 = to
100RH)
% a coeff = row 1, b coeff = row 2, c coeff = row 3, and d coeff
= row 4
% example: ambient_T = x15C_abcd
%           RH = x15C_abcd(:,3)

%   trans_coeffs = trans_coeffs(:, round(RH));
%   rad_coeffs = rad_coeffs(:, round(RH));

%   exp2 equation = f(x) = a*exp(b*x)+ c*exp(d*x), where x =
distance (in km) and f(x) =
%   average transmittance for the wavelength of the camera (7.5-
13um).

%   transm_map =
((trans_coeff(1)*exp(trans_coeff(2)*distance_map))+((trans_coeff(3)*e
xp(trans_coeff(4)*distance_map)));
%   UpRad_map =
((rad_coeff(1)*exp(rad_coeff(2)*distance_map))+rad_coeff(3)*exp((rad
_coeff(4)*distance_map));

% ATM_file_Trans_coeff = Aug29_horiz_avg_trans_abcd(:,fileID);
% exp2 equation = f(x) = a*exp(b*x)+ c*exp(d*x), where x =
distance (in km) and f(x) =
%   average transmittance for the wavelength of the camera (7.5-
13um).
%   transm_map =
((ATM_file_Trans_coeff(1)*exp(ATM_file_Trans_coeff(2)*distance_map))+
(ATM_file_Trans_coeff(3)*exp(ATM_file_Trans_coeff(4)*distance_map));

%   Compute UpRad Map for ATM correction
%   ATM_file_rad_coeff =
Aug12_horiz_integrated_uprad_abcde(:,fileID);
%   ATM_file_rad_coeff = Aug12_horiz_avg_uprad_abcde(:,fileID);
%   UpRad_map =
((ATM_file_rad_coeff(1)*exp(ATM_file_rad_coeff(2)*distance_map))+
(ATM_file_rad_coeff(3)*exp((ATM_file_rad_coeff(4)*distance_map));

```

```

% Image correction
% Load uncorrected thermal image
raw_thermal_image = load( fullfile(working_folder,
'Image_files_csv', im_file) );
raw_tempK_image = raw_thermal_image+273.15;

% Convert raw temp in K to radiance
%      rad_image = Planck_radconverts(1.025e-5,raw_tempK_image);
      rad_image = raw_tempK_image.^4.*5.57033e-8./pi;

% Corretion of radaince by transmissivity and emissivity
% Note - transmissivity is selected based on the distance of the
target pixel.
% Rad_image_cor = radiance/transmittance/emissivity
rad_image_cor = (rad_image-UpRad_map)./(Emissivity.*transm_map);

% Convert corrected radiance image to corrected temp image in K
%      tempK_image_cor = Planck_rad2temp(1.025e-5,rad_image_cor);
%changed from ran_image_cor to rad_image_eff for angle correction
      tempK_image_cor = (pi.*rad_image_cor./5.57033e-8).^ (1/4);
% Write corrected file to disk
      save( fullfile(working_folder, 'Trans_corrected_images',
[im_file(1:(end-4)) '_corr.mat']), 'tempK_image_cor' );
end

%% Rectify transmittance corrected thermal images
R3_img_T = EMCTim;
cd(fullfile( working_folder, 'Trans_corrected_images'))
list=dir('*.mat');
cd( working_folder )

xmin = min(Xdem(:));
xmax = max(Xdem(:));
ymin = min(Ydem(:));
ymax = max(Ydem(:));

for zz=1:length(list)

    filename=list(zz).name;

    output_name=['tempK_rect_' filename(8:20)];

    load(fullfile( working_folder, 'Trans_corrected_images',
list(zz).name));
    R3_img_T.image=tempK_image_cor;
    %clearvars Ir*

    T_im = resamp_image(R3_img_T, cdem');
    tempK_rect = zeros( (ymax-ymin)/step+1, (xmax-xmin)/step+1);
    for i = 1:size(cdem, 1)
        tempK_rect((ymax-cdem(i, 2))/step+1, (cdem(i, 1)-xmin)/step+1)
= ...
        T_im(i, :);
    end

    save(fullfile(working_folder, 'Rectified_thermal_im', output_name),
'tempK_rect');

```

```

%         hot_px = tempK_rect > 400; %Value in K?

        %Write an image to show the area identified as hot (white)
        %MyImageName = sprintf('image_name%d.jpg',zz);
%         imwrite( uint8( cat(3, hot_px, hot_px, hot_px)*255 ),
MyImageName , 'Quality', 100)
%         imwrite( uint8( cat(3, hot_px, hot_px, hot_px)*255 ),
'MyImageName.jpg', 'Quality', 100);
end
%% Apply angle correction to rectified tranmittance corrected thermal
images
% Calculate orientation angle for cells in dem
cd(fullfile(working_folder, 'Rectified_thermal_im'))
list=dir('*.mat');
cd(working_folder)

% Calculate viewing distance components and angle
vectdist_x = x0-Xdem;
vectdist_y = y0-Ydem;
vectdist_z = z0-Zdem;
cosang = -(vectdist_x.*theta + vectdist_y.*phi + vectdist_z ) ./ ...
( sqrt( theta.^2+phi.^2+1 ) .*
sqrt(vectdist_x.^2+vectdist_y.^2+vectdist_z.^2) );

cosang( cosang<0 ) = NaN;

for zz=1:length(list)

    filename=list(zz).name;

    output_name=fullfile(working_folder, 'Full_corr_rect_im',
['Temp_fullcorr_' filename(12:24)]);

    load(fullfile(working_folder, 'Rectified_thermal_im',
list(zz).name));

%         rect_rad_image = Rect_Planck_radconvers(1.025e-
5,tempK_rect);
        rect_rad_image = tempK_rect.^4.*5.57066e-8./pi;

        rad_rect_corrected = NaN*rect_rad_image;
%         temp_rect_corrected = NaN*tempK_rect;

        hot_px = tempK_rect >=380; %Value in K?

rad_rect_corrected(hot_px)=rect_rad_image(hot_px)./cosang(hot_px);

%temp_rect_corrected(hot_px)=tempK_rect(hot_px)./(cosang(hot_px).^(1/
4));
%         temp_rect_corrected = rad_rect_corr2temp_rect_corr(1.025e-
5,rad_rect_corrected);
        temp_rect_corrected = (pi.*rad_rect_corrected./5.57033e-
8).^ (1/4);

        save(output_name, 'temp_rect_corrected');

```

```

        %Write an image to show the area identified as hot (white)
    %         MyImageName = sprintf('image_name%d.jpg',zz);
    %         imwrite( uint8( cat(3, hot_px, hot_px, hot_px)*255 ),
MyImageName , 'Quality', 100)
    %         imwrite( uint8( cat(3, hot_px, hot_px, hot_px)*255 ),
'MyImageName.jpg', 'Quality', 100);

end

%% %% Compute Radiant Heat and estimate effusion rate
cd(fullfile(working_folder, 'Full_corr_rect_im'))
list=dir('*.mat');
cosapp=ones(760,1020);
cosapp=cosang(1:end,1:end);

pixel_area=25;

th=500; %100;
%th1=380;
sigma=5.67*10^(-8);
%eps=.98;

% Preallocate arrays
data = NaN(1, length(list));
TotArea = data;
RadiantHeat = data;

for zz=1:length(list)
    filename = list(zz).name;
    load(list(zz).name);
    info(zz) = regexp(filename, '(-\d+)', 'match');
    time = info{zz};
    h = str2double(time(2:end-4));
    m = str2double(time(4:end-2));

    % Remove pixels below th1 threshold and correct remainder for
angle
    temp_rect_corrected(temp_rect_corrected<th) = NaN;
    %     teff = temp_rect_corrected./cosapp.^(1/4);
    teff = temp_rect_corrected;
    teff(teff>1500) = NaN;

    data(zz) = datenum(2011,8,29,h,m,0);
    hot_pixel = teff>th;
    Temp_hot_pixels = teff(hot_pixel);
    TotArea(zz) = pixel_area*length(Temp_hot_pixels);

    MyImageName = sprintf('image_name%d.jpg',zz);
    imwrite( uint8( cat(3, hot_pixel, hot_pixel, hot_pixel)*255 ),
MyImageName , 'Quality', 100)

    RadiantHeat(zz) =
sum(Emissivity*pixel_area*sigma*(Temp_hot_pixels).^4);
end
% plot(TotArea)
% plot(RadiantHeat)
max_radheat=max(RadiantHeat);

```

```

%% Computes Total pixel sum of "hot" pixels
folder =
'C:\Users\anson_000\Documents\MATLAB\Correction_Aug12_29\Full_corr_re
ct_im';
for k = 1 : 73 %numberOfImages
    filename = sprintf('image_name%d.jpg', k);
    fullFileName = fullfile(folder, filename);
    if exist(fullFileName, 'file')
        thisImage = imread(fullFileName);

        %binaryImage = thisImage > 0;
        binaryImage = squeeze( thisImage(:,:,1) ) > 0;
        if k == 1
            output = binaryImage;
        else
            output = output | binaryImage;
        end
    end
end
SumTotal_HotPix = sum(sum(output > 0));

```

## Appendix 7 – Comparison of meteorological data for 29/05/2011 Event, Mt. Etna, Sicily

**Data spans the time period of activity for the 29 August 2011 event.**

Primoti Met Station Data			NCEP/NCAR Reanalysis 1 Data					
Elevation	1.154		1.154	2.077		3.00		
Time	ATM Temp	RH	ATM Temp	RH	ATM Temp	RH	ATM Temp	RH
29/08/2011 02:00	292.49	52.36	292.40	49.87	287.70	31.37	283.07	19.43
29/08/2011 02:05	292.45	52.32	292.40	49.90	287.70	31.44	283.06	19.46
29/08/2011 02:10	292.40	52.28	292.41	49.93	287.70	31.51	283.06	19.48
29/08/2011 02:15	292.36	52.25	292.41	49.96	287.70	31.58	283.05	19.50
29/08/2011 02:20	292.32	52.21	292.42	49.99	287.70	31.64	283.04	19.52
29/08/2011 02:25	292.27	52.18	292.42	50.03	287.70	31.71	283.04	19.54
29/08/2011 02:30	292.23	52.14	292.43	50.06	287.70	31.78	283.03	19.57
29/08/2011 02:35	292.19	52.10	292.43	50.09	287.70	31.85	283.03	19.59
29/08/2011 02:40	292.15	52.07	292.43	50.12	287.70	31.92	283.02	19.61
29/08/2011 02:45	292.10	52.03	292.44	50.15	287.70	31.99	283.02	19.63
29/08/2011 02:50	292.06	51.99	292.44	50.19	287.70	32.06	283.01	19.66
29/08/2011 02:55	292.02	51.96	292.45	50.22	287.70	32.13	283.01	19.68
29/08/2011 03:00	291.97	51.92	292.45	50.25	287.70	32.20	283.00	19.70
29/08/2011 03:05	291.97	52.24	292.45	50.28	287.70	32.27	282.99	19.72
29/08/2011 03:10	291.97	52.56	292.46	50.31	287.70	32.34	282.99	19.74
29/08/2011 03:15	291.97	52.88	292.46	50.35	287.70	32.41	282.98	19.77
29/08/2011 03:20	291.97	53.20	292.47	50.38	287.70	32.48	282.98	19.79
29/08/2011 03:25	291.97	53.52	292.47	50.41	287.70	32.55	282.97	19.81
29/08/2011 03:30	291.97	53.84	292.48	50.44	287.70	32.62	282.97	19.83

29/08/2011 03:35	291.97	54.16	292.48	50.47	287.70	32.69	282.96	19.86
29/08/2011 03:40	291.97	54.48	292.48	50.51	287.70	32.76	282.96	19.88
29/08/2011 03:45	291.97	54.80	292.49	50.54	287.70	32.83	282.95	19.90
29/08/2011 03:50	291.97	55.12	292.49	50.57	287.70	32.89	282.94	19.92
29/08/2011 03:55	291.97	55.44	292.50	50.60	287.70	32.96	282.94	19.94
29/08/2011 04:00	291.97	55.76	292.50	50.63	287.70	33.03	282.93	19.97
29/08/2011 04:05	292.13	55.20	292.50	50.67	287.70	33.10	282.93	19.99
29/08/2011 04:10	292.29	54.64	292.51	50.70	287.70	33.17	282.92	20.01
29/08/2011 04:15	292.45	54.08	292.51	50.73	287.70	33.24	282.92	20.03
29/08/2011 04:20	292.60	53.52	292.52	50.76	287.70	33.31	282.91	20.06
29/08/2011 04:25	292.76	52.96	292.52	50.79	287.70	33.38	282.91	20.08
29/08/2011 04:30	292.92	52.41	292.53	50.83	287.70	33.45	282.90	20.10
29/08/2011 04:35	293.08	51.85	292.53	50.86	287.70	33.52	282.89	20.12
29/08/2011 04:40	293.24	51.29	292.53	50.89	287.70	33.59	282.89	20.14
29/08/2011 04:45	293.40	50.73	292.54	50.92	287.70	33.66	282.88	20.17
29/08/2011 04:50	293.56	50.17	292.54	50.95	287.70	33.73	282.88	20.19
29/08/2011 04:55	293.71	49.61	292.55	50.98	287.70	33.80	282.87	20.21
29/08/2011 05:00	293.87	49.05	292.55	51.02	287.70	33.87	282.87	20.23
29/08/2011 05:05	294.39	45.48	292.55	51.05	287.70	33.94	282.86	20.26
29/08/2011 05:10	294.91	41.90	292.56	51.08	287.70	34.01	282.86	20.28
29/08/2011 05:15	295.43	38.33	292.56	51.11	287.70	34.08	282.85	20.30
29/08/2011 05:20	295.95	34.75	292.57	51.14	287.70	34.14	282.84	20.32
29/08/2011 05:25	296.47	31.18	292.57	51.18	287.70	34.21	282.84	20.34
29/08/2011 05:30	296.99	27.60	292.58	51.21	287.70	34.28	282.83	20.37
29/08/2011 05:35	297.51	24.03	292.58	51.24	287.70	34.35	282.83	20.39

29/08/2011 05:40	298.03	20.46	292.58	51.27	287.70	34.42	282.82	20.41
29/08/2011 05:45	298.55	16.88	292.59	51.30	287.70	34.49	282.82	20.43
29/08/2011 05:50	299.07	13.31	292.59	51.34	287.70	34.56	282.81	20.46
29/08/2011 05:55	299.59	9.73	292.60	51.37	287.70	34.63	282.81	20.48
29/08/2011 06:00	300.11	6.16	292.60	51.40	287.70	34.70	282.80	20.50
29/08/2011 06:05	300.03	6.96	292.58	51.45	287.69	34.74	282.80	20.46
29/08/2011 06:10	299.94	7.75	292.55	51.51	287.68	34.77	282.81	20.42
29/08/2011 06:15	299.86	8.55	292.53	51.56	287.67	34.81	282.81	20.38
29/08/2011 06:20	299.77	9.35	292.50	51.62	287.66	34.84	282.82	20.33
29/08/2011 06:25	299.69	10.15	292.48	51.67	287.64	34.88	282.82	20.29
29/08/2011 06:30	299.60	10.95	292.45	51.73	287.63	34.92	282.83	20.25
29/08/2011 06:35	299.52	11.75	292.43	51.78	287.62	34.95	282.83	20.21
29/08/2011 06:40	299.43	12.55	292.40	51.83	287.61	34.99	282.83	20.17
29/08/2011 06:45	299.35	13.35	292.38	51.89	287.60	35.03	282.84	20.13
29/08/2011 06:50	299.26	14.15	292.35	51.94	287.59	35.06	282.84	20.08
29/08/2011 06:55	299.18	14.95	292.33	52.00	287.58	35.10	282.85	20.04
29/08/2011 07:00	299.09	15.75	292.30	52.05	287.57	35.13	282.85	20.00
29/08/2011 07:05	299.24	15.03	292.28	52.10	287.56	35.17	282.85	19.96
29/08/2011 07:10	299.38	14.32	292.25	52.16	287.54	35.21	282.86	19.92
29/08/2011 07:15	299.53	13.60	292.23	52.21	287.53	35.24	282.86	19.88
29/08/2011 07:20	299.67	12.89	292.20	52.27	287.52	35.28	282.87	19.83
29/08/2011 07:25	299.82	12.17	292.18	52.32	287.51	35.31	282.87	19.79
29/08/2011 07:30	299.96	11.46	292.15	52.38	287.50	35.35	282.88	19.75
29/08/2011 07:35	300.11	10.74	292.13	52.43	287.49	35.39	282.88	19.71
29/08/2011 07:40	300.25	10.03	292.10	52.48	287.48	35.42	282.88	19.67

29/08/2011 07:45	300.40	9.31	292.08	52.54	287.47	35.46	282.89	19.63
29/08/2011 07:50	300.54	8.60	292.05	52.59	287.46	35.49	282.89	19.58
29/08/2011 07:55	300.69	7.88	292.03	52.65	287.44	35.53	282.90	19.54
29/08/2011 08:00	300.83	7.17	292.00	52.70	287.43	35.57	282.90	19.50

## Appendix 8 – Model atmospheres for slant-path geometry

**Input parameters for the 3, 5, 8, 10, 15 and 20-layer model atmospheres using the NCEP/NCAR Reanalysis 1 meteorological data for 29 Aug 2011 at 12:00 and the viewing geometry of the INGV-Catania fix ground-based thermal camera. Additional parameters include the inclusion of the “Rural, Visibility = 23 km” aerosol model.**

ATM Layer	Parameters	3-layer Model	5-layer Model	8-layer Model	10-layer Model	15-layer Model	20-layer Model
1	Elevation (km)	1.154	1.154	1.154	1.154	1.154	1.154
	Pressure (mb)	905.711	905.711	905.711	905.711	905.711	905.711
	Temperature (K)	291.963	291.963	291.963	291.963	291.963	291.963
	Relative Humidity (%)	47.137	47.137	47.137	47.137	47.137	47.137
2	Elevation (km)	2.077	1.616	1.418	1.359	1.286	1.251
	Pressure (mb)	825.856	864.819	882.113	887.333	893.834	896.968
	Temperature (K)	286.623	289.278	290.426	290.769	291.193	291.397
	Relative Humidity (%)	29.712	37.414	41.308	42.545	44.126	44.905
3	Elevation (km)	3.000	2.077	1.681	1.564	1.418	1.348
	Pressure (mb)	753.042	825.856	859.216	869.328	882.113	888.310
	Temperature (K)	281.380	286.623	288.902	289.579	290.426	290.833
	Relative Humidity (%)	18.729	29.712	36.218	38.400	41.308	42.779
4	Elevation (km)		2.539	1.945	1.769	1.550	1.445
	Pressure (mb)		788.570	836.830	851.688	870.546	879.735
	Temperature (K)		283.987	287.381	288.394	289.660	290.269
	Relative Humidity (%)		23.584	31.739	34.659	38.670	40.754
5	Elevation (km)		3.000	2.209	1.974	1.681	1.543

	Pressure (mb)		753.042	815.027	834.406	859.216	871.156
	Temperature (K)		281.380	285.867	287.214	288.902	289.700
	Relative Humidity (%)		18.729	27.814	31.282	36.218	38.805
6	Elevation (km)			2.473	2.180	1.813	1.640
	Pressure (mb)			793.791	817.394	847.949	862.746
	Temperature (K)			284.362	286.033	288.140	289.139
	Relative Humidity (%)			24.375	28.221	33.905	36.968
7	Elevation (km)			2.736	2.385	1.945	1.737
	Pressure (mb)			773.187	800.808	836.830	854.418
	Temperature (K)			282.870	284.863	287.381	288.579
	Relative Humidity (%)			21.371	25.471	31.739	35.218
8	Elevation (km)			3.000	2.590	2.077	1.834
	Pressure (mb)			753.042	784.558	825.856	846.170
	Temperature (K)			281.380	283.697	286.623	288.019
	Relative Humidity (%)			18.729	22.990	29.712	33.551
9	Elevation (km)				2.795	2.209	1.931
	Pressure (mb)				768.638	815.027	838.002
	Temperature (K)				282.536	285.867	287.461
	Relative Humidity (%)				20.750	27.814	31.962
10	Elevation (km)				3.000	2.341	2.028
	Pressure (mb)				753.042	804.339	829.913
	Temperature (K)				281.380	285.114	286.904
	Relative Humidity (%)				18.729	26.038	30.449

11	Elevation (km)					2.473	2.126
	Pressure (mb)					793.791	821.819
	Temperature (K)					284.362	286.342
	Relative Humidity (%)					24.375	28.993
12	Elevation (km)					2.604	2.223
	Pressure (mb)					783.460	813.886
	Temperature (K)					283.618	285.787
	Relative Humidity (%)					22.830	27.620
13	Elevation (km)					2.736	2.320
	Pressure (mb)					773.187	806.030
	Temperature (K)					282.870	285.233
	Relative Humidity (%)					21.371	26.313
14	Elevation (km)					2.868	2.417
	Pressure (mb)					763.048	798.249
	Temperature (K)					282.124	284.681
	Relative Humidity (%)					20.006	25.067
15	Elevation (km)					3.000	2.514
	Pressure (mb)					753.042	790.543
	Temperature (K)					281.380	284.129
	Relative Humidity (%)					18.729	23.880
16	Elevation (km)						2.611
	Pressure (mb)						782.912
	Temperature (K)						283.578
							22.750

	Relative Humidity (%)						
17	Elevation (km)						2.709
	Pressure (mb)						775.277
	Temperature (K)						283.023
	Relative Humidity (%)						21.662
18	Elevation (km)						2.806
	Pressure (mb)						767.793
	Temperature (K)						282.474
	Relative Humidity (%)						20.636
19	Elevation (km)						2.903
	Pressure (mb)						760.382
	Temperature (K)						281.927
	Relative Humidity (%)						19.659
20	Elevation (km)						3.000
	Pressure (mb)						753.042
	Temperature (K)						281.380
	Relative Humidity (%)						18.729

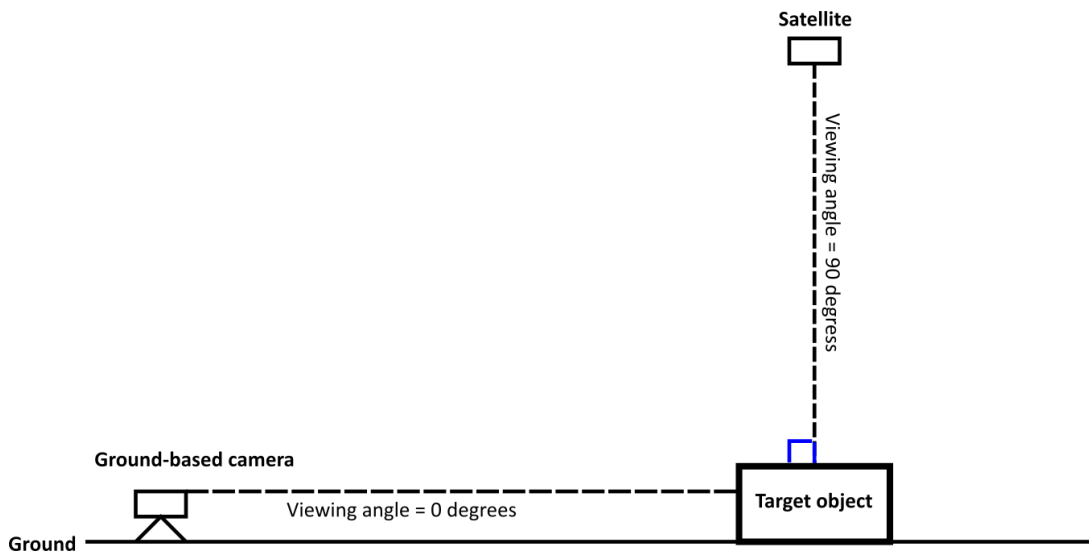
Appendix 9 – Calculated surface temperatures for an apparent temperature of 500 K using model atmospheres created with the NCEP/NCAR Reanalysis 1 meteorological data for 29/08/2011 12:00.

**Calculated surface temperatures for an apparent temperature of 500 K using a slant-path viewing geometry with the different model atmospheres created using the NCEP/NCAR Reanalysis 1 meteorological data for 29 Aug 2011 at 12:00.**

Path-Length (km)	3-layer	5-layer	8-layer	10-layer	15-layer	20-layer
2.0	515.02	513.03	515.17	514.96	515.13	515.07
2.1	515.47	513.43	515.64	515.41	515.60	515.53
2.2	515.91	513.82	516.08	515.85	516.04	515.97
2.3	516.36	514.21	516.53	516.28	516.48	516.41
2.4	516.79	514.59	516.96	516.71	516.91	516.84
2.5	517.20	514.96	517.39	517.13	517.35	517.26
2.6	517.62	515.32	517.81	517.55	517.77	517.68
2.7	518.03	515.69	518.23	517.95	518.17	518.08
2.8	518.42	516.05	518.64	518.35	518.58	518.49
2.9	518.82	516.41	519.04	518.74	518.98	518.89
3	519.22	516.75	519.43	519.14	519.37	519.29
3.1	519.60	517.10	519.83	519.52	519.76	519.67
3.2	519.98	517.43	520.22	519.90	520.16	520.05
3.3	520.36	517.78	520.59	520.28	520.53	520.44
3.4	520.73	518.10	520.98	520.65	520.90	520.81
3.5	521.10	518.43	521.35	521.02	521.28	521.19
3.6	521.46	518.75	521.71	521.38	521.65	521.55
3.7	521.82	519.08	522.09	521.74	522.02	521.91
3.8	522.17	519.40	522.46	522.09	522.38	522.27
3.9	522.52	519.71	522.81	522.44	522.73	522.62
4	522.87	520.02	523.17	522.79	523.10	522.99
4.1	523.22	520.33	523.53	523.14	523.43	523.33
4.2	523.56	520.65	523.86	523.48	523.79	523.68
4.3	523.92	520.95	524.22	523.83	524.14	524.02
4.4	524.24	521.25	524.56	524.16	524.48	524.36
4.5	524.58	521.55	524.90	524.50	524.82	524.70
4.6	524.91	521.85	525.25	524.82	525.15	525.04
4.7	525.23	522.14	525.57	525.15	525.50	525.37
4.8	525.56	522.42	525.92	525.48	525.82	525.70
4.9	525.89	522.73	526.25	525.81	526.15	526.03
5.0	526.22	523.00	526.57	526.14	526.47	526.36
5.1	526.54	523.30	526.90	526.45	526.80	526.68
5.2	526.86	523.59	527.22	526.77	527.12	526.99

5.3	527.17	523.86	527.55	527.09	527.44	527.31
5.4	527.48	524.14	527.87	527.39	527.76	527.63
5.5	527.80	524.42	528.19	527.71	528.08	527.95
5.6	528.10	524.70	528.50	528.01	528.40	528.26
5.7	528.41	524.98	528.82	528.32	528.71	528.56
5.8	528.71	525.25	529.13	528.62	529.01	528.89
5.9	529.02	525.53	529.44	528.93	529.32	529.19
6.0	529.31	525.79	529.75	529.24	529.63	529.49
6.1	529.62	526.06	530.06	529.53	529.94	529.80
6.2	529.91	526.33	530.35	529.83	530.24	530.09
6.3	530.21	526.60	530.67	530.14	530.55	530.40
6.4	530.51	526.87	530.96	530.43	530.85	530.70
6.5	530.80	527.14	531.26	530.73	531.14	530.99
6.6	531.10	527.39	531.57	531.01	531.44	531.29
6.7	531.40	527.65	531.86	531.31	531.74	531.59
6.8	531.68	527.92	532.16	531.59	532.04	531.87
6.9	531.96	528.18	532.46	531.89	532.32	532.17
7.0	532.26	528.44	532.74	532.17	532.63	532.46
7.1	532.55	528.69	533.05	532.46	532.91	532.76
7.2	532.83	528.95	533.33	532.74	533.20	533.05
7.3	533.10	529.20	533.62	533.03	533.49	533.33
7.4	533.39	529.46	533.91	533.31	533.77	533.62
7.5	533.68	529.70	534.20	533.58	534.06	533.89
7.6	533.95	529.96	534.49	533.87	534.35	534.18
7.7	534.24	530.21	534.78	534.15	534.63	534.45
7.8	534.51	530.45	535.05	534.42	534.92	534.75
7.9	534.79	530.70	535.35	534.71	535.19	535.02
8.0	535.06	530.95	535.62	534.98	535.47	535.29
8.1	535.34	531.20	535.90	535.26	535.76	535.59
8.2	535.61	531.45	536.20	535.53	536.04	535.86
8.3	535.89	531.69	536.47	535.79	536.32	536.14
8.4	536.15	531.93	536.75	536.07	536.59	536.40
8.5	536.43	532.18	537.03	536.35	536.86	536.68
8.6	536.69	532.41	537.30	536.61	537.14	536.96
8.7	536.97	532.66	537.58	536.89	537.42	537.22
8.8	537.23	532.90	537.86	537.15	537.68	537.51
8.9	537.49	533.14	538.12	537.41	537.96	537.77
9.0	537.76	533.37	538.41	537.68	538.23	538.03
9.1	538.02	533.61	538.67	537.94	538.49	538.32
9.2	538.29	533.85	538.94	538.21	538.76	538.58
9.3	538.55	534.09	539.21	538.47	539.05	538.85
9.4	538.82	534.32	539.48	538.74	539.32	539.12
9.5	539.09	534.56	539.75	539.01	539.57	539.39
9.6	539.34	534.80	540.02	539.26	539.84	539.64
9.7	539.61	535.03	540.29	539.53	540.11	539.91
9.8	539.86	535.27	540.56	539.78	540.38	540.18
9.9	540.13	535.49	540.83	540.05	540.63	540.43
10.0	540.38	535.73	541.09	540.30	540.90	540.70

Appendix 10 – Viewing angle of ground-based sensor with 0 degrees defining the horizontal and viewing angle of 90 degrees (nadir) of satellite-based sensor.



Appendix 11 – vbs code used by Ganci et al. (2013) for temperature correction which caused the source of the bug in the correction.

```
' VBScript to save all open images in a Researcher session as ir bitmaps only (.bmp)
' Files are not renamed. with the exception of their extensions being updated

Dim WSHShell

Dim sess

Set sess = GetObject("C:\Users\anson_000\Desktop\dist_test\New folder\no_dist.irs")

Dim fs, F, Nomefile, Cartella

Set fs = CreateObject("Scripting.FileSystemObject")

Set F = fs.GetFolder("C:\Users\anson_000\Desktop\dist_test\zero_dist_IR")

Set Cartella = F.Files

Dim temperature (18), rh(18)

temperature(1)= 23.988842
rh(1)= 31.257451
temperature(2)=25.533832
rh(2)=20.080111
temperature(3)=26.411235
rh(3)=-7.534214
temperature(4)=24.933003
rh(4)=3.50484
temperature(5)=23.07806
rh(5)=10.266559
temperature(6)=24.336941
rh(6)=8.802632
temperature(7)=25.023604
rh(7)=2.193505
temperature(8)=25.238186
rh(8)=11.186877
```

temperature(9)=25.080826  
rh(9)=4.849554  
temperature(10)=24.999762  
rh(10)=15.588193  
temperature(11)=24.856707  
rh(11)=22.273616  
temperature(12)=23.712269  
rh(12)=55.924849  
temperature(13)=20.956082  
rh(13)=74.083258  
temperature(14)=19.759191  
rh(14)=77.511802  
temperature(15)=18.924706  
rh(15)=82.022793  
temperature(16)=18.133136  
rh(16)=85.422727  
temperature(17)=18.223738  
rh(17)=84.345048  
temperature(18)=17.479853  
rh(18)=83.625006

For Each Nomefile In Cartella

```
thermimg ="C:\Users\anson_000\Desktop\dist_test\zero_dist_IR\" & Nomefile.Name  
'Wscript.Echo Nomefile.Name  
ora1=Mid(Nomefile.Name,15,2)  
'Wscript.Echo ora1  
ora2=FormatNumber(ora1)  
'Wscript.Echo ora2
```

For d = 1 To 10001 Step 100

'For d = 1 To 502 Step 100

With sess

```

.LoadImage (therming)
.ObjectDistance = d
.RelativeHumidity = rh(ora2-5)
.AmbientTemperature = temperature(ora2-5)
.AtmosphericTemperature = temperature(ora2-5)
.ExtOpticsTemperature = temperature(ora2-5)
.Refresh
End With

    imnameStr = sess.ObjectDistance & "_" & Left(sess.ImageFilename,
Len(sess.ImageFilename) - 3) & ".csv"
    imnameStr = Replace(imnameStr, ":", "-")
    b = sess.SaveImage(imnameStr, 5)
Next
' Wscript.Echo imnameStr
' Wscript.Echo ora2
' ora=ora+1

Next

Set WSHShell = Nothing
set sess = Nothing

```